

Doctoral theses at NTNU, 2020:106

Felix Kelberlau

# Turbulence measurements with fixed and floating profiling wind lidar

ISBN 978-82-326-4564-0 (printed ver.)  
ISBN 978-82-326-4565-7 (electronic ver.)  
ISSN 1503-8181

Doctoral theses at NTNU, 2020:106

**NTNU**  
Norwegian University of  
Science and Technology  
Thesis for the degree of  
Philosophiae Doctor  
Faculty of Engineering  
Department of Energy and Process Engineering

Felix Kelberlau

# Turbulence measurements with fixed and floating profiling wind lidar

Thesis for the degree of Philosophiae Doctor

Trondheim, November 2020

Norwegian University of Science and Technology  
Faculty of Engineering  
Department of Energy and Process Engineering



Norwegian University of  
Science and Technology

**NTNU**

Norwegian University of Science and Technology

Thesis for the degree of Philosophiae Doctor

Faculty of Engineering

Department of Energy and Process Engineering

© Felix Kelberlau

ISBN 978-82-326-4564-0 (printed ver.)

ISBN 978-82-326-4565-7 (electronic ver.)

ISSN 1503-8181

Doctoral theses at NTNU, 2020:106



Printed by Skipnes Kommunikasjon AS

# Summary

Knowledge about turbulence in the wind helps estimate and optimize the profitability of wind turbines. Light detection and ranging (lidar) is a cost-efficient, flexible, and accurate remote sensing technology for measuring wind velocities. Comparisons of mean wind data from lidar and in situ anemometry show good agreement, but estimates of turbulence such as turbulence velocity spectra and turbulence intensity deviate significantly.

In this thesis, we present methods to predict lidar-derived turbulence velocity spectra. For the case of a velocity–azimuth display (VAD) scanning continuous-wave wind lidar, we introduce a numerical model that filters a spectral tensor so the resulting spectra resemble those derived from lidar measurement data. For a Doppler beam swinging (DBS) pulsed wind lidar, we sample computer-generated turbulence data in a similar way to how a lidar measures real wind velocities. Averaging the results from many data series leads to comparable results between simulated and measured lidar spectra. With the help of the spectra, we then identify the causes of systematic deviations between lidar measurements and in situ anemometry. These are, first, spatial averaging along the measurement volumes and, second, cross-contamination between the three turbulence components, which we show has a strong influence on the shape of the spectra and the total variance of the measurement signal.

Two methods are presented to improve lidar measurements of the longitudinal and vertical components of turbulence. First, we describe the method of squeezing that reduces the cross-contamination effect and can be applied to DBS and VAD scanning lidar. The method successfully reduces the effective separation distances between the line-of-sight measurement locations involved in the wind vector reconstruction. Second, we present a two-beam method that removes the spatial

averaging along the measurement cone of VAD scanning lidars by only using the two lidar beams that point into the upstream and downstream directions.

Floating lidar introduces additional challenges in accurately measuring turbulence, since the translational and rotational movement on water influences the measurement data. Using data collected on a VAD scanning lidar mounted on a floating buoy, we investigate the influence of motion in all six degrees of freedom on the wind measurements. We present a motion-compensation method that can correct for the motion-induced error on estimates of turbulence intensity, in cases when time series of motion data and line-of-sight velocities are available.

This thesis concludes that turbulence measurements with currently available profiling wind lidars deviate significantly from one-point measurements. The data processing methods proposed here can overcome some of the measurement errors and can be implemented with existing lidars without changes to their hardware. Turbulence measurements from motion-compensated floating lidars can have an accuracy similar to measurements from fixed lidars. Overall, more work is needed to decrease the remaining uncertainty.

# Sammendrag

Kunnskap om vindens turbulens er viktig for å bestemme og optimalisere lønnsomheten til vindmøller. Lidar (engelsk for light detection and ranging) er en kostnadseffektiv, fleksibel og nøyaktig teknologi for fjernmåling av vindhastigheter. Sammenligninger mellom målte middelhastigheter fra lidar og lokale vindmålinger viser godt samsvar. Karakteristiske verdier som turbulensspektra og turbulensintensitet, som gir informasjon om styrken til fluktuasjoner i vindhastigheten, skiller seg betydelig fra referansemålingene når det gjelder målinger med fjernmåling.

I denne avhandlingen presenterer vi metoder for å forutsi turbulensspektre basert på lidarmålinger. Når det gjelder målinger med kontinuerlige bølgelasere i VAD-modus (engelsk for velocity–azimuth display) presenterer vi en numerisk modell som filtrerer en spektral tensor slik at de resulterende spektrene ligner dem i lidarmålingene. For målinger med pulserte lasere i DBS-modus (engelsk for Doppler beam swinging) forarbeider vi datamaskingenererte turbulensdata på samme måte som en ekte lidar-enhet måler vinden. Hvis resultatene er gjennomsnittet for mange dataserier, er de resulterende spektrene fra simulering og måling sammenlignbare. Vi bruker deretter spektrene for å identifisere årsakene til systematiske avvik mellom lidar-målinger og lokale vindstyrkemålinger. Årsakene er for det første gjennomsnittet av de romlig fordelte målte verdiene langs målevolumene, og for det andre kryssforurensningen mellom de tre turbulenskomponentene, som har en sterk innflytelse på spektrumsformen og målesignalets totale varians.

To metoder blir presentert for å forbedre lidemålingene av de longitudinale og vertikale turbulenskomponentene. Først beskriver vi klemmetoden, som reduserer kryssforurensning og kan brukes både i DBS-modus og i VAD-modus. Metoden reduserer de effektive avstandene mellom måleplassene for siktlinjer som er involvert i rekonstruksjonen av en vindvektor. Etterpå presenterer vi en to-stråle-

metode som forhindrer romlig gjennomsnitt langs målekjeglen i VAD-modus ved bare å bruke de to lidarstrålene som peker i og mot den midlere vindretningen.

Flytende lidar-enheter innebærer ytterligere utfordringer for nøyaktige turbulensmålinger fordi translasjonen og rotasjonen av måleenheten på vann påvirker dens måledata. Basert på data fra en flytende målebøye med en lidar-måleenhet som opereres i VAD-modus, undersøker vi påvirkning av bevegelse i alle seks frihetsgrader på vindmålingene. Vi presenterer en metode som kan kompensere for feilen forårsaket av bevegelsen på målinger av turbulensintensitet når tidsserier med bevegelsesdata og de radielle vindhastighetene målt langs strålens retning er tilgjengelige.

Denne avhandlingen konkluderer med at turbulensmålinger med de for øyeblikket tilgjengelige profilskapende lidarmåleinstrumentene avviker betydelig fra enkeltpunktsmålinger. Databehandlingsmetodene som er foreslått her kan forhindre noen av målefeilene og dessuten implementeres på eksisterende lidar-måleenheter uten endringer av maskinvare. Turbulensmålinger av bevegelseskompenserte flytende lidarenheter har en nøyaktighet som er sammenlignbar med den for en fast lidarenhet. Videre arbeid er nødvendig for å redusere den gjenværende unøyaktigheten.

# Zusammenfassung

Kenntnis über die Turbulenz des Windes hilft bei der Bestimmung und Optimierung der Rentabilität von Windenergieanlagen. Lidar (engl. für light detection and ranging) ist eine kosteneffiziente, flexible und genaue Technologie zur fernerkundlichen Messung von Windgeschwindigkeiten. Vergleiche zwischen gemessenen mittleren Windgeschwindigkeiten von Lidargeräten und lokalen Windmessungen zeigen gute Übereinstimmung. Kennwerte wie Turbulenzspektren und Turbulenzintensität, die Auskunft über die Stärke von Windgeschwindigkeitsschwankungen geben, weichen bei fernerkundlicher Messung jedoch signifikant von Referenzmessungen ab.

In dieser Dissertation präsentieren wir Methoden um auf Lidarmessungen basierende Turbulenzspektren vorherzusagen. Für den Fall von Messungen mit Dauerstrichlasern im VAD-Modus (engl. für velocity–azimuth display) stellen wir ein numerisches Modell vor, das einen spektralen Tensor so filtert, dass die resultierenden Spektren denen von Lidarmessungen ähneln. Für Messungen mit gepulsten Lasern im DBS-Modus (engl. für Doppler beam swinging) tasten wir computer-generierte Turbulenzdaten auf die gleiche Weise ab, wie ein reales Lidargerät den Wind misst. Wenn die Ergebnisse für viele Datenreihen gemittelt werden, sind die resultierenden Spektren aus Simulation und Messung miteinander vergleichbar. Mithilfe der Spektren identifizieren wir anschließend die Ursachen für systematische Abweichungen zwischen Lidarmessungen und lokalen Messungen der Windgeschwindigkeit. Die Ursachen sind, erstens, die Mittelung der räumlich verteilten Messwerte entlang der Messvolumina und, zweitens, die Kreuzkontamination zwischen den drei Turbulenzkomponenten, die einen starken Einfluss auf die Form der Spektren und die totale Varianz des Messsignals hat.

Zwei Methoden werden präsentiert, um Lidarmessungen der longitudinalen und

vertikalen Turbulenzkomponenten zu verbessern. Zum einen beschreiben wir die Quetschmethode, die die Kreuzkontamination reduziert und sowohl im DBS-Modus als auch im VAD-Modus angewendet werden kann. Die Methode reduziert die effektiven Abstände zwischen den einzelnen Messpunkten entlang der Sichtlinien, die an der Rekonstruktion eines Windvektors beteiligt sind. Zum anderen präsentieren wir eine Zweistrahlmethode, die im VAD-Modus die räumliche Mittelung entlang des Messkonus verhindert, indem ausschließlich die zwei Lidarstrahlen genutzt werden, die in und gegen die mittlere Windrichtung zeigen.

Schwimmende Lidargeräte stellen zusätzliche Herausforderungen an genaue Turbulenzmessungen, da die Translation und Rotation des Messgeräts auf dem Wasser dessen Messdaten beeinflussen. Auf Grundlage von Daten einer schwimmenden Messboje mit einem im VAD-Modus betriebenen Lidarmessgerät, untersuchen wir den Einfluss von Bewegung in allen sechs Freiheitsgraden auf die Windmessungen. Wir präsentieren eine Methode, die den durch Bewegung verursachten Fehler auf Turbulenzintensitätsmessungen ausgleichen kann, wenn Zeitreihen von Bewegungsdaten und die entlang der Strahlrichtung gemessenen radialen Windgeschwindigkeiten verfügbar sind.

Diese Dissertation schlussfolgert, dass Turbulenzmessungen mit den zurzeit verfügbaren profilerzeugenden Lidarmessgeräten von Punktmessungen signifikant abweichen. Die hier vorgeschlagenen Datenverarbeitungsmethoden können manche der Messfehler verhindern und sind ohne Hardwareänderungen auf existierenden Lidarmessgeräten umsetzbar. Turbulenzmessungen von bewegungskompensierten schwimmenden Lidargeräten haben eine Genauigkeit, die mit der eines fixierten Lidargeräts vergleichbar ist. Weitere Arbeit ist nötig, um die verbleibende Ungenauigkeit zu reduzieren.

# Acknowledgments

This thesis presents the results of my work since September 2016. Many people helped me along my way and deserve my gratitude. My main supervisor Tania Bracchi has been a reliable companion along the way and has always believed in my abilities. She helped me to get in contact with several local companies in the early phase of my doctorate to give my work a direction. She supported all my ideas and gave me the freedom to work on whatever I believed was useful. I am also grateful for the trust involved in handing over her wind energy course during the time of her maternity leave. I could not have learned more during fulfilment of my teaching duties.

Co-supervisor Lars Sætran offered his two lidar devices and gave me the keys to his field station Skipheia on Frøya. He introduced me to his group, gave me a friendly start at NTNU and taught me the mindset of having fun while doing research. Thanks for motivating me to keep up the good work. Jon Pharoah visited many times, showed genuine interest in my work and helped me troubleshoot some of my programming attempts. Odne Burheim is another co-supervisor in my team and was always generous with supplying ENERSENSE funding for all my monetary demands. He encouraged me to do research stays abroad and travel whenever I considered it useful for my work.

This brings me to expressing my deepest appreciation to my co-supervisor Jakob Mann. I remember the evening he sent me an email two weeks after I presented my squeezed processing approach to all my lidar heroes at DTU. He wrote that he started to think about how to calculate the model spectra for the approach and shared his equations with me. From then on, I knew that my PhD would be a success. Throughout the past two years, his continuous excellent and friendly guidance taught me a lot and his feedback makes me feel proud.

Jakob, Torben Mikkelsen, and Mikael Sjöholm invited me to stay at DTU in Risø where I spent three productive months surrounded by very kind and open-minded wind experts. Alfredo, Anna-Maria, Dominique, Ebba, Elliot, Leonardo, Robert, Nikola, Nikolas, Pedro, and Tobias are just a selection of all the great people I got to know in Denmark and who made me feel welcome away from home.

For working with floating lidar, the collaboration with Fugro Norway AS was essential and I would like to thank Vegar Neshaug and Lasse Lønseth for including me in the team and sharing their measurement data. Your trust in my work is very motivating.

Most of the time at work I spent in one of my three offices in Trondheim that I consecutively occupied and shared happily with Laura, Jake, Shiplu, Ebi, and Ailo. I thank you all for making my work days fun. I also thank the rest of my dear colleagues, Benham, Ellen, Faranak, Frank, Hujjat, Ian, Kjersti, Lena, Markus, Pauline, Robert, Yash, and Zoreh who distracted me from work whenever it got too lonesome. You made my work days and many social evenings very entertaining.

Working in Trondheim has been very enjoyable because I have always felt comfortable as a member of the Norwegian society, surrounded by mountains, lakes, and fjords. I am very grateful for having found several wonderful friends here.

The biggest downside of living in Norway is certainly the distance from my family in Germany. I am blessed with my parents and brothers who are always there for me. Your support is very important to me and feels so unconditional.

My beloved Kam has contributed to my work in many ways. She improved my writings by proofreading every single word of this thesis and has always been interested in explanations of my most recent ideas. She truly became the second lidar expert in Trondheim, but most importantly, she provided unlimited trust and comfort. Thank you, Kuku.

Lastly, I would like to acknowledge the work of Joachim Reuder and Sandrine Aubrun involved in taking the task of being my opponents and the efforts of Pål-Tore Selbo Storli to manage the work of the scientific committee.

# Contents

<b>Summary</b>	<b>iii</b>
<b>Sammendrag (Summary in Norwegian)</b>	<b>v</b>
<b>Zusammenfassung (Summary in German)</b>	<b>vii</b>
<b>Acknowledgments</b>	<b>ix</b>
<b>List of Articles</b>	<b>xiii</b>
<b>1 Introduction</b>	<b>1</b>
1.1 State of the art . . . . .	1
1.2 Research questions and aim . . . . .	5
1.3 Overview of the articles . . . . .	7
<b>2 Background</b>	<b>11</b>
2.1 Origin of wind . . . . .	11
2.2 Turbulence in the atmospheric boundary layer . . . . .	13
2.3 Lidar measurements of wind velocity . . . . .	19
<b>3 Methods</b>	<b>23</b>
3.1 Time series analysis . . . . .	23
3.2 Turbulence velocity spectra . . . . .	27
3.3 Comparison of field measurements . . . . .	28
3.4 Scatter analysis: Deming regression . . . . .	29
3.5 Lidar modeling . . . . .	31
3.6 Lidar simulation . . . . .	31
3.7 Motion compensation . . . . .	32
<b>4 Discussion</b>	<b>35</b>
4.1 Discussion of the results . . . . .	35
4.2 Recommendations for further work . . . . .	38
<b>5 Article 1: Better turbulence spectra from VAD scanning lidar</b>	<b>51</b>
<b>6 Article 2: Cross-contamination effect on turbulence spectra from DBS lidar</b>	<b>71</b>
<b>7 Article 3: Taking the Motion out of Floating Lidar: TI Estimates with a CW Lidar</b>	<b>95</b>



# List of Articles

1. Kelberlau, F. and Mann, J. (2019). Better turbulence spectra from velocity–azimuth display scanning wind lidar. *Atmospheric Measurement Techniques*, 12(3):1871–1888. doi: 10.5194/amt-12-1871-2019.
2. Kelberlau, F. and Mann, J. (2020). Cross-contamination effect on turbulence spectra from Doppler beam swinging wind lidar. *Wind Energy Science*, 5(2):519–541. doi: 10.5194/wes-5-519-2020.
3. Kelberlau, F., Neshaug, V., Lønseth, L., Bracchi, T., and Mann, J. (2020). Taking the Motion out of Floating Lidar: Turbulence Intensity Estimates with a Continuous-Wave Wind Lidar. *Remote Sensing*, 12(5):898. doi: 10.3390/rs12050898.



# Chapter 1

## Introduction

### 1.1 State of the art

This thesis is about wind velocity measurements which have many applications. Some examples are weather forecasts incorporating wind speed data from different locations [Ernst et al., 2007], wind load estimations on tall structures like bridges and buildings being often based on wind speed measurements at the planned site [Cheynet et al., 2017b], and aviation relying on information about the wind conditions to provide safety [Shun and Chan, 2008]. In the field of wind energy, wind speed measurements are used for two main purposes: first, the prediction of electricity production, and second, the determination of structural loads of wind turbines. The work presented here has applications in the wind energy sector, but its findings can be applied to other sectors.

Knowledge about the mean wind velocity at the location of a wind turbine is key to predict its electricity production because of the cubic relation between wind velocity and power [Sempreviva et al., 2008], and the amount of turbulence is also relevant for electricity production [Bardal and Sætran, 2017, Kaiser et al., 2007, Gottschall and Peinke, 2008, Clifton and Wagner, 2014]. This is because the cubic relation between wind velocity and power implies that turbulent wind always contains more kinetic energy than steady wind of the same mean velocity. In Kelberlau and Bracchi [2017] we show that not all of the excess energy that is contained in turbulent wind can be extracted by wind turbines. This is caused, first, by the high inertia of their rotors that leads to a slow response of the rotor rotational speed to varying wind speeds and, second, by their long rotor blades that do not offer ideal aerodynamic performance under the influence of turbulence with length scales smaller than the blade length.

Estimating the turbulence at a designated wind turbine site can also assist in selection of a wind turbine type which is best suited to the expected structural loads in order to minimize the levelized cost of energy [IEC61400, 2019, Fuglsang et al., 2002, Thomsen et al., 2001, Sathe et al., 2012]. Real time information about changes in wind velocity at a wind turbine site can be used to mitigate aerodynamic loads [e.g. Aubrun et al., 2017, Schlipf et al., 2012].

Wind speed measurements are conventionally taken by in situ sampling with cup or sonic anemometers on tall meteorological masts that reach the hub height of the envisioned wind turbines. But the construction of tall meteorological masts is expensive and requires construction permits and transportation of heavy building materials to the site. After a mast has been erected, it is immobile and measurements at changing locations are not feasible. A possibility to measure the wind remotely from the ground is therefore favorable, and profiling wind light detection and ranging (lidar) devices open up this possibility. These devices are placed on the ground and can measure radial wind velocities along laser beams that they direct into changing directions. Two different scanning strategies are currently used for commercially available profiling wind lidar units. One is called velocity–azimuth display (VAD) scanning and refers to lidar units that maintain a fixed elevation angle of their laser beam while performing complete azimuth rotations. The other scanning strategy is called Doppler beam swinging (DBS) and lets the laser beam accumulate measurement data from one beam direction before it swings into the next direction. Several of these radial wind velocities measured along the lines of sight are then combined to reconstruct three-dimensional wind vectors.

The averages of these reconstructed wind vectors are accurate representations of the real mean wind velocities at several adjustable height levels above the lidar [Emeis et al., 2007, Smith et al., 2006]. One important limitation to this statement is that the flow field above the lidar must be horizontally homogeneous in the mean [Bingöl et al., 2008]. In other words, the mean wind vectors at each elevation must be identical at all measurement locations. This requirement is fulfilled in non-complex terrain, like offshore or in flat terrain without significant obstacles.

Measurements of instantaneous wind velocity, however, show errors because even when the flow field is horizontally homogeneous in the mean, it is not homogeneous at each instance in time and space due to the spatial structure of wind speed variations in the atmospheric boundary layer [Sjöholm et al., 2008]. This makes turbulence measurements with profiling wind lidars challenging. Eberhard et al. [1989] were the first to estimate second-order turbulence statistics from Doppler lidar measurements. But comparisons of lidar-estimated velocity variance with reference values from meteorological masts show large deviations [Peña et al., 2009]. Sathe and Mann [2013] present a comprehensive overview of turbulence

measurements with ground-based wind lidar.

Sathe et al. [2011] model the errors in the second-order statistics calculated from lidar-measured time series of wind velocities. They find that the velocity variance calculated from lidar measurements of the three wind vector components often lies far below the real value. But under conditions characterized by unstable atmospheric stratification, the horizontal components show systematically higher values. There are several causes for these deviations. Among them are, first, the line-of-sight velocity estimates are weighted averages of the radial wind velocities within extended measurement volumes. This line-of-sight averaging effect has been extensively investigated [e.g. Sjöholm et al., 2009, Lindelöw, 2008, Kristensen et al., 2011, Held and Mann, 2018]. Second, the combination of line-of-sight velocities from spatially separated measurement locations leads to a cross-contamination error during the wind vector reconstruction, when the relevant real wind vectors are not identical. Wyngaard [1968] describes the effect for small-scale turbulence measured with hot wires. However, little research has studied the influence of cross-contamination on measurements with profiling wind lidar. Sathe et al. [2011, 2015] and Newman et al. [2016a,b] mention contamination as a source of error but do not describe it in detail.

In order to better understand the origin and magnitude of the cross-contamination error, it is helpful to look at the turbulence velocity spectra derived from lidar measurements. However, previous research has left important gaps. Hardesty et al. [1982] observed interference effects when using lidar measurements that were sampled along a vertical circular path to create turbulence velocity spectra. However, their interpretation is not directly transferable to the situation of profiling wind lidars because of the different orientation of the lidar beams. Canadillas et al. [2010] present spectra from DBS pulsed wind lidar measurements and observe an increase of spectral energy that cannot be caused by line-of-sight averaging. But the real cause remains unknown. Sathe and Mann [2012] develop a model for predicting the spectra of DBS pulsed wind lidar and interpret the shape of the resulting spectra. Their model is unfortunately limited to the case of inflow being aligned with two of the lidar beams. For VAD scanning profiling wind lidar, no model for predicting spectra is currently available.

Several methods to improve profiling wind lidar's ability to measure turbulence have been suggested. One of them is the six-beam method, which calculates the second-order wind statistics from the variances of the lidar measured line-of-sight velocities [Sathe et al., 2015]. The estimates resulting from this method are not influenced by cross-contamination, and line-of-sight averaging is the primary remaining cause of error. The first drawback of this method is that its mathematical requirements are not fulfilled (without any further assumptions) by VAD scanning

with only one beam elevation angle, nor by DBS scanning with only five beam directions. The second drawback is that the six-beam method cannot be used to create time series of wind vectors. The spectral distribution of turbulent energy therefore cannot be estimated with this method.

Another method to compensate for the effect of cross-contamination between the velocity components is included in the turbulence error reduction model suggested by Newman and Clifton [2017]. It works by applying a cascade of techniques like noise removal, spectral fitting, using uncontaminated data from the vertical beam, and machine learning with reference data from a collocated mast. In Newman et al. [2016b], they present a more direct approach that works by means of auto-correlation functions derived from collocated mast measurements. This method is, however, only applicable when a meteorological mast is available. Additional details about the different methods to improve lidar estimates of turbulence are provided in articles 1 and 2 of this thesis.

Currently around 96% of the global installed wind power is located onshore, but the share of offshore wind turbines is growing [GWEC, 2019]. Cost reductions are essential to make electricity from offshore wind farms cheaper than conventional power generation [Jansen et al., 2020]. The costs of constructing meteorological masts offshore are very high, and in situ anemometry becomes prohibitively expensive as offshore wind farms move further away from the coast into deeper water regions [Berkhout et al., 2019]. Floating buoys that carry profiling lidar devices can be a cost-efficient alternative to acquire bankable wind data. But their motion in waves and wind must be considered when measurement data from floating lidar are analyzed. In general, estimates of average wind velocity are only slightly influenced by the motion of the floating buoy. Tiana-Alsina et al. [2017] show with numerical simulations that the error on horizontal mean wind speed with a moving lidar is small. Measurements show that good agreement with reference measurements can be reached even without any form of motion compensation [Mathisen, 2013, Gottschall et al., 2014a]. For reliable determination of the mean wind direction it is sufficient to compensate the measurement values for changes of the average orientation in yaw direction [Gottschall et al., 2017].

In contrast, measurements of instantaneous wind vectors and the turbulence statistics derived from them are strongly influenced by motion of the floating lidar in all six degrees of freedom [Gottschall et al., 2014b]. Different methods have been proposed to mitigate the influence of motion on turbulence estimates from floating lidar devices. They include mechanical motion compensation [Tiana-Alsina et al., 2015], low-pass filtering of measurement data [Gutiérrez et al., 2015], a motion compensation algorithm based on simulations of lidar sampling [Gutiérrez-Antuñano et al., 2018, Yamaguchi and Ishihara, 2016], and compensation of the

lidar data for the measured motion. None of these methods has proven to be reliable for measuring turbulence with profiling lidars with an accuracy similar to a fixed lidar unit of the same type. Further details about these methods are provided in article 3 of this thesis. In summary, the science of floating lidar is an emerging research area, and the current state-of-the-art techniques have still not addressed several knowledge gaps.

## 1.2 Research questions and aim

The work presented in this thesis is motivated by first, the importance of reliable turbulence estimates from wind lidars; second, the difficulties involved in measuring fluctuating wind velocities with profiling wind lidars; and third, the additional challenges imposed by offshore deployment.

The overall research aim is to develop and evaluate methods that improve turbulence estimates from commercially available fixed and floating profiling wind lidars. My hypothesis is that turbulence measurements from commercially available profiling wind lidar can be improved by smart data processing.

In the following, three research questions are defined that direct the work presented in the three articles that form the main part of this thesis.

### Research question 1:

*How does the effect of cross-contamination between the three turbulence velocity components influence lidar-based wind velocity measurements in conjunction with other systematic sources of error?*

Answering this question requires a more detailed analysis of lidar sampling of turbulent wind than what is currently available in the state of the art. As described in section 1.1, previous works show that cross-contamination exists in lidar measurements with diverging beams, but a deeper insight into the mechanisms that create it is missing. The first research goal is to close this gap by presenting and analyzing turbulence velocity spectra for both continuous-wave (cw) VAD scanning and pulsed DBS lidar measurements in arbitrary wind directions. Turbulence velocity spectra are good means of visualization for lidar measurement errors, especially when the contribution of the different wind velocity components to the measurements can be predicted. Finding possibilities to create such theoretical spectra is therefore an important milestone in order to be able to investigate the influence of the different error sources on lidar-measured turbulence. In addition, the spatial and temporal aspects of the scanning strategies must be considered to understand all features that appear in the spectra.

### **Research question 2:**

*Can advanced data processing methods effectively reduce the error introduced by cross-contamination and averaging along the measurement cone?*

As mentioned in the description of the state of the art in section 1.1, none of the previously described methods to improve turbulence estimates from profiling lidar are able to correct lidar-measured time series of wind data. The work presented in this thesis aims to improve lidar measurements of turbulent wind by reducing the influence of cross-contamination on the measurement data. Cross-contamination is caused by reconstructing wind vectors from line-of-sight velocities whose measurement volumes are spatially separated. The goal is to mitigate the effect of longitudinal separations, i.e., separations along the mean wind direction, from the measurement data. This goal might be achieved by considering the time it takes an air volume to move from its first to a second measurement location where it can get measured again. The wind vectors can then be reconstructed from line-of-sight velocities that were measured at locations that lie seemingly closer together. This approach requires Taylor's frozen turbulence hypothesis to be valid for the relevant length and time scales. To prove the validity of this assumption is therefore a milestone.

Averaging along the measurement cone is an effect that occurs when more line-of-sight velocities than mathematically necessary are included in the wind vector reconstruction process of VAD scanned line-of-sight data. This type of averaging might be circumvented by limiting the number of line-of-sight velocities taking into account the mean wind direction. After completion of the work on research questions one and two, the thesis might also be able to give an answer about which of the two lidar types, cw VAD or pulsed DBS, is better suited for measuring turbulence.

### **Research question 3:**

*Is it possible to measure turbulence intensity with a floating lidar as accurately as with a fixed lidar, when its motion is compensated for at a line-of-sight level?*

When a lidar unit is mounted on a floating device like a buoy, it can move and its measurement data is corrupted by the influence of the relative motion between the lidar and the wind field, as described in section 1.1. A gap in research, though, is the missing description and validation of a motion compensation algorithm that can remove the effect of lidar motion on measurements in the field. Thus, the last goal of this thesis is to develop and test such an algorithm. A prerequisite for successful development of such an algorithm is to explain the different sources of error caused by lidar motion. In this context, it is important to have the work on

research question 1 completed because it helps to understand that motion in one degree of freedom can influence more than one component of the reconstructed wind vectors and that the magnitude of this contamination depends on frequency and phase of the motion.

### 1.3 Overview of the articles

For *article 1*, "Better turbulence spectra from velocity–azimuth display scanning wind lidar," published in *Atmospheric Measurement Techniques*, we work with a VAD scanning cw wind lidar. The device we chose is an early predecessor of the ZX 300 that is one of the two currently most widely used lidar devices in the wind industry. Findings from work with this machine can thus easily be adapted by the manufacturer of this lidar. We decided to base our analysis on the lidar-derived turbulence velocity spectra of the three wind vector components and compare them to spectra from reference instruments. In contrast to a comparison of only the variances that is found in previous studies, a comparison of the spectra makes it easier to determine causes for lidar specific measurement errors. This accounts in particular in cases where the damping effects of averaging along the lidar lines-of-sight and along the measurement cone, as well as the limited scanning rate is counteracted for by the effect of cross-contamination. The article gives a thorough description of these different sources of error that are inherent in VAD sampling of turbulent wind by means of a cw Doppler lidar. Knowledge about the error causes can help find methods for systematic error correction.

Following this, we present two new methods of processing line-of-sight velocity data. One of these, which we named the method of squeezing, aims at eliminating the cross-contamination effect, i.e., influence on one velocity component by a different velocity component. The second method is two-beam processing which eliminates the averaging along the measurement circle. We model the lidar-derived auto-spectra from conventional VAD processing and with the novel methods, and compare them with results from measurement data from a collocated meteorological mast. The model spectra allow it to analyse the contribution of the individual wind velocity components, which is very useful in the process of understanding deviations between the shape of lidar-derived spectra and reference spectra. Such an analysis can also help to find causes for deviations between the model and experimental spectra. Furthermore, the availability of model spectra makes it possible to identify the effects of the new data processing methods in the measurements and to validate or discard the assumptions we made. This study is seeking an answer to research questions 1 and 2.

*Article 2*, "Cross-contamination effect on turbulence spectra from Doppler beam swinging wind lidar," published in *Wind Energy Science*, extends the findings of

article 1 to a pulsed DBS wind lidar, which is another type frequently used in research and industry. The article describes the application of the method of squeezing that we introduced in article 1 to this lidar type. It illuminates the limitations involved in the low number of available beam directions and low scanning rate. The low number of lidar beam directions make the velocity spectra sensitive to the wind direction relative to the beam directions which we consider in our analysis. We put emphasis on this aspect because the current literature shows spectra from this lidar type only for aligned inflow, yet the impact of the wind direction is large. Applying the two-beam method is not useful here because the mean wind direction in most cases does not coincide with one of the azimuth angles of the lidar beams and because averaging along the measurement circle is not relevant for this lidar type.

The measurement geometry also prevents that a handy mathematical model like in article 1 can be developed. We therefore decided to simulate the lidar processing by sampling numerically generated wind data in a turbulence box for our comparisons with measurement data of a collocated meteorological mast. The resulting simulated spectra are not as smooth as modeled spectra but serve the same purpose well, i.e., having the possibility to visualize the influence of the different velocity components on the lidar-derived spectra and to see the impact of the method of squeezing. The article completes the answers to research questions 1 and 2 by extending our findings to the case of a pulsed DBS lidar.

In *article 3*, "Taking the Motion out of Floating Lidar: Turbulence Intensity Estimates with a Continuous-Wave Wind Lidar," published in *Remote Sensing*, we determine, analyze, and compensate for the motion-induced error on a floating lidar. I chose to include floating lidar into this thesis because of its high relevance for offshore wind industry and because my previous work with line-of-sight velocity data for article 1 and 2 created a solid foundation for studying the effects of motion on a floating profiling wind lidar.

We chose the ZX 300, a VAD scanning cw wind lidar for our study because it is the standard instrument for being mounted on the Fugro SEAWATCH Wind LiDAR Buoy and because the available land-based reference lidar is of the same type. We apply a motion compensation algorithm to the line-of-sight data of the floating lidar. This advances the current state of the art for floating VAD lidar, and makes it possible to correct not only the turbulence statistics but also each single reconstructed wind vector. We measure a vertical velocity profile at eleven altitudes. Thus, due to the consecutive focusing of cw lidar, we are confronted with a sampling rate at each height level that is too low to create conclusive turbulence velocity spectra. Therefore, we limit our work to the processing of turbulence intensities which we compare with reference data from a land-based fixed lidar of

the same type. This comparison makes it possible to isolate the effects caused by the motion of the floating lidar from the lidar-specific errors that we determined in article 1. The study uses also the findings of article 1 about cross-contamination to describe the undesired influence of the motion in all six degrees of freedom on the wind velocity measurements. The article aims to answer research question 3.

Fig. 1.1 gives an overview of the three articles.

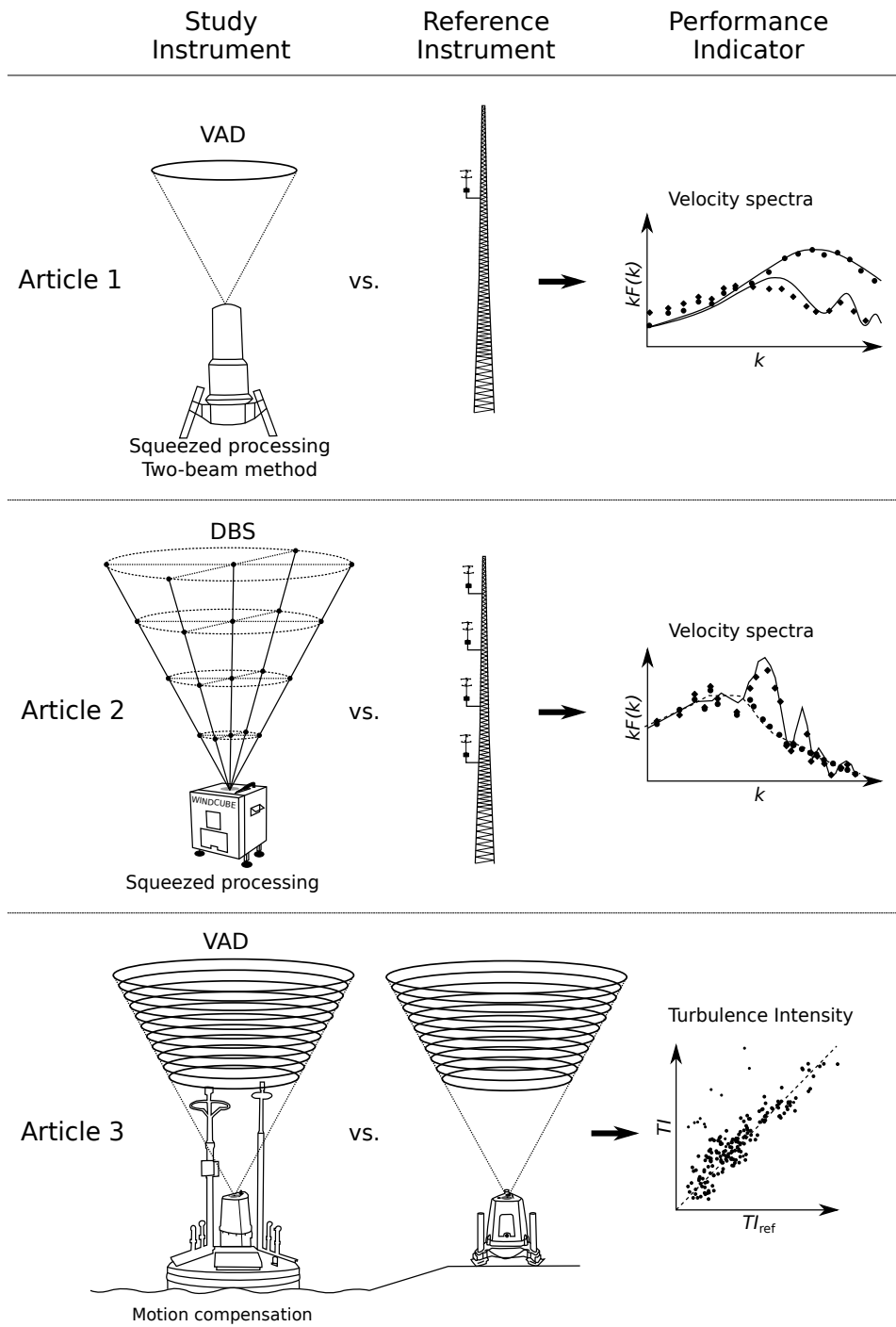


**Figure 1.1:** Overview of the three articles included in this thesis.

## Chapter 2

# Background

The initial source of wind energy is solar radiation. Fig. 2.1 shows that the amount of solar energy that reaches the world's surface is unevenly distributed. Close to the equator and along the desert belts where the light's mean angle of incidence is high, the solar power is several times stronger than close to the poles where the light hits the planet's surface nearly tangentially [Manwell et al., 2010]. In addition, the steady rotation of the earth and its ecliptic lead to a diurnal cycle of illumination that is more pronounced at the equator than towards the poles. This uneven distribution of solar radiation leads to differences in the surface temperatures around the globe.

### 2.1 Origin of wind

The surface transfers its heat to the surrounding air that expands according to the general gas equation. The resulting pressure forces accelerate the air molecules along the pressure gradients. The latitudinal component of the resulting motion, i.e., motion in the north or south direction, is influenced by the Coriolis force that originates from the earth's rotation and its nearly spherical shape. For example, air moving north in the northern hemisphere is deflected east by the Coriolis force. Fig. 2.2 shows the major wind belts, i.e., a simplified global pattern of wind directions without consideration of the shape and properties of the continents [Hiester and Pennell, 1981]. Over the big oceans, this model often agrees with the prevailing wind conditions. But the different absorption coefficients and heat capacities of oceans, glaciers, and land masses make onshore and nearshore conditions more complex and cause regional effects like the Mistral, Chinook, and Harmattan winds [Lynn, 2011]. The weather and other local effects like monsoons, hurricanes, sea breezes, mountain winds, thunderstorms, etc. make wind conditions often un-

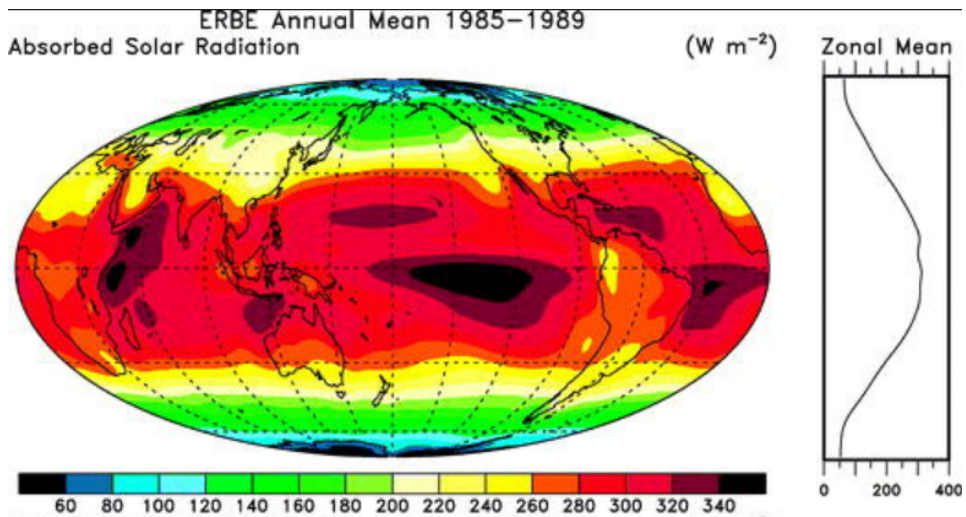


**Figure 2.1:** Annualized mean measurements for the period Feb 1985 – Apr 1989 for the absorbed solar radiation in  $W m^{-2}$ . The color key is under the plot and the contour interval is  $20 W m^{-2}$ . Zonal mean profile panel is given at right. With permission adapted from Trenberth and Stepaniak [2003]

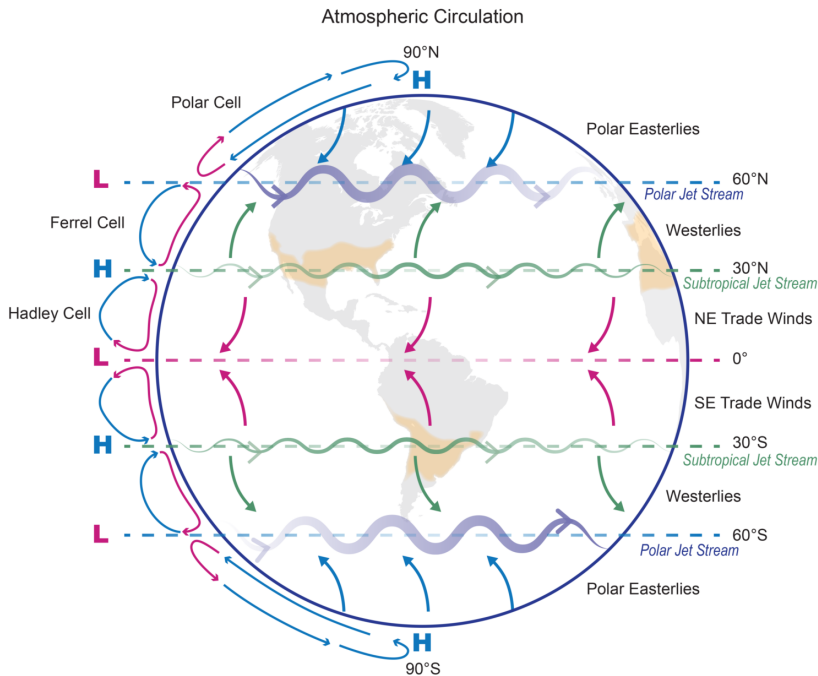


**Figure 2.2:** Model of global wind zones and atmospheric pressure over the planet without consideration of real topography. Adapted from Perlwitz et al. [2017]

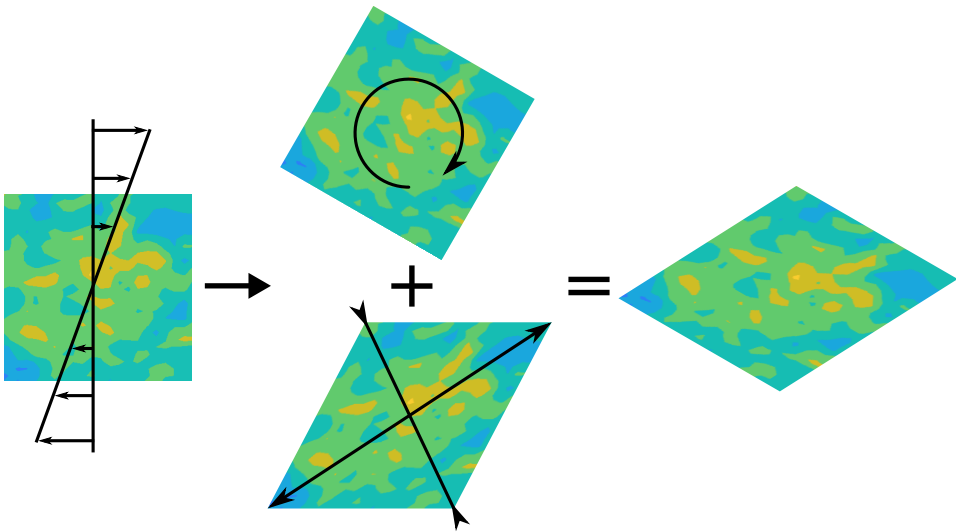


**Figure 2.3:** The effect of linear shear on a fluid volume can be decomposed into rigid-body rotation and irrotational shear strain. Reproduced from Davidson [2015].

predictable. More comprehensive information about the large-scale atmospheric circulation is described by e.g., Lorenz [1967].

## 2.2 Turbulence in the atmospheric boundary layer

At a single location the wind velocity is not constant but fluctuates. Long-term measurements show seasonal fluctuations. Synoptic scale weather events are represented by fluctuations with periods of a few days. And diurnal changes of the horizontal wind speed cause fluctuations with periods of 12 or 24 hours. For fluctuations with shorter periods down to approximately one hour, the spectral energy content decreases before it increases again for higher frequencies [Van der Hoven, 1957]. This frequency band of low energy content is called the spectral gap. Its pronunciation varies with measurement height and from location to location as shown in Larsén et al. [2016]. The spectral gap acts as the separation between what is called mean wind speed variations and turbulence.

### Turbulence production

The research object throughout this thesis is the turbulent wind velocity fluctuations that occur faster than once per ten minutes. They are mostly created in the atmospheric boundary layer, which is the lowest part of the troposphere from the ground up to a few hundreds or thousands of meters above. In the atmospheric boundary layer, the air flow is influenced by the presence of the ground. Depend-

ing on its surface roughness, the ground exerts weaker or stronger frictional forces which slow down the mean flow and create the vertical profile of wind velocity. (An example can be seen in Fig. 7 of article 3.) The resulting shear forces are also an important source of turbulence. A simplified visualization of this effect is depicted in Fig. 2.3. In an air volume that is moving with the mean wind velocity, the top side is attacked by faster surrounding air than the lower end. The resulting shear stress will rotate and stretch the air package. This process is a transfer of energy from the steady mean flow to the wind speed fluctuations and can be seen as production of turbulence.

A second effect that can produce turbulence kinetic energy in the wind is caused by thermal buoyancy. Besides having a vertical profile of horizontal mean wind velocity, the atmospheric boundary layer has also a vertical temperature profile which usually shows lower temperatures at high altitudes but can in some cases also be inverted. The temperature profile determines the atmospheric stability class and if buoyancy produces or suppresses vertical turbulence. An important value for atmospheric stability is the adiabatic lapse rate. It is the temperature rate of change with height at which air in an insulated flexible air balloon cools down while it is moved upwards. The decreasing ambient pressure leads to a decrease in density and temperature of the air inside the balloon. If the rate of temperature change in the atmospheric boundary layer is identical to this adiabatic lapse rate at all heights, the atmospheric stability condition is called neutral. Under neutral atmospheric conditions, buoyancy does not have any effect on turbulence production. But usually, the temperature profile deviates from the neutral stratification. Unstable atmosphere is found when the local temperature profile is steeper than the adiabatic lapse rate. Air warmed up close to the ground is then accelerated by the force of buoyancy on its way upwards because it cools down more slowly than the surrounding air. The resulting vertical motion produces turbulence kinetic energy because an identical amount of cooler air sinks down and a circulation occurs. Such a situation is often found during daytime, when the heating of the ground is the strongest. Stable atmospheric stratification, on the contrary, suppresses turbulence because vertical motion is slowed down when buoyancy acts against convection.

### **Atmospheric stability**

The qualitative description of turbulence production by shear and buoyancy forces given above has to be quantified because for example a slightly unstable temperature profile can create large turbulent eddies when the shear forces are low in low wind phases. The same temperature profile contributes less to the creation of turbulence in strong wind phases when turbulent structures are rapidly torn apart by high shear forces. Such a quantification can be made by means of the flux Richard-

son number  $R_f$ . It sets the terms of turbulence production by buoyancy and shear into a relation.

$$R_f = \frac{\frac{g}{\theta} \overline{w'\theta'}}{\overline{u'w'} \frac{\delta \bar{u}}{\delta z}} \quad (2.1)$$

where  $g$  is gravity,  $z$  height,  $\theta$  potential temperature,  $u$  and  $w$  are the longitudinal and vertical wind velocity components, the prime denotes fluctuations around the mean, and the overline represents averaging.

Since measurement values of the heat and momentum fluxes are not always available, the gradient Richardson number  $R_i$

$$R_i = \frac{\frac{g}{\theta} \frac{\delta \bar{\theta}}{\delta z}}{\left(\frac{\delta \bar{u}}{\delta z}\right)^2} \quad (2.2)$$

can be used instead. It uses the vertical gradients of mean temperature and wind speed that are easier to measure. Both Richardson numbers indicate neutral atmospheric stability when they are zero due to high shear forces and a weak contribution of buoyancy. Stable and unstable conditions are determined by the sign of the Richardson numbers with a negative value indicating unstable conditions and a positive value indicating stable conditions. Since the denominator in both formulas keeps a constant sign, the eddy sensible heat flux in  $R_f$  and the vertical potential temperature gradient in  $R_i$  decide about stable or unstable atmosphere.

Both buoyancy and shear forces are usually the strongest close to the ground. But shear forces decrease faster with height than buoyancy. The Richardson number is therefore sensitive to the measurement height  $z$ . To express this height dependency more explicitly the Monin-Obukhov stability parameter  $\zeta$  can be used which is a variation of the flux Richardson number  $R_f$

$$R_f \approx \zeta = \frac{z}{L} \quad (2.3)$$

where the Obukhov length

$$L = \frac{-\bar{\theta} u_*^3}{k g \overline{w'\theta'}} \quad (2.4)$$

with  $k$  being the von Kármán constant and  $u_*$  the friction velocity. Like for the Richardson number the sign of  $L$  determines the stability. The magnitude of the Obukhov length is a measure for up to what height the shear production is the dominant production term. A high absolute value of the Obukhov length means therefore that the occurring turbulence is hardly affected by buoyancy which defines neutral atmospheric conditions. Low positive  $L$  values indicate very stable conditions in which the buoyancy forces suppress shear driven turbulence effectively.

Low negative  $L$  values mean accordingly that buoyancy is amplifying turbulence production and that the atmospheric stratification is very unstable. A frequently used stability classification based on the Obukhov length is for example given in Gryning et al. [2007].

### Turbulence modeling

Both production mechanisms create large-scale turbulent structures which have a limited lifetime. They decay and transfer their energy into smaller eddies which again distribute their energy into even smaller eddies and so on until the turbulence kinetic energy is finally dissipated at the smallest scales of turbulence.

The spectral distribution of atmospheric turbulence can be modeled. Kaimal et al. [1972] give universal equations for the auto-spectra of the three velocity components for neutrally stratified flow over flat terrain according to

$$\frac{k_1 F_{u(k_1)}}{u_*^2} = \frac{52.5 k_1 z}{(1 + 33 k_1 z)^{\frac{5}{3}}} \quad (2.5)$$

$$\frac{k_1 F_{v(k_1)}}{u_*^2} = \frac{8.5 k_1 z}{(1 + 9.5 k_1 z)^{\frac{5}{3}}} \quad (2.6)$$

and

$$\frac{k_1 F_{w(k_1)}}{u_*^2} = \frac{1.05 k_1 z}{(1 + 5.3 k_1 z)^{\frac{5}{3}}} \quad (2.7)$$

where  $k_1 = 2\pi f/U$  is the wavenumber in longitudinal direction. These equations describe the two-sided one-point spectra normalized by the friction velocity. The IEC61400 [2019] standard suggests a slightly modified equation and parameters so that the spectra are defined by the horizontal mean velocity and its variance. Eqs. 2.5–2.7 do not contain information about the spatial structure of turbulence, and a coherence model must be used to calculate two-point spectra based on the Kaimal spectra.

The purpose of a coherence model is to represent the spatial extension of turbulent structures. With two adjacent anemometers, identical wind velocities are measured at the same time. But with increasing distance between them, only large-scale fluctuations are measured simultaneously, while small-scale fluctuations become uncorrelated. IEC61400 [2019] suggests using equation 2.8 to estimate the coherence between two points on a vertical rotor plane as a function of the wavenumber.

$$\gamma(r, k) = \exp \left[ -12 \sqrt{\left( \frac{kr^2}{2\pi} \right)^2 + \left( \frac{0.12r}{L_C} \right)^2} \right] \quad (2.8)$$

is the coherence between two points separated by the distance  $r$  in vertical or lateral direction.  $L_C$  is a coherence scale parameter. The use of the Kaimal model with a coherence function assumes zero phase shift between the separated points. This assumption does not hold in sheared flow [Chougule et al., 2012]. The non-zero  $uw$ -cross-spectra are also not represented in the Kaimal model of turbulence.

A more sophisticated model of the complete second-order structure of atmospheric boundary-layer turbulence is presented in Mann [1994]. It modifies the isotropic spectral tensor presented in von Kármán [1948] to include the effects of uniform shear by using Rapid Distortion Theory and eddy lifetime considerations. A second model includes the blocking effect of the surface in addition. It is more complex and because both models give very similar predictions, the second model is not used in this thesis. The influence of thermal buoyancy is not considered in the models which are therefore only valid for neutral atmospheric conditions. Extensions for non-neutral conditions have been proposed [Chougule et al., 2017, 2018], but they are more difficult to implement and are also not used in this thesis.

Based on only three input parameters, the uniform shear model is able to create a spectral tensor. This tensor can be used to create spectra of all velocity components as well as cross-spectra of any combination of components for arbitrary separation distances. The three input parameters are the turbulence length scale  $L$ , the eddy lifetime constant  $\Gamma$ , and the spectral multiplier in the inertial subrange  $\alpha\epsilon^{\frac{2}{3}}$ . Fig. 2.4 gives an overview of the effect of each of the three parameters on the shape the resulting spectra. In Fig. 2.4a it can be seen that increased values of turbulence length scale  $L$  shift the peaks of the spectra towards smaller wavenumbers, i.e., larger eddies. The total variance increases accordingly due to the longer lifetime of large eddies. The plots in Fig. 2.4b show that the spectral multiplier in the inertial subrange  $\alpha\epsilon^{\frac{2}{3}}$  can be seen as a measure of energy dissipation. Increasing the  $\alpha\epsilon^{\frac{2}{3}}$  value results in scaled up spectral values without any change in the distribution of eddy sizes. Lastly as is visible in Fig. 2.4c, the eddy lifetime constant  $\Gamma$  is a measure for the degree of anisotropy. Increased  $\Gamma$  values result in wider spreading between the variances of the velocity components. The variance sum of all components increases with  $\Gamma$ . For  $\Gamma = 0$  the isotropic von Kármán tensor would be recovered.

The three parameters can be determined by fitting modeled single point spectra to measured turbulence spectra according to Mann [1998]. Resulting model spectra and coherences show overall good agreement with measured spectra [Mann, 1994, Chougule et al., 2014, Cheynet et al., 2017a, Eliassen and Obhrai, 2016].

Furthermore, the Mann model does not include wind evolution but assumes frozen turbulence, which means that the coherence for longitudinal separations equals

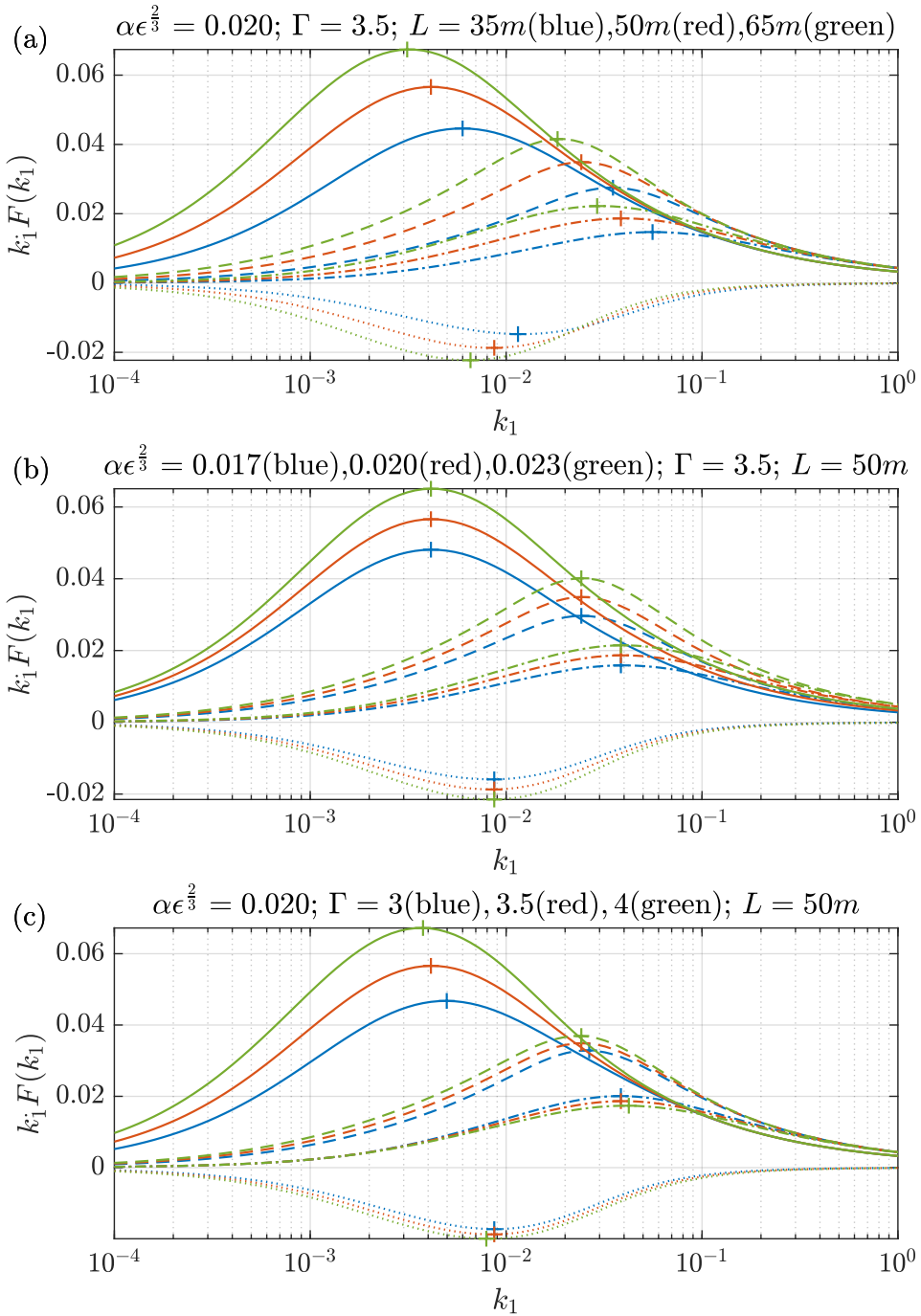


**Figure 2.4:** Variation of the three input parameters (a)  $L$ , (b)  $\alpha\epsilon_{33}^{\frac{2}{3}}$ , and (c)  $\Gamma$  to show their effect on the  $uu$  (solid),  $vv$  (dashed),  $ww$  (dashed-dotted), and  $uv$  (dotted) one point spectra created by the uniform shear model by Mann [1994]. The baseline case with  $\alpha\epsilon_{33}^{\frac{2}{3}} = 0.02$ ,  $\Gamma = 3.5$ , and  $L = 50$  m is shown in red, lower (higher) values are plotted in blue (green). Extremes are marked with ‘+’.

unity, while field measurements regularly show values that are significantly lower than one when the separation distance is large in comparison to the eddy size [Kristensen, 1979, Simley and Pao, 2015, Chen et al., 2020]. For a more detailed description of the model and the equations that define it, see Mann [1994].

## 2.3 Lidar measurements of wind velocity

Lidar is an acronym for light detection and ranging which describes a technology used for many applications. In the fields of meteorology and wind energy, it can be used to measure wind velocities by determining the velocity of tiny particles and liquid droplets moving with the air. Lidar devices emit laser light in a defined direction. On its way, the light will occasionally hit particles that scatter a small fraction of the emitted laser light into all directions. A very small portion of this scattered radiation is directed back into the direction of its origin and will reach the lidar unit where it is received and analyzed. While the emitted laser radiation has a constant frequency  $f_0$  that is determined by the laser source, the received radiation has a varying frequency that is a function of  $\Delta v$ , the relative velocity between the stationary lidar unit and the moving object that scatters the light. The cause for the variation in the frequency of the backscattered light  $\Delta f$  is the Doppler effect according to

$$\Delta f = \frac{\Delta v}{c} f_0 \quad (2.9)$$

where  $c$  is the speed of light. The magnitude of the Doppler shift can therefore be used to determine the wind velocity component in the beam direction.

It is unfortunately not possible to permanently receive backscattered radiation from a narrowly defined measurement distance because particles and aerosols as potential scatterers of the laser light are stochastically distributed in the air and no scattering objects might be at the desired measurement location while a measurement is taken. That means in order to generate a sufficient Doppler signal, the lidar must determine the radial velocities from accumulating data for some time and it must accept values from a range of measurement distances. This results in averaging of radial wind velocities measured along the beam directions, called the line-of-sight averaging.

Throughout this thesis, two different types of wind lidars are used that tackle the issue of line-of-sight averaging in different ways. Table 2.1 gives an overview of the lidars used in this thesis. In article 1 and 3 we use data from a cw velocity–azimuth–display (VAD) scanning wind lidar that emits laser radiation continuously. The laser beam is focused onto one measurement distance. The signal processing unit of the lidar cannot determine the measurement distance from where received radiation originates. In principle, the received radiation could be backscattered

Model name	Windcube V2	ZX 300
Manufacturer	Leosphere	ZX Lidars
Country	France	United Kingdom
Laser technology	pulsed	continuous-wave (cw)
Scanning strategy	Doppler beam swinging (DBS)	Velocity–azimuth display (VAD)
Beam layout	4 inclined, 1 vertical	49 inclined
Zenith angle	28°	30.4° – 30.6°
Elevation processing	parallel	consecutive
Time per cycle (one height)	3.9 s	1 s
Time per cycle (ten heights)	3.9 s	14.8 s
Averaging along lines of sight	Range gate: $l_P \approx 26$ m	Optical focussing (HWHM): $l_R \approx 0.745h^2 \times 10^{-3} \text{ m}^{-1}$ with measurement height $h$

**Table 2.1:** Overview of the two most widely used profiling wind lidars

anywhere along the beam but due to the focusing, it is more likely that it was backscattered in the proximity of the focus point. The symmetric spatial sensitivity around the focus point of a Gaussian beam is approximated by a Lorentzian function [Mikkelsen, 2009]

$$\varphi_{cw}(s) = \frac{l_R/\pi}{s^2 + l_R^2} \quad (2.10)$$

where  $s$  is the distance from the focus position and  $l_R$  is the Rayleigh length that can be approximated by

$$l_R = \frac{\lambda d_f^2}{\pi a_0^2} \quad (2.11)$$

where  $\lambda$  is the laser wavelength,  $d_f$  is the focal distance, and  $a_0$  is the effective aperture diameter of the telescope of the cw lidar. The operation principle of VAD scanning implies a continuous motion of the laser beam describing a cone. This motion during the accumulation time for one radial velocity estimate adds to the line-of-sight averaging of a VAD scanning wind lidar. The accumulation time of the cw lidar used in this work is very short ( $t_a \approx \frac{1}{49}$  s). The arc length of the measurement cone that is scanned during the measurement of each line-of-sight velocity is

$$l_A = f_s D_C \pi \quad (2.12)$$

where  $f_s \approx 49$  Hz is the sampling frequency of the VAD scanning lidar and  $D_C$  is the diameter of the measurement cone at the current focal distance.

The Doppler beam swinging (DBS) lidar we use for article 2 is a pulsed lidar that determines line-of-sight velocities in a different way. It emits short pulses of laser light and considers the time of flight in the analysis of the backscattered radiation. A single laser pulse of the pulsed lidar used in our study has a duration of  $\Delta t = 175$  ns, which equals half a pulse length of  $l_P = \frac{\Delta t c}{2} \approx 26.2$  m. Backscattered radiation that is detected for example 500 ns after the pulse emission started could have traveled for  $t = 325$  ns–500 ns with the speed of light ( $tc \approx 97.4$  m–149.9 m). This means the backscattered radiation must have originated from a scatterer within the range gate of 48.7 m–74.9 m from the lidar because the total travel distance equals twice the distance between the lidar and the scatterer. It is more likely that backscattered radiation originates from the center of the range gate than from its ends because only the tip of the light pulse could have traveled the furthest and illuminated a scatterer 74.9 m away, while the complete light pulse had the chance to illuminate particles in the center of the range gate. This results in a triangular weighting function

$$\varphi_p(s) = \frac{l_P - |s|}{l_P} \text{ for } |s| < l_P \text{ and } \varphi(s) = 0 \text{ for } |s| \geq l_P. \quad (2.13)$$

In contrast to  $\varphi_{cw}(s)$ , the line-of-sight weighting function of a cw lidar,  $\varphi_p(s)$  is independent of the measurement distance  $d$ .

During the measurement of one radial velocity, the beam direction of a DBS lidar is fixed. The averaging along the line-of-sight is therefore the only spatial averaging effect that occurs, but temporal averaging comes in addition. The accumulation time of  $t_a = 0.5$  s during which data for one radial velocity value is collected leads to temporal averaging along the mean wind direction. For determining the severity of this temporal averaging it can be helpful to estimate the temporal averaging length  $l_T$  by multiplying the accumulation time  $t_a$  by the prevailing mean wind velocity  $U$

$$l_T = t_a U. \quad (2.14)$$

The averaging along the beams plus the temporal averaging during the accumulation time constitute the total line-of-sight velocity averaging effect.

The measured one-dimensional radial wind velocity does not fully describe the three-dimensional wind velocity vector. In order to reconstruct all three vector components, line-of-sight velocity measurements from at least three different beam directions must be merged. The Windcube with its five beams uses a vertical beam to estimate the vertical component of the wind velocity and two opposing

inclined beams for the reconstruction of each of the two horizontal wind velocity components. A VAD scanning lidar like the ZX 300 combines measurements from one or if desired three full prism rotations to reconstruct one single wind vector.

In articles 1 and 2, we describe in detail how the combination of measurements sampled at different times and locations introduces additional averaging plus an error in the reconstructed wind vector components. In line with Courtney and Hasager [2016] and Pauscher et al. [2016], we call this error the cross-contamination effect. It is also named contamination by the two-point correlation between the components of the wind field [Sathe et al., 2015], variance contamination [Newman et al., 2016a], and crosstalk [Wyngaard, 1968]. It can be understood as undesired redistribution of spectral energy from one wind velocity component to the other caused by different instantaneous wind velocities at the measurement locations. Both effects, averaging and cross-contamination, do not affect the mean values of the measured wind velocity and direction but only the estimates of the instantaneous wind vectors and turbulence parameters based on them.

# Chapter 3

## Methods

### 3.1 Time series analysis

Many different parameters can be used to describe the statistical properties of turbulence. We concentrate on spectra of the three turbulence velocity components in articles 1 and 2 and on turbulence intensity in article 3. First follows a description of how these values are calculated from wind velocity data. Wind can be seen as a time-variant three-dimensional field of three-dimensional velocity vectors. That means for every point in space, the wind conditions can be described by a time series of velocity vectors. For analyzing wind data it is useful to separate the time series of the velocity vector  $\vec{u}$  into two parts which are, first, the mean velocity  $\vec{U}$  and, second, the turbulent velocity fluctuations  $\vec{u}'$  so that

$$\vec{u} = \vec{U} + \vec{u}'. \quad (3.1)$$

For determining the mean wind velocity vector, an averaging period must be chosen. The two most common values are ten minutes in wind energy research and thirty minutes in meteorology. Both periods lay in the spectral gap that separates microscale turbulence from mesoscale effects [Van der Hoven, 1957, Kang and Won, 2016, Larsén et al., 2016]. Throughout this thesis, we use ten minutes as the averaging period because it is most commonly used in wind energy. The assumption that wind velocity fluctuations  $\vec{u}'$  are advected by the mean wind vector  $\vec{U}$  is not exactly true because low-frequency velocity drifts occur due to weather variability. If such trends are not removed from the data, increased velocity variance might occur [Hansen and Larsen, 2005]. The actual advection speed also determines at which wavenumbers cross-contamination occurs. Deviations from the theory are expected when it differs significantly from  $\vec{U}$ . Also the efficacy of

the method of squeezing can be impeded when the transportation of the turbulent wind field occurs faster or slower than what is expected from  $\vec{U}$ .

The standard output of wind velocity measurement devices is usually based on a fixed coordinate system, i.e., the wind velocity vectors are given in three Cartesian coordinates  $x$ ,  $y$ , and  $z$  that are aligned with the physical orientation of the measurement device. One example interval of 10 minutes of wind data is shown in Fig. 3.1a. The  $x$ -axis of the anemometer is oriented north, the  $y$ -axis is pointing east and the  $z$ -axis is directed vertically downwards. It can be seen that the vertical  $z$ -component has an average value of approximately zero which is typical for measurements in non-complex terrain. For useful interpretations of the horizontal wind components, the values of  $x$  and  $y$  can easily be transformed into combinations of horizontal wind velocity

$$v_{\text{hor}} = \sqrt{x^2 + y^2} \quad (3.2)$$

and wind direction

$$\theta = -\arctan(y, -x) \quad (3.3)$$

defined as the direction from which the air is approaching. These polar components are the native data format of a cup-anemometer and a wind vane. The vertical component  $v_{\text{ver}} = z$  remains unchanged. Fig. 3.1b shows the same data in polar coordinates. From these values, we can estimate the mean wind velocity and direction and can calculate the turbulence intensity that is defined as

$$TI = \frac{\sigma_{v_{\text{hor}}}}{V_{\text{hor}}} \quad (3.4)$$

where  $\sigma_{v_{\text{hor}}}$  is the standard deviation of the horizontal wind speed fluctuations and  $V_{\text{hor}}$  is the horizontal mean wind speed. Often, only the mean wind velocity and the turbulence intensity are used to describe the wind conditions at a wind site. However, it is clear that this description is incomplete when it comes to describing the wind energy potential [Martin et al., 2016, Bardal and Sætran, 2017] and especially aerodynamic loads on wind turbines [Thomsen and Sørensen, 1999, Noda and Flay, 1999].

The longitudinal or along-wind component  $u$  of the wind has interesting properties that differ in a characteristic way from the lateral or crosswind component  $v$ . However, the combination of horizontal wind speed  $v_{\text{hor}}$  and wind direction  $\theta$  is not well suited to compare the two horizontal turbulence components with each other. Thus, for a more in-depth analysis it is necessary to rotate the  $xyz$ -coordinate system around the vertical axis, so that the first horizontal axis points into the mean wind direction  $\Theta$ , while the second horizontal axis points into a lateral direction. The longitudinal wind component  $u$  is calculated according to

$$u = -x \cos(-\Theta) + y \sin(-\Theta) \quad (3.5)$$

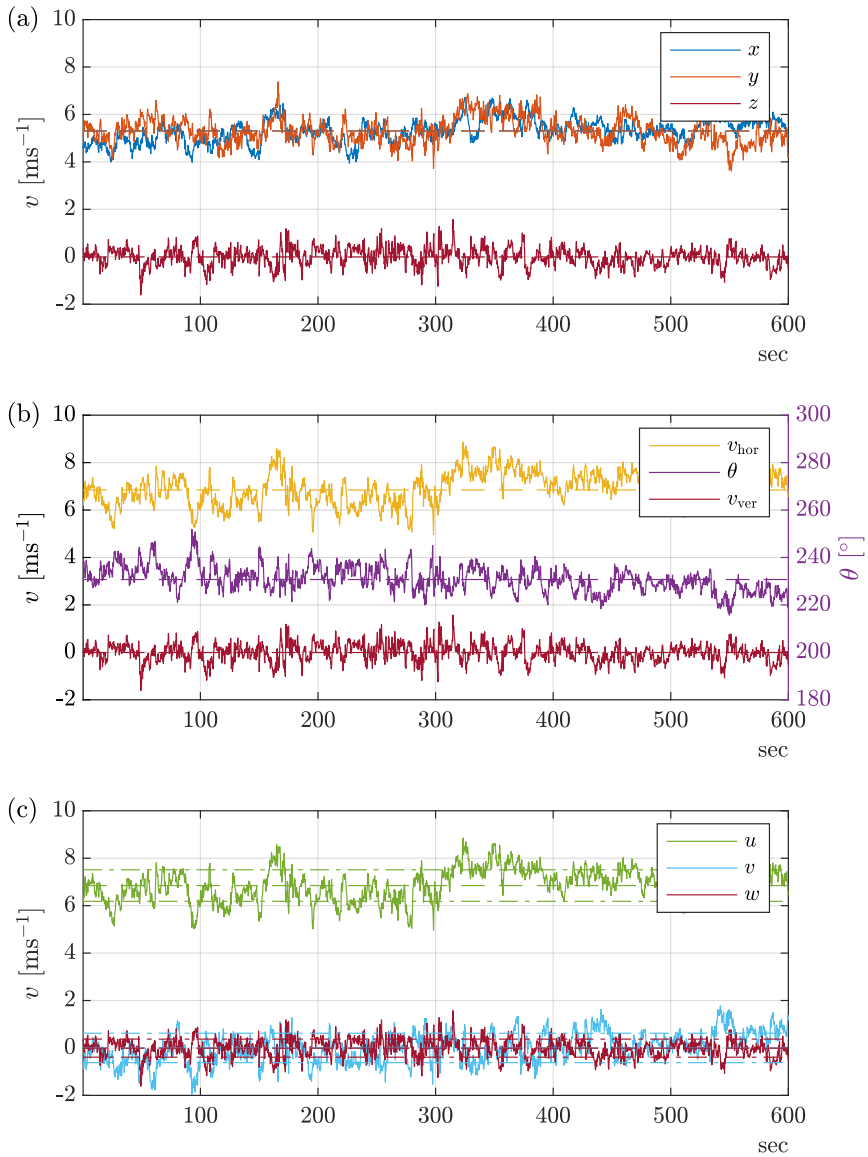


**Figure 3.1:** Timeseries of one arbitrary ten-minute interval of wind velocity vector data given in fixed cartesian coordinates  $x$ ,  $y$ , and  $z$  (top), in polar coordinates  $v_{\text{hor}}$ ,  $\theta$ , and  $v_{\text{ver}}$  (middle), as well as aligned with the mean wind direction in a  $u$ ,  $v$ , and  $w$  coordinate system (bottom). Dashed lines show the mean values of the wind vector components and dashed-dotted lines have a distance of one standard deviation around the mean values of  $u$ ,  $v$ , and  $w$ .

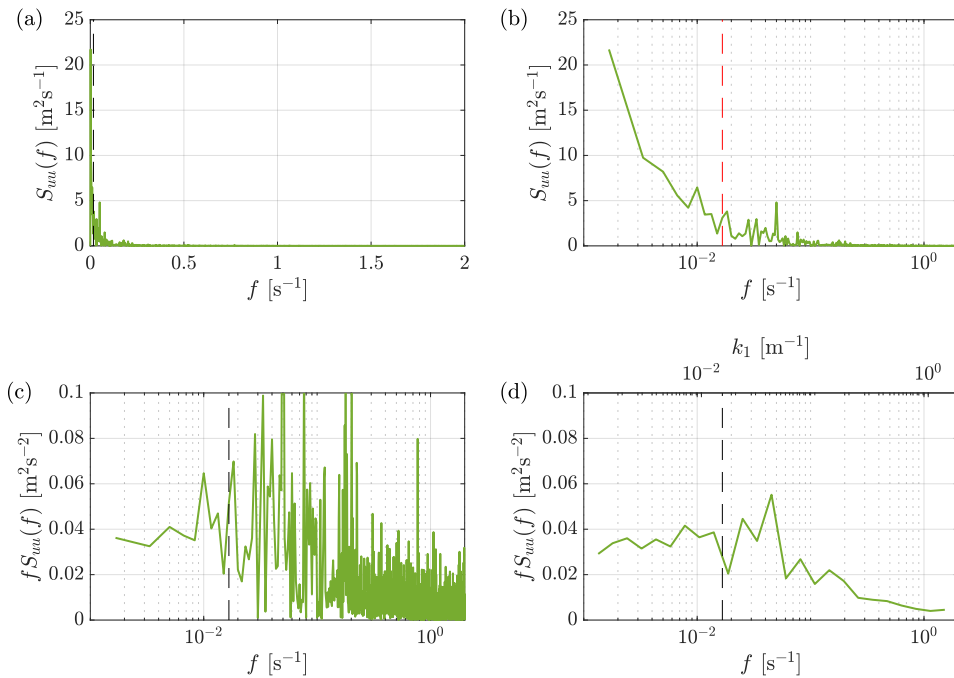


**Figure 3.2:** Different visualizations of spectral data of  $u$  from Fig. 3.1c. Logarithmic abscissa (b–d), vertical axis pre-multiplied by  $f$  (c&d), spectral values averaged into logarithmically spaced bins (d) and additional wavenumber scale (d). Vertical dashed lines at  $f_{50} = 0.017$  Hz divides the spectra into two halves of identical variance.

and the lateral component  $v$  is

$$v = x \sin(-\Theta) + y \cos(-\Theta) \quad (3.6)$$

where  $\Theta$  is the mean wind direction. Fig. 3.1c shows the time series of  $u$ ,  $v$ , and  $w$  for the example data.  $u$  is nearly identical to  $v_{hor}$ . The mean value of  $v$  is zero by definition and the vertical component  $w = z$  remains unchanged. A comparison of the velocity variances shows that  $\sigma_u^2 > \sigma_v^2 > \sigma_w^2$ . This anisotropy is typical for turbulence in the atmospheric boundary layer. We can also recognize that the turbulent fluctuations around the mean occur with a wide range of frequencies. In order to quantify the spectral composition of the time series, it must be transferred into the frequency domain.

## 3.2 Turbulence velocity spectra

In order to calculate the spectral distribution of the velocity variance we apply a discrete Fourier transformation to the time series of  $u$  according to

$$\mathcal{F}(u(f)) = \sum_{n=1}^N u(n) \exp \frac{-i2\pi(f-1)(n-1)}{N} \quad (3.7)$$

where  $u(n)$  are the wind speed samples  $n = 1 \dots N$  where  $N$  is the total number of samples in the interval and  $f$  is the frequency that is being evaluated. The real part of  $\mathcal{F}(u(f))$  is the double-sided amplitude spectrum of  $u$  and the energy spectrum can be calculated according to

$$S_{uu}(f) = \frac{|\mathcal{F}(u(f))|^2}{N f_s} \quad (3.8)$$

The first half of  $S_{uu}(f)$  for  $f = 0 \text{ Hz} - 2 \text{ Hz}$  is plotted in Fig. 3.2a on linear axes. The total area under the curve equals half of the velocity variance  $\sigma_u^2$  and the dashed vertical line divides this area into two halves. It is difficult to see that half of the variance is contained in the fluctuations that occur with a very low frequency below  $f_{50} = 0.017 \text{ Hz}$ . A semi-logarithmic presentation of the same spectrum is given in Fig. 3.2b. The logarithmic display of the abscissa puts focus on the energy containing range of the auto-spectrum. Unfortunately, the stretching of the abscissa causes that the vertical line at  $f_{50}$  no longer divides the area under the curve into two halves. In Fig. 3.2c this problem is solved again by pre-multiplying the spectral values on the vertical axis by the frequency. The area under the curve is now proportional to the velocity variance again but the high density of values at high frequencies impedes the readability of the spectrum. Therefore, we sort the spectral values into logarithmically spaced frequency bins and plot their average for Fig. 3.2d. The resulting spectrum shows the spectral distribution of velocity variance nicely. A peak is visible at  $f_1 \approx 4.5 \times 10^{-2} \text{ Hz}$  that corresponds to a period of  $T_1 \approx 22 \text{ s}$ . This peak in the spectrum could be associated with the approx. 22 s long wind speed variations visible in Fig. 3.1c that have their peak around  $t = 95 \text{ s}$  and  $t = 164 \text{ s}$ . When the spectra of very many ten-minute intervals are averaged such distinct peaks disappear and the results become smoother. With

$$k = \frac{2\pi f}{U} \quad (3.9)$$

we can transform the spectra from being functions of the frequency to depend on the wavenumber  $k_1$ . In article 1 and 2 we compare spectra from wind lidar measurements to spectra from reference measurements, models or simulations.

### 3.3 Comparison of field measurements

In all three articles we compare datasets acquired from field measurements, i.e., measurements under uncontrolled wind conditions. It is important to evaluate the accuracy of the measurements that serve as reference values. Most studies that aim at evaluating the performance of profiling wind lidars are comparisons with measurements from in situ anemometers that are attached to meteorological masts [e.g. Courtney et al., 2008, Smith et al., 2006, Peña et al., 2009, Sathe et al., 2011]. These can be cup-anemometers that measure only the horizontal components of wind speed and are known to show some attenuation of small-scale turbulence in their data [Yahaya and Frangi, 2004]. In most cases ultrasonic anemometers are used, which are calibrated in wind tunnels according to ISO16622 [2002]. However, there is some controversy if the wind tunnel calibrations can always be trusted in atmospheric turbulence and which flow-distortion compensation algorithm should be applied [Peña et al., 2019, Wyngaard, 1981]. When they are carefully installed and well maintained, ultrasonic anemometers are usually accurate and reliable enough to draw valuable conclusions from comparisons of spectra and  $TI$  values from lidar and sonic anemometers. But this accounts only for data that are averaged over many measurement intervals.

For individual intervals of only ten minutes, random deviations are significant. Contini et al. [2006] report random errors of variance measurements with two identical high frequency ultrasonic anemometers that are separated by only 1m. They show that the lowest achievable uncertainty for turbulence intensity in their campaigns is as low as  $\sigma_{TI_{1m}} \approx 0.01$  when the averaging period is set to ten minutes. When the spatial separation between the anemometers is increased to 9 m, the uncertainty nearly doubles to  $\sigma_{TI_{9m}} \approx 0.02$ . This shows how sensitive measurements of second-order statistics are even for small separation distances.

In addition to the uncertainty that is created by the reduced coherence between measurements at separated locations, the number of samples taken in each ten-minute interval influences the statistical error. Fig. 3.3 shows the time series  $v_{hor}$  from Fig. 3.1b and two sets of 40 linearly spaced sample values. It can be seen that the blue series of samples show a slightly higher variance than the samples marked in red. The only difference between the two sets of samples is their position on the time series. For all possible positions on the time series an uncertainty of  $\sigma_{TI_{N40}} \approx 0.0063$  can be calculated for this example with  $N = 40$  samples which corresponds to one value every 15 s. This is approximately the time it takes a cw lidar like the ZX 300 to scan and refocus to each of the ten elevation levels one after another. A more universal approach to quantifying the uncertainty of sampling of random processes would be for example to use the formulas presented in Benedict

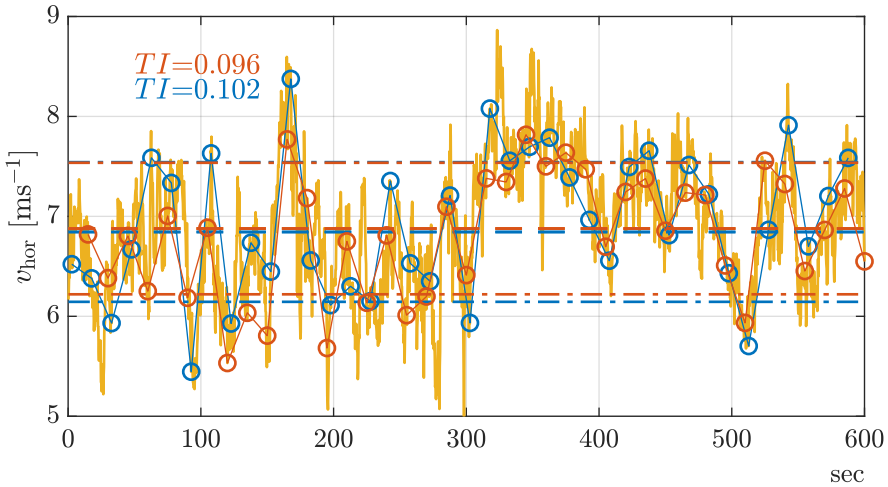


**Figure 3.3:** Time series of  $v_{\text{hor}}$ . Red and blue markers show each 40 linearly spaced sample values separated by an arbitrary time lag. Mean values (dashed) and one standard deviation around it (dashed-dotted) are given. Resulting turbulence intensities are shown.

and Gould [1996]. Their application, however, requires independence between the samples, which is not given in the example presented here because the sampling period is similar to the integral time scale  $T \approx 15$  s of  $v_{\text{hor}}$ .

### 3.4 Scatter analysis: Deming regression

Presenting two sets of measurement data in a scatter plot visualizes their dependency. In Fig. 3.4 the arbitrary ten-minutes of  $v_{\text{hor}}$  data from Fig. 3.1b are plotted on the  $x$ - and  $y$ -axis, but a temporal offset of 2 s is introduced in order to create scatter. Both datasets have the same statistics, so no trend is expected in the data. It is possible to apply a linear regression model and determine the line that intersects the cloud of data points while minimizing the sum of the squares of the vertical distances between regression line and data points. The result of this simple linear regression is shown in blue in Fig. 3.4. The linear regression line has a positive intercept with the  $y$ -axis ( $b = 0.63 \text{ m s}^{-1}$ ) and a slope below unity ( $m = 0.91$ ). This regression line does not predict the correlation between the  $x$  and  $y$  data correctly. The reason is that both data sets have the same non-zero statistical error. The "reference" values on the  $x$ -axis are not closer to the "real" values than the sample values on the  $y$ -axis.

In this situation it is better to calculate the Deming regression line that minimizes the sum of the squares of the diagonal distances between data points and regression line [Cornbleet and Gochman, 1979, Adcock, 1878]. It is plotted in red in

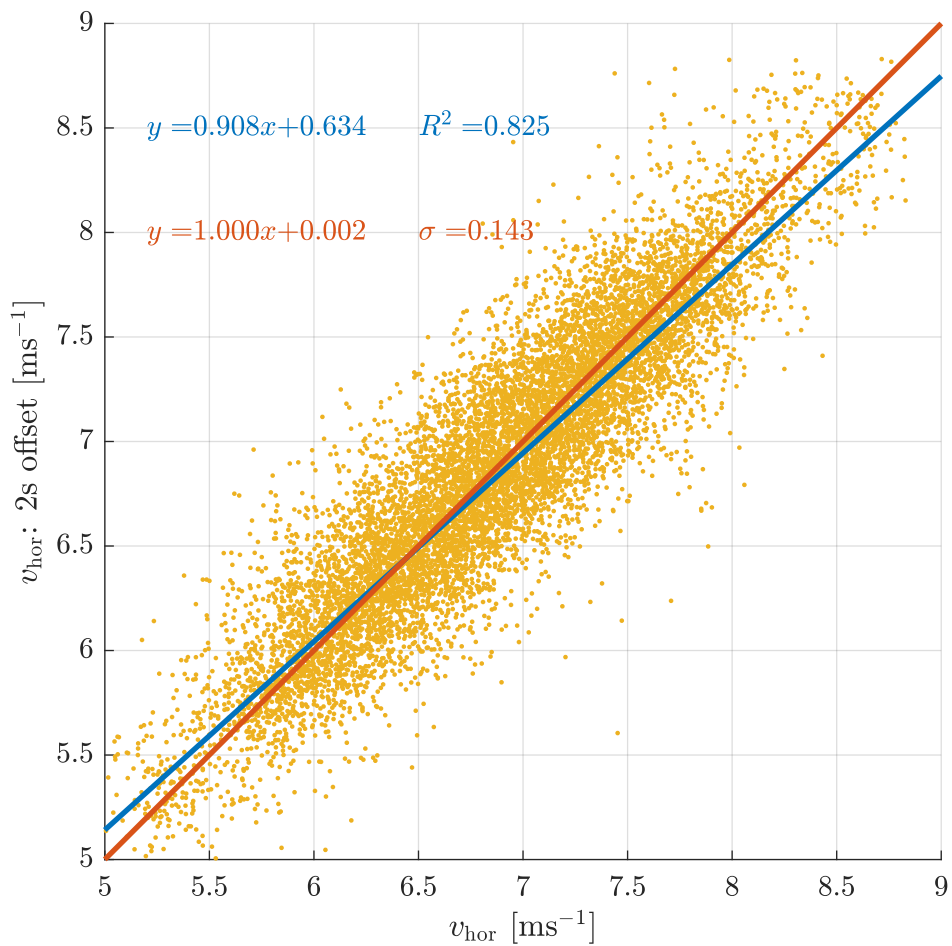


**Figure 3.4:** Scatter plot of measured horizontal wind velocities. The  $y$ -axis shows the same data like the  $x$ -axis but the values are shifted by 2 s. Linear (blue) and Deming (red) regression lines and their equations are shown in the plot.

Fig. 3.4 and its equation is approximately  $y = x$ . This example shows that when the statistical error of the data on the abscissa is non-zero and identical to the uncertainty of the data on the vertical axis, only the Deming regression line allows valid conclusions about correlations in the data. The comparison of measurements from two similar measurement devices is such a situation. Another example is a situation in which the statistical error resulting from the measurement set-up dominates the measurement uncertainty of the measurement devices. We therefore used the Deming regression for the scatter plot in article 3.

### 3.5 Lidar modeling

In article 1 we present a model for predicting turbulence velocity spectra from VAD scanning cw lidar like the ZX 300. The model considers the line-of-sight averaging effect, the averaging along the measurement circle and also the redistribution of spectral energy between the different velocity components  $u$ ,  $v$ , and  $w$  that we call the cross-contamination effect in articles 1–3. The model is a mathematical representation of how the lidar measures turbulence. It can be understood as a spectral filter function that is multiplied by a spectral tensor that represents the spatial structure of turbulent wind speed fluctuations. We use the Mann [1994] model of turbulence to create spectral tensors  $\Phi_{ij}(k)$  that contain the auto- and cross-spectra of all three velocity components as well as the two-point second-order statistics, i.e., the coherences and phases for any combination of wind velocity components at any spatial separation. The same method of modeling filter functions that represent the lidar sampling of turbulence is used for example in Sathe et al. [2011].

Modeling makes it possible to get smooth spectra that allow for a detailed analysis of the results of all filtering effects that are considered in the model. The components of the model spectral tensor can be switched on or off to determine their individual influence on the modeled lidar spectra. The range and resolution of wavenumbers at which the model is evaluated and the computational precision can be selected freely to allow for fast computations in the development phase and final results of the desired accuracy. The disadvantage of modeling lidar processing is that the resulting equations are not always easy to grasp and can get increasingly cumbersome when the scanning strategy becomes more complex. Sometimes assumptions need to be made to simplify the model equations that might introduce errors that can be difficult to quantify.

### 3.6 Lidar simulation

A model for the prediction of turbulence velocity spectra from a pulsed DBS wind lidar is presented in Sathe and Mann [2012]. This model assumes that the angle

between the mean wind direction and two of the lidar beam directions is zero, but from Sathe et al. [2011] we know that DBS lidar measurements of velocity variances are sensitive to this relative angle. It is unfortunately very cumbersome to develop a model that works for all wind directions. To be still able to predict the spectra of a pulsed DBS wind lidar for arbitrary inflow directions, we chose an approach for article 2 that is different from the numerical modeling in article 1. Instead of finding an appropriate filter function which resembles the lidar processing, we sampled computer-generated velocity vectors in the same way a real wind lidar measures the wind. That means we first generated three-dimensional boxes of three-dimensional wind vectors based on the Mann spectral tensor according to Mann [1998]. A lidar simulator was then programmed to sample the data in the same way the Windcube measures in the field. The sampling considers the line-of-sight averaging including accumulation time, the scanning geometry, the beam timing, and the wind vector reconstruction process. The resulting time series can then be transformed into spectra which can be compared with the spectra from the model tensor. One computer-generated turbulence box represents one single realization of the underlying statistics based on a random seed. The ensemble average of all possible realizations show the statistics of the turbulence model but every single realization contains strong random deviations from the model spectra. Therefore, sampling in a turbulence box requires a high amount of computer memory because data for many ten-minute intervals must be sampled and averaged to get spectra that are relatively smooth, especially at low wavenumbers.

Sampling in a turbulence box as a method to simulate lidar measurements is flexible and easy to implement. For a very high number of realizations, the simulation results are comparable to the results of a corresponding model. Simulations make it easy to predict the effect of lidar accurately even for complex scanning geometries and beam timing.

### **3.7 Motion compensation**

For offshore applications at great water depths, the construction of meteorological masts becomes prohibitively expensive. Wind measurements with lidar units installed on floating buoys can therefore be an economical alternative. But wind lidars measure the relative velocity between the laser light and scatterers in the atmosphere. Therefore, the motion of the buoy and variations in its orientation influence the reconstructed wind vectors in such a way that turbulence estimates from floating lidar are higher than from fixed lidar.

In contrast to the case of a lidar being mounted on a vessel, the motion of a buoy mounted lidar is characterized by motion around a fixed zero position. Different studies are available that investigate the effects of such motion on measurements of

wind velocity in different ways. Hellevang and Reuder [2013] compare mean wind velocity values from lidar units mounted on a motion platform with measurements from collocated fixed reference lidar and find small deviations. Wolken-Möhlmann et al. [2010] show with lidar sampling simulations of the two most commonly used profiling lidar types that the time series of reconstructed wind velocities are influenced by lidar motion and that tilting of the lidar is the largest contributor to the motion-induced deviations. In Wolken-Möhlmann et al. [2017] they show that the effect of motion on mean wind speed and turbulence intensity is frequency dependent. In Bischoff et al. [2018] a lidar simulator is coupled with a hydrodynamic model of a buoy that computes realistic motion data based on sea state data as input parameters. The results of such a simulation environment might be used to predict the expected uncertainty in floating lidar results.

For our own description of the motion-induced error on the turbulence estimates of floating lidar in article 3, we use some of the findings of article 1 where we analyze the cross-contamination effect, i.e., how wind velocity fluctuations of one orientation can be attributed to the measurement of a different wind vector component when they occur within certain frequency ranges. The same effect occurs when the motion of a floating lidar resonates with the lidar sampling frequency. An example is fore and back motion of the lidar in mean wind direction. If this motion occurs with a very low frequency, the lidar interprets the motion correctly as what it is: horizontal motion superimposed on the wind vector. But when the oscillations of buoy motion coincide with the lidar prism rotation frequency the motion is attributed to the estimates of vertical wind velocity. Thus, it is important to compensate for the motion in all six degrees of freedom on a line-of-sight level instead of assuming that the measurement cone is static throughout a measurement cycle. In article 3, section 2.3 we give a comprehensive description of the different motion-induced error sources that influence the reconstructed wind vectors of a VAD scanning profiling wind lidar.

For article 3, we stored the Doppler spectra of a floating ZX 300 wind lidar and recorded its motion data. We compensated the line-of-sight velocities for the effects of measured motion by, first, subtracting the contribution of the translational lidar movement and, second, corrected the scanning geometry by considering the deviations from the standard azimuth and elevation angles for each beam direction. The minor impact of measuring at varying elevations where wind shear leads to differences in mean wind velocity is, thirdly, also considered in the motion compensation approach.

What makes our approach unique in floating lidar research is that it is able to correct the time series of measurement data instead of just the turbulence statistics. A prerequisite for this ability is to synchronize the motion and lidar data. We

solved this by determining the timing at which the motion compensation has the strongest effect. A detailed description of the motion compensation algorithm and its ability to synchronize the measurement data is given in article 3, sections 3.2 and 3.3.

# Chapter 4

## Discussion

### 4.1 Discussion of the results

Articles 1, 2, and 3 included in this thesis address all three research questions successfully that directed this doctoral work. In section 1.1 it is pointed out that several publications on turbulence estimates of profiling wind lidar refer to cross-contamination as a source of error but none of them describes it in enough detail for a complete analysis. This gap in knowledge led to the first research question of this thesis: "How does the effect of cross-contamination between the three turbulence velocity components influence lidar-based wind velocity measurements in conjunction with other systematic sources of error?" In answering this question, turbulence velocity spectra are a powerful tool. But a model to predict spectra from profiling lidar was only available for a pulsed DBS lidar like the Windcube and it can predict the spectra only if the wind direction is aligned with two of the lidar beams. The model for spectra from a VAD scanning cw lidar presented in article 1 as well as the DBS pulsed wind lidar spectra presented in article 2 are therefore novel. A limitation to the usefulness of the predicted spectra is that they require a spectral tensor that represents the real wind conditions sufficiently accurately. In cases where the spatial structure of turbulence deviates from the two-point statistics of the chosen spectral tensor, the predicted spectra cannot be correct. Also instrument noise and other factors that lead to imperfect measurements are not represented in our model spectra. The analytical solutions to calculate characteristic points in the spectra are another contribution of this thesis to the previous state of the art.

The answer to research question 1 is as follows. DBS and VAD scanning profiling wind lidars reconstruct wind vectors from line-of-sight measurements which orig-

inate from measurement volumes that are separated in space. While the average of many of such wind vectors lies close to the reference mean wind speed, each single value is erroneous. The cause for this error lies in the spatial structure of turbulence. Velocity measurements at two widely spatially separated points show low coherence, but the wind vector reconstruction algorithms used by profiling lidar devices assume identical wind velocities within all measurement volumes during each sampling cycle. The instantaneous inhomogeneity of the wind field leads to a redistribution of spectral energy between the three velocity components. Articles 1 and 2 give a detailed description of this cross-contamination effect.

The body of literature does not offer any method that is successful at removing the effect of cross-contamination on the reconstructed wind vectors from profiling wind lidars. The second research question of this thesis is thus: "Can advanced data processing methods effectively reduce the error introduced by cross-contamination and averaging along the measurement cone?" We introduce the method of squeezing and apply it to both market-leading profiling wind lidar. The novelty of the method lies in the approach to measure an air volume from two different directions with only one lidar device. We also suggest two-beam processing of VAD measurement data as a method to avoid averaging along the measurement cone.

The details of the two methods are described in articles 1 and 2. The application of the method of squeezing to measurement data and comparison with model spectra proves that it is a reliable tool to minimize cross-contamination caused by longitudinal separation of the measurement locations. The results also indirectly prove that the assumption of frozen turbulence is sufficiently valid for our approach. The ZX 300 lidar measures once per second in each azimuthal direction. Squeezed processing can therefore reduce the effect of longitudinal separation to nearly zero when only one elevation level is scanned. This is a minor limitation because when turbulence shall be estimated, a high scanning rate is required in any case. The two-beam processing also eliminates the lateral spacing and averaging along the measurement cone for the determination of the longitudinal and vertical wind velocity components. With both methods applied, line-of-sight averaging is the only lidar-specific effect that remains in the determination of these two wind velocity components. Unfortunately, we found no possibility to improve measurements of the lateral wind component that always suffer from lateral separations when it is measured with diverging beams from a single lidar unit. Fortunately, the lateral turbulence is of low importance in most wind energy applications.

The situation is different for the Windcube lidar which scans each of its four cardinal beam directions once every 3.9 s. This slow sampling in comparison with the ZX 300 lidar leads to longer remaining longitudinal separations after squeezing,

but we still show satisfactory efficacy of the method of squeezing in the results. A more critical issue is that the low number of only four scanned azimuth angles makes the measurements sensitive to whether the mean wind direction is aligned with any of the beams. Measurements of longitudinal turbulence show good results for inflow from one of the four beam directions when squeezed processing is applied. But large errors that cannot be eliminated by squeezed processing occur for all other wind directions. For applications in which the vertical component of turbulence is of interest, the fifth beam of the Windcube is a crucial advantage. As with VAD scanning lidar, lateral wind velocity estimates of a DBS lidar cannot be corrected by the method of squeezing.

For measurements of turbulence spectra, a high sampling frequency is desirable to cover a wide range of wavenumbers. In this context it becomes relevant that the two market-leading wind profilers, besides employing a different scanning strategy, also use different laser technology. The ZX 300 as a cw lidar requires optical focusing onto the desired measurement elevation. That means only one wind vector can be reconstructed from each scanning cycle. When a vertical profile of wind speeds shall be measured, the sampling frequency decreases because each height is measured subsequently and additional time is required to refocus the laser beam. The Windcube, being a pulsed lidar, needs more time for one scan cycle but measures at all height levels simultaneously. The sampling frequency of the ZX 300 lidar is therefore only higher when no more than two elevations are scanned. For more measurement heights, the Windcube measures faster. Example times for one and ten height levels are listed in table 2.1.

Although averaging along the beams is not the primary focus in this thesis, we point out that line-of-sight averaging of cw lidar measurements is advantageous at short focal distances, as the Rayleigh length depends quadratically on the focal distance. Pulsed lidars are superior for high measurement distances because their range gate length is independent of the measurement distance. Access to line-of-sight velocity data is straightforward when a Windcube lidar is used. Its standard output data contain line-of-sight velocities and signal-to-noise ratios. The ZX 300 on the contrary requires the user to stream Doppler-spectra manually to a connected PC. Line-of-sight velocities can then be calculated from the Doppler-spectra, but it is difficult to filter them for bad data.

Considering the advantages and drawbacks of both lidar systems, it is not possible to determine whether one of them is better suited to all tasks. The ideal lidar device for measurements of turbulence spectra would have a short line-of-sight averaging length of not more than approximately 10 m that is independent of the measurement distance. It would measure at a set of relevant elevations with a high frequency around 1 Hz. It would furthermore follow a VAD scanning strategy and

should still have a vertical beam. Another desirable property from a research point of view is convenient availability of the line-of-sight velocities.

The third research question that drives the work presented in this thesis is regarding lidar measurements from a floating buoy. I wanted to find out: "Is it possible to measure turbulence intensity with a floating lidar as accurately as with a fixed lidar, when its motion is compensated for on a line-of-sight level?" Prior to this thesis the literature was lacking a proven and reproducible method to compensate the time series of a floating profiling lidar for the effects of motion. Also the description of the effects of motion on the measurements was incomplete. Thus, after having understood how fixed profiling wind lidars measure wind vectors, a logical step was to analyze in what way the motion of a floating lidar influences its turbulence measurements.

The increase in measured turbulence intensity on floating lidar can be ascribed mostly to rotation and to a lesser extent to translational motion of the lidar unit. The effect of wind shear on the measurements is minor. With our motion compensation algorithm we show that when accurate motion measurements and the individual lidar line-of-sight velocities are available, the influence of motion on turbulence intensity can be compensated for. This is true even if the timing of both signals is not synchronized before the motion-compensation processing. The ability of our processing to synchronize the signals is another contribution to the state of the art. The amount of motion-induced turbulence intensity is dependent on the motion state (i.e., mean tilt angle, tilt direction, and tilt period) and the mean wind conditions (i.e., wind speed and direction). The method we present can unfortunately not be used when either motion data or line-of-sight velocities are not available.

The methods presented in this thesis offer novel smart processing of data from commercially available fixed and floating profiling wind lidar and improve their turbulence estimates. The thesis reaches thus its overall research goal and confirms its hypothesis.

## **4.2 Recommendations for further work**

The method of squeezing can be used to reduce the effect of longitudinal separation of the measurement volumes, but it does not counteract the effect of lateral separations. One possibility to eliminate the cross-contamination due to lateral spacing would be to deflect two of the Windcube beams twice. First, in such a way that they point horizontally in two different directions away from the lidar unit and then a second time so that they intersect with the vertical beam at a common point. Such a setup as depicted in Fig. 4.1 could reduce cross-contamination to

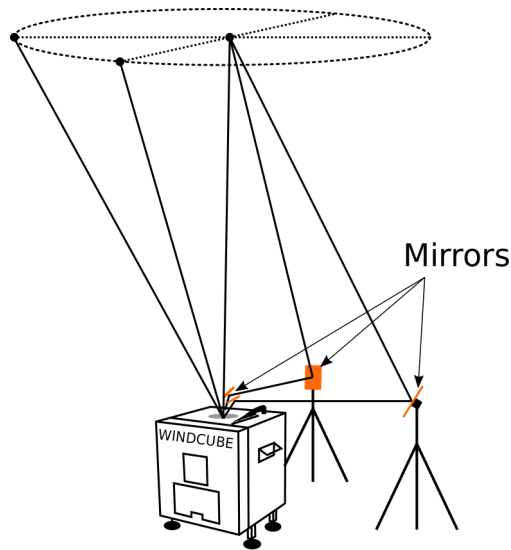


**Figure 4.1:** Deflecting two lidar beams by mirrors (orange) so that they intersect with the vertical beam in one point above the lidar. This measurement setup allows for turbulence measurements with low cross-contamination between turbulence components.

a very low degree without the need for a multi-lidar setup like the Windscanner [Mikkelsen et al., 2008]. The three remaining unchanged beams can help with the challenging task of determining the correct azimuth and elevation angles of the deflected beams. With a robust procedure to estimate the scanning geometry in place, measurements in non-homogeneous wind fields could also be valid.

For determining turbulence velocity spectra, it is necessary to reconstruct individual wind vectors. When only the second-order turbulence statistics are required, it could be advantageous to derive them from the variance of the line-of-sight velocities according to Sathe et al. [2015]. With a few assumptions, their six-beam method could be adapted to the five beams of the Windcube. Processed like this, the lidar measurement results would not be affected by cross-contamination, and averaging along the lines-of-sight would be the only remaining filtering effect.

This line-of-sight averaging effect is the biggest remaining challenge for lidar remote sensing of wind turbulence, and efforts should be made to mitigate it. Brinkmeyer and Waterholter [2013] show how the measurement volume of cw lidars could be reduced. Another much simpler possibility could be to average all Doppler spectra from all individual beam directions that were acquired during one ten (or 30)-minute interval like shown in Branlard et al. [2013] before processing them according to the six-beam method [Sathe et al., 2015]. The resulting compo-

nents of the Reynolds stress tensor would then be free of cross-contamination and would also not be impacted by line-of-sight averaging.

For floating lidar research, a method should be developed that can achieve results that are similar to the results we present in article 3 but acquired without the need for radial velocities. A study could be performed in which measured motion data and ten-minute average wind data could be used as input for a lidar simulator that determines the motion-induced turbulence intensity.

# Bibliography

- R. J. Adcock. A problem in least squares. *The Analyst*, 5(2):53–54, March 1878. doi: 10.2307/2635758.
- S. Aubrun, A. Leroy, and P. Devinant. A review of wind turbine-oriented active flow control strategies. *Experiments in Fluids*, 58(10), September 2017. doi: 10.1007/s00348-017-2412-0.
- L. M. Bardal and L. R. Sætran. Influence of turbulence intensity on wind turbine power curves. *Energy Procedia*, 137:553–558, October 2017. doi: 10.1016/j.egypro.2017.10.384.
- L. H. Benedict and R. D. Gould. Towards better uncertainty estimates for turbulence statistics. *Experiments in Fluids*, 22:129–136, 1996. doi: 10.1007/s003480050030.
- V. Berkhout, A. Bisevic, M. Claußner, M. Dörenkämper, M. Durstewitz, S. Faulstich, P. Görg, L. Große, B. Hahn, F. Huneke, D. Kuhl, M.-A. Lutz, J. Mayer, J. Mergner, M. Noonan, S. Pfaffel, F. Rehwald, J. Schmidt, S. Priestersbach, B. Stoevesandt, and L. Vollmer. Windenergie report deutschland 2018. Technical report, Fraunhofer IEE, 2019.
- F. Bingöl, J. Mann, and D. Foussekis. LiDAR error estimation with WAsP Engineering. In Mann, J and Bingol, F and Courtney, M and Jorgensen, HE and Lindelow, P and Mikkelsen, T and Pena, A and Sjöholm, M and Wagner, R, editor, *14th International Symposium for the Advancement of Boundary Layer Remote Sensing*, volume 1 of *IOP Conference Series Earth and Environmental Science*, pages U461–U469, 2008. doi: 10.1088/1755-1307/1/1/012058. Copenhagen, Denmark, June 23-25, 2008.

- O. Bischoff, W. Yu, J. Gottschall, and P. W. Cheng. Validating a simulation environment for floating lidar systems. *Journal of Physics: Conference Series*, 1037:052036, June 2018. doi: 10.1088/1742-6596/1037/5/052036.
- E. Branlard, A. T. Pedersen, J. Mann, N. Angelou, A. Fischer, T. Mikkelsen, M. Harris, C. Slinger, and B. Montes. Retrieving wind statistics from average spectrum of continuous-wave lidar. *Atmospheric Measurement Techniques*, 6(7):1673–1683, 2013. doi: 10.5194/amt-6-1673-2013.
- E. Brinkmeyer and T. Waterholter. Continuous wave synthetic low-coherence wind sensing lidar: motionless measurement system with subsequent numerical range scanning. *Optics Express*, 21(2):1872–1897, Jan 2013. doi: 10.1364/OE.21.001872.
- B. Canadillas, A. Bégué, and T. Neumann. Comparison of turbulence spectra derived from lidar and sonic measurements at the offshore platform fino1. *10th German Wind Energy Conference (DEWEK 2010)*, 2010.
- Y. Chen, D. Schlipf, and P. W. Cheng. Parameterization of wind evolution using lidar. *Wind Energy Science Discussions*, 2020. doi: 10.5194/wes-2020-50.
- E. Cheynet, J. B. Jakobsen, and C. Obhrai. Spectral characteristics of surface-layer turbulence in the north sea. *Energy Procedia*, 137:414–427, October 2017a. doi: 10.1016/j.egypro.2017.10.366.
- E. Cheynet, J. B. Jakobsen, J. Snæbjörnsson, J. Reuder, V. Kumer, and B. Svardal. Assessing the potential of a commercial pulsed lidar for wind characterisation at a bridge site. *Journal of Wind Engineering and Industrial Aerodynamics*, 161: 17–26, February 2017b. doi: 10.1016/j.jweia.2016.12.002.
- A. Chougule, J. Mann, M. Kelly, J. Sun, D. H. Lenschow, and E. G. Patton. Vertical cross-spectral phases in neutral atmospheric flow. *Journal of Turbulence*, 13 (36):1–13, August 2012. doi: 10.1080/14685248.2012.711524.
- A. Chougule, J. Mann, A. Segalini, and E. Dellwik. Spectral tensor parameters for wind turbine load modeling from forested and agricultural landscapes. *Wind Energy*, 18(3):469–481, February 2014. doi: 10.1002/we.1709.
- A. Chougule, J. Mann, M. Kelly, and G. Larsen. Modeling atmospheric turbulence via rapid distortion theory: Spectral tensor of velocity and buoyancy. *Journal of the Atmospheric Sciences*, 74(4):949–974, 2017. doi: 10.1175/JAS-D-16-0215.1.

- A. Chougule, J. Mann, M. Kelly, and G. C. Larsen. Simplification and validation of a spectral-tensor model for turbulence including atmospheric stability. *Boundary-Layer Meteorology*, 167(3):371–397, February 2018. doi: 10.1007/s10546-018-0332-z.
- A. Clifton and R. Wagner. Accounting for the effect of turbulence on wind turbine power curves. *Journal of Physics: Conference Series*, 524, June 2014. doi: 10.1088/1742-6596/524/1/012109.
- D. Contini, A. Donato, and F. Belosi. Accuracy of measurements of turbulent phenomena in the surface layer with an ultrasonic anemometer. *Journal of Atmospheric and Oceanic Technology*, 23(6):785–801, June 2006. doi: 10.1175/jtech1881.1.
- P. J. Cornbleet and N. Gochman. Incorrect least-squares regression coefficients in method-comparison analysis. *Clinical Chemistry*, 25(3):432–438, March 1979. doi: 10.1093/clinchem/25.3.432.
- M. Courtney and C. Hasager. Remote sensing technologies for measuring offshore wind. In *Offshore Wind Farms*, pages 59–82. Elsevier, 2016. doi: 10.1016/B978-0-08-100779-2.00004-0.
- M. Courtney, R. Wagner, and P. Lindelöw. Testing and comparison of lidars for profile and turbulence measurements in wind energy. *IOP Conference Series: Earth and Environmental Science*, 1, May 2008. doi: 10.1088/1755-1307/1/1/012021.
- P. A. Davidson. Turbulent shear flows and simple closure models. In *Turbulence*, pages 105–187. Oxford University Press, June 2015. doi: 10.1093/acprof:oso/9780198722588.003.0004.
- W. L. Eberhard, R. E. Cupp, and K. R. Healy. Doppler lidar measurement of profiles of turbulence and momentum flux. *Journal of Atmospheric and Oceanic Technology*, 6:809–819, Oct 1989. doi: 10.1175/1520-0426(1989)006<0809:DLMOP>2.0.CO;2.
- L. Eliassen and C. Obhrai. Coherence of turbulent wind under neutral wind conditions at fino1. *Energy Procedia*, 94:388–398, September 2016. doi: 10.1016/j.egypro.2016.09.199.
- S. Emeis, M. Harris, and R. M. Banta. Boundary-layer anemometry by optical remote sensing for wind energy applications. *Meteorologische Zeitschrift*, 16(4):337–347, August 2007. ISSN 0941-2948. doi: 10.1127/0941-2948/2007/0225.

- B. Ernst, B. Oakleaf, M. Ahlstrom, M. Lange, C. Moehrlen, B. Lange, U. Focken, and K. Rohrig. Predicting the wind. *IEEE Power and Energy Magazine*, 5(6): 78–89, November 2007. doi: 10.1109/MPE.2007.906306.
- P. Fuglsang, C. Bak, J. G. Schepers, B. Bulder, T. T. Cockerill, P. Claiden, A. Olesen, and R. van Rossen. Site-specific design optimization of wind turbines. *Wind Energy*, 5(4):261–279, 2002. doi: 10.1002/we.61.
- J. Gottschall and J. Peinke. How to improve the estimation of power curves for wind turbines. *Environmental Research Letters*, 3(1), January 2008. doi: 10.1088/1748-9326/3/1/015005.
- J. Gottschall, G. Wolken-Möhlmann, and B. Lange. About offshore resource assessment with floating lidars with special respect to turbulence and extreme events. *Journal of Physics: Conference Series*, 555, 2014a. doi: 10.1088/1742-6596/555/1/012043.
- J. Gottschall, G. Wolken-Möhlmann, T. Viergutz, and B. Lange. Results and conclusions of a floating-lidar offshore test. *Energy Procedia*, 53:156–161, 2014b. doi: 10.1016/j.egypro.2014.07.224.
- J. Gottschall, B. Gribben, D. Stein, and I. Würth. Floating lidar as an advanced offshore wind speed measurement technique: current technology status and gap analysis in regard to full maturity. *WIREs Energy Environment*, 6(5), May 2017. doi: 10.1002/wene.250.
- S.-E. Gryning, E. Batchvarova, B. Brümmer, H. Jørgensen, and S. Larsen. On the extension of the wind profile over homogeneous terrain beyond the surface boundary layer. *Boundary-Layer Meteorology*, 124(2):251–268, Mar. 2007. doi: 10.1007/s10546-007-9166-9.
- M. A. Gutiérrez, J. Tiana-Alsina, O. Bischoff, J. Cateura, and F. Rocadenbosch. Performance evaluation of a floating doppler wind lidar buoy in mediterranean near-shore conditions. In *2015 IEEE International Geoscience and Remote Sensing Symposium (IGARSS)*, Milan, Italy, 2015. doi: 10.1109/IGARSS.2015.7326228.
- M. A. Gutiérrez-Antuñano, J. Tiana-Alsina, A. Salcedo, and F. Rocadenbosch. Estimation of the motion-induced-horizontal-wind-speed standard deviation in an offshore doppler lidar. *Remote Sensing*, 10(12), December 2018. doi: 10.3390/rs10122037.
- GWEC. Global wind report 2018. Technical report, Global Wind Energy Council, April 2019.

- K. S. Hansen and G. C. Larsen. Characterising turbulence intensity for fatigue load analysis of wind turbines. *Wind Engineering*, 29(4):319–329, 2005. doi: 10.1260/030952405774857897.
- R. Hardesty, J. Korrell, and F. J. Hall. Lidar measurement of wind velocity turbulence spectra encountered by a rotating turbine blade. Technical report, Office of Scientific and Technical Information (OSTI), January 1982.
- D. P. Held and J. Mann. Comparison of methods to derive radial wind speed from a continuous-wave coherent lidar doppler spectrum. *Atmospheric Measurement Techniques*, 11:6339–6350, 2018. doi: 10.5194/amt-11-6339-2018.
- J. O. Hellevang and J. Reuder. Effect of wave motion on wind lidar measurements - comparison testing with controlled motion applied. In *Proceedings of DeepWind 2013 – 10th Deep Sea Offshore Wind R&D Conference*, Trondheim, Norway, Jan. 2013. 24-25 January 2013.
- T. R. Hiester and W. T. Pennell. Meteorological aspects of siting large wind turbines. Technical report, Pacific Northwest Laboratory, January 1981.
- IEC61400. *IEC61400-1:2019 Wind energy generation systems - Part 1: Design requirements*. International Electrotechnical Commission, 4.0 edition, February 2019.
- ISO16622. *Meteorology – Sonic anemometers/thermometers – Acceptance test methods for mean wind measurements*. International Organization for Standardization, first edition, September 2002.
- M. Jansen, I. Staffell, L. Kitzing, S. Quoilin, E. Wiggelinkhuizen, B. Bulder, I. Riepin, and F. Müsgens. Offshore wind competitiveness in mature markets without subsidy. *Nature Energy*, July 2020. doi: 10.1038/s41560-020-0661-2.
- J. C. Kaimal, J. C. Wyngaard, Y. Izumi, and O. R. Coté. Spectral characteristics of surface-layer turbulence. *Quarterly Journal of the Royal Meteorological Society*, 98:563–589, 1972. doi: 10.1002/qj.49709841707.
- K. Kaiser, W. Langreder, H. Hohlen, and J. Højstrup. Turbulence correction for power curves. In *Wind Energy*, pages 159–162. Springer Berlin Heidelberg, 2007. doi: 10.1007/978-3-540-33866-6\_28.
- S. Kang and H. Won. Spectral structure of 5 year time series of horizontal wind speed at the boulder atmospheric observatory. *JGR Atmospheres*, 121(20): 11946–11967, 2016. doi: 10.1002/2016JD025289.

- F. Kelberlau and T. Bracchi. Influence of turbulence characteristics on power production. In *Proceedings DEWEK 2017 - German Wind Energy Conference*, Bremen, Germany, Oct. 2017.
- L. Kristensen. On longitudinal spectral coherence. *Boundary-Layer Meteorology*, 16(2):145–153, June 1979. doi: 10.1007/BF02350508.
- L. Kristensen, P. Kirkegaard, and T. Mikkelsen. Determining the velocity fine structure by a laser anemometer with fixed orientation. Technical Report Risø-R-1762(EN), Risø DTU, 2011.
- X. G. Larsén, S. E. Larsen, and E. L. Petersen. Full-scale spectrum of boundary-layer winds. *Boundary-Layer Meteorology*, 159(2):349–371, February 2016. doi: 10.1007/s10546-016-0129-x.
- P. Lindelöw. *Fiber Based Coherent Lidars for Remote Wind Sensing*. PhD thesis, Danish Technical University, 2008.
- E. N. Lorenz. *The nature and theory of the general circulation of the atmosphere*. World Meteorological Organization, 1967.
- P. A. Lynn. Introduction. In *Onshore and Offshore Wind Energy*, pages 1–29. John Wiley & Sons, Ltd, October 2011. doi: <https://doi.org/10.1002/9781119954613.ch1>.
- J. Mann. The spatial structure of neutral atmospheric surface-layer turbulence. *Journal of Fluid Mechanics*, 273:141–168, 1994. doi: 10.1017/S0022112094001886.
- J. Mann. Wind field simulation. *Probabilistic Engineering Mechanics*, 13(4): 269–282, 1998. doi: 10.1016/S0266-8920(97)00036-2.
- J. Manwell, J. McGowan, and A. Rogers. Wind characteristics and resources. In *Wind Energy Explained*, pages 23–89. John Wiley & Sons, Ltd, December 2010. doi: 10.1002/9781119994367.ch2.
- C. M. S. Martin, J. K. Lundquist, A. Clifton, G. S. Poulos, and S. J. Schreck. Wind turbine power production and annual energy production depend on atmospheric stability and turbulence. *Wind Energy Science*, 1(2):221–236, November 2016. doi: 10.5194/wes-1-221-2016.
- J.-P. Mathisen. Measurement of wind profile with a buoy mounted lidar. In *Proceedings of DeepWind'2013*, Trondheim, Norway, Jan. 2013.

- T. Mikkelsen, J. Mann, M. Courtney, and M. Sjöholm. Windscanner: 3-d wind and turbulence measurements from three steerable doppler lidars. *IOP Conference Series: Earth and Environmental Science*, 2008. doi: 10.1088/1755-1307/1/1/012018.
- T. K. Mikkelsen. On mean wind and turbulence profile measurements from ground-based wind lidars: limitations in time and space resolution with continuous wave and pulsed lidar systems. *European Wind Energy Conference and Exhibition 2009*, 6:4123–4132, 2009.
- J. F. Newman and A. Clifton. An error reduction algorithm to improve lidar turbulence estimates for wind energy. *Wind Energy Science*, 2:77–95, 2017. doi: 10.5194/wes-2-77-2017.
- J. F. Newman, A. Clifton, M. J. Churchfield, and P. Klein. Improving lidar turbulence estimates for wind energy. *Journal of Physics: Conference Series*, 753, September 2016a. doi: 10.1088/1742-6596/753/7/072010.
- J. F. Newman, P. M. Klein, S. Wharton, A. Sathe, T. A. Bonin, P. B. Chilson, and A. Muschinski. Evaluation of three lidar scanning strategies for turbulence measurements. *Atmospheric Measurement Techniques*, (9):1993–2013, 2016b. doi: 10.5194/amt-9-1993-2016.
- M. Noda and R. Flay. A simulation model for wind turbine blade fatigue loads. *Journal of Wind Engineering and Industrial Aerodynamics*, 83(1–3):527–540, November 1999. doi: 10.1016/S0167-6105(99)00099-9.
- L. Pauscher, N. Vasiljevic, D. Callies, G. Lea, J. Mann, T. Klaas, J. Hieronimus, J. Gottschall, A. Schwesig, M. Kühn, and M. Courtney. An inter-comparison study of multi- and db-s-lidar measurements in complex terrain. *Remote Sensing*, 8(9):782, 2016. doi: 10.3390/rs8090782.
- A. Peña, C. B. Hasager, S.-E. Gryning, M. Courtney, I. Antoniou, and T. Mikkelsen. Offshore wind profiling using light detection and ranging measurements. *Wind Energy*, 12(2):105–124, March 2009. doi: 10.1002/we.283.
- A. Peña, E. Dellwik, and J. Mann. A method to assess the accuracy of sonic anemometer measurements. *Atmospheric Measurement Techniques*, 12(1):237–252, January 2019. doi: 10.5194/amt-12-237-2019.
- J. Perlwitz, T. Knutson, J. Kossin, and A. LeGrande. Ch. 5: Large-scale circulation and climate variability. climate science special report: Fourth national climate assessment, volume i. Technical report, U.S. Global Change Research Program, 2017.

- A. Sathe and J. Mann. Measurement of turbulence spectra using scanning pulsed wind lidars. *Journal of Geophysical Research: Atmospheres*, 117:D01201, Jan. 2012. doi: 10.1029/2011JD016786.
- A. Sathe and J. Mann. A review of turbulence measurements using ground-based wind lidars. *Atmospheric Measurement Techniques*, 6(11):3147–3167, November 2013. doi: 10.5194/amt-6-3147-2013.
- A. Sathe, J. Mann, J. Gottschall, and M. S. Courtney. Can wind lidars measure turbulence? *Journal of Atmospheric and Oceanic Technology*, 28(7):853–868, July 2011. doi: 10.1175/JTECH-D-10-05004.1.
- A. Sathe, J. Mann, T. Barlas, W. Bierbooms, and G. van Bussel. Influence of atmospheric stability on wind turbine loads. *Wind Energy*, 16(7):1013–1032, July 2012. doi: 10.1002/we.1528.
- A. Sathe, J. Mann, N. Vasiljevic, and G. Lea. A six-beam method to measure turbulence statistics using ground-based wind lidars. *Atmospheric Measurement Techniques*, 8(2):729–740, 2015. doi: 10.5194/amt-8-729-2015.
- D. Schlipf, D. J. Schlipf, and M. Kühn. Nonlinear model predictive control of wind turbines using LIDAR. *Wind Energy*, 16(7):1107–1129, August 2012. doi: 10.1002/we.1533.
- A. M. Sempreviva, R. J. Barthelmie, and S. C. Pryor. Review of methodologies for offshore wind resource assessment in european seas. *Surveys in Geophysics*, 29(6):471–497, December 2008. doi: 10.1007/s10712-008-9050-2.
- C. M. Shun and P. W. Chan. Applications of an infrared doppler lidar in detection of wind shear. *Journal of Atmospheric and Oceanic Technology*, 25(5):637–655, May 2008. doi: 10.1175/2007JTECHA1057.1.
- E. Simley and L. Y. Pao. A longitudinal spatial coherence model for wind evolution based on large-eddy simulation. In *2015 American Control Conference (ACC)*, 2015. doi: 10.1109/ACC.2015.7171906.
- M. Sjöholm, T. Mikkelsen, J. Mann, K. Enevoldsen, and M. Courtney. Time series analysis of continuous-wave coherent Doppler lidar wind measurements. *IOP Conference Series: Earth and Environmental Science*, 1, May 2008. doi: 10.1088/1755-1307/1/1/012051.
- M. Sjöholm, T. Mikkelsen, J. Mann, K. Enevoldsen, and M. Courtney. Spatial averaging-effects on turbulence measured by a continuous-wave coherent lidar. *Meteorologische Zeitschrift*, 18(3):281–287, June 2009. doi: 10.1127/0941-2948/2009/0379.

- D. A. Smith, M. Harris, A. S. Coffey, T. Mikkelsen, H. E. Jørgensen, J. Mann, and R. Danielian. Wind lidar evaluation at the Danish wind test site Høvsøre. *Wind Energy*, 9(1–2):87–93, January 2006. doi: 10.1002/we.193.
- K. Thomsen and P. Sørensen. Fatigue loads for wind turbines operating in wakes. *Journal of Wind Engineering and Industrial Aerodynamics*, 80(1–2):121–136, March 1999. doi: 10.1016/S0167-6105(98)00194-9.
- K. Thomsen, P. Fuglsang, and G. Schepers. Potentials for site-specific design of MW sized wind turbines. *Journal of Solar Energy Engineering*, 123(4):304–309, June 2001. doi: 10.1115/1.1408611.
- A. J. Tiana-Alsina, M. A. Gutiérrez, I. Würth, J. Puigdefàbregas, and F. Rocadenbosch. Motion compensation study for a floating doppler wind lidar. In *2015 IEEE International Geoscience and Remote Sensing Symposium (IGARSS)*, Milan, Italy, 2015. doi: 10.1109/IGARSS.2015.7327051.
- J. Tiana-Alsina, F. Rocadenbosch, and M. A. Gutiérrez-Antuñano. Vertical azimuth display simulator for wind-doppler lidar error assessment. In *2017 IEEE International Geoscience and Remote Sensing Symposium (IGARSS)*, pages 1614–1617, Fort Worth, USA, 2017. doi: 10.1109/IGARSS.2017.8127282.
- K. E. Trenberth and D. P. Stepaniak. Seamless poleward atmospheric energy transports and implications for the hadley circulation. *Journal of Climate*, 16(22):3706–3722, November 2003. doi: 10.1175/1520-0442(2003)016<3706:SPAETA>2.0.CO;2.
- I. Van der Hoven. Power Spectrum of Horizontal Wind Speed in the Frequency Range from 0.0007 to 900 Cycles per Hour. *Journal of Meteorology*, 14(2):160–164, April 1957. doi: 10.1175/1520-0469(1957)014<0160:PSOHWS>2.0.CO;2.
- T. von Kármán. Progress in the statistical theory of turbulence. *Proceedings of the National Academy of Sciences*, 34:530–539, 1948. doi: 10.1073/pnas.34.11.530.
- G. Wolken-Möhlmann, H. Lilov, and B. Lange. Simulation of motion induced measurement errors for wind measurements using lidar on floating platforms. In *Proceedings of ISARS 2010 - 15th International Symposium for the Advancement of Boundary Layer Remote Sensing*, Paris, France, 2010. Fraunhofer IWES.

- G. Wolken-Möhlmann, L. Baise, and D. Kuchma. About the frequency dependency of floating-lidar motion effects. In *Proceedings of DEWEK 2017 - German Wind Energy Conference*, Bremen, Germany, Oct. 2017.
- J. C. Wyngaard. Measurement of small-scale turbulence structure with hot wires. *Journal of Physics E: Scientific Instruments*, 1(11):1105–1108, November 1968. doi: 10.1088/0022-3735/1/11/310.
- J. C. Wyngaard. The effects of probe-induced flow distortion on atmospheric turbulence measurements. *Journal of Applied Meteorology*, 20(7):784–794, July 1981. doi: 10.1175/1520-0450(1981)020<0784:TEOPIF>2.0.CO;2.
- S. Yahaya and J. P. Frangi. Cup anemometer response to the wind turbulence-measurement of the horizontal wind variance. *Annales Geophysicae*, 22(10): 3363–3374, November 2004. doi: 10.5194/angeo-22-3363-2004.
- A. Yamaguchi and T. Ishihara. A new motion compensation algorithm of floating lidar system for the assessment of turbulence intensity. *Journal of Physics: Conference Series*, 753, 2016. doi: 10.1088/1742-6596/753/7/072034.

## **Chapter 5**

### **Article 1:**

### **Better turbulence spectra from velocity–azimuth display scanning wind lidar**



Atmos. Meas. Tech., 12, 1871–1888, 2019  
https://doi.org/10.5194/amt-12-1871-2019  
© Author(s) 2019. This work is distributed under  
the Creative Commons Attribution 4.0 License.



Atmospheric  
Measurement  
Techniques  
Open Access  
EGU

## Better turbulence spectra from velocity–azimuth display scanning wind lidar

Felix Kelberlau<sup>1</sup> and Jakob Mann<sup>2</sup>

<sup>1</sup>NTNU, Department of Energy and Process Engineering, Norwegian University of Science and Technology, 7491 Trondheim, Norway

<sup>2</sup>DTU Wind Energy, Technical University of Denmark, 4000 Roskilde, Denmark

**Correspondence:** Felix Kelberlau (felix.kelberlau@ntnu.no) and Jakob Mann (jmsq@dtu.dk)

Received: 21 November 2018 – Discussion started: 4 December 2018

Revised: 5 February 2019 – Accepted: 3 March 2019 – Published: 21 March 2019

**Abstract.** Turbulent velocity spectra derived from velocity–azimuth display (VAD) scanning wind lidars deviate from spectra derived from one-point measurements due to averaging effects and cross-contamination among the velocity components. This work presents two novel methods for minimizing these effects through advanced raw data processing. The squeezing method is based on the assumption of frozen turbulence and introduces a time delay into the raw data processing in order to reduce cross-contamination. The two-beam method uses only certain laser beams in the reconstruction of wind vector components to overcome averaging along the measurement circle. Models are developed for conventional VAD scanning and for both new data processing methods to predict the spectra and identify systematic differences between the methods. Numerical modeling and comparison with measurement data were both used to assess the performance of the methods. We found that the squeezing method reduces cross-contamination by eliminating the resonance effect caused by the longitudinal separation of measurement points and also considerably reduces the averaging along the measurement circle. The two-beam method eliminates this averaging effect completely. The combined use of the squeezing and two-beam methods substantially improves the ability of VAD scanning wind lidars to measure in-wind ( $u$ ) and vertical ( $w$ ) fluctuations.

### 1 Introduction

Wind speed measurements are an integral element of wind site assessment. Traditionally such measurements have been based on in situ sampling with anemometers attached to tall meteorological masts that reach up to hub height. Such masts are immobile and expensive to erect. It is therefore favorable to implement remote-sensing devices, such as conically scanning profiling lidars, that measure wind velocities at adjustable height levels above the ground remotely.

Pulsed and continuous-wave wind lidars are the two types of profiling lidars that are currently commercially available. The velocity–azimuth display (VAD) scanning strategy was introduced by Browning and Wexler (1968) and is usually applied for continuous-wave profiling lidars like the ZX 300 (previously ZephIR 300) produced by Zephir Ltd. Advanced processing of VAD-acquired data is the object of investigation here.

Validation studies that compare measurements from meteorological masts and ground-based profiling lidars report good agreement for first-order statistics, namely the 10 min mean wind velocities and directions (Kindler et al., 2007; Smith et al., 2006; Medley et al., 2015; Kim et al., 2016). The estimation of second-order statistics of the turbulence in the wind by means of VAD scanning pulsed Doppler lidar was first demonstrated by Eberhard et al. (1989). But such turbulence estimates from VAD scanning lidars deviate from classical measurements with cup or sonic anemometers (Sathe and Mann, 2013; Peña et al., 2009; Canadillas et al., 2010). Sathe et al. (2011) model the second-order statistics of pulsed and continuous-wave profiling lidars. The resulting velocity variances are influenced by the effects that arise from sensing

the three-dimensional wind field by averaging over spatially distributed volumes. In order to better understand the actual behavior of the lidar in comparison to reference measurements, turbulence spectra of the three wind components  $u$ ,  $v$  and  $w$  can provide much-needed insight. Sathe and Mann (2012) model and analyze turbulence spectra, but only for pulsed lidars that use Doppler beam swing (DBS) scanning. A simplified model for turbulence spectra from VAD scanning wind lidars is presented in Wagner et al. (2009). However, it does not include the effect of cross-contamination and cannot be used to predict the turbulence spectra of real lidars.

The six-beam method developed by Sathe et al. (2015) is an alternative to VAD scanning that results in more accurate second-order statistics of turbulence. But its application requires a vertical laser beam and a half-cone opening angle of  $45^\circ$ , which makes it unusable with commercially available profiling wind lidars.

Newman et al. (2016) propose another method to compensate for the contamination by means of autocorrelation functions derived from collocated mast measurements. This method is, however, only applicable when a meteorological mast is available. In comparing and evaluating the ability of different lidar scanning strategies to measure turbulence, Newman et al. (2016) conclude that cross-contamination of the different velocity components is one of the primary disadvantages of current profiling lidars.

The research presented here demonstrates two methods aimed at overcoming the effects of cross-contamination and averaging along the measurement circle that are inherent in the standard VAD scanning strategy. Both methods are based on modified line-of-sight velocity data processing and can be applied to currently available lidars without changes in their hardware. The line-of-sight averaging effect remains unresolved.

The first method incorporates Taylor's frozen turbulence hypothesis and introduces a time lag into the wind vector reconstruction process. Bardal and Sætran (2016) measure two-point correlations of horizontal wind speeds from two meteorological masts that are separated by 79 m in line with the mean wind direction. They find that the cross-correlation coefficient is around 0.8 when a temporal lag compensates for the time required for the wind to cover the distance between the two measurement points. Without delaying the signal, the cross-correlation coefficient reaches only half of that value. Applied to VAD scanning lidars, that justifies the assumption that when the processing of line-of-sight measurement data is delayed by the time needed to cross the measurement circle, the lidar measurements will be more realistic. This approach is hereafter called "squeezing" and reduces the cross-contamination effect that currently distorts the shape of turbulence spectra acquired with VAD scanning lidars.

The second method is to use only the radial velocities from lines of sight that point into the mean wind direction (downwind) and against it (upwind) to determine the components

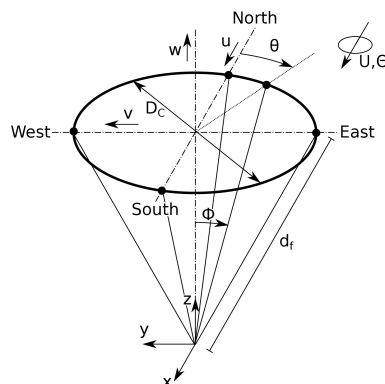


Figure 1. Lidar geometry definitions and coordinate system.

of the wind that are oriented in line with the mean wind direction ( $u$ ) and vertical direction ( $w$ ). This eliminates the averaging along the measurement circle.

The aim of the research presented here is to demonstrate whether one of the two modified data processing algorithms or their combination leads to improved turbulence measurements from standard VAD wind lidars. For each method, we present a numerical model and experimental results. We discuss the effects of the two methods individually and combined.

This research has several practical applications. The reliable elimination of cross-contamination and averaging along the measurement circle would lead to a reduction of the systematic error of wind lidar measurements that is dependent on the prevailing wind conditions and the measurement height. In particular, estimations of the timescale of turbulence could be made with higher certainty, which would support future boundary layer research by means of profiling wind lidars. In addition, estimating the energy content of the wind components at specific wave numbers with higher certainty could also help to better predict the operational wind loads of wind turbines and other structures.

Section 2 summarizes the VAD scanning process and describes, in detail, the averaging and cross-contamination effects it implies for the measurement of turbulence. In Sect. 3 the suggested modified data processing methods are described before they are modeled alongside the conventional processing in Sect. 4. The measurements are described in Sect. 5 before the results are compared with the model predictions in Sect. 6. Section 7 concludes with the most important findings.

## 2 Lidar theory

### 2.1 Coordinate system and preliminaries

Figure 1 shows the measurement circle of diameter  $D_C$  of a VAD scanning lidar and how it is created by the laser beams that are deflected from the zenith by the half-cone opening angle  $\phi$  and rotate around the zenith with continuously changing azimuth angle  $\theta$ . The beams are focused at a point at distance  $d_f$  from the lidar, which is located at the origin of a three-dimensional left-handed coordinate system. Five of the laser beams are depicted, four in the cardinal directions and one with an arbitrary azimuth angle. The mean wind direction  $\Theta$  determined from 10 min intervals is zero when the wind blows from north to south. The wind vector

$$\mathbf{u} = \begin{pmatrix} u \\ v \\ w \end{pmatrix} \quad (1)$$

is composed of the wind components  $u$ ,  $v$  and  $w$  that are aligned with the axes of the coordinate system when  $\Theta = 0^\circ$ . Reynolds decomposition is used for the description of the wind field so that

$$\mathbf{u} = \mathbf{U} + \mathbf{u}', \quad (2)$$

where  $\mathbf{u}'$  represents the wind speed fluctuations in all three directions and  $\mathbf{U}$  is the mean wind velocity vector.

### 2.2 Taylor's frozen turbulence hypothesis

The frozen turbulence hypothesis published by Taylor (1938) assumes that turbulence is advected by the mean wind velocity  $\mathbf{U}$  into the mean wind direction  $\Theta$ . During the transport process the turbulence remains unchanged, i.e., turbulence measured at one point in space gives information about the turbulence found further downwind some time later. That means for a velocity vector field  $\mathbf{u}$  when  $\mathbf{U}$  is aligned with the  $x$  axis that

$$\mathbf{u}(x, y, z, t) = \mathbf{u}(x - \mathbf{U}t, y, z, 0). \quad (3)$$

The hypothesis is widely used and it is known from experiments that the assumption of frozen turbulence is valid to a high degree for large eddies. For example, Schlipf et al. (2010) measured the inflow velocities of an operating wind turbine at different distances from the rotor plane in order to test the hypothesis of frozen turbulence. They found it to be valid for large-scale wind fluctuations with wave numbers  $k > 1.25 \times 10^{-1} \text{ m}^{-1}$ . Willis and Deardorff (1976) show that the hypothesis lacks validity when

$$\sigma_u / \mathbf{U} > 0.5. \quad (4)$$

This implies that the validity of the hypothesis depends on the amount of turbulence and that a high degree of validity is expected when the velocity variance is low compared to the mean wind speed.

### 2.3 VAD measurement principle

Continuous-wave wind lidars continuously emit a focused infrared laser beam into the air and detect the small portion of the radiation that is backscattered by particles along the beam path towards the beam's origin. The velocity of the backscattering particles relative to the beam direction is then determined by analyzing the Doppler shift between the frequencies of outgoing and incoming radiation. It is assumed that the backscatterers are lightweight enough to move with the instantaneous wind speed  $\mathbf{u}$ . The measured radial line-of-sight velocities  $v_r$  are hence equal to the wind velocity projected onto the beam direction. In order to estimate the three-dimensional wind vector  $\mathbf{u}$ , a minimum of three independent line-of-sight measurements from different directions must be combined.

When VAD scanning is used, the beam is deflected by a wedge prism by a constant half-cone opening angle  $\phi$  from the zenith and rotated around the zenith with a steadily changing azimuth angle  $\theta$ . Many radial velocities  $v_r$  are acquired during one full rotation of the prism. For example in the case of the ZX 300 (previously ZephIR 300),  $N = 49$  Doppler spectra are calculated and used to determine the same number of radial velocities. All of them are used to reconstruct one wind vector by applying a least-squares fit to

$$v_r = |A \cos(\theta - B) + C|, \quad (5)$$

where the best fit parameters  $A$ ,  $B$  and  $C$  represent the wind data according to

$$\begin{aligned} v_{\text{hor}} &= A / \sin(\phi) \\ \Theta &= B \pm 180^\circ \\ v_{\text{ver}} &= C / \cos(\phi). \end{aligned} \quad (6)$$

The sign of the radial velocity is usually unknown. We are thus faced with a directional ambiguity of  $\pm 180^\circ$ , but this does not affect the turbulence analysis here. The wind data  $v_{\text{hor}}$ ,  $\Theta$  and  $v_{\text{ver}}$  can be translated into wind vectors  $\mathbf{u}$  easily.

The wind velocity estimations that result from this processing underlie several effects that distinguish them from one-point measurements. These effects can be divided into

- averaging
  - a. along the lines of sight
  - b. along the measurement circle and
- cross-contamination
  - a. due to longitudinal separation
  - b. due to lateral separation.

### 2.4 Averaging effects

#### 2.4.1 Line-of-sight averaging

In situ wind speed measurements taken with cup anemometers or ultrasonic anemometers have a small measurement

**Table 1.** Key specifications of the lidar used in the measurements.

Description	Abbr.	Value	Unit
Measurement height	$h$	78	[m]
Half-cone angle	$\phi$	30.6	[°]
Cone diameter	$D_C$	92.3	[m]
Focus distance	$d_f$	90.6	[m]
Prism rotation	$f_S$	1	[Hz]
Measurements per cycle	$N$	50	[1]
Laser wave length	$\lambda$	1550	[nm]
Effec. aperture diam.	$a_0$	24	[mm]
Mean wind speed	$U_{\text{mean}}$	19.5	[m s <sup>-1</sup> ]
1. Resonance	$\lambda_{\text{res1}}$	184.5	[m]
	$k_{\text{res1}}$	0.034	[m <sup>-1</sup> ]
2. Resonance	$\lambda_{\text{res2}}$	61.5	[m]
	$k_{\text{res2}}$	0.102	[m <sup>-1</sup> ]
No. of cycles to cover $\tau$	$M$	0–5	[1]
Rayleigh length	$l_R$	7.03	[m]
Full width at half maximum	$2l_R$	14.07	[m]

volume that can be considered a point. Lidar measurements, in contrast, sense wind velocities along an extended stretch of the line of sight of the laser beam. In the case of continuous-wave lidars, the laser beam leaves the lidar optics with a diameter that corresponds to its effective aperture size  $a_0$  and is focused onto a focus point. The distance between the lidar optics and the focus point is the focal distance  $d_f$ . The signal of the backscattered radiation originates from anywhere along the illuminated beam, according to a distribution function that has its maximum at the focus point and is proportional to the intensity of the laser light along the beam (Sonnenschein and Horrigan, 1971).

A definite range gate, such as for pulsed lidars, is therefore not applicable to continuous-wave lidars. Instead, the Rayleigh length  $l_R$  is a measure of the distance between the focus point and the point at which the cross section of the beam has twice the area of the cross section at the focus point. According to Harris et al. (2006), it is given by

$$l_R = \frac{\lambda d_f^2}{\pi a_0^2}, \quad (7)$$

where  $\lambda$  is the laser wavelength and  $a_0$  is the effective aperture diameter. The Rayleigh length is quadratically proportional to the focal distance  $d_f$  that increases linearly with the selected measurement height level. The degree of line-of-sight averaging is thus strongly dependent on the measurement height level and is higher for larger heights. The values of  $l_R$ ,  $a_0$  and  $d_f$  for the lidar used in our experiments are given in Table 1.

The intensity of backscattered radiation is a function of the distance  $s$  from the focus point along the beam. It is sufficiently well approximated by a Lorentzian function,

$$F(s) = \frac{l_R/\pi}{s^2 + l_R^2}, \quad (8)$$

where  $s$  is the distance from the focus position (Mikkelsen, 2009).

All Doppler spectra that are retrieved during the radial velocity acquisition time are averaged, and the focus point sweeps over a considerable arc of the measurement circle during this time. This arc length  $l_A$  is

$$l_A = \frac{D_C \pi}{N}, \quad (9)$$

where  $N$  is the number of line-of-sight measurements  $v_r$  taken during one rotation. In experimental data, the arc averaging effect is contained in the radial velocities. In the models here, we account for this by averaging along the measurement circle.

The Doppler spectra of each line-of-sight measurement resemble the probability density function of the radial wind velocities along the line of sight (Branlard et al., 2013). But by determining one single velocity value for each line-of-sight measurement, the turbulence information they contain is filtered out.

The additional temporal averaging along the lines of sight is very low, as one measurement takes only  $\frac{1}{N}$  s. The effect of line-of-sight averaging is very strong for high wave numbers but has some effect on long turbulent structures as well. The effect of line-of-sight averaging is considered in the numerical models and the discussion in this study. But none of the presented data processing methods can avoid the line-of-sight averaging effect.

#### 2.4.2 Measurement circle averaging

As described in Sect. 2.3 lidars use all measurement data of at least one full rotation of the prism to reconstruct one wind vector. The resulting system of equations is overdetermined, and in order to find a solution a quadratic best fit is applied. The more line-of-sight velocities that are used to reconstruct a wind vector, the stronger the averaging and thereby the larger the loss of turbulent kinetic energy in the measurement data. The residual of the best fit is a measure of the degree of this form of averaging but is usually not used in the processing.

The diameter  $D_C$  of the measurement circle is

$$D_C = 2h \tan \phi, \quad (10)$$

with  $h$  being the measurement height and  $\phi$  the half-cone opening angle. The spatial separation between the points that one reconstructed wind vector is composed of thus linearly increases with measurement height. The larger the cone diameter, the stronger the circle averaging. Turbulence with a length scale below the diameter of the averaging circle is affected the most.

In addition to the spatial separation of the measurement points along the measurement circle, the acquisition time must be considered. The mean wind motion carries the air

while it is probed, which might further increase the separation of measurement points in the mean wind direction. The ZephIR 300 measures one full rotation in 1 s, and the distance the air moves within this time is usually small compared to  $D_C$ . The effect of temporal averaging is therefore often small compared to the spatial averaging. One example for the path of measurements that is averaged over is given in Fig. 4a. The circle diameter represents the spatial averaging, and the shift along-wind with the speed  $U$  represents the temporal averaging.

2.5 Cross-contamination

2.5.1 Cross-contamination due to longitudinal separation

Another cause for differences in the shape of turbulence spectra from one-point measurements and their counterparts from VAD scanning lidars is cross-contamination of different velocity components. VAD scanning lidars combine measurements from spatially separated locations where differing velocities may prevail as if they were collected at one point. This leads to a redistribution of turbulent energy among the velocity components  $u$ ,  $v$  and  $w$ . Lidar-derived spectra of one of the components can at certain wave numbers show lower energy values than the original wind spectrum of that component but may also show too high values due to a contribution from a different velocity component. To better understand cross-contamination we divide the effect into two different types of separations. First we look into longitudinal separations, i.e., separation along the mean wind direction. Fluctuations at two points separated in line with the wind are highly correlated. If the assumption of frozen turbulence is correct, the coherence would be 1 for all separation lengths and all wave numbers. One example of cross-contamination of correlated fluctuations between two longitudinally separated points is visualized in Fig. 2. The chosen wavelength of the wind fluctuations equals twice the separation distance. This can be called the first resonance wavelength. The resonance wavelengths are given by

$$\lambda_{res,n} = \frac{2D_C}{2n-1} \tag{11}$$

The corresponding resonance wave numbers are

$$k_{res,n} = \frac{(2n-1)\pi}{D_C} \tag{12}$$

where  $n = 1, 2, 3, \dots$ . The resulting values for the first two resonance points are given in Table 1.

The two beam directions in line with and against the mean wind direction can be used to determine  $u_{lidar}$  and  $w_{lidar}$  by using the formulas on the right-hand side of the figure. This example looks at these two lines of sight. The  $v$  component can be ignored because transverse fluctuations are not detected by the upstream and downstream beams. The example

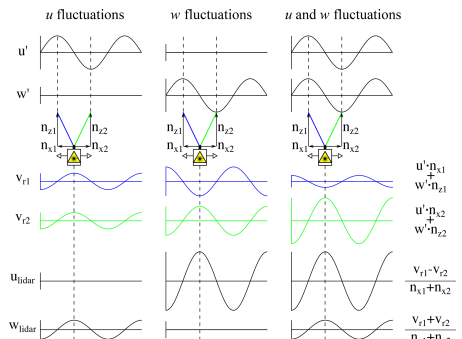


Figure 2. Visualization of cross-contamination caused by longitudinal spacing of measurement points 1 and 2. The wavelength of  $u'$  and  $w'$  equals twice the separation distance of the focus points of the lidar (indicated by box with yellow symbol). The resulting measurement values of the  $u$  component are contaminated by fluctuations in the  $w$  direction and vice versa.

demonstrates a case with isotropic turbulence, i.e., arbitrary but identical amplitudes for fluctuations in all orientations. Averaging along the lines of sight is ignored here for simplicity. The first column of graphs in the figure isolates the  $u$  fluctuations  $u'$  and shows the resulting lidar-measured signal for the two radial velocities in the upwind and downwind directions, i.e.,  $v_{r1}$  and  $v_{r2}$ . When these two signals are combined in the usual way, the reconstructed wind speed components  $u'_{lidar}$  and  $w'_{lidar}$  differ strongly from the real inflow conditions  $u'$  and  $w'$ . The lidar is blind to wind speed fluctuations in the  $u$  direction and instead attributes the fluctuations to some extent to the estimation of  $w'_{lidar}$ . The same is done for  $w'$  in the second column, and the resulting effect is the reverse. The vertical fluctuations  $w'$  are interpreted solely as amplified fluctuations of  $u'_{lidar}$ .

The last column combines the two previous cases and shows the resulting distribution of amplitudes that depends on the half-cone opening angle  $\phi$ . When  $\phi < 45^\circ$  the lidar is more sensitive to vertical variations than to horizontal ones, and the contamination of  $u'$  caused by  $w'$  is more severe than vice versa.

In a more realistic situation, turbulence is non-isotropic and the amplitude of  $w'$  at this first resonance wave number is often considerably lower than the amplitude of  $u'$ , which leads to a different distribution of contamination, which can be estimated as follows. We use Eqs. (31) and (33) to define the lidar-derived variance in the  $u$  direction:

$$\sigma_{u,lidar}^2 = \left\langle \left( \frac{\Delta v}{-2 \sin \phi} \right)^2 \right\rangle \tag{13}$$

In general, the differences of the line-of-sight velocities aligned with the mean wind  $\Delta v$  contain contributions from wind fluctuations in the  $u$  and  $w$  directions  $\Delta v_u$  and  $\Delta v_w$ , respectively. Here we look at the resonance case in which  $\Delta v_u = 0$  and thus  $\Delta v = \Delta v_w$ . We get

$$\begin{aligned}\sigma_{u,\text{lidar, res}}^2 &= \left\langle \left( \frac{\Delta v_w}{-2 \sin \phi} \right)^2 \right\rangle = \left\langle \left( \frac{2w' \cos \phi}{-2 \sin \phi} \right)^2 \right\rangle \\ &= \cot^2 \phi \sigma_{w, \text{res}}^2 \approx 2.86 \sigma_{w, \text{res}}^2,\end{aligned}\quad (14)$$

when  $\phi = 30.6^\circ$  as for the lidar we used in this study. The subscript “res” indicates that the equation is only valid for inflow fluctuations at resonance, as in the example given before.

In Sect. 4 we develop a model to predict lidar-derived spectra. This model was used to create the plots shown in Fig. 3. Figure 3a shows the modeled spectra of the wind components,  $u_{\text{wind}}$  and  $w_{\text{wind}}$ , as solid black and red lines. The parameters of the underlying spectral tensor are given in Table 1. They were chosen to best represent the wind conditions found during the experiment presented in Sect. 6. The model was used to estimate the  $u$  component of the wind from two lidar beams that point in the upwind and downwind directions. Also here, we did not include line-of-sight averaging to isolate the effect of cross-contamination. The principle of the setup is the same as explained for Fig. 2 but now we see results for all inflow wave numbers and use anisotropic turbulence. The resulting lidar-derived spectrum  $u_{\text{lidar, sum}}$  of the  $u$  component of the wind is the sum of the lidar’s interpretation of the wind components  $u_{\text{lidar, u}}$  and  $u_{\text{lidar, w}}$ . We see that the lidar-estimated spectrum of  $u_{\text{lidar, sum}}$  lies a bit below the target spectrum of  $u_{\text{wind}}$  for most wave numbers but not at the first and second resonance points that are marked with grey dashed vertical lines. There it exceeds the target spectrum. The reason becomes apparent when we look at the components  $u_{\text{lidar, u}}$  and  $u_{\text{lidar, w}}$  that  $u_{\text{lidar, sum}}$  is composed of. We find that the lidar sees  $u_{\text{wind}}$  nearly to its full extent for very low wave numbers but when we come close to the resonance points  $u_{\text{lidar, u}}$  drops to zero. The contribution of the vertical wind  $u_{\text{lidar, w}}$  shows a mirrored behavior and is amplified according to Eq. (14) since  $\phi < 45^\circ$ .

## 2.5.2 Cross-contamination due to lateral separation

When the lines of sight under consideration are not longitudinally but laterally separated, they do not face resonance but instead a second form of cross-contamination. The strength of the contamination depends then on the coherence of the turbulence for the given lateral separation. When the fluctuations at the two selected focus points are very coherent i.e., their correlation is close to unity, we can expect that the lidar-derived wind speed estimates are correct and no cross-contamination occurs. This can be observed at very low wave numbers at which a high degree of coherence is expected. The other extreme is found at the other end of the spectrum

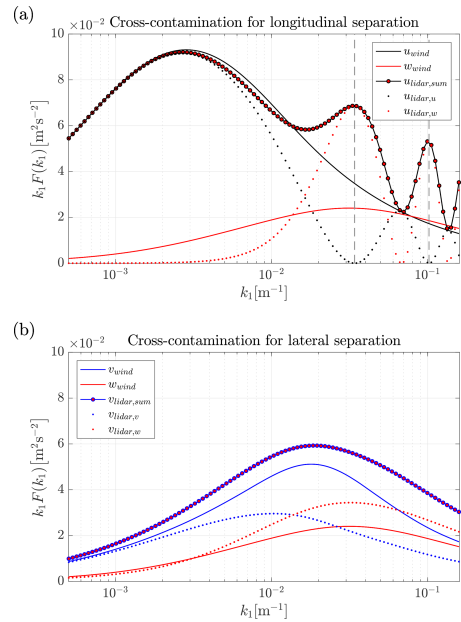


**Figure 3.** Modeled cross-contamination effect inherent in (a) the  $u$  spectrum from two longitudinally separated points with  $\Delta x = D_C$  and (b) the  $v$  spectrum from two laterally separated points with  $\Delta y = D_C$ . The solid lines are the spectra of the involved wind components. The dotted lines show the contribution of these wind components to the lidar spectra (circle markers). Averaging along the lines of sight is excluded.

at which small fluctuations measured at both focus points are uncorrelated. The lidar-derived spectrum is there a linear combination of the variances of the involved components  $v$  and  $w$  according to

$$\begin{aligned}\sigma_{v,\text{lidar}}^2 &= \left\langle \left( \frac{\Delta v}{-2 \sin \phi} \right)^2 \right\rangle \\ &= \left\langle \left( \frac{\Delta v_v}{-2 \sin \phi} \right)^2 \right\rangle + \left\langle \left( \frac{\Delta v_w}{-2 \sin \phi} \right)^2 \right\rangle.\end{aligned}\quad (15)$$

In the case of fully uncorrelated fluctuations we know that  $\Delta v_v = -v' \sin \phi$  and  $\Delta v_w = w' \cos \phi$  and the variance

$\sigma_{v,\text{lidar,unc}}^2$  of the lidar-derived  $v$  velocity is

$$\begin{aligned}\sigma_{v,\text{lidar,unc}}^2 &= \left\langle \left( \frac{-v' \sin \phi}{-2 \sin \phi} \right)^2 \right\rangle + \left\langle \left( \frac{w' \cos \phi}{-2 \sin \phi} \right)^2 \right\rangle \\ &= \frac{1}{2} \left( \sigma_{v,\text{unc}}^2 + \sigma_{w,\text{unc}}^2 \cot^2 \phi \right) \\ &\approx 0.5 \sigma_{v,\text{unc}}^2 + 1.43 \sigma_{w,\text{unc}}^2\end{aligned}\quad (16)$$

for the lidar with a half-cone opening angle of  $\phi = 30.6^\circ$ . These two situations and all cases in between are shown in Fig. 3b. The difference from the plots in Fig. 3a is that the two beams that point into and against the  $v$  direction are used here to estimate the  $v$ -spectrum  $v_{\text{lidar,sum}}$ . The target spectrum of the  $v$  component of the wind  $v_{\text{wind}}$  is given as well as the  $w$ -spectrum  $w_{\text{wind}}$  that contaminates the signal. From the  $v_{\text{lidar,v}}$  and  $v_{\text{lidar,w}}$  curves it can be seen that at very low wave numbers hardly any contamination occurs but mainly because the  $w$ -component  $w_{\text{wind}}$  itself contains a low energy density at low wave numbers. As it increases for higher wave numbers, the contamination also becomes more severe. In this example  $w_{\text{wind}}$  dominates the lidar spectrum  $v_{\text{lidar,sum}}$  for all wave numbers above approximately  $k_1 = 1.4 \times 10^{-2} \text{ m}^{-1}$ . The result is that the lidar overestimates the  $v$  variances for all wave numbers. Such an effect is also reported by Wyngaard (1968). Thus, it is essential for accurate turbulence measurements to minimize spatial separation.

VAD scanning along the whole measurement circle is more complex than using only two beams. Examining the two beams aligned with or perpendicular to the mean wind direction is not sufficient to fully understand the effect of cross-contamination. For circle scans, all three wind speed components are involved in contaminating all the beams that do not point in the four cardinal directions. We refer to the model presented in Sect. 4.1 and especially Eqs. (24), (25) and (26) of the spectral weighting functions therein to better understand which components influence another.

The lidar can also be configured to perform a so-called 3 s scan, in which one measurement cycle is built from data from three full rotations. This limits the cross-contamination but comes at the cost of much stronger averaging along the measurement circle, especially in strong wind cases, and a sampling rate that is 3 times slower. The ability to measure turbulence with this approach is so weak that it is not further investigated in this paper. Instead, the next chapter suggests two methods that can be used to reduce both averaging and cross-contamination.

### 3 Modified data processing

#### 3.1 Squeezed measurement circles

In conventional VAD data processing, each measurement cycle consists of the radial velocities that are acquired during

one full rotation of the prism. The data used in the reconstruction of one wind vector thus originates from an air volume with the shape of a cone with a diameter of  $D_C$  at the height of focus. This results in the abovementioned cross-contamination effects.

One way to eliminate the cross-contamination due to longitudinal separation and mitigate the averaging along the measurement circle lies in making use of Taylor's frozen turbulence hypothesis. As mentioned in Sect. 2.2, the hypothesis assumes that turbulent structures are transported by the mean wind motion without changing. This implies that all turbulent structures that enter the measurement cone at one time are identical after some time  $t$  when they leave the cone. The time it takes to cross the measurement circle can be estimated for all azimuth directions  $\theta$  by

$$t(\theta) = \cos \theta \frac{D_C}{U}, \quad (17)$$

where  $U$  is the mean wind velocity calculated from conventional VAD processing.

The basic idea here is to introduce a time lag  $\tau = t$  into the data processing so that each air package that is involved in the reconstruction of one wind vector is scanned twice: once when it enters and again when it leaves the measurement cone. The composition of the measurement circles is shown in Fig. 4 from a coordinate system that is moving with the mean wind  $U$ . In this example  $D_C = 92.3 \text{ m}$  and  $U = 19.5 \text{ m s}^{-1}$ . With conventional VAD data processing, the measurement circle is made up of all  $N$  consecutive measurements from one cycle (red segment). By contrast, the lower part of Fig. 4 illustrates the introduction of the time delay  $\tau$ , in which line-of-sight measurements from a total of  $M = 6$  different measurement cycles are combined to estimate one wind vector (green segments). In other words, with conventional data processing, a measurement cycle is composed of volumes that are widely spatially distributed. The new proposed method picks measurement data taken from what we term a squeezed measurement circle (SMC).

A restriction that comes with the idea of squeezing is that the circle sample rate  $f_S$  must be high enough to be able to select measurements that were acquired with a time difference reasonably close to  $\tau$ . That drastically limits the number of measurement heights that should be selected, especially in strong wind cases. For the measurements analyzed in this paper, the lidar scanned continuously at only one height level, which in general makes sense to measure turbulence effectively.

#### 3.2 Two-beam method

The conventional method of averaging data from all available lines of sight to reconstruct three-dimensional wind vectors leads to strong averaging along the measurement circle. The method is known to deliver reliable values for the mean wind speed and direction. The directional information allows

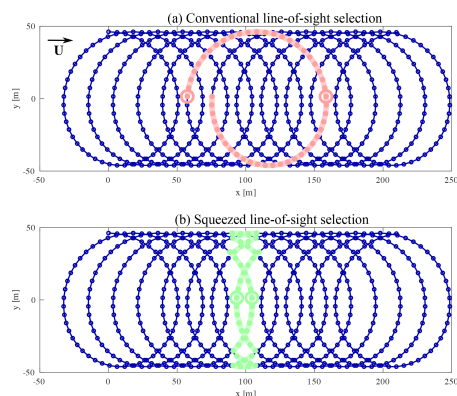


**Figure 4.** Selection of line-of-sight measurements for the reconstruction of one wind vector for when (a, in red) conventional VAD processing and (b, in green) the method of squeezed measurement circles is applied. Within the red and green segments, small red and green rings indicate the particular beams selected for two-beam processing. In this example,  $U = 19.5 \text{ m s}^{-1}$ ,  $D_C = 92.3 \text{ m}$  and  $f_S = 1 \text{ Hz}$ .

it to determine the two beams that lie in the upstream and downstream directions. Within the red and green segments of Fig. 4, small red and green rings indicate these particular beams. These two beams can in a second processing step be used to estimate the  $u$  and  $w$  components of the wind vectors for turbulence estimations. The resulting values are then not averaged along the measurement circle. This is comparable to the DBS method in cases in which the mean wind blows in line with two of the lines of sight. But an advantage of the two-beam method over the DBS strategy is that the relative angle between the mean wind and the two beams is kept constant in any prevailing wind direction. This is an advantage since beams pointing upwind and downwind are immune to contamination by the cross-wind component  $v$ .

When the two-beam method is combined with the idea of squeezing, then measurements of the  $u$  and  $w$  components are taken at virtually one focus point following the flow. Only the line-of-sight averaging and some minor longitudinal separation among the different locations along the two beams remain.

That is unfortunately not true when estimating the  $v$  component of turbulence. Instead, several problems occur. Intuitively, one would choose a beam direction perpendicular to the mean wind direction in order to estimate the  $v$  component of the wind. But the radial velocities in this line-of-sight direction are often close to zero, and such estimates from continuous-wave lidars are usually not reliable (Mann et al., 2010; Dellwik et al., 2010). The transverse  $v$  compo-

nent must therefore be estimated by either VAD processing or selecting a different third beam direction. In the latter case the results would then be influenced by contamination not only from  $w$  but also from the  $u$  component. This lies outside the scope of this study. Therefore no  $v$  data from measurements are processed with the two-beam method.

Like conventional VAD processing, the SMC method and two-beam method require a wind field that is statistically homogeneous in the horizontal directions to yield correct results.

## 4 Description of the model

The mathematics of deducing the lidar-measured spectrum from the second-order statistics of turbulence is very convoluted. Therefore, we make the assumption that the measurements are performed much faster than it takes the air to move from one side of the scanning circle to the other; i.e., we assume that  $\frac{1}{f_S} \ll \tau$ . Effectively, the scanning circle is measured continuously. It is difficult to assess the magnitude of the error committed by the assumption of continuous measurements, but we assume it is negligible.

### 4.1 VAD and SMC

In order to model spectra obtained from conventionally VAD-processed lidar data, we closely follow the method of Sathe et al. (2011). They use the geometry of the lidar scan and its along-beam weighting function together with information on the spatial structure of surface-layer turbulence (Mann, 1994). The focus point of the lidar is at a distance  $d_f$  away in the direction given by the unit vector

$$\mathbf{n}(\theta) = (-\cos\theta \sin\phi, -\sin\theta \sin\phi, \cos\phi), \quad (18)$$

where  $\theta$  is the azimuth angle and  $\phi$  is the half-cone opening angle. The line of sight or radial wind speed that the lidar is measuring is modeled as

$$v_r(\theta, x) = \int_{-\infty}^{\infty} \varphi(s) \mathbf{n}(\theta) \cdot \mathbf{u}((s + d_f)\mathbf{n}(\theta) + x\mathbf{e}_1) ds, \quad (19)$$

where  $\varphi$  is the spatial weighing function of the continuous-wave lidar that we assume to be a Lorentzian function with the Rayleigh length  $l_R$ .  $\mathbf{u}$  is the three-dimensional velocity field suppressing the time argument since we are assuming Taylor's hypothesis. The integration variable  $s$  is the distance along the beam from the focus point. The dot product assures that we obtain the line-of-sight velocity. We use  $x$ , the coordinate aligned with the mean wind vector, instead of time.  $\mathbf{e}_1$  is the unit vector aligned with  $x$ .

The  $w$ ,  $u$  and  $v$  components of the velocity are calculated by the first three Fourier coefficients of  $v_r$  as a function of  $\theta$ ;

i.e.,  $w$  is calculated from

$$A(x) = \frac{1}{2\pi} \int_0^{2\pi} v_r(\theta, x) d\theta. \quad (20)$$

In Sathe et al. (2011) variances are calculated for a conically scanning continuous-wave lidar and it is trivial to extend that to spectra. Spectra were in fact calculated in Sathe and Mann (2012) but only for a pulsed system. In Sathe et al. (2011) the variances for a conically scanning continuous-wave system, e.g., a ZephIR 300 (Smith et al., 2006; Kindler et al., 2007), were given by

$$\langle w^2 \rangle \cos^2 \phi = \int \Phi_{ij}(\mathbf{k}) \alpha_i(\mathbf{k}) \alpha_j^*(\mathbf{k}) d\mathbf{k}, \quad (21)$$

$$\langle u^2 \rangle \sin^2 \phi = \int \Phi_{ij}(\mathbf{k}) \beta_i(\mathbf{k}) \beta_j^*(\mathbf{k}) d\mathbf{k}, \quad (22)$$

$$\langle v^2 \rangle \sin^2 \phi = \int \Phi_{ij}(\mathbf{k}) \gamma_i(\mathbf{k}) \gamma_j^*(\mathbf{k}) d\mathbf{k}, \quad (23)$$

where  $*$  means complex conjugation. The spectral weighting functions  $\alpha$ ,  $\beta$  and  $\gamma$  are

$$\alpha_i(\mathbf{k}) = \frac{1}{2\pi} \int_0^{2\pi} n_i(\theta) e^{id_i \mathbf{k} \cdot \mathbf{n}(\theta)} e^{-l|\mathbf{k} \cdot \mathbf{n}(\theta)|} d\theta, \quad (24)$$

$$\beta_i(\mathbf{k}) = \frac{1}{\pi} \int_0^{2\pi} \cos \theta n_i(\theta) e^{id_i \mathbf{k} \cdot \mathbf{n}(\theta)} e^{-l|\mathbf{k} \cdot \mathbf{n}(\theta)|} d\theta, \quad (25)$$

$$\gamma_i(\mathbf{k}) = \frac{1}{\pi} \int_0^{2\pi} \sin \theta n_i(\theta) e^{id_i \mathbf{k} \cdot \mathbf{n}(\theta)} e^{-l|\mathbf{k} \cdot \mathbf{n}(\theta)|} d\theta. \quad (26)$$

The spectra measured by the conically scanning lidar will be

$$\cos^2 \phi F_w^Z(k_1) = \hat{T}_f(k_1) \iint_{-\infty}^{\infty} \Phi_{ij}(\mathbf{k}) \alpha_i(\mathbf{k}) \alpha_j^*(\mathbf{k}) dk_2 dk_3 \quad (27)$$

and likewise for the  $u$  and  $v$  components.

$$\hat{T}_f(k_1) = \text{sinc}^2\left(\frac{k_1 L_f}{2}\right), \quad (28)$$

where  $\text{sinc} x = \frac{\sin x}{x}$  is included in Eq. (28) to account for the finite time of circle scanning before a velocity estimate is obtained.  $L_f$  is the mean wind speed multiplied with this finite time (see Sathe et al., 2011, for details).

To apply the method of squeezing and model the spectra we obtain from SMC processing, we now substitute Eq. (19) with

$$\tilde{v}_r(\theta, x) = \int_{-\infty}^{\infty} \varphi(s) \mathbf{n}(\theta) \cdot \mathbf{u}((s+d_f)\mathbf{n}(\theta) + (x-d_f n_1(\theta))\mathbf{e}_1) ds.$$

Following the exact same steps as in Sathe et al. (2011) but using Eq. (29) instead of Eq. (19) we arrive at Eqs. (21)–(23) but with the complex exponential in Eqs. (24)–(26) exchanged with

$$e^{id_i(\mathbf{k} \cdot \mathbf{n}(\theta) - k_1 n_1(\theta))}. \quad (30)$$

#### 4.2 Two-beam method

Only the up- and downwind beams to determine the  $u$  and  $w$  components of the wind vector could introduce less averaging than using the whole circle.

When the mean wind is blowing from the north, the unit vectors in the up- and downwind directions are called  $\mathbf{n}^u$  and  $\mathbf{n}^d$ , respectively. Their unit vectors are

$$\mathbf{n}^u = (-\sin \phi, 0, \cos \phi) \quad (31)$$

and with the opposite sign on the first component for  $\mathbf{n}^d$ .

Parallel to Eq. (19) the line-of-sight velocity measured by the upwind beam is assumed to be

$$v^u(x) = \int_{-\infty}^{\infty} \varphi(s) \mathbf{n}^u \cdot \mathbf{u}(s\mathbf{n}^u + d_f \mathbf{n}^u + x\mathbf{e}_1) ds. \quad (32)$$

The  $u$  component estimated by the lidar is normally

$$u_{\text{lidar}} = \frac{\Delta v}{n_1^u - n_1^d}, \quad (33)$$

where

$$\begin{aligned} \Delta v &= v^u(x) - v^d(x) \\ &= \int_{-\infty}^{\infty} \varphi(s) [\mathbf{n}^u \cdot \mathbf{u}((s+d_f)\mathbf{n}^u + x\mathbf{e}_1) \\ &\quad - \mathbf{n}^d \cdot \mathbf{u}((s+d_f)\mathbf{n}^d + x)] ds. \end{aligned} \quad (34)$$

The correlation function of  $\Delta v$  is

$$\begin{aligned} R_{\Delta v}(r) &= \langle \Delta v(x) \Delta v(x+r) \rangle \\ &= \iint_{-\infty}^{\infty} \varphi(s) \varphi(s') \times \left[ \mathbf{n}^u \cdot \mathbf{u}((s+d_f)\mathbf{n}^u + x\mathbf{e}_1) \right. \\ &\quad \left. - \mathbf{n}^d \cdot \mathbf{u}((s+d_f)\mathbf{n}^d + x\mathbf{e}_1) \right] \\ &\quad \times \left[ \mathbf{n}^u \cdot \mathbf{u}((s'+d_f)\mathbf{n}^u + (x+r)\mathbf{e}_1) \right. \\ &\quad \left. - \mathbf{n}^d \cdot \mathbf{u}((s'+d_f)\mathbf{n}^d + (x+r)\mathbf{e}_1) \right] ds ds'. \end{aligned} \quad (35)$$

Expanding the product inside the ensemble average ( $\langle \rangle$ ) and using the definition of the correlation tensor of the velocity

field,  $R_{ij}(\mathbf{r}) \equiv \langle u_i(\mathbf{x})u_j(\mathbf{x} + \mathbf{r}) \rangle$ , one obtains

$$R_{\Delta v}(r) = \iint_{-\infty}^{\infty} \varphi(s)\varphi(s') \times \left\{ n_i^u n_j^u R_{ij}((-s + s')\mathbf{n}^u + r\mathbf{e}_1) + n_i^d n_j^d R_{ij}((-s + s')\mathbf{n}^d + r\mathbf{e}_1) - n_i^u n_j^d R_{ij}(s'\mathbf{n}^d - s\mathbf{n}^u + d_t(\mathbf{n}^d - \mathbf{n}^u) + r\mathbf{e}_1) - n_i^d n_j^u R_{ij}(s'\mathbf{n}^u - s\mathbf{n}^d + d_t(\mathbf{n}^u - \mathbf{n}^d) + r\mathbf{e}_1) \right\} ds ds'. \quad (36)$$

Now we use the relation between the velocity covariance tensor and the spectral velocity tensor

$$R_{ij}(\mathbf{r}) = \int \Phi_{ij}(\mathbf{k}) \exp(i\mathbf{k} \cdot \mathbf{r}) d\mathbf{k}, \quad (37)$$

where  $\int d\mathbf{k} \equiv \int \int_{-\infty}^{\infty} dk_1 dk_2 dk_3$ , to express the auto-covariance function as

$$R_{\Delta v}(r) = \iint_{-\infty}^{\infty} \varphi(s)\varphi(s') \times \left\{ n_i^u n_j^u \int \Phi_{ij}(\mathbf{k}) \exp(i\mathbf{k} \cdot ((-s + s')\mathbf{n}^u + r\mathbf{e}_1)) d\mathbf{k} + n_i^d n_j^d \int \Phi_{ij}(\mathbf{k}) \exp(i\mathbf{k} \cdot ((-s + s')\mathbf{n}^d + r\mathbf{e}_1)) d\mathbf{k} - n_i^u n_j^d \int \Phi_{ij}(\mathbf{k}) \exp(i\mathbf{k} \cdot (s'\mathbf{n}^d - s\mathbf{n}^u + d_t(\mathbf{n}^d - \mathbf{n}^u) + r\mathbf{e}_1)) d\mathbf{k} - n_i^d n_j^u \int \Phi_{ij}(\mathbf{k}) \exp(i\mathbf{k} \cdot (s'\mathbf{n}^u - s\mathbf{n}^d + d_t(\mathbf{n}^u - \mathbf{n}^d) + r\mathbf{e}_1)) d\mathbf{k} \right\} ds ds'. \quad (38)$$

By interchanging the order of integration of  $\mathbf{k}$  and the  $s$ 's we can cast the expression in terms of the Fourier transform of  $\varphi$ , which in the case of a Lorentzian function is  $\hat{\varphi}(\mathbf{k}) = \exp(-l_R|\mathbf{k}|)$ . Thereafter, we Fourier transform  $R_{\Delta v}$  with respect to  $r$  to obtain the spectrum  $F_{\Delta v}(k_1)$ . After that process the first term in Eq. (38) becomes

$$n_i^u n_j^u \int \Phi_{ij}(\mathbf{k}) \hat{\varphi}(\mathbf{k} \cdot \mathbf{n}^u) \hat{\varphi}(\mathbf{k} \cdot \mathbf{n}^u) dk_2 dk_3,$$

and upon rearrangement we finally obtain

$$F_{\Delta v,n}(k_1) = \int \Phi_{ij}(\mathbf{k}) \left\{ n_i^u n_j^u |\hat{\varphi}(\mathbf{k} \cdot \mathbf{n}^u)|^2 + n_i^d n_j^d |\hat{\varphi}(\mathbf{k} \cdot \mathbf{n}^d)|^2 - 2n_i^u n_j^d \hat{\varphi}(\mathbf{k} \cdot \mathbf{n}^u) \hat{\varphi}(\mathbf{k} \cdot \mathbf{n}^d) \right\} \times \cos(d_t \mathbf{k} \cdot (\mathbf{n}^d - \mathbf{n}^u)) dk_2 dk_3. \quad (39)$$

The derivation of the spectrum obtained from squeezed processing is parallel to the normal spectrum. The only difference lies in the definition of  $\Delta v$ . Now we define it as

$$\Delta v_s(x) = v^u(x - n_1^u d_t) - v^d(x - n_1^d d_t). \quad (40)$$

Using the exact same steps that led to Eq. (39), we see that the cosine term in that equation has to be substituted with 1 and we get

$$F_{\Delta v,s}(k_1) = \int \Phi_{ij}(\mathbf{k}) \left\{ n_i^u n_j^u |\hat{\varphi}(\mathbf{k} \cdot \mathbf{n}^u)|^2 + n_i^d n_j^d |\hat{\varphi}(\mathbf{k} \cdot \mathbf{n}^d)|^2 - 2n_i^u n_j^d \hat{\varphi}(\mathbf{k} \cdot \mathbf{n}^u) \hat{\varphi}(\mathbf{k} \cdot \mathbf{n}^d) \right\} dk_2 dk_3. \quad (41)$$

To obtain the spectrum of  $u$ ,  $F_{\Delta v,(s)}$  simply has to be divided by  $(n_1^u - n_1^d)^2$  according to Eq. (33).

When obtaining the spectrum of  $v$ , we simply exchange the unit vectors of the up- and downwind beams  $\mathbf{n}^u$  and  $\mathbf{n}^d$  in all equations by the values of the west- and eastbound beams  $\mathbf{n}^w$  and  $\mathbf{n}^e$ . In order to obtain the spectrum of  $w$ ,  $\Delta v$  defined in Eq. (34) has to be replaced by the sum of both radial velocities  $v^u(x) + v^d(x)$ , and  $F_{\Delta v,(s)}$  must eventually be divided by  $(n_3^u + n_3^d)^2$ .

To compare the different methods to calculate spectra from a lidar, Eqs. (39) and (41) have to be evaluated with a model for the spectral tensor. We chose the spectral tensor from Mann (1994) and select the model parameters so that the model spectra resemble the spectra from available sonic measurements. The selected parameters are  $L = 65$  m,  $\Gamma = 4$  and  $\alpha \epsilon^{\frac{2}{3}} = 0.023 \text{ m}^{\frac{2}{3}} \text{ s}^{-2}$ . The unfiltered  $u$  target model spectrum that we will later compare the model results against is given by

$$F_u(k_1) = \int \Phi_{11}(\mathbf{k}) dk_2 dk_3 \quad (42)$$

and parallelly for the second and third wind components. The model was tested by comparing the theoretical spectra with results from processing computer-generated wind field turbulence data (Mann, 1998) and was found to predict all four data processing methods, i.e., VAD, SMC, two-beam and squeezed two-beam, accurately for all three wind speed components.

## 5 Description of the measurements

### 5.1 Test site and instrumentation

The test data were collected at the Danish National Test Center for Large Wind Turbines at Høvsøre. The test site is located in West Jutland, Denmark, 1.7 km east of the North Sea. Apart from the dunes along the coastline, the terrain is nearly flat. The Høvsøre meteorological mast is located to the south of a row of five wind turbines. The reference data were acquired with a Metek USA-1 sonic anemometer that is mounted at 80.5 m in height above the ground. It is attached to a 4.3 m long boom pointing north. Mast effects can be observed when the wind is blowing from the south. Turbine wake effects influence the measurement signal when the wind blows from the north. For the data set in this study, the inflow is undisturbed. A detailed description of the test site is given in Peña et al. (2016).

Collocated with the meteorological mast, the lidar measurements were taken by a Qinetiq lidar that was configured to continuously scan at 78 m above the ground. The lidar is comparable to the current ZX 300 (previously ZephIR 300) but the effective aperture size is slightly lower, which results in a longer Rayleigh length and thus greater line-of-sight averaging. The lidar was equipped with an opto-acoustic modulator that makes it possible to detect the direction of the radial velocities. Line-of-sight velocities calculated from the centroid of the Doppler spectra are used in the data processing. The precision of these lidar measurements is not exactly known but is in general better than 1 % (Pedersen et al., 2012).

Measurement data of 32 subsequent 10 min intervals are used. The data were acquired on 20 November 2008 between 10:30 and 15:50 local time. The mean wind velocity measured by the sonic anemometer during this period varied from 14.2 to 22.6 m s<sup>-1</sup> with an average of 19.5 m s<sup>-1</sup> and a standard deviation of 2.0 m s<sup>-1</sup>. The turbulence intensity varied from 4.7 % to 14.0 %, with a mean of 8.8 % and standard deviation of 2.0 %. The wind blew from the northwest and the atmospheric stability was neutral. Table 1 summarizes the most important information about the experimental setup.

### 5.2 Data processing

The time series of all 10 min intervals derived from all processing methods are used to compute turbulence spectra. The measurement rate for the lidar is 1 Hz. Although it would have been possible in the two-beam processing to calculate measurement values with a rate of 2 Hz by using every newly retrieved radial velocity together with its predecessor, it was decided to use only independent measurements acquired every full second. The sonic anemometer measures with a rate of 20 Hz. These high-frequency data are down-sampled by the use of the MATLAB function “resample” to a frequency of 1 Hz. The function includes a low-pass filter to avoid anti-

aliasing. The data rate is thus for all methods 1 Hz. The analyzed frequency range from  $\frac{1}{600}$  to  $\frac{1}{2}$  Hz equals the wave number range from roughly  $5.4 \times 10^{-4}$  to  $1.6 \times 10^{-1} \text{ m}^{-1}$ . The spectra are then averaged for all intervals and the results are then binned into 30 logarithmically spaced wave number intervals spread across the wave number axis to avoid high density of values and maintain readability towards higher wave numbers.

The effects of de-trending (Hansen and Larsen, 2005) and spike removal (Hojstrup, 1993) on the spectra were both negligible for this data set, so neither was applied here.

## 6 Discussion of the results

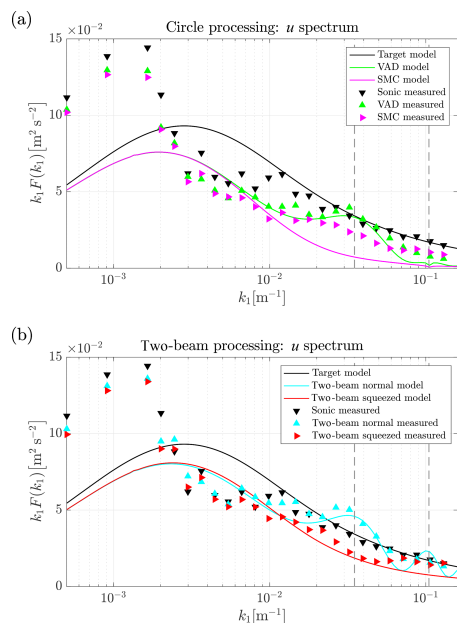
### 6.1 $u$ spectra

Figure 5 shows the spectra of the  $u$  fluctuations for all processing methods from measurement data (triangle markers) and the corresponding model predictions (solid lines). We will first discuss the results from processing the whole measurement circle shown in Fig. 5a, followed by the discussion of the results of the two-beam method, shown in Fig. 5b.

#### 6.1.1 Circle processing

To begin with, the model predictions of conventional VAD processing and the new SMC method are compared against each other and with regard to the true  $u$  target model spectrum acquired from the spectral tensor according to Eq. (42). The model prediction of the conventionally processed VAD lidar data shows some attenuation of the spectral energy even for very low wave numbers. This can be partly explained by the infinitely long tails of the line-of-sight averaging function given in Eq. (8). That means that even very large eddies are slightly weakened by the underlying Lorentzian function. Averaging along the measurement circle might also have some small additional impact on large-scale turbulence. Both averaging effects become more and more severe for increasing wave numbers until the measured spectral energy reaches values close to zero at roughly  $k_1 = 10^{-1} \text{ m}^{-1}$  and above. The tendency of increasing attenuation with regard to the target spectrum is interrupted around the first resonance frequency that is indicated by a vertical grey dashed line at  $k_1 = 3.4 \times 10^{-2} \text{ m}^{-1}$ . Here the energy density increases and reaches coincidentally roughly the value of the target spectrum. This behavior is as expected an effect of the cross-contamination with energy from both the  $w$  spectrum and to a small extent also from  $v$ . A resonance effect at the second resonance frequency is hardly pronounced since the energy is nearly fully consumed by the line-of-sight averaging.

The SMC model spectrum predicts a similar shape but without the cross-contamination effect from longitudinal separation. Thus, we find no resonance in the computations. The total variance of the  $u$  fluctuations  $\sigma^2(u')$  is lower here since less additional energy from the  $w$  component is con-



**Figure 5.** Modeled (solid lines) and measured (triangle markers)  $u$  spectra from data processing for which (a) all radial measurements are used and (b) only two beams are used. Colors correspond to the processing method. The grey vertical dashed lines represent the first and second resonance wave numbers.

tained in the  $u_{SMC}$  signal. The signal is still contaminated by contributions from other components because the lateral separation cannot be reduced by squeezing. But the averaging along the measurement circle is so strong that for example for wave numbers above around  $k_1 = 10^{-2} \text{ m}^{-1}$  less than half of the energy of the target spectrum is expected to be detected by the lidar.

First, when the model is compared with the measurement data, the chosen spectral tensor does not fit the actual wind conditions in the wave number range below  $k_1 = 10^{-2} \text{ m}^{-1}$ . The extra energy at low wave numbers compared to the spectral tensor model for this site has been observed before and is related to the inhomogeneous landscape at Høvsøre with its sea-to-land transition in the main wind direction (Sathe et al., 2015) and mesoscale effects that overlay the expected spectral gap (Larsén et al., 2016). Luckily, this does not severely impede the analysis since the most interesting effects are expected at higher wave numbers and tendencies can still be determined from the relative distances between the markers and lines without matching the absolute values. Next, the

comparison of data from sonic measurements and VAD as well as SMC-processed lidar data shows in the very low wave number range at  $k_1 < 3 \times 10^{-3} \text{ m}^{-1}$  that VAD processing and SMC processing produce similar results with a slight tendency towards lower energy densities in the SMC-measured spectrum that is not found in the model computations. A possible explanation is that the fluctuations of the  $u$  and especially the  $w$  component in the real wind field are not perfectly correlated, i.e., the frozen turbulence hypothesis that the model assumes is slightly violated. The result is a small contribution of  $w_{\text{wind}}$  to  $u_{\text{lidar}}$  that appears to a greater extent in the VAD-processed spectrum. The reason for the difference is that the correlation is closer to unity in the case of SMC processing.

Apart from some exceptions (e.g., at  $k_1 = 3 \times 10^{-3} \text{ m}^{-1}$ ), a relatively increasing averaging effect towards higher wave numbers is found for the lowest wave numbers as expected. In the wave number range  $k_1 = 10^{-2}$  to  $6 \times 10^{-2} \text{ m}^{-1}$  the sonic spectrum and the VAD spectrum follow the corresponding modeled spectra nicely through the first resonance point. That shows that the cross-contamination caused by longitudinal separation is present in the measurements and is properly modeled.

The spectrum derived from SMC-processed data shows a clear tendency towards its modeled spectrum but does not completely reach it. It does not show the resonance effect seen for VAD processing, but the overall energy level is higher than predicted for  $k_1 > 10^{-2} \text{ m}^{-1}$ . It is not possible to determine what causes this deviation. One possible reason is that the model assumes a perfect delay of the measurement timing. In reality this is not possible due to only discrete acquisition times being available. Also the air packages are in reality not always advected with the exact mean wind speed and direction. Both imperfections justify that the behavior of real SMC processing lies in between the modeled SMC and VAD processing.

For  $k_1 > 7 \times 10^{-2} \text{ m}^{-1}$  VAD- and SMC-processed data are nearly identical. As shown in Schlipf et al. (2010), the assumption of frozen turbulence is not valid for high wave numbers. In this region, fluctuations separated by the distances between the relevant focus points are uncorrelated and the squeezing has no effect. The lack of coherence also explains that the values are higher than predicted because the  $u$  spectrum is highly contaminated by  $w$  and  $v$  fluctuations.

### 6.1.2 Two-beam processing

The plotted model spectrum for the conventional two-beam processing method shows a significantly lower averaging effect compared to whole circle processing methods at all wave numbers except in the very low wave number region, where the methods are expected to perform similarly well.

With the two-beam method it is expected that fluctuations with the highest wave numbers analyzed are to some extent included in the spectrum, while they were close to zero

when circle processing was applied. The normal two-beam processing in the model is prone to cross-contamination at both resonance points (vertical dashed lines). This situation is explained in detail in Sect. 2.5. In contrast, the method of squeezing applied to the two-beam processing shows as expected no cross-contamination in the model calculations.

Overall, spectra calculated from the two-beam processed measurement data show good agreement to the model. It is important to keep in mind that, due to the poor fit of the measured spectra of the horizontal wind components and the modeled spectra at low wave numbers, we can compare the relations between the different methods but not absolute values. At low wave numbers, the measured spectra are on average closer to the target spectrum than in the case of circle processing. The slightly lower energy content of squeezed measurements that we observed and explained for circle processing is found here as well. Also, when it comes to deviations from the modeled behavior, like for example the higher energy density at some wave numbers (e.g.,  $k_1 = 3 \times 10^{-3} \text{ m}^{-1}$ ), we find similar tendencies as in circle processing, and the reason is likewise unclear.

The strong cross-contamination at the first resonance frequency is clearly represented in the normal two-beam processing and can be completely avoided by squeezing the two focus points to virtually one point. It is worth mentioning that the squeezing procedure works more like expected when applied to the two-beam method than when applied to the circle processing. This can be explained by the error caused by not having continuous but only discrete delaying times  $\tau$  available. The relative impact of this error is lower in the case of the two-beam method because then the maximum separation distance  $D_C$  must be compensated for. In circle processing mode, the shorter separations for which the relative error is larger also contribute to the result.

At  $k_1 > 7 \times 10^{-2} \text{ m}^{-1}$  the two processing methods result in nearly identical values again, and we assume the lack of coherence of short eddies to also be the cause here.

## 6.2 $v$ spectra

Figure 6 shows the spectra of the  $v$  fluctuations for all available data processing methods from both measurement data (triangle markers) and the corresponding model predictions (solid lines). Also here, we first discuss the results from processing the whole measurement circle shown in Fig. 6a, followed by the discussion of the results of the two-beam method shown in Fig. 6b.

### 6.2.1 Circle processing

The modeled spectra of conventionally VAD-processed lidar measurements predict energy densities that slightly exceed the target spectrum for very long fluctuations with  $k_1 < 1.3 \times 10^{-2} \text{ m}^{-1}$ . This behavior can be explained by uncorrelated  $w$  fluctuations between the eastern and western sides of

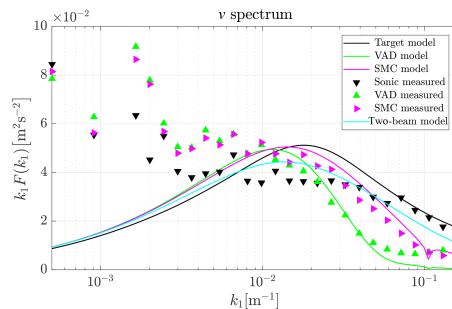


**Figure 6.** Modeled (solid lines) and measured (triangle markers)  $v$  spectra from all data processing methods. Colors correspond to processing method.

the measurement circle that contaminate the  $v$  signal. This contamination is slightly stronger than averaging that is very weak at low wave numbers.

By contrast, fluctuations shorter than approximately  $k_1 = 1.3 \times 10^{-2} \text{ m}^{-1}$  appear dampened in the spectrum, and fluctuations with higher wave numbers  $k_1 > 10^{-1} \text{ m}^{-1}$  are not even present in the  $v$  spectrum due to the strong averaging. Unlike the  $u$  spectrum, the  $v$  spectrum does not have characteristic behavior around the first resonance wave number. This is not surprising because the lines of sight that are the most important for the detection of  $v$  fluctuations lie, according to Eq. (26), orthogonal to the mean wind direction in which turbulence is advected. Thus, no resonance occurs.

When the model spectrum for SMC processing is analyzed, we find a higher variance for all wave numbers above approximately  $k_1 = 1.3 \times 10^{-2} \text{ m}^{-1}$ . Reduced averaging along the measurement circle is the reason for the higher energy in the SMC spectrum. It is caused by the following: the process of squeezing reduces the longitudinal separation of the focus points ideally to zero while the lateral separation remains unchanged. We know that the lines of site perpendicular to the mean wind direction on both sides of the measurement circle are the most important for the determination of  $v_{\text{lidar}}$ . Let us assume these are the easterly and westerly beams. The exact east- and westbound beams are not affected by the process of squeezing. But for example the northeast and the southeast beams (respectively the northwest and northeast on the other side) see different turbulent structures in conventional VAD processing. With SMC processing, these two beams see the same structure. In the subsequent calculation of the  $v$  component all lines of sight are combined and the pairs of radial velocities that lie in line with the mean wind contribute with the average of their amplitudes. This average of amplitudes is lower than the common amplitude measured by the beam pairs under SMC processing. More simply, there is less averaging along the measure-

ment circle when SMC is applied. As a result, the spectrum of SMC shows higher energy densities for all wave numbers at which uncorrelated fluctuations dominate.

Now we compare the measurements with the model. Unfortunately, similar to the  $u$  fluctuations, the target spectrum does not represent the sonic measured values properly, especially for low wave numbers. We will therefore concentrate on the tendencies and proportions between the spectra from different methods. While the model predicts the behavior at the lowest wave numbers more or less satisfactorily, we are faced with two outliers at  $k_1 = 1.65 \times 10^{-3} \text{ m}^{-1}$  and  $k_1 = 2 \times 10^{-3} \text{ m}^{-1}$  for which both the VAD and SMC processing lead to excessive energy estimations. The reason is unclear and not further investigated. At all other wave numbers, the agreement of model and measurements is very satisfactory. In particular, the differences between the two methods are found in the measurements, as predicted. The good agreement between model spectra and measurement spectra at wave numbers above approximately  $k_1 = 2 \times 10^{-2} \text{ m}^{-1}$  might be surprising with regard to the poor agreement of sonic measurements and target spectrum. The reason is that the shape of the lidar  $v$  spectra is mainly determined by the cross-contamination from the  $w$  component, which, as we describe in Sect. 6.3, agrees better with its model representation.

The identity of VAD- and SMC-derived measurement spectra that we saw for  $u$  fluctuations for  $k_1 > 7 \times 10^{-2} \text{ m}^{-1}$  is found here at  $k_1 > 10^{-1} \text{ m}^{-1}$ . The reason is obvious when we look at the relevant longitudinal separation distances. They are much shorter when processing  $v$  fluctuations than  $u$  fluctuations, and the assumption of frozen turbulence is more valid for short separation distances. Therefore squeezing can maintain its effect into a somewhat higher wave number region.

### 6.2.2 Two-beam processing

When the two-beam method is applied, i.e., using only the east and west beams to derive the  $v$  component of the wind vector, the method of squeezing has no effect. In comparison with the whole circle processing, the two-beam method is characterized by lower energy estimates at low wave numbers and higher energy estimates at higher wave numbers (see Fig. 6). One reason for the first is assumed to be the lower coherence of  $v$  fluctuations separated by the full distance  $D_C$ . That implies that two-beam processing gets a somewhat lower contribution of  $v_{\text{wind}}$  to  $v_{\text{lidar}}$ . A second reason is that there is not cross-contamination from  $u$  on  $v$  occurring for the two-beam processing. The higher energy content at high wave numbers results from the absence of averaging along the measurement circle.

The model cannot be compared with measurements because the line-of-sight velocities of the east and west beams were erroneous. The absolute values we measured are unrealistically biased towards nonzero values. This effect has been

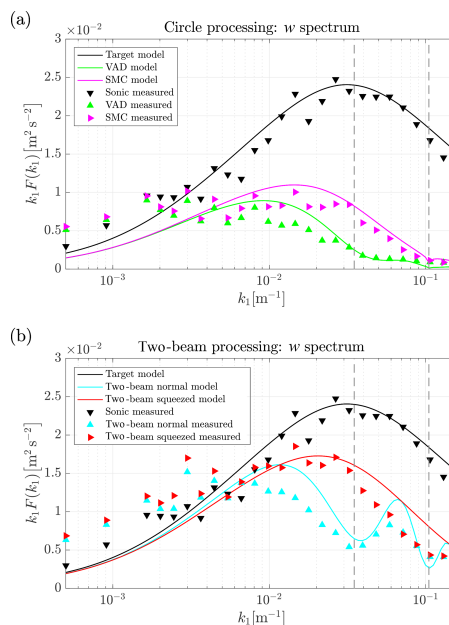


**Figure 7.** Modeled (solid lines) and measured (triangle markers)  $w$  spectra from data processing for which (a) all radial measurements are used and (b) only two beams are used. Colors correspond to processing method. The grey vertical dashed lines represent the first and second resonance wave numbers.

previously reported (Mann et al., 2010; Dellwik et al., 2010). We included the model behavior of two-beam processing for the sake of completeness and to show that the availability of reliable measurement data for the east and west beams would be of hardly any use.

### 6.3 $w$ spectra

Figure 7 shows the spectra of the  $w$  fluctuations for all processing methods from both measurement data and the corresponding model predictions. Again, we discuss the results from processing the whole measurement circle first and then the results of the two-beam method.

#### 6.3.1 Circle processing

To begin with, we compare the model predictions of conventional VAD processing and the new SMC method against one another and with regards to the  $w$  target spectrum. The results of the actual measurements follow. The model prediction of the conventionally processed VAD lidar data shows

some attenuation of the spectral energy even for very low wave numbers. The reason is mainly the infinitely long tails of the line-of-sight averaging function and to a lesser extent the averaging along the measurement circle. Both averaging effects become quickly stronger for increasing wave numbers. The spectrum from VAD processed data is expected to drop at the first resonance point marked with a grey dashed vertical line in Fig. 7. This drop is minor due to the overall low energy level present in the spectrum. The spectrum reaches a value near its final minimum with variance values close to zero already at around  $k_1 = 5 \times 10^{-2} \text{ m}^{-1}$  just after crossing the first resonance point.  $w$  fluctuations with higher wave numbers are not detectable with conventional VAD processing. According to the model, the SMC processing improves the situation slightly by removing the longitudinal separation that makes lidar blind to  $w$  fluctuations at the resonance points with VAD processing. Squeezing the measurements also helps improve the measurements well above and below the resonance wave number. But still, due to the remaining averaging effects, only a minor fraction of the energy in the vertical wind can be detected with both methods at wave numbers above roughly  $k_1 = 10^{-2} \text{ m}^{-1}$ .

The fit between target spectrum and measurement data in the low wave number region is good for the  $w$  component. This was not the case for the  $u$  and  $v$  components. The results of Larsén et al. (2016) show that the spectra for vertical fluctuations are not prone to contributions from the mesoscale spectrum. The measurement data overall support these model predictions and show that the process of squeezing functions well over the entire frequency range in this study. In detail, we only find some mismatch for very low wave numbers at which  $k_1 < 10^{-3} \text{ m}^{-1}$ . The measured spectra lie above the target spectrum here although we expected some attenuation. The discrepancy is caused by the real  $u$ -wind spectrum being much higher than the underlying target spectrum; see Fig. 5. We already found that large-scale  $u$  fluctuations are also not perfectly correlated and thus contaminate the measured lidar spectra, which is not considered in the model. At higher wave numbers we find reasonable forecasting of measured  $w$  spectra by the model.

### 6.3.2 Two-beam processing

The modeled two-beam spectra in Fig. 7b lie considerably closer to the target  $w$  spectrum for all wave numbers. That can be explained by the absence of circle averaging. The strong influence of resonance visible at the two first resonance wave numbers underlines the importance of squeezing when striving for more realistic spectra from lidar measurements.

At low wave numbers with  $k_1 < 10^{-2} \text{ m}^{-1}$  the measured spectra contain higher energy densities than modeled spectra. A similar but less pronounced effect was found in circle processing only at the lowest wave numbers. The explanation we gave there must therefore be supplemented by mentioning

that the assumed decorrelation is stronger for the maximal separations that are involved in the two-beam method. The further comparison of spectra from experiment and model shows that the process of squeezing also leads to the expected effect in the case of using only two beams to determine the  $w$  component of the wind vector. As in the case of  $u$  fluctuations, this statement must be limited to wave numbers  $k_1 < 7 \times 10^{-2} \text{ m}^{-1}$ .

### 6.4 Extended discussion

The results discussed here are extracted from a single data set that covers one measurement height and a narrow band of mean wind speeds, turbulence conditions and inflow directions at a single location. The reason for working with such a limited data set lies in the fact that very few data are available where a commercial VAD scanning wind lidar, collocated to a meteorological mast, is scanning continuously at one height level, while saving at least the line-of-sight velocities. Currently, the only option to save line-of-sight velocities acquired by a ZephIR 300 is to stream the data manually to a connected PC. The situation is further complicated by the fact that in the normal “profiling mode” the lidar focuses to a reference height of 38 m periodically for filtering purposes. Therefore, the only known way to focus at one particular altitude continuously is to switch the unit to “turbine mode”. In this way, we acquired some data for the investigation, but their overall quality was lower than the historic data that we eventually selected as the best available data.

In further studies different setups and turbulence conditions should be investigated. Changing the measurement height has the strongest influence on the lidar-derived spectra. For example, increasing the measurement height would, first, make the averaging along the measurement circle more severe due to the increased measurement circle diameter. Second, the resonance wave numbers are then shifted towards lower values, which leads to different cross-contamination due to lateral separation. Third, the cross-contamination due to lateral separation becomes even more severe due to the longer separation distances of opposite line-of-sight beams. Fourth, a further increase in the focus distance leads to even stronger line-of-sight averaging. Fifth, the time lag that is introduced for squeezing must be longer, and the frozen turbulence hypothesis loses some more of its validity. Changing the half-cone opening angle to a smaller value would on the one hand reduce the first three of the aforementioned effects effectively, but on the other hand it would lead to much stronger cross-contamination due to the increased sensitivity to  $w$  fluctuations according to Eqs. (14) and (16). Lidar measurements at lower mean wind speeds give the turbulence more time to evolve while crossing the measurement circle, which might lead to a deviation from the predicted spectra at somewhat lower wave numbers than observed in our results. The numerical models will work for all turbulence intensities, and the shape of the spectra is

mainly determined by the degree of anisotropy and the turbulence length scale. Atmospheric stability conditions other than neutral would not change the way the lidar measures. But a modified spectral tensor model like the one presented in Chougule et al. (2017) could be used to better compare model values with experimental results.

## 7 Conclusions

This paper presents two advanced data processing methods for improving turbulence spectrum estimations with VAD scanning wind lidars, with an aim to reduce cross-contamination and averaging effects. The models of these approaches, developed in Sect. 4, are supported by the comparison with experimental data. Discrepancies can be explained for the most part by the limitations of the frozen turbulence hypothesis that underlies the model calculations yet has slightly reduced validity in real measurements. The fact that the spectra in the experiment do not agree very well with the spectral tensor model is also a cause of differences.

We found that the method of squeezing eliminates the resonance effect caused by the longitudinal separation of combined measurement points successfully. It also considerably reduces the averaging along the measurement circle.

The method of using only two beams for the estimation of the  $u$  and  $w$  components of the wind vector eliminates the averaging along the measurement circle completely. When it is combined with the method of squeezing, the measurements deviate from the sonic measurements mainly due to line-of-sight averaging. This combination of both methods substantially improves the measurability of the  $w$  spectrum, which is hardly measurable with current VAD processing.

Accurate measurements of the  $v$  spectrum remain difficult, even with the approaches described here. The two-beam method is not applicable to current continuous-wave lidars, which in most cases are homodyne. Whether the use of squeezed measurement circles always leads to systematically better results is unclear because the resulting spectra are dominated by contamination from  $w$  fluctuations of the wind.

In conventionally processed lidar data, cross-contamination compensates for averaging effects, meaning that in general total variance might be close to target values but for the wrong reasons. For systematically better turbulence measurements from VAD scanning lidars, the findings presented here should be included in raw data processing. Both approaches presented here can be applied to any existing VAD scanning continuous-wave profiling lidar unit.

*Code and data availability.* Inquiries about and requests for access to data and source codes used for the analysis in this study should be directed to the authors.

*Author contributions.* FK contributed the initial idea for SMC, performed the data processing, analyzed the results and wrote the paper. JM suggested the two-beam method, developed the numerical model in Sect. 4 and supplied the measurement data.

*Competing interests.* The authors declare that they have no conflict of interest.

*Acknowledgements.* This research project was supported by Energy and Sensor Systems (ENERSENSE) at the Norwegian University of Science and Technology.

*Review statement.* This paper was edited by Marcos Portabella and reviewed by two anonymous referees.

## References

- Bardal, L. M. and Sætran, L. R.: Spatial correlation of atmospheric wind at scales relevant for large scale wind turbines, *J. Phys. Conf. Ser.*, 753, 32–33, <https://doi.org/10.1088/1742-6596/753/3/032033>, 2016.
- Branlard, E., Pedersen, A. T., Mann, J., Angelou, N., Fischer, A., Mikkelsen, T., Harris, M., Slinger, C., and Montes, B. F.: Retrieving wind statistics from average spectrum of continuous-wave lidar, *Atmos. Meas. Tech.*, 6, 1673–1683, <https://doi.org/10.5194/amt-6-1673-2013>, 2013.
- Browning, K. A. and Wexler, R.: The Determination of Kinematic Properties of a Wind Field Using Doppler Radar, *J. Appl. Meteorol. Clim.*, 7, 105–113, [https://doi.org/10.1175/1520-0450\(1968\)007<0105:TDOKPO>2.0.CO;2](https://doi.org/10.1175/1520-0450(1968)007<0105:TDOKPO>2.0.CO;2), 1968.
- Canadillas, B., Bégué, A., and Neumann, T.: Comparison of turbulence spectra derived from LiDAR and sonic measurements at the offshore platform FINO1, 10th German Wind Energy Conference (DEWEK 2010), 17–18 November 2010, Bremen, Germany, 2010.
- Chougule, A., Mann, J., Kelly, M., and Larsen, G.: Modeling Atmospheric Turbulence via Rapid Distortion Theory: Spectral Tensor of Velocity and Buoyancy, *J. Atmos. Sci.*, 74, 949–974, <https://doi.org/10.1175/JAS-D-16-0215.1>, 2017.
- Dellwik, E., Mann, J., and Bingöl, F.: Flow tilt angles near forest edges – Part 2: Lidar anemometry, *Biogeosciences*, 7, 1759–1768, <https://doi.org/10.5194/bg-7-1759-2010>, 2010.
- Eberhard, W. L., Cupp, R. E., and Healy, K. R.: Doppler Lidar Measurement of Profiles of Turbulence and Momentum Flux, *J. Atmos. Ocean. Technol.*, 6, 809–819, [https://doi.org/10.1175/1520-0426\(1989\)006<0809:DLMOP>2.0.CO;2](https://doi.org/10.1175/1520-0426(1989)006<0809:DLMOP>2.0.CO;2), 1989.
- Hansen, K. S. and Larsen, G. C.: Characterising Turbulence Intensity for Fatigue Load Analysis of Wind Turbines, *Wind Eng.*, 29, 319–329, <https://doi.org/10.1260/030952405774857897>, 2005.
- Harris, M., Hand, M., and Wright, A.: Lidar for Turbine Control, Tech. Rep. NREL/TP-500-39154, National Renewable Energy Laboratory, Golden, Colorado, USA, 2006.
- Højstrup, J.: A statistical data screening procedure, *Meas. Sci. Technol.*, 4, 153–157, 1993.
- Kim, D., Kim, T., Oh, G., Huh, J., and Ko, K.: A comparison of ground-based LiDAR and met mast wind measurements for wind resource assessment over various terrain conditions, *J. Wind Eng. Ind. Aerodyn.*, 158, 109–121, <https://doi.org/10.1016/j.jweia.2016.09.011>, 2016.
- Kindler, D., Oldroyd, A., Macaskill, A., and Finch, D.: An eight month test campaign of the Qinetiq ZephIR system: Preliminary results, *Meteorol. Z.*, 16, 479–489, <https://doi.org/10.1127/0941-2948/2007/0226>, 2007.
- Larsén, X. G., Larsen, S. E., and Petersen, E. L.: Full-Scale Spectrum of Boundary-Layer Winds, *Bound.-Lay. Meteorol.*, 159, 349–371, <https://doi.org/10.1007/s10546-016-0129-x>, 2016.
- Mann, J.: The spatial structure of neutral atmospheric surface-layer turbulence, *J. Fluid Mech.*, 273, 141–168, <https://doi.org/10.1017/S0022112094001886>, 1994.
- Mann, J.: Wind Field Simulation, *Probab. Eng. Mech.*, 13, 269–282, [https://doi.org/10.1016/S0266-8920\(97\)00036-2](https://doi.org/10.1016/S0266-8920(97)00036-2), 1998.
- Mann, J., Peña, A., Bingöl, F., Wagner, R., and Courtney, M. S.: Lidar scanning of momentum flux in and above the surface layer, *J. Atmos. Ocean. Tech.*, 27, 959–976, <https://doi.org/10.1175/2010JTECHA1389.1>, 2010.
- Medley, J., Wylie, S., Slinger, C., Harris, M., des Roziers, E. B., Pitter, M., and Mangat, M.: Classification of ZephIR 300 Lidar at the UK Remote Sensor Test Site, EWEA Resource Assessment 2015, Helsinki, Finland, 2015.
- Mikkelsen, T. K.: On mean wind and turbulence profile measurements from ground-based wind lidars: limitations in time and space resolution with continuous wave and pulsed lidar systems, European Wind Energy Conference and Exhibition 2009, 16–19 March 2009, Marseille, France, 6, 4123–4132, 2009.
- Newman, J. F., Klein, P. M., Wharton, S., Sathe, A., Bonin, T. A., Chilson, P. B., and Muschinski, A.: Evaluation of three lidar scanning strategies for turbulence measurements, *Atmos. Meas. Tech.*, 9, 1993–2013, <https://doi.org/10.5194/amt-9-1993-2016>, 2016.
- Pedersen, A. T., Montes, B. F., Pedersen, J. E., Harris, M., and Mikkelsen, T.: Demonstration of short-range wind lidar in a high-performance wind tunnel, in: Poster presented at EWEA 2012 – European Wind Energy Conference & Exhibition, 16–19 March 2012, Copenhagen, Denmark, 2012.
- Peña, A., Hasager, C. B., Gryning, S.-E., Courtney, M., Antoniou, I., and Mikkelsen, T.: Offshore Wind Profiling Using Light Detection and Ranging Measurements, *Wind Energy*, 12, 105–124, <https://doi.org/10.1002/we.283>, 2009.
- Peña, A., Floors, R., Sathe, A., Gryning, S.-E., Wagner, R., Courtney, M. S., Larsen, X. G., Hahmann, A. N., and Hasager, C. B.: Ten Years of Boundary-Layer and Wind-Power Meteorology at Høvsøre, Denmark, *Bound.-Lay. Meteorol.*, 158, 1–26, <https://doi.org/10.1007/s10546-015-0079-8>, 2016.
- Sathe, A. and Mann, J.: Measurement of turbulence spectra using scanning pulsed wind lidars, *J. Geophys. Res.-Atmos.*, 117, D01201, <https://doi.org/10.1029/2011JD016786>, 2012.
- Sathe, A. and Mann, J.: A review of turbulence measurements using ground-based wind lidars, *Atmos. Meas. Tech.*, 6, 3147–3167, <https://doi.org/10.5194/amt-6-3147-2013>, 2013.
- Sathe, A., Mann, J., Gottschall, J., and Courtney, M. S.: Can wind lidars measure turbulence?, *J. Atmos. Ocean. Tech.*, 28, 853–868, <https://doi.org/10.1175/JTECH-D-10-05004.1>, 2011.
- Sathe, A., Mann, J., Vasiljevic, N., and Lea, G.: A six-beam method to measure turbulence statistics using ground-based wind lidars, *Atmos. Meas. Tech.*, 8, 729–740, <https://doi.org/10.5194/amt-8-729-2015>, 2015.
- Schlipf, D., Trabucchi, D., Bischoff, O., Hofsaß, M., Mann, J., Mikkelsen, T., Rettenmeier, A., Trujillo, J. J., and Kühn, M.: Testing of frozen turbulence hypothesis for wind turbine applica-

- tions with a scanning LIDAR system, ISARS 2010, 28–30 June 2010, Paris, <https://doi.org/10.18419/opus-3915>, 2010.
- Smith, D. A., Harris, M., Coffey, A. S., Mikkelsen, T., Jørgensen, H. E., Mann, J., and Danielian, R.: Wind lidar evaluation at the Danish wind test site Høvsøre, *Wind Energy*, 9, 87–93, <https://doi.org/10.1002/we.193>, 2006.
- Sonnenschein, C. M. and Horrigan, F. A.: Signal-to-Noise Relationships for Coaxial Systems that Heterodyne Backscatter from the Atmosphere, *Appl. Optics*, 10, 1600, <https://doi.org/10.1364/AO.10.001600>, 1971.
- Taylor, G. I.: The Spectrum of Turbulence, *P. Roy. Soc. A*, 164, 476–490, <https://doi.org/10.1098/rspa.1938.0032>, 1938.
- Wagner, R., Mikkelsen, T., and Courtney, M.: Investigation of turbulence measurements with a continuous wave, conically scanning LiDAR, Risø-R-1682(EN), DTU, Risø, Denmark, 2009.
- Willis, G. E. and Deardorff, J.: On the use of Taylor's translation hypothesis for diffusion in the mixed layer, *Q. J. Roy. Meteorol. Soc.*, 102, 817–822, <https://doi.org/10.1002/qj.49710243411>, 1976.
- Wyngaard, J. C.: Measurement of small-scale turbulence structure with hot wires, *J. Phys. E*, 1, 1105–1108, <https://doi.org/10.1088/0022-3735/1/11/310>, 1968.





## **Chapter 6**

### **Article 2:**

# **Cross-contamination effect on turbulence spectra from Doppler beam swinging wind lidar**





## Cross-contamination effect on turbulence spectra from Doppler beam swinging wind lidar

Felix Kelberlau<sup>1</sup> and Jakob Mann<sup>2</sup>

<sup>1</sup>NTNU, Department of Energy and Process Engineering, Norwegian University of Science and Technology, 7491 Trondheim, Norway

<sup>2</sup>DTU Wind Energy, Technical University of Denmark, 4000 Roskilde, Denmark

**Correspondence:** Felix Kelberlau ([felix.kelberlau@ntnu.no](mailto:felix.kelberlau@ntnu.no)) and Jakob Mann ([jmsq@dtu.dk](mailto:jmsq@dtu.dk))

Received: 30 September 2019 – Discussion started: 14 October 2019

Revised: 25 March 2020 – Accepted: 6 April 2020 – Published: 30 April 2020

**Abstract.** Turbulence velocity spectra are of high importance for the estimation of loads on wind turbines and other built structures, as well as for fitting measured turbulence values to turbulence models. Spectra generated from reconstructed wind vectors of Doppler beam swinging (DBS) wind lidars differ from spectra based on one-point measurements. Profiling wind lidars have several characteristics that cause these deviations, namely cross-contamination between the three velocity components, averaging along the lines of sight and the limited sampling frequency. This study focuses on analyzing the cross-contamination effect. We sample wind data in a computer-generated turbulence box to predict lidar-derived turbulence spectra for three wind directions and four measurement heights. The data are then processed with the conventional method and with the method of squeezing that reduces the longitudinal separation distances between the measurement locations of the different lidar beams by introducing a time lag into the data processing. The results are analyzed and compared to turbulence velocity spectra from field measurements with a Windcube V2 wind lidar and ultrasonic anemometers as reference. We successfully predict lidar-derived spectra for all test cases and found that their shape is dependent on the angle between the wind direction and the lidar beams. With conventional processing, cross-contamination affects all spectra of the horizontal wind velocity components. The method of squeezing improves the spectra to an acceptable level only for the case of the longitudinal wind velocity component and when the wind blows parallel to one of the lines of sight. The analysis of the simulated spectra described here improves our understanding of the limitations of turbulence measurements with DBS profiling wind lidar.

### 1 Introduction

Wind energy research and industry depend on reliable measurements of wind velocities for wind site assessment and load prediction. Remote sensing devices such as vertical profiling lidars can measure wind velocities at adjustable height levels from the ground. The ease of installation and mobility of ground-based lidars make them superior to conventional in situ anemometry on tall meteorological masts.

Vertical profiling wind lidars emit a laser beam in different directions and can estimate the radial component of the wind velocity along sections of the beam. Measurements of the radial velocity in at least three different directions are then used

to reconstruct three-dimensional wind vectors. Depending on the type of lidar being applied, either velocity–azimuth display (VAD) scanning or Doppler beam swinging (DBS) is used as the scanning strategy. When VAD scanning is applied, the laser beam performs continuous azimuth scans at a fixed elevation angle (Browning and Wexler, 1968). With DBS the beam is directed into certain directions, where it accumulates measurement data for a defined time before it swings into the next direction. Turbulence statistics can be derived from VAD scanning (e.g., Eberhard et al., 1989; Krishnamurthy et al., 2011; Smalikho, 2003) or DBS (e.g., Frehlich et al., 1998; Kumer et al., 2016; Bodini et al., 2019). An advantage of DBS is that the signal-to-noise ratio of each

radial velocity estimate increases with accumulation time in each direction. The possibility to measure in a vertical direction is another advantage of DBS wind lidars. The Windcube produced by Leosphere (Saclay, France) is a widely used vertical profiling pulsed Doppler wind lidar that uses DBS to reconstruct three-dimensional wind vectors from five independent line-of-sight (LOS) velocity measurements.

Profiling lidars have proven to be accurate tools for measuring mean wind speed and direction in noncomplex terrain (Emeis et al., 2007; Smith et al., 2006; Gottschall et al., 2012; Kim et al., 2016). However, the measurement of turbulence with ground-based profiling wind lidars is inaccurate, due to their extended measurement volumes, the limited sampling frequency for each line-of-sight measurement and the large spatial separation between the measurement volumes (Sathe and Mann, 2013; Newman et al., 2016). The second-order statistics of turbulence measured by profiling wind lidars show that the measurement error depends on several factors: the measurement principle of the lidar used, the conditions of the atmospheric boundary layer, the measurement height, and, in the case of the Windcube, also on the angle between the mean wind direction and the orientation of the lidar beams (Sathe et al., 2011).

Measured auto- and co-spectra of the three turbulent wind velocity components show the spectral distribution of the wind velocity variance. IEC standard 61400-1 (IEC, 2019) recommends using such one-point spectra for finding the model parameters anisotropy  $\gamma$ , length scale  $L$  and dissipation factor  $\alpha e^{2/3}$  of the uniform shear model of turbulence (Mann, 1994). This can be done by fitting the parameters to the measured spectra. The found parameters can then be used in the process of determining aerodynamic loads on wind turbines and other built structures. But estimations of turbulence spectra from wind lidar data deviate significantly from reference measurements taken at meteorological masts due to their measurement principle. Canadillas et al. (2010) present measured turbulence velocity spectra from a Windcube that show characteristic differences in comparison to reference measurements from sonic anemometers. The lidar spectra show, e.g., spectral energies that are too high in a wide range of frequencies due to cross-contamination and gaps at frequencies that correspond to the limited sampling frequency of the lidar beams. Such spectra are modeled in Sathe and Mann (2012) for an older Windcube version. The same model can, with minor modifications, be used to predict spectra from the current version of the Windcube, which samples faster and includes a vertical beam. The major drawback of the model is that it cannot predict spectra for cases in which the wind inflow is not parallel to two of the lidar beams.

In the study we present here, we overcome this limitation by sampling velocity values in a computer-generated turbulence box and processing them in a similar fashion to how DBS scanning pulsed lidar samples wind velocities in the atmosphere. The results of this artificial sampling are com-

pared to measured DBS pulsed lidar spectra acquired from field measurements. This method makes it possible to predict lidar-derived turbulence velocity spectra for all relative wind directions.

In addition to conventional DBS processing of radial wind velocities, we reconstruct the three-dimensional wind vectors with the method of squeezing introduced in Kelberlau and Mann (2019a). This method minimizes cross-contamination for VAD scanning wind lidars (e.g., ZX 300) by introducing a time lag into the data processing that compensates for the duration it takes to advect an air volume from one lidar beam to the other.

In this study, we assess whether the method of squeezing is also advantageous for DBS scanning wind lidar such as the Windcube and to what extent it improves estimation of turbulence velocity spectra. The aim of the work presented here is prediction of turbulence velocity spectra from DBS scanning wind lidars and making turbulence measurements more accurate by applying a modified data processing algorithm.

Following this, Sect. 2 presents the theory of how a pulsed Doppler beam swinging wind lidar determines radial wind velocities and reconstructs three-dimensional wind vectors. The method of squeezing is also briefly presented. In Sect. 3, we describe the methods applied in this study. These consist of (i) field measurements with a Windcube V2 and collocated reference measurements with sonic anemometers on a large meteorological mast and (ii) sampling of computer-generated turbulence data. We present and discuss the results of both field measurements and simulations in Sect. 4 and describe our key findings in the conclusions in Sect. 5. A nomenclature can be found in Appendix A.

## 2 Lidar theory

### 2.1 Coordinate system and preliminaries

This study uses a right-handed coordinate system aligned with the horizontal mean wind vector. The component  $u$  points in the mean wind direction,  $v$  is the transversal wind component, and  $w$  points vertically upwards, such that for the wind vector  $\mathbf{u}$  it accounts for the following equation:

$$\mathbf{u} = \begin{bmatrix} u \\ v \\ w \end{bmatrix}. \quad (1)$$

We also use Reynolds decomposition with a timescale of 10 min to divide the wind vectors into a mean part  $U$  and a fluctuating part  $\mathbf{u}'$ , such that

$$\mathbf{u} = U + \mathbf{u}'. \quad (2)$$

$U$  is the mean wind speed, the transversal component  $V$  is by definition zero, and the vertical mean velocity  $W$  in non-complex terrain is typically also close to zero. The mean values of the components of  $\mathbf{u}'$  are by definition zero, but their

statistical variance provides important information about the amount of turbulence in the wind. It is defined as follows:

$$\sigma_u^2 = \langle u'u' \rangle, \tag{3}$$

where  $\langle \rangle$  means ensemble averaging. The variance of the other two components  $\sigma_v^2$  and  $\sigma_w^2$  can be calculated accordingly.

2.2 Line-of-sight velocity retrieval

The Windcube lidar emits laser beams into five fixed directions. As shown in Fig. 1, four beams are inclined by the zenith angle  $\phi$  from the vertical and separated along the horizon by the azimuth angle  $\theta$ . The fifth beam points vertically upwards. The beam directions define the internal fixed right-handed coordinate system of the Windcube. In accordance with the documentation of the Windcube, the  $x$  component is oriented from LOS1 towards LOS3, the  $y$  component points from LOS2 towards LOS4, and the vertical  $z$  component points downwards along LOS5. In the default setup, the LOS1 beam is oriented towards north. If this is not the case, a directional offset  $\theta_0$  must be considered in the data processing. Unit vectors  $n_i$  that point into the direction of the five beams are defined as

$$n_i = \begin{bmatrix} \cos(\frac{i-3}{2}\pi) \sin \phi \\ \sin(\frac{i-3}{2}\pi) \sin \phi \\ -\cos \phi \end{bmatrix} \text{ for } i = 1 \dots 4,$$

and

$$n_5 = \begin{bmatrix} 0 \\ 0 \\ -1 \end{bmatrix}. \tag{4}$$

A small portion of the emitted laser radiation is backscattered in the direction of origin. This backscattered radiation has a wavelength that is slightly different from the emitted radiation. The difference in wavelength is caused by the Doppler effect and is proportional to the component of the wind in the respective beam direction, which is as follows:

$$v_{r_i} = n_i \cdot x_i, \tag{5}$$

where  $x_i$  is the wind velocity vector at the measurement points in the coordinate system of the Windcube. The Doppler shift can be detected and is used to determine the line-of-sight velocities, i.e., the radial velocities in the corresponding beam direction. Unlike continuous-wave lidars, pulsed lidars can determine signed line-of-sight velocities for multiple height levels simultaneously. These line-of-sight velocities are the weighted average of the radial wind velocities along the stretch of the lidar beam that is illuminated by the range gate. A reasonable weighting function to model the line-of-sight averaging is the convolution of the laser pulse

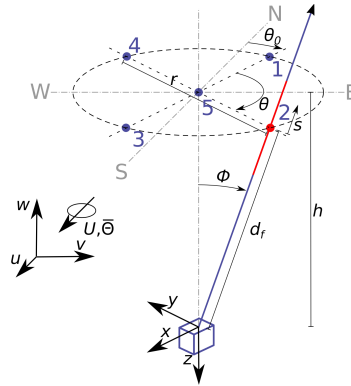


Figure 1. Visualization of the beam configuration of the Windcube V2, relevant lengths and angles, and the two coordinate systems used by the lidar and in wind data analysis. For better visibility, only LOS2 is depicted as a beam, with the range gate indicated in red along the blue laser beam.

shape with the interrogation window. In the case of the Windcube, the emitted laser pulses are 175 ns long and thus illuminate air volumes of  $175 \text{ ns} \times c = 52.46 \text{ m}$  in length along the line of sight, where  $c$  is the speed of light. The backscattered radiation recorded by the laser detector at one point in time originates from a line-of-sight segment that cannot be shorter than half of this length. If the laser beams were perfectly collimated and rectangular and interrogation windows of the same length were chosen, a triangular function would be the correct weighting function to account for the higher likelihood of a scatterer to be located closer to the center of the pulse than its ends. However, the beams of the Windcube are not collimated but focused permanently to a height level of approximately 100 m in order to optimize the carrier-to-noise ratio. In addition, its light pulses are not perfectly cut-in and cut-out at their ends. The triangular function is thus only an approximation of the real situation. We refer to Lindelöw (2008) for more details. However, as in Sathe and Mann (2012), we use a triangular weighting function

$$\varphi(s) = \frac{l_p - |s|}{l_p^2} \text{ for } |s| < l_p,$$

and

$$\varphi(s) = 0 \text{ for } |s| \geq l_p, \tag{6}$$

where  $s$  is the distance from the midpoint of the range gate and  $l_p = 26 \text{ m}$  is the approximate half length of the range gate

to simulate the lidar-derived weighted radial velocity

$$\tilde{v}_{r_i} = \int_{-\infty}^{\infty} \varphi(s) \mathbf{n}_i \cdot \mathbf{u}((s + d_f) \mathbf{n}_i) ds, \quad (7)$$

where  $d_f$  is the distance of the center of the range gate from the lidar.

### 2.3 DBS measurement principle

The line-of-sight velocities are processed in order to reconstruct three-dimensional wind vectors. These are based on the fixed right-handed coordinate system of the Windcube. The Windcube calculates one new wind vector component whenever a new line-of-sight measurement becomes available. The  $x$  component is calculated when a radial velocity of either LOS1 or LOS3 is retrieved. The newly updated line-of-sight velocity is then combined with the immediate precursor of the opposing direction according to

$$x = \frac{\tilde{v}_{r_1} - \tilde{v}_{r_3}}{2 \sin \phi}. \quad (8)$$

The  $y$  component is calculated from LOS2 and LOS4 according to

$$y = \frac{\tilde{v}_{r_2} - \tilde{v}_{r_4}}{2 \sin \phi}. \quad (9)$$

Here, the latest LOS2 beam is combined with the previous LOS4 beam and vice versa. In Fig. 2 it can be seen that, e.g., the measurement of the 17th beam that the lidar emits (LOS2) is combined with the 14th beam (LOS4) and the 19th beam (LOS4) is combined with the 17th beam (LOS2) to calculate two values of  $y$ .

The vertical  $z$  component can be estimated directly from the vertical beam result whenever a new LOS5 measurement becomes available so that

$$z = \tilde{v}_{r_5}. \quad (10)$$

In addition to the three wind components, the Windcube estimates the horizontal wind velocity

$$V_{\text{hor}} = \sqrt{x^2 + y^2}, \quad (11)$$

the horizontal wind direction clockwise from north

$$\Theta = \theta_0 - \arctan(y, -x), \quad (12)$$

and their 10 min average values  $\bar{V}_{\text{hor}}$  and  $\bar{\Theta}$  marked with an overline.

In order to rotate the three wind vector components into the coordinate system aligned with the mean wind direction, we calculate

$$\mathbf{u}_{\text{DBS}} = \begin{bmatrix} u_{\text{DBS}} \\ v_{\text{DBS}} \\ w_{\text{DBS}} \end{bmatrix} = \begin{bmatrix} x \cos \alpha + y \sin \alpha \\ x \sin \alpha - y \cos \alpha \\ -z \end{bmatrix}, \quad (13)$$

**Table 1.** Line-of-sight beam geometry and timing:  $t$  is the accumulated time after the first beam measurement, and  $\Delta t$  is the time difference between the current and the previous beam measurement.

LOS no.	$\phi$	$\theta$	$t$	$\Delta t$
1	28°	0°	0.00 s	–
2	28°	90°	0.72 s	0.72 s
3	28°	180°	1.44 s	0.72 s
4	28°	270°	2.16 s	0.72 s
5	0°	–	3.13 s	0.97 s
1	28°	0°	3.85 s	0.72 s
⋮	⋮	⋮	⋮	⋮

where  $\alpha = \bar{\Theta} - \theta_0$  is the relative inflow angle. The resulting wind vectors are updated at slightly varying times because swinging the Doppler beam from one line of sight to the next and accumulating measurements takes approximately 0.72 s for the inclined beams and 0.97 s for the vertical beam. We do not know the reason for the different times required to change the beam direction. This leads to an average wind vector refresh rate of approximately 1.3 Hz, although each beam is updated with a frequency of no more than 0.26 Hz. Table 1 provides an overview of the beam geometry and the timing.

### 2.4 Measurement errors due to cross-contamination

The  $w$  component is measured directly from the vertical beam. However, the reconstruction of the horizontal wind components  $u$  and  $v$  involves the combination of measurement values from two spatially separated air volumes. These reconstructions are correct only if the wind vector is identical at all measurement volumes. For the calculation of average wind speeds, it is sufficient that the average wind vector is identical at all measurement volumes. But for every single wind vector to be correct, the wind field would need to be static. In a turbulent wind field, the single reconstructed wind vectors are erroneous due to cross-contamination of the different wind velocity components.

The cause of this error lies in combining radial velocities from spatially separated air volumes. The separations can be categorized into longitudinal separations (along the direction of the mean wind) and lateral separations (orthogonal to the mean wind direction). Assuming Taylor's frozen turbulence hypothesis (Taylor, 1938), wind velocities sampled at two longitudinally separated points are perfectly correlated but have a temporal offset between the two measurement signals that corresponds to the time needed for the mean wind speed to cover the distance between the two points. Whenever the wavelength of the measured turbulence equals  $2/n$  times the separation distance, with  $n = 1, 3, 5, \dots$ , a resonance effect occurs. The wind speed component being measured cannot be detected in these cases and is replaced by contributions of

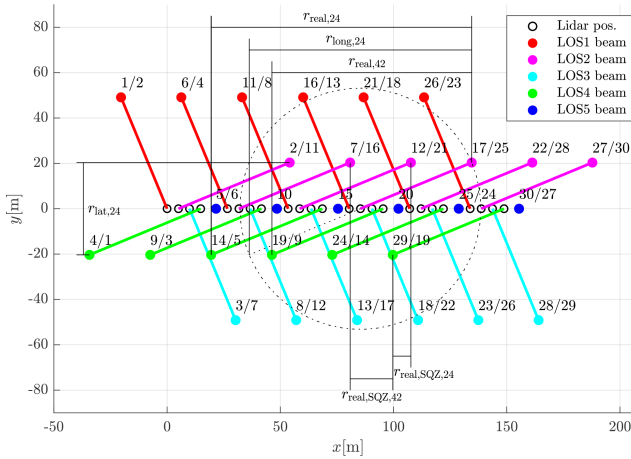


**Figure 2.** Visualization of the measurement geometry of the Windcube V2 with the five beam directions: LOS1–LOS5 (color coded). Top view of 30 consecutive line-of-sight measurements in a coordinate system that is moving with the mean wind. The angle between the mean wind and the LOS1–LOS3 axis is  $\alpha = 67.5^\circ$ . Measurement locations (dots) are numbered by their order in time (first number) and position in wind direction (second number). Longitudinal and lateral separation distances for combinations of LOS2 and LOS4 beams are shown.

other wind speed components. In contrast, for  $n = 0, 2, 4, \dots$  no resonance effect occurs (see Fig. 2 in Kelberlau and Mann, 2019a).

The distance  $D$  between two opposing measurement points is

$$D = 2h \tan \phi, \tag{14}$$

where  $h$  is the measurement height, and  $D$  is the diameter of the dotted circle in Fig. 2. The longitudinal separation distances for the beam combination LOS1 and LOS3 can be calculated according to

$$r_{\text{long},13} = |D \cos \alpha|. \tag{15}$$

$r_{\text{long},24}$  for the beam combination LOS2 and LOS4 can be estimated by swapping the cosine in Eq. (15) by a sine.  $r_{\text{long},24}$  is also shown in Fig. 2.

Equation (13) shows that the components  $u$  and  $v$  in the reconstructed wind vectors are composed of contributions from two different beam combinations. These are LOS1 and LOS3 (see Eq. 8) as well as LOS2 and LOS4 (see Eq. 9). In order to calculate longitudinal separations that are representative for the reconstructed wind velocity components, we must introduce a weighting and calculate

$$r_{\text{rep},u} = \frac{|\cos \alpha| \times r_{\text{long},13} + |\sin \alpha| \times r_{\text{long},24}}{|\cos \alpha| + |\sin \alpha|} = \frac{D}{|\cos \alpha| + |\sin \alpha|}, \tag{16}$$

for the  $u$  component and

$$r_{\text{rep},v} = \frac{|\sin \alpha| \times r_{\text{long},13} + |\cos \alpha| \times r_{\text{long},24}}{|\cos \alpha| + |\sin \alpha|} = \frac{|\sin(2\alpha)| D}{|\cos \alpha| + |\sin \alpha|}, \tag{17}$$

for the  $v$  component. The resulting representative longitudinal separation distance values for the Windcube for four measurement heights 40, 60, 80, and 100 m and for three relative wind inflow angles  $\alpha = 0, 22.5, \text{ and } 45^\circ$  are given in Table 2. From these distances, the wave numbers at which we expect resonance can easily be determined with  $k_{\text{res}} = n\pi/r_{\text{rep}}$ , where  $n$  is an odd integer. Lateral separation distances  $r_{\text{lat},ij}$  could be estimated in a similar way. But compared to longitudinal separations, the situation is different for wind velocity fluctuations measured at two laterally separated points. The spatial structure of turbulence leads to the wind velocity fluctuations becoming less correlated as the distance between the two measurement points increases. The coherence of the fluctuations is also weaker for small eddies than for large turbulent structures. That means that a turbulent structure can only be detected at two laterally separated points if the length scale of the turbulent structure is large compared to the separation distance. Lateral separation leads to contamination that occurs gradually without resonance points at specific wave numbers.

If the mean wind is aligned with two opposing lines of sight, e.g., blows in the LOS1–LOS3 direction, then the

**Table 2.** Representative longitudinal separation distances influencing the  $u$  and  $v$  component of  $u_{\text{DBS}}$  for all investigated test cases. All values given in m.

$h$	$\alpha = 0^\circ$		$\alpha = 22.5^\circ$		$\alpha = 45^\circ$	
	$r_{\text{rep},u}$	$r_{\text{rep},v}$	$r_{\text{rep},u}$	$r_{\text{rep},v}$	$r_{\text{rep},u}$	$r_{\text{rep},v}$
40	42.5	0.0	32.6	23.0	30.1	30.1
60	63.8	0.0	48.8	34.5	45.1	45.1
80	85.1	0.0	65.1	46.0	60.2	60.2
100	106.3	0.0	81.4	57.6	75.2	75.2

$u$  component of the wind vector is reconstructed from two points that are only separated longitudinally. That means each turbulent structure is measured twice: once when it passes the LOS1 location and then some time later at the LOS3 location. Assuming frozen turbulence, measurements from points that are separated longitudinally are fully correlated, and resonance occurs at specific wave numbers. The  $v$  component, in contrast, is in this case reconstructed from the laterally separated points of LOS2 and LOS4, and a reduced correlation is found depending on the size of the turbulent structure and the separation distance. No specific resonance wave numbers are found. For a comprehensive description of the cross-contamination effects due to isolated longitudinal and isolated lateral separation, see Kelberlau and Mann (2019a). Here we look at the more complex case when the mean wind inflow is not aligned with two opposing line-of-sight directions. Estimates of one horizontal wind velocity component can then be contaminated by contributions from both other wind velocity components. For a manual estimation of the cross-contamination effect for non-aligned inflow we first derive the lidar-estimated wind vector component  $u_{\text{DBS}}$  as a function of the real wind vector at all four measurement locations. When, Eqs. (8) and (9) are set into Eq. (13) we get

$$u_{\text{DBS}} = \frac{(\tilde{v}_{r1} - \tilde{v}_{r3}) \cos \alpha}{2 \sin \phi} + \frac{(\tilde{v}_{r2} - \tilde{v}_{r4}) \sin \alpha}{2 \sin \phi}. \quad (18)$$

We assume no line-of-sight averaging, thus  $v_{ri} = \tilde{v}_{ri}$  and use Eqs. (4) and (5). After rearranging we get

$$u_{\text{DBS}} = \frac{\cos \alpha}{2} (-x_1 + z_1 \cot \phi - x_3 - z_3 \cot \phi) + \frac{\sin \alpha}{2} (-y_2 + z_2 \cot \phi - y_4 - z_4 \cot \phi). \quad (19)$$

After transferring the wind velocity components  $x$ ,  $y$ ,  $z$  into the  $u$ ,  $v$ ,  $w$  coordinate system we get

$$u_{\text{DBS}} = \frac{\cos \alpha}{2} (-u_1 \cos \alpha - v_1 \sin \alpha - w_1 \cot \phi - u_3 \cos \alpha - v_3 \sin \alpha + w_3 \cot \phi) + \frac{\sin \alpha}{2} (-u_2 \sin \alpha + v_2 \cos \alpha - w_2 \cot \phi - u_4 \sin \alpha + v_4 \cos \alpha + w_4 \cot \phi). \quad (20)$$

With Eq. (3) we can describe the total lidar variance as a function of the wind vector fluctuations at the four measurement points as

$$\sigma_{u,\text{DBS}}^2 = \left\langle u_{\text{DBS}}^2 \right\rangle = \frac{1}{4} \left\langle \left( (u'_1 \cos \alpha + v'_1 \sin \alpha + w'_1 \cot \phi + u'_3 \cos \alpha + v'_3 \sin \alpha - w'_3 \cot \phi) \cos \alpha + (u'_2 \sin \alpha - v'_2 \cos \alpha + w'_2 \cot \phi + u'_4 \sin \alpha - v'_4 \cos \alpha - w'_4 \cot \phi) \sin \alpha \right)^2 \right\rangle. \quad (21)$$

A similar formula can be found for the transversal component

$$\sigma_{v,\text{DBS}}^2 = \left\langle v_{\text{DBS}}^2 \right\rangle = \frac{1}{4} \left\langle \left( (u'_1 \cos \alpha + v'_1 \sin \alpha + w'_1 \cot \phi + u'_3 \cos \alpha + v'_3 \sin \alpha - w'_3 \cot \phi) \sin \alpha - (u'_2 \sin \alpha - v'_2 \cos \alpha + w'_2 \cot \phi + u'_4 \sin \alpha - v'_4 \cos \alpha - w'_4 \cot \phi) \cos \alpha \right)^2 \right\rangle. \quad (22)$$

Power spectral densities  $F_{\text{DBS}}$  at particular wave numbers are composed of the same linear combinations of wind components as the total variances in Eqs. (21) and (22). These equations are thus helpful when analyzing the extent of cross contamination at particular wave numbers. As an example, we now take the case when the mean wind direction and one of the lines of sight create an angle of  $45^\circ$ . We assume  $\Theta = 90^\circ$  and  $\theta_0 = 45^\circ$  because this situation is found in the measurements described later in this study. However, the results are identical for all setups in which the relative wind inflow  $\alpha = 45^\circ$ . In this case, LOS4 and LOS3 are separated purely longitudinally from LOS1 and LOS2, and LOS2 and LOS3 are separated purely laterally from LOS1 and LOS4, as shown in Fig. 3. This opens up the possibility of determining the cross-contamination effect for four extreme conditions. These four extreme conditions are characterized by either full or no longitudinal resonance, as well as either perfect or no lateral correlation. In the first case (a) when no resonance occurs and the lateral correlation is perfect, we assume identical wind vectors at all four points. We use  $u'_{1,a} = u'_{2,a} = u'_{3,a} = u'_{4,a} = u'_1$ . In the second case (b) when no resonance occurs but the lateral correlation is zero, we use  $u'_{1,b} = u'_{4,b} = u'_1$  and  $u'_{2,b} = u'_{3,b} = u'_2$ , where  $u'_1$  and  $u'_2$  are independent vectors. In the third case (c) resonance between the longitudinally separated points occurs and the fluctuations at laterally separated points are perfectly correlated. We use  $u'_{1,c} = u'_{2,c} = -u'_{3,c} = -u'_{4,c} = u'_1$ . The fourth case (d) is characterized by longitudinal resonance and zero lateral correlation. We use  $u'_{1,d} = -u'_{4,d} = u'_1$  and  $u'_{2,d} = -u'_{3,d} = u'_2$ , where  $u'_1$  and  $u'_2$  are independent vectors. Figure 3 gives an overview of the conditions we assume for these four cases (a) to (d). With these assumptions, Eq. (21) provides the lidar estimates of the power spectral density values  $F_{u,\text{DBS}}$  as linear combinations of the spectral values of the three wind components  $F_u$ ,  $F_v$  and  $F_w$ , as

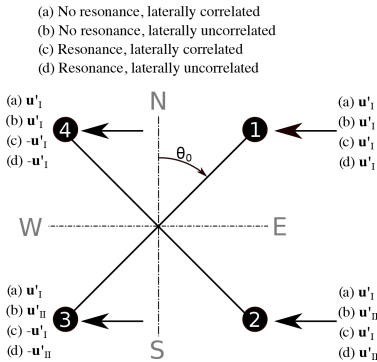


**Figure 3.** Overview of the assumptions made to determine the cross-contamination values listed in Table 3. In cases with no resonance, the wind vectors  $u'_{I,II}$  are identical at the longitudinally separated measurement points. In resonance cases they have an opposite sign. In cases with laterally correlated velocities, the wind vectors at laterally separated measurement points are identical. In cases with no correlation at points that are laterally separated, the wind vectors  $u'_{I}$  and  $u'_{II}$  are independent.

shown in the lower half of Table 3. The resulting linear combinations of power spectral densities that compose the lidar-measured  $u$  and  $v$  components of turbulence for the case with  $\alpha = 0^\circ$  are shown in the upper half of the same table.

Table 3 can be read as follows. First, choose the aligned ( $\alpha = 0^\circ$ ) or non-aligned case ( $\alpha = 45^\circ$ ). Then select the wind component of interest:  $F_{u,DBS}$  or  $F_{v,DBS}$ . Next, decide if the situation with or without resonance is more relevant for the wave number of interest. Finally, select a block of values that either represents the case with perfect lateral correlation or that assumes laterally uncorrelated fluctuations. The sum of the variances of the wind components multiplied by the values given in this block is the theoretical lidar-derived variance of the selected component. It is usually unclear to which degree the fluctuations are correlated, but the table can still be used for rough estimations. If you look for example at the resonance case for  $u$ , you will find that the lidar does not detect longitudinal wind fluctuations at all, while the lidar estimated  $u$  variance  $F_{u,DBS}$  is composed of a weakened  $v$  signal of between 0.00 and 0.50 times the real  $v$  fluctuations and an amplified  $w$  signal of between 3.54 and 7.07 times the real  $w$  fluctuations, depending on the degree of lateral correlation. The values given in the table can explain many of the effects we later see in the lidar-derived spectra for non-aligned inflow.

Table 1 shows that the radial velocity for each line of sight is determined not continuously but once every 3.85 s. This means turbulent fluctuations that occur with a corresponding frequency cannot be detected by any of the Windcube's lidar

**Table 3.** Expected contribution of the power spectral densities  $F_u$ ,  $F_v$  and  $F_w$  of the wind velocity components on the lidar-derived values of  $F_{u,DBS}$  and  $F_{v,DBS}$  for aligned and non-aligned inflow with  $\alpha = 0^\circ$  and  $45^\circ$ .

	$\alpha = 0^\circ$			
	$F_{u,DBS}$		$F_{v,DBS}$	
	–	lat. corr.	lat. uncorr.	
No resonance	1.00 $F_u$ 0.00 $F_v$ 0.00 $F_w$	0.00 $F_u$ 1.00 $F_v$ 0.00 $F_w$	0.00 $F_u$ 0.50 $F_v$ 1.77 $F_w$	
Resonance	0.00 $F_u$ 0.00 $F_v$ 3.54 $F_w$	–	–	
	$\alpha = 45^\circ$			
	$F_{u,DBS}$		$F_{v,DBS}$	
	lat. corr.	lat. uncorr.	lat. corr.	lat. uncorr.
No resonance	1.00 $F_u$ 0.00 $F_v$ 0.00 $F_w$	0.50 $F_u$ 0.00 $F_v$ 0.00 $F_w$	0.00 $F_u$ 1.00 $F_v$ 0.00 $F_w$	0.00 $F_u$ 0.50 $F_v$ 3.54 $F_w$
Resonance	0.00 $F_u$ 0.00 $F_v$ 7.07 $F_w$	0.00 $F_u$ 0.50 $F_v$ 3.54 $F_w$	0.00 $F_u$ 0.00 $F_v$ 0.00 $F_w$	0.50 $F_u$ 0.00 $F_v$ 0.00 $F_w$

beams. The respective wave numbers are

$$k_{scan} = \frac{2\pi}{U \cdot 3.85 \text{ s}} \tag{23}$$

At these wave numbers ( $k_{scan}$ ) we expect sudden drops in all lidar-derived spectra.

Because the data are not acquired continuously we expect a second effect that influences the shape of the lidar-derived turbulence velocity spectra. In the previous subsection we estimated the longitudinal separations (Table 2). These separations represent statistical averages and not actual separations. The actual separations could only be identical to these values if the lidar acquired line-of-sight velocity values continuously, which is not the case. Take the example of wind blowing along the  $x$  axis from LOS1 to LOS3. When an air volume is measured at LOS1, it continues moving towards LOS3. When the lidar subsequently takes a sample at LOS3, the actual separation distance between these two air volumes is less than the physical distance between the lines of sight. Conversely, when an air volume is measured at LOS3 first, it will have advected further away by the time the next sample is taken at LOS1. In this case, the actual separation distance will be larger than the physical distance between LOS1 and LOS3. As in Table 1, the time difference of  $\Delta t_{13} = 1.44$  s between a measurement of LOS1 and LOS3 deviates from the time difference  $\Delta t_{31} = 2.41$  s between measurements at

LOS3 and LOS1. The actual separation distances are then

$$r_{\text{real},13} = r_{\text{long},13} + \Delta t_{13}U,$$

and

$$r_{\text{real},31} = r_{\text{long},13} - \Delta t_{31}U. \quad (24)$$

The turbulence velocity spectra that we later derive from the lidar measurements can be seen as the average of two types of spectra: the ones we get from reconstructing the wind vector components of only LOS1 with the previous LOS3 measurements and the ones we get from reconstructing the wind vector components of only LOS3 with the previous LOS1 measurement. These averaged spectra deviate significantly from the spectra expected from continuous sampling if the product of mean wind speed and the time between the measurements is large compared to the average separation distances. The resonance peaks are then less pronounced and extend over a wider range of wave numbers.

### 2.5 Squeezed wind vector reconstruction

One method to avoid cross-contamination caused by longitudinal separation is presented in Kelberlau and Mann (2019a). It is called the method of squeezing and aims to remove the longitudinal separation distances  $r_{\text{real},ij}$  by introducing a temporal delay  $\tau = \frac{r_{\text{real},ij}}{U}$  into the data processing. The length of this temporal delay corresponds to the time it takes the mean wind to transport the frozen turbulence field along the separation distance. The approach assumes the frozen turbulence hypothesis. This assumption makes it possible to measure one turbulent structure at different points in space when the separation between the points is aligned with the mean wind direction and when the time between the measurements equals the time it takes the mean wind to transport the turbulent structure from one point to the other. The line-of-sight measurements taken by the Windcube are unfortunately not continuous. Therefore, the chosen temporal delay can only be a multiple  $n$  of the refresh rate of a particular line-of-sight measurement, i.e.,  $\tau = n \cdot 3.85$  s. As a consequence, the actual longitudinal separation distances for a squeezed pair of radial velocity measurements cannot become zero. But geometrical considerations show that they are reduced to

$$r_{\text{real,SQZ},ij} = \Delta t_{ij}U,$$

where the subscript SQZ indicates the squeezed wind vector reconstruction. An example is given in Fig. 2, where the lengths of  $r_{\text{real},ij}$  can be compared with the lengths of  $r_{\text{real,SQZ},ij}$ . This shows that it is impossible to completely avoid the resonance effect due to longitudinal separation. However, it is possible to shift the resonance wave number away from the high-energy region into a lower-energy region where the measurement signal is already strongly attenuated

by the line-of-sight averaging. The lateral separations, on the contrary, remain unchanged by the application of squeezed processing.

## 3 Methods

### 3.1 Field measurements

The measurement data used for this study originate from a measurement campaign in which a Windcube V2 was collocated to the 116.5 m high meteorological mast at the Danish National Test Center for Large Wind Turbines at Høvsøre, Denmark. The test location lies approximately 1.7 km east of the North Sea, which is bordered by a stretch of dunes. Otherwise the terrain has no significant elevations. For reference measurements, the meteorological mast is equipped with Metek USA-1 ultrasonic anemometers at 10, 20, 40, 60, 80, and 100 m heights. For a more detailed description of the test site we refer to Peña et al. (2016).

The measurements span a period from 11 September 2015 until 26 May 2016, with no measurements taken between 9 November 2015 and 17 February 2016. The lidar is positioned around 13 m to the west of the meteorological mast and oriented with its LOS1 in the northeast direction so that  $\theta_0 = 45^\circ$ . An overview about the orientation of the lidar beams is given in Fig. 4.

### 3.2 Sampling in a turbulence box

Sampling in a turbulence box is a method to simulate wind lidar measurements in very large computer-generated wind fields. The creation of such wind fields, according to Mann (1998), requires less computational power than, for example, large eddy simulation (LES). LES was successfully used before to analyze coherent structures in wind fields (e.g., Stawiariski et al., 2015) and wind profiles (e.g., Gasch et al., 2020) but predicting lidar-derived turbulence velocity spectra requires much more turbulence data. An advantage of using LES is that Taylor's frozen turbulence hypothesis does not need to be applied, but a drawback is that fine-scale turbulence would be suppressed.

To be able to predict lidar-derived spectra in a turbulence box, we first determined the three model parameters, i.e., the turbulence length scale  $L$ , the degree of anisotropy  $\Gamma$ , and the dissipation factor  $\alpha\epsilon^{2/3}$  for all test cases by fitting the sonic-derived spectra to the Mann (1994) uniform shear model of turbulence. We then used these parameters to create large turbulence files that contain possible values of the three velocity components  $u$ ,  $v$ , and  $w$ . In order to limit the required memory, we divided the desired box size into 32 separate files with different random seeds for each test case. Each of the files consists of  $32768 \times 128 \times 32$  points. The selected spatial resolution is 2 m per point so that all files for one test case represent an air volume of 2097152 m length, 256 m width and 64 m height. These boxes contain turbulence statis-

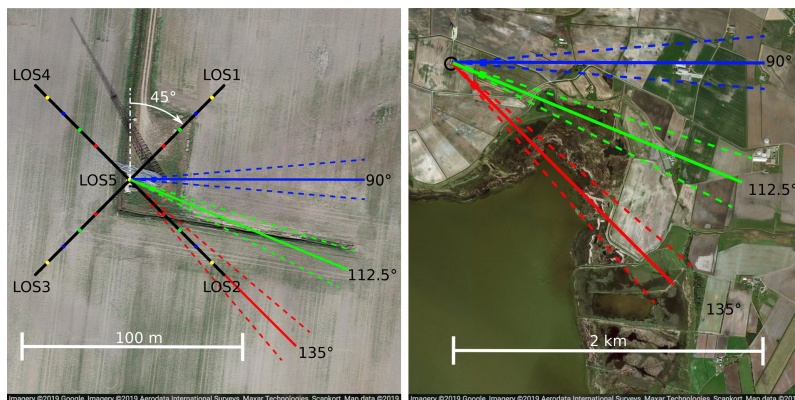


**Figure 4.** Aerial pictures of the location of the Windcube 13 m to the west of the meteorological mast at Høvsøre with the location of the measurement points along the lines of sight (left) and the landscape around the measurement location in the inflow directions (right). The top of the map is oriented to the north. Adapted from © Google Maps.

tics that are similar to what the underlying spectral tensor describes. We created a MATLAB script that samples data within the turbulence boxes similar to how a Windcube samples wind velocities in the real atmosphere. The script first imports the turbulence files and cuts them into 10 min intervals, whose spatial length depends on the desired mean wind speed  $U$ . The script then considers a realistic timing by importing the timestamp data of an arbitrary Windcube .rtd file, which is a standard output data file type that contains the line-of-sight velocities of every single beam including their timing and carrier-to-noise ratio. Next, it defines the location of the center of the range gate for all beams at all desired height levels within a 10 min interval. Different inflow directions are imitated by altering the orientation of the beams with  $\theta_0$ . These locations are then moved into the horizontal central plain of the turbulence box. The program defines a total of 27 points along all lines of sight, centered around the midpoints of the range gates. These points have a distance of 1 m from each other. The turbulence velocities are then interpolated to these 27 points and projected onto the line-of-sight direction. A triangular weighting function is eventually multiplied to calculate the line-of-sight averaged radial velocities. From this point on, the data processing is identical to the processing of the lidar measurement data as described in Sect. 2.3.

### 3.3 Data selection

We filter the field data to include only the 10 min intervals in which the mean wind velocity at 80 m above the ground was within an interval of  $U = 8 \pm 0.5 \text{ m s}^{-1}$ . The reference height of 80 m was selected arbitrarily. Using only one ref-

erence height in the filtering process assures that the same 10 min intervals are used for all four investigated height levels:  $h_1 = 40 \text{ m}$ ,  $h_2 = 60 \text{ m}$ ,  $h_3 = 80 \text{ m}$  and  $h_4 = 100 \text{ m}$ . The mean wind velocity  $U = 8 \text{ m s}^{-1}$  was selected because it is the most frequent in the dataset. A narrow velocity bin is selected, thus the time delay used in the processing of actual measurements is identical with the time delay chosen for sampling in a turbulence box. Three narrow wind sectors around  $\bar{\Theta}_1 = 135^\circ$ ,  $\bar{\Theta}_2 = 112.5^\circ$  and  $\bar{\Theta}_3 = 90^\circ$  are chosen for the analysis. The width of the sectors is  $\pm 5^\circ$ . In the first case, the wind is aligned with two of the lines of sight, namely LOS2 and LOS4 ( $\alpha = 90^\circ$ ), in the second case the offset is  $22.5^\circ$  ( $\alpha = 67.5^\circ$ ), and in the third case the offset is  $45^\circ$  ( $\alpha = 45^\circ$ ). As shown in Fig. 4, the three inflow directions are dominated by flat farm land and the water of Nissum Fjord. The small town of Bøvlingbjerg lies in the east-southeast direction and is approximately 3 km away. Within 2 km, only one farm might have some minor influence on the measurements in the first wind sector. The selected measurement sectors are neither affected by the wind turbines to the north nor by the sea-to-land transition to the west of Høvsøre. The data are additionally filtered to only contain intervals of neutrally stratified atmospheric conditions in order to achieve a good fit with the Mann model of turbulence. The filter criterion is a Monin–Obukhov length  $|L_{MO}| > 500 \text{ m}$  based on measurements 20 m above the ground. Furthermore, to assure high quality of the analyzed measurement data, we filter out intervals with less than 100 % data availability. Therefore, each line-of-sight measurement in the filtered dataset has a carrier-to-noise ratio better than the Windcube's standard threshold of  $-23 \text{ dB}$ . After filtering, 49, 31 and 27 in-

tervals of 10 min remain for the analysis of the first, second and third wind sector, respectively.

### 3.4 Data processing

The lidar data from field measurements and sampling in a turbulence box are processed according to Eqs. (8) to (13). For every line-of-sight measurement, this processing creates a new component of the  $\mathbf{u}_{\text{DBS}}$  and the  $\mathbf{u}_{\text{SQZ}}$  vectors. In Fig. 2, two numbers are assigned to most of the measurement locations. The first number increases with the time of measurement. The second number though is increasing with the location along the mean wind direction. Where only one number is shown, both numbers would be identical. In the process of reconstructing the squeezed wind vectors, it is essential to assign new timestamps that follow the order of the second numbers according to where the measurements were taken. In practice, we project all measurement locations onto a vector that is pointing into the mean wind direction and evaluate all line-of-sight velocities in the order they fall along this vector. For reconstructing the horizontal wind speed components with the method of squeezing, we combine every radial velocity with the closest radial velocity originating from a beam with the opposite azimuth angle taken behind the current measurement location. The timestamp of this reconstructed component then depends on the average position of both measurement locations on the mean wind vector. In order to create equidistant timestamps for the wind vectors  $\mathbf{u}_{\text{DBS}}$  and  $\mathbf{u}_{\text{SQZ}}$ , we generate a linearly spaced time axis with  $\Delta t = 0.96$  s and assign the wind components with the nearest neighbor method. This time step equals one quarter of the Windcube's cycle time and was chosen because the Windcube generates four wind vectors during one measurement cycle. Thus, we reach that all measurement data are used with no change in velocity variance, which would occur if interpolation would be applied. The data from the ultrasonic anemometers is uniformly spaced with a sample rate of 20 Hz and is resampled to a rate of 4 Hz with an anti-aliasing filter applied to reduce the amount of data.

We calculate double-sided power spectral densities as functions of the wave number  $k_1$

$$F_{ij}(k_1) = \frac{\langle \hat{u}_i \hat{u}_j^* \rangle}{N k_s}, \quad (25)$$

where  $\hat{\cdot}$  is the discrete Fourier transformation,  $*$  the complex conjugate,  $\langle \cdot \rangle$  the ensemble average of all 10 min intervals,  $N$  the number of measurements in one interval, and  $k_s = \frac{2\pi f_s}{U}$  is the sampling wave number, where  $f_s$  is the sampling frequency. For the cross-spectra ( $i \neq j$ ) we use the real part of  $F_{ij}$ . We then divide the  $k_1$  axis into 35 logarithmically spaced bins and average the spectral values in each bin. By doing so we even out the spectra in the low wave number region, avoid the high density of data points in the high wave number region, and align the sonic and lidar values for ease of com-

parison. The spectral values are eventually pre-multiplied with their wave numbers and plotted on a linear vertical axis, while the wave numbers are on a logarithmic horizontal axis. Displayed like this, any portion of the area under the spectra for a range of wave numbers is proportional to the variance of the signal in this wave number range (Stull, 1988).

## 4 Results

Complete results are presented in Figs. A1 to A3 in the Appendix. Here we will present the results of two measurement height levels  $h_2 = 60$  m and  $h_4 = 100$  m and two inflow wind directions  $\bar{\Theta} = 135^\circ$  and  $\bar{\Theta} = 90^\circ$ . These four cases alone show all relevant effects.

### 4.1 Simulation results

For the presentation of the results of our study, we will first discuss the simulated spectra without considering the experimental results. The lidar simulator opens up the possibility of analyzing the influence of the single wind velocity components on the spectra by switching them on or off in the turbulence box. This method helps in understanding what the final lidar spectra consist of. Figures 5 and 6 show these simulated spectra for the inflow wind directions  $\bar{\Theta} = 135^\circ$  and  $\bar{\Theta} = 90^\circ$ , respectively. The solid black lines are the target spectra that originate from sampling single points along the  $u$  direction of the turbulence box with a frequency of 4 Hz. These target spectra are not completely smooth due to the finite length of the generated turbulence files, but they resemble the model spectra well enough for the purpose of this study. The red and yellow lines show the shape of the lidar spectra with conventional DBS processing and squeezed SQZ processing, respectively. Solid lines are the resulting spectra when all three wind velocity components are switched on. Dashed lines show the spectra when only the  $u$  component is activated. Dashed-dotted lines represent spectra generated from the  $v$  component alone and dotted lines are for the  $w$  component alone. The method of showing the influence of the single components on the resulting lidar spectra cannot be used for cross-spectra. That is why we do not discuss the  $uw$  spectra here but only show the results together with the measurements in Sect. 4.2.

#### 4.1.1 Aligned inflow

To begin with, we take a look at the results from  $\bar{\Theta} = 135^\circ$  inflow, i.e., the wind field is moving parallel to the azimuth angle of LOS2 and LOS4 (see Fig. 4). We see in Fig. 5 that only the  $u$  and  $w$  components of the wind field are involved in creating the lidar spectra of the  $u$  component. With the method of DBS applied, the resulting lidar spectrum is correct only for very low wave numbers where  $k_1 < 4 \times 10^{-3} \text{ m}^{-1}$ . At increasing wave numbers the lidar underestimates the  $u$  fluctuations in the wind field more and more, until it hardly detects

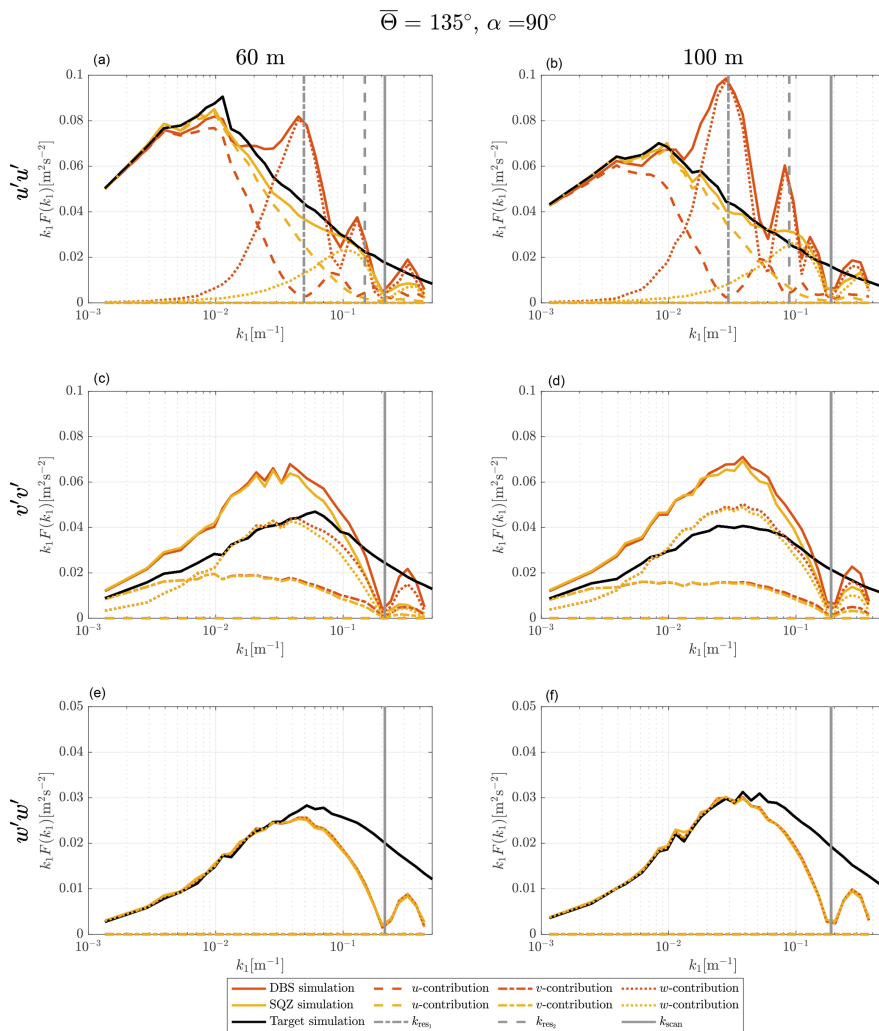


**Figure 5.** Turbulence velocity auto-spectra derived from sampling in a turbulence box for the case of aligned inflow with  $\bar{\Theta} = 135^\circ$  and  $\theta_0 = 45^\circ$ . The measurement heights are  $h_2 = 60$  m (a, c, e) and  $h_4 = 100$  m (b, d, f). Black, red and yellow lines are target, DBS-processed and SQZ-processed lidar spectra. Dashed, dashed–dotted and dotted lines show the influence of the  $u$ ,  $v$  and  $w$  component on the resulting spectra. The vertical solid line marks the wave number that corresponds to the lidar sampling frequency  $k_{scan}$  and the vertical dashed lines show the first and second resonance wave numbers  $k_{res}$ .

them at the first resonance wave number, which is marked with a dashed grey vertical line. In parallel, the  $w$  fluctuations increasingly contaminate the lidar measurements. Between the first and the second resonance wave number, the cross-contamination effect is lower again but it does not disappear completely. The reason is that two different longitudinal separation distances are involved in the wind vector reconstruction process, as described at the end of Sect. 2.4 ( $r_{\text{real}} \neq r_{\text{rep}}$ ). We also see that the energy content at the second resonance wave number is much lower than at the first resonance wave number, although the  $w$  fluctuations in the target spectrum in this wave number region are similarly strong. The reason is that the line-of-sight averaging is stronger for higher wave numbers and limits how much of the turbulence in the signal is being detected. The main difference between the two elevation levels 60 and 100 m is that the resonance peaks are higher and shifted to the left for measurements at 100 m. The reason is mostly that the longer longitudinal separation distance at higher elevations corresponds to lower resonance wave numbers according to Table 2 and less line-of-sight averaging comes into effect at these lower wave numbers. The slightly different parameters of the underlying spectral tensors also influence the results of course.

The wave number that corresponds to the sampling frequency of each lidar beam is marked with a solid grey vertical line. We cannot detect any turbulence at this wave number and the signal is strongly weakened close to it. This effect accounts for all test cases, wind velocity components and elevations. For even higher wave numbers the measurement signal recovers, until the lidar spectra stop at the wave number that corresponds to half of the wind vector reconstruction frequency.

Comparing the results from conventional DBS processing with the results for squeezed processed SQZ sampling shows the striking advantage of the new method for aligned wind cases. The method of squeezing leads to  $u$  spectra that are very similar to the target spectra. The region of the spectra that contains most of its kinetic energy is hardly contaminated. That is advantageous, for example, when the turbulence length scale is determined. The resonance point is shifted into the region where line-of-sight averaging and the attenuation due to the limited sampling frequency are strong. In the transition zone, the increasing averaging effect compensates for the increasing contamination. That means the very good agreement between target and lidar spectra is partly misleading and should not be interpreted as a perfect spectrum of pure  $u$  fluctuations.

The situation is very different for the  $v$  spectra. The conventional DBS processing hardly deviates from the squeezed processing. The small differences visible between the red and the yellow curves are due to the modified time scalar that is used in squeezed processing, according to the description in the first paragraph of Sect. 3.4. The lidar measured  $v$  spectra contain the correct amount of spectral energy from the  $v$  fluctuations only in the very low wave number region. As the

coherence of the  $v$  fluctuations declines at higher wave numbers, they become less detectable by the lidar. In addition, the lidar-derived  $v$  spectra are dominated by uncorrelated  $w$  fluctuations due to the lateral separation of the involved measurement volumes. The squeezed processing does not improve the situation because it cannot decrease lateral separations.

The simulated spectra of the vertical wind velocity fluctuations  $w$  are not contaminated by other wind speed components. The line-of-sight averaging becomes relevant for wave numbers of approximately  $k_1 > 3 \times 10^{-2} \text{ m}^{-1}$ . The strongest deviation from the target spectrum is found at the wave number  $k_{\text{scan}}$  that corresponds to the sampling frequency of the Windcube.

#### 4.1.2 Non-aligned inflow

The situation is more complex for cases in which the incoming wind is not aligned with two of the lidar beams. As an example, we take a closer look at Fig. 6, which shows the simulation results for wind from  $90^\circ$ . The inflow in this case is centered between two neighboring beams, which can be seen as the strongest case of non-aligned inflow. The behavior of all other inflow angles lies between this case and the previously discussed case of aligned wind from  $135^\circ$ .

Even at the lowest wave numbers the estimation of the  $u$  component is not correct. This is the most problematic characteristic of non-aligned inflow. From Table 3, we know that even without resonance, we cannot measure the  $u$  component of turbulence correctly if the lateral correlation is below unity. The spectra show that we indeed measure lower values of kinetic energy at low wave numbers by underestimating the  $u$  fluctuations in the turbulence box. The contribution of  $u$  fluctuations at increasing wave numbers becomes further reduced by the influence of the longitudinal resonance. Towards the resonance wave number contamination occurs. In addition to the contamination by the  $w$  component like in the aligned wind case, we are also faced with some contamination from  $v$  fluctuations. Due to the shorter longitudinal separations listed in Table 2 compared to the aligned wind case, the second resonance point is weakly pronounced, especially at 60 m elevation. The application of squeezed processing shifts the cross-contamination successfully into a region of lower energy content, but it cannot help derive better estimates of the turbulent energy in the low wave number region.

We now look at the predicted spectra of the transversal wind component  $v$ . In the very low wave number region, the actual  $v$  fluctuations are nearly correctly interpreted due to the assumption of high lateral coherence of the  $v$  component for very low values of  $k_1$ . Unfortunately, the spectra are contaminated by a significant parasitic contribution of  $w$  fluctuations for which the coherence in the spectral tensor model is lower. With increasing decorrelation of the three wind velocity components at increasing wave numbers, the contamination becomes rapidly stronger. At the first resonance point,

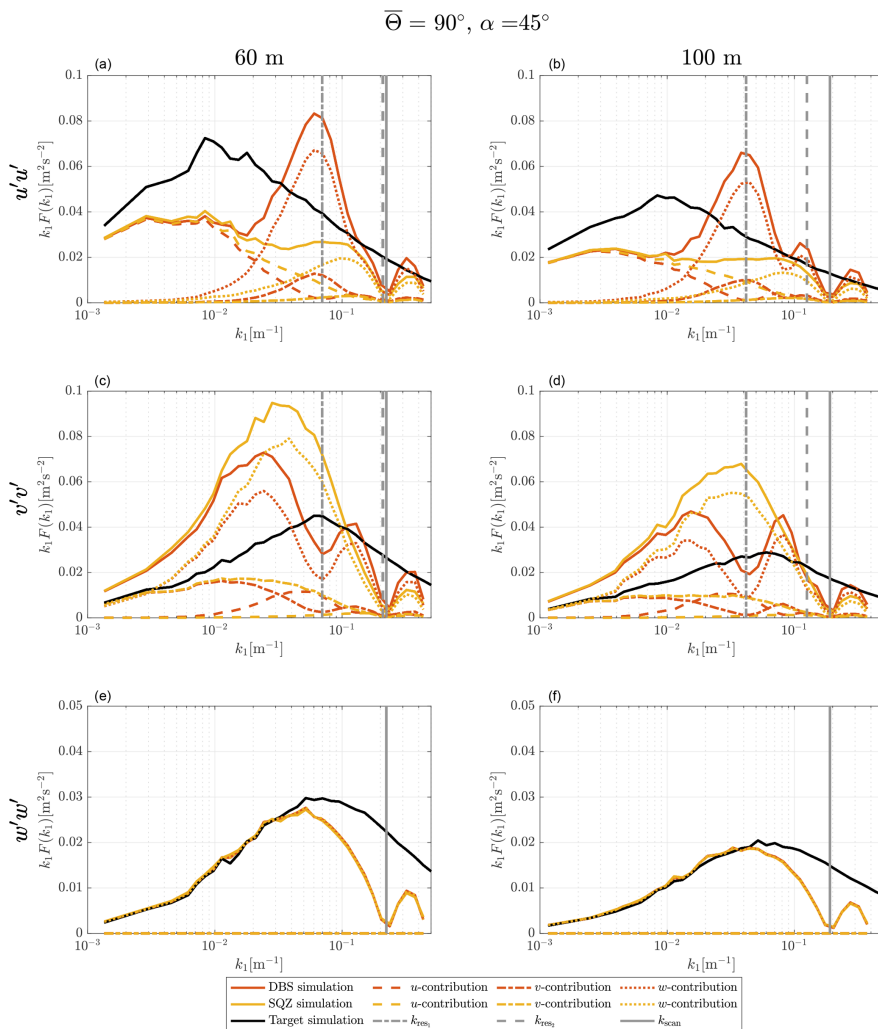


**Figure 6.** Turbulence velocity auto-spectra derived from sampling in a turbulence box for the case of non-aligned inflow with  $\bar{\Theta} = 90^\circ$  and  $\theta_0 = 45^\circ$ . The measurement heights are  $h_2 = 60$  m (a, c, e) and  $h_4 = 100$  m (b, d, f). Black, red and yellow lines are target, DBS-processed and SQZ-processed lidar spectra. Dashed, dashed–dotted and dotted lines show the influence of the  $u$ ,  $v$  and  $w$  component on the resulting spectra. The vertical solid line marks the wave number  $k_{scan}$  that corresponds to the lidar sampling frequency and the vertical dashed lines show the first and second resonance wave number  $k_{res}$ .

the cross-contamination of  $v$  by  $w$  is reduced but is to some degree replaced by cross-contamination from  $u$  fluctuations.

The decreasing influence of  $w$  and the additional cross-contamination by  $u$  on the DBS lidar-derived  $v$  spectra can be removed by applying the method of squeezing. Nonetheless, the cross-contamination effect due to lateral separation is so strong that the spectra are not significantly better than the conventionally acquired ones. The DBS lidar-derived velocity spectra for non-aligned wind are thus of limited use as they do not represent the actual wind conditions.

#### 4.2 Comparison with measurements

Figures 7 and 8 show the spectra for the same test cases as discussed in the subsection above. Now we compare the simulation results with measurement values. Markers in the plots are the spectra resulting from the field measurements, while solid lines, as before, correspond to the results from sampling in a turbulence box. First, we take a look at how well the theoretical target spectra displayed as solid black lines represent the spectra derived from the measurements of the sonic anemometers, which are depicted as black markers. The fitting of measurement data to the Mann spectral tensor model was successful. Overall, the model represents the measurements to a satisfactory degree. The measurement spectra show more scatter in the low wave number region, which is random variation caused by the limited amount of analyzed measurement data for the corresponding test cases. The agreement in the high wave number region where high statistical significance smooths out the derived spectra is in most cases very accurate. Discrepancies between sonic measurements and the spectral tensor in a certain wave number range have an effect on how well the theoretical spectra predict the lidar measurements. For example, the  $v$  target spectra at both heights and wind directions show lower values for medium wave numbers than the measured spectra. The  $uw$  target spectra, by contrast, show higher energy values in the low wave number region than what we actually measured. This has previously been reported by Mann (1994, Fig. 7a) and in Held and Mann (2019, their Fig. C1). The uniform shear plus blocking (US+B) model by Mann (1994) and the model by de Maré and Mann (2016) match observations of the  $uw$  spectrum better than the uniform shear (US) model of Mann (1994) that was used here, but they are much harder to implement and perform calculations with.

The method of sampling in a turbulence box is successful at predicting the shape of velocity spectra from a DBS scanning wind lidar. All characteristic features, i.e., cross-contamination, line-of-sight averaging, and limited sampling frequencies are found in the spectra of both measurements and simulations. But some deviations must be pointed out. In the test cases with non-aligned inflow from  $90^\circ$  and most other cases (Figs. A1–A3), the measured DBS-processed  $u$  spectra show increased values at wave numbers below the first interference wave number. That means that cross-

contamination is likely stronger than predicted by the model at wave numbers below the first resonance point. We see three possible explanations for this behavior. First, Table 3 shows that the cross-contamination of the  $u$  component by  $w$  fluctuations for non-aligned wind inflow in the resonance case is much stronger when the coherence is high. Eliassen and Obhrai (2016) show for an offshore location and a vertical separation of 40 m that the Mann model of turbulence underestimates the amount of coherence of the  $w$  component in a wide range of wave numbers (see also Mann, 1994, Fig. 8). Assuming that the same occurs with transversal separations, we found a potential explanation for why the simulations of the non-aligned cases underestimate the  $u$  variance at wave numbers below the resonance point. At higher wave numbers, the prediction is correct again because the correlation is close to zero, both in the spectral tensor and in reality. A second possible explanation lies in the limited validity of the frozen turbulence assumption. Real turbulence is not perfectly correlated over long separation distances, so uncorrelated  $w$  fluctuations might contaminate the  $u$  measurements. And third, we must also expect that turbulence is not always advected with the 10 min mean wind speed  $U$  but is sometimes slower or faster. This influences at which wave numbers the cross-contamination occurs.

The prediction of the  $u$  spectra resulting from squeezed processing is overall precise but has a slight tendency towards underestimating the spectral values in the medium wave number range. Based on the available data, it is not possible to determine the definite cause of the higher spectral values in the DBS- and SQZ-processed  $u$  measurements. However, we assume that the main reason is inaccurate representation of the co-coherences in the wind by the chosen spectral tensor. Sathe et al. (2011) also predict slightly lower total  $u$  variances and significantly lower  $v$  variances with their model than they get from measurements. However, our predictions of  $v$  variances are more accurate, and we therefore cannot draw conclusions from the comparison with their work.

The shape of the lidar-derived spectra of the transversal component  $v$  for both processing methods is fairly accurately predicted by the simulation. The few significant differences can in most cases be explained by the aforementioned discrepancies between the spectral tensor and the actual wind conditions. For example, at  $135^\circ$  at 60 m elevation, the lidar measured  $v$  fluctuations in the wave number range around  $k = 2 \times 10^{-2} \text{ m}^{-1}$  are considerably stronger than predicted because the actual wind fluctuations in the  $v$  and  $w$  directions are also higher than assumed by the selected spectral tensor.

The spectra of the vertical wind fluctuations  $w$  are in some cases very accurately predicted by the simulations, for example in the case with inflow from  $135^\circ$  at 60 m elevation. In other cases, we predict considerably higher values than what is measured, e.g., at  $135^\circ$  at 100 m elevation and vice versa, for example, at  $112.5^\circ$  at 80 m where we measure stronger

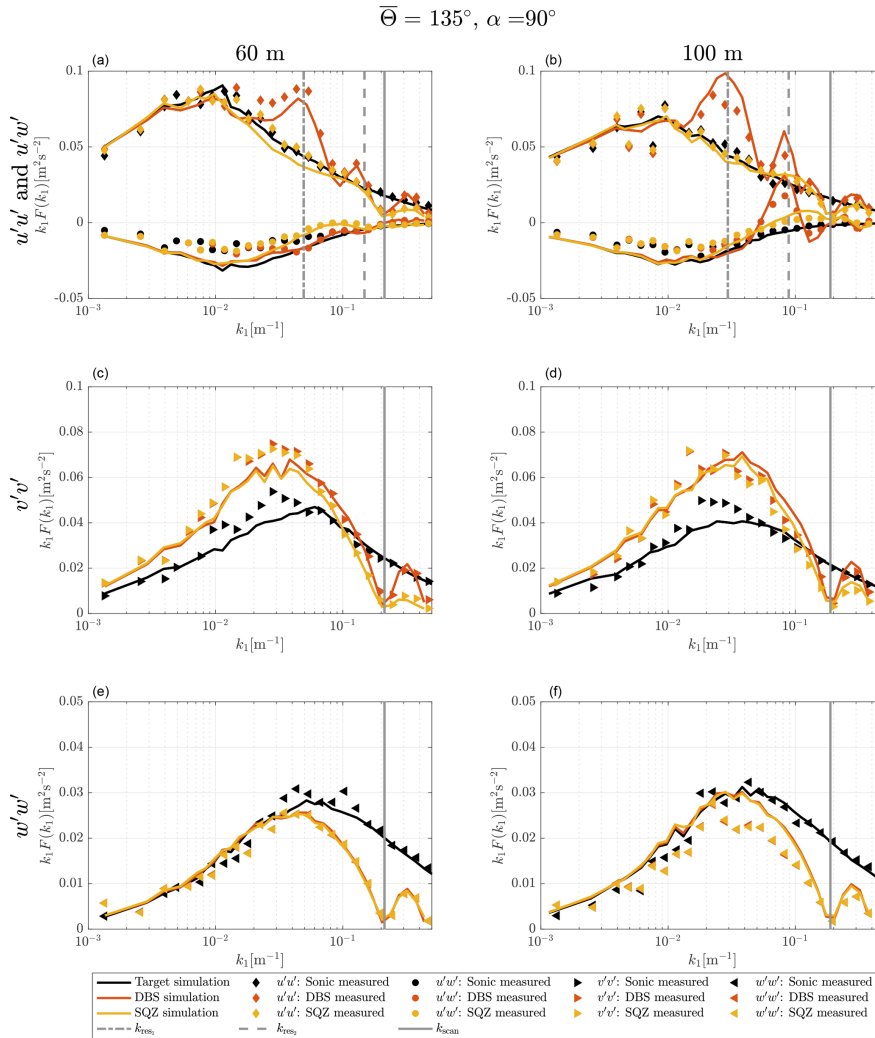


**Figure 7.** Turbulence velocity auto-spectra and  $uw$  cross-spectra derived from sampling in a turbulence box and measurements for the case of aligned inflow with  $\bar{\Theta} = 135^\circ$  and  $\theta_0 = 45^\circ$ . The measurement heights are  $h_2 = 60$  m (a, c, e) and  $h_4 = 100$  m (b, d, f). Black, red and yellow lines are target, DBS-processed and SQZ-processed lidar spectra from sampling in a turbulence box. Markers are spectra from field measurements. The vertical solid line marks the wave number that corresponds to the lidar sampling frequency and the vertical dashed lines show the first and second resonance wave number.

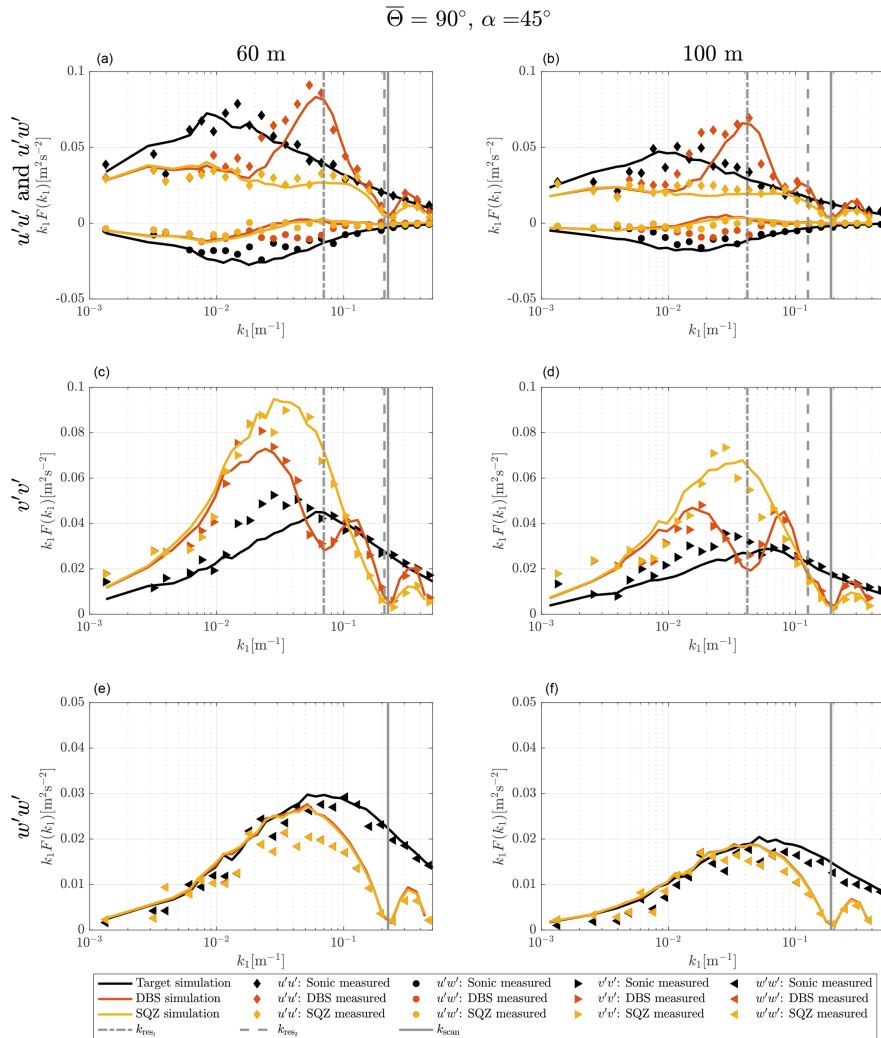


**Figure 8.** Turbulence velocity auto-spectra and  $uw$  cross-spectra derived from sampling in a turbulence box and measurements for the case of non-aligned inflow with  $\bar{\Theta} = 90^\circ$  and  $\theta_0 = 45^\circ$ . The measurement heights are  $h_2 = 60$  m (a, c, e) and  $h_4 = 100$  m (b, d, f). Black, red and yellow lines are target, DBS-processed and SQZ-processed lidar spectra in a turbulence box. Markers are spectra from field measurements. The vertical solid line marks the wavenumber  $k_{scan}$  that corresponds to the lidar sampling frequency and the vertical dashed lines show the first and second resonance wavenumber  $k_{res}$ .

low-frequency turbulence with the lidar than with the sonic anemometer (Fig. A2). The reason for this behavior is unknown.

The  $uw$  cross-spectra are predicted well for both data processing methods for aligned inflow. For inflow conditions in which the wind direction is not aligned with two of the beams, the prediction of the DBS-processed data is off. We assume that the reason for this behavior is the same as what caused the differences between the DBS-processed  $u$  measurements and simulations.

## 5 Conclusions

We have shown that with the help of sampling in a turbulence box, it is possible to predict turbulence velocity spectra from DBS wind lidar for all wind directions. We have analyzed these spectra theoretically and in comparison with field measurements.

The shape of the spectra from a Windcube V2 DBS lidar is influenced by the effects of line-of-sight averaging, its limited sampling frequency, and strongly by cross-contamination. We have shown that the influence of cross-contamination on the spectra of the horizontal components of turbulence is dependent on the alignment of the lidar beams to the incoming wind direction. Only the measurement of vertical wind fluctuations is independent of wind direction due to the availability of a beam pointing vertically upwards. The auto-spectrum of each horizontal wind speed component is distorted by the influence of the other two wind components. The  $uw$  cross-spectrum also suffers from cross-contamination.

The method of squeezing applied in the wind vector reconstruction process minimizes the cross-contamination effect on the measured  $u$  component of turbulence when the wind blows parallel to one of the beam's azimuth angles. Only in this case are the lidar-derived spectra reasonably close to the spectra of the  $u$  component of the wind, thus turbulence parameters like turbulence length scale and the dissipation factor might be estimated from it.

In all other cases, the estimations of the horizontal component spectra of turbulence are very erroneous due to the parasitic influence of the components of turbulence on one another, and one should not trust them. In no case should turbulence velocity spectra from DBS wind lidar be fitted to a turbulence model.

Multi-lidar arrangements use three separate lidar devices, whose beams intersect at one point in space and minimize separation distances (Mann et al., 2009). A different possibility to avoid cross-contamination would be to deflect the inclined beams of one single DBS wind lidar first into a horizontal direction away from the device and second towards a point above the device where they intersect. Such a setup requires precise alignment of the deflected beams but would not require horizontal homogeneity of the wind field and could measure turbulence more accurately.

### Appendix A: Nomenclature

$c$	Speed of light ( $\text{m s}^{-1}$ )
$D$	Diameter of measurement cone (m)
$d_f$	Distance from lidar to center of range gate (m)
$F$	Power spectral density ( $\text{m}^2 \text{s}^{-1}$ )
$f_s$	Sampling frequency ( $\text{s}^{-1}$ )
$h$	Measurement height (m)
$i, j$	Beam numbers 1 to 5; Wind vector components 1 to 3
$k$	Wave number ( $\text{m}^{-1}$ )
$k_s$	Sampling wave number ( $\text{m}^{-1}$ )
$k_{\text{res}}$	Resonance wave number ( $\text{m}^{-1}$ )
$k_{\text{scan}}$	Wave number of LOS sampling frequency 0.26 Hz ( $\text{m}^{-1}$ )
$l_p$	Half length of range gate (m)
$N$	Number of measurements per 10 min interval
$n$	Integer index
$\mathbf{n}_i$	Unit vector along beam $i$
$r_{\text{lat},ij}$	Nominal separation distance in lateral direction w.r.t. $\bar{\Theta}$ for beam combination $ij$ (m)
$r_{\text{long},ij}$	Nominal separation distance in longitudinal direction w.r.t. $\bar{\Theta}$ for beam combination $ij$ (m)
$r_{\text{rep},u}$	Representative separation distance in longitudinal direction w.r.t. $\bar{\Theta}$ for the reconstruction of $u$ (m)
$r_{\text{rep},v}$	Representative separation distance in longitudinal direction w.r.t. $\bar{\Theta}$ for the reconstruction of $v$ (m)
$r_{\text{real},ij}$	Real separation distance in longitudinal direction w.r.t. $\bar{\Theta}$ for beam combination $ij$ considering $t$ (m)
$r_{\text{real,SQZ},ij}$	Actual separation distance in longitudinal direction w.r.t. $\bar{\Theta}$ for beam combination $ij$ considering $t$ , squeezed processing (m)
$s$	Distance from center of range gate (m)
$t$	Beam timing (s)
$\mathbf{u}, \mathbf{U}, \mathbf{u}'$	Total, mean and fluctuating part of wind velocity vector ( $\text{m s}^{-1}$ )
$u, v, w$	Longitudinal, transversal and vertical wind velocity component w.r.t. $\bar{\Theta}$ ( $\text{m s}^{-1}$ )
$V_{\text{hor}}, \bar{V}_{\text{hor}}$	Horizontal wind velocity, 10 min mean ( $\text{m s}^{-1}$ )
$v_{r_i}$	Radial wind velocity in beam $i$ direction ( $\text{m s}^{-1}$ )
$\tilde{v}_{r_i}$	Line-of-sight velocity of beam $i$ ( $\text{m s}^{-1}$ )
$\mathbf{x}$	Wind velocity vector in Windcube coordinates ( $\text{m s}^{-1}$ )
$x, y, z$	Wind velocity component in LOS1–LOS3, LOS2–LOS4 and LOS5 directions ( $\text{m s}^{-1}$ )
$\alpha$	Relative inflow angle $\bar{\Theta} - \theta_0$ ( $^\circ$ )
$\theta_0$	Heading of LOS1 (offset from north) ( $^\circ$ )
$\theta$	Beam azimuth angle ( $^\circ$ )
$\Theta, \bar{\Theta}$	Wind direction, 10 min mean ( $^\circ$ )
$\sigma^2$	Velocity variance ( $\text{m}^2 \text{s}^{-2}$ )
$\phi$	Zenith angle (half cone opening angle) ( $^\circ$ )
$\varphi$	Triangular weighting function

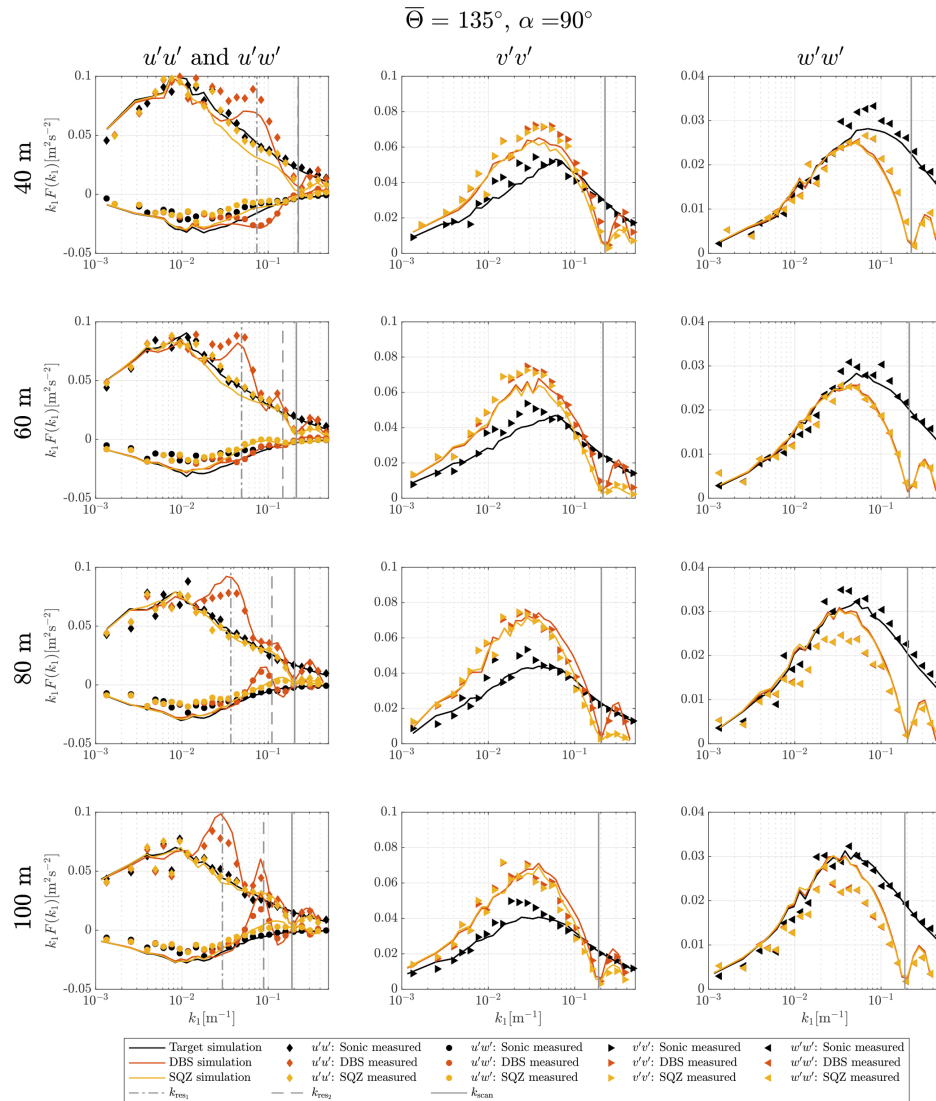


**Figure A1.** Turbulence velocity auto-spectra and  $uw$  cross-spectra derived from sampling in a turbulence box and measurements for the case of aligned inflow with  $\bar{\Theta}_1 = 135^\circ$  and  $\theta_0 = 45^\circ$ .

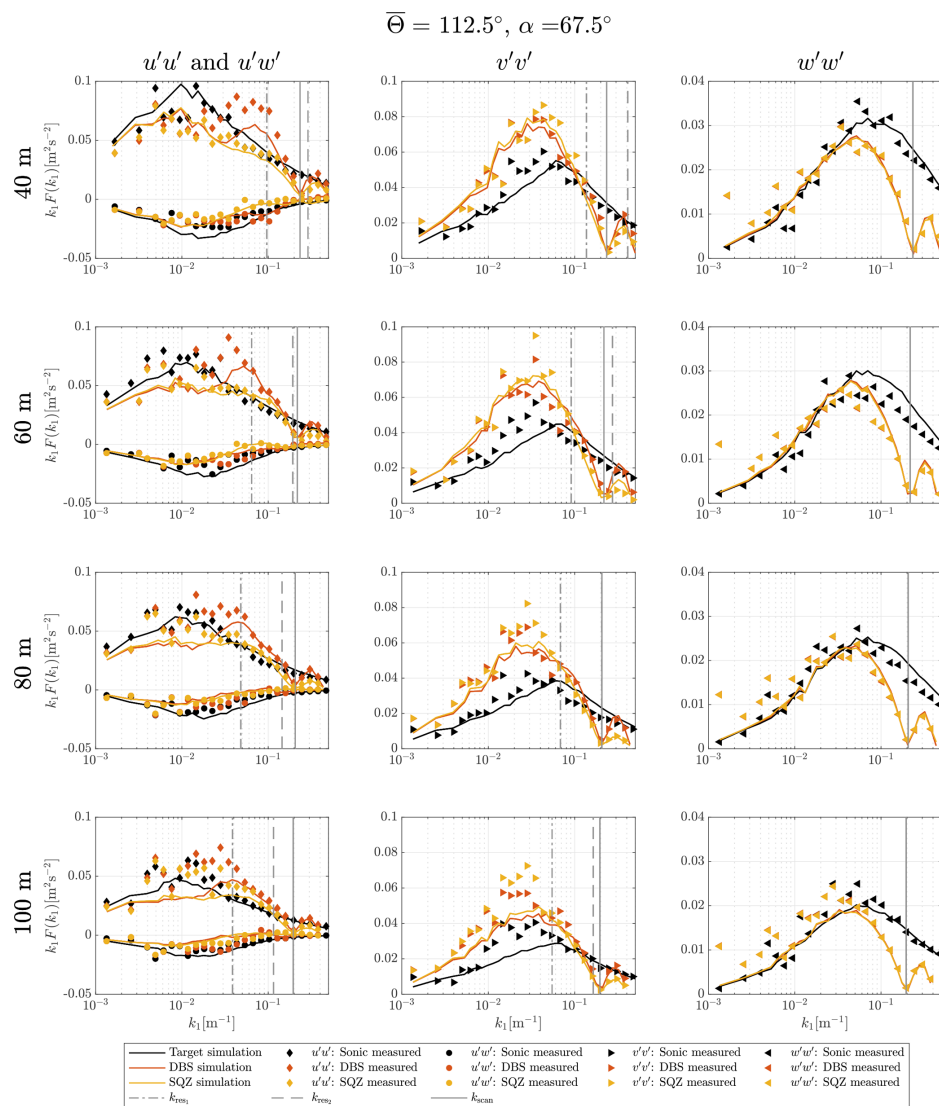


**Figure A2.** Turbulence velocity auto-spectra and  $uw$  cross-spectra derived from sampling in a turbulence box and measurements for the case of non-aligned inflow with  $\bar{\Theta}_2 = 112.5^\circ$  and  $\theta_0 = 45^\circ$ .

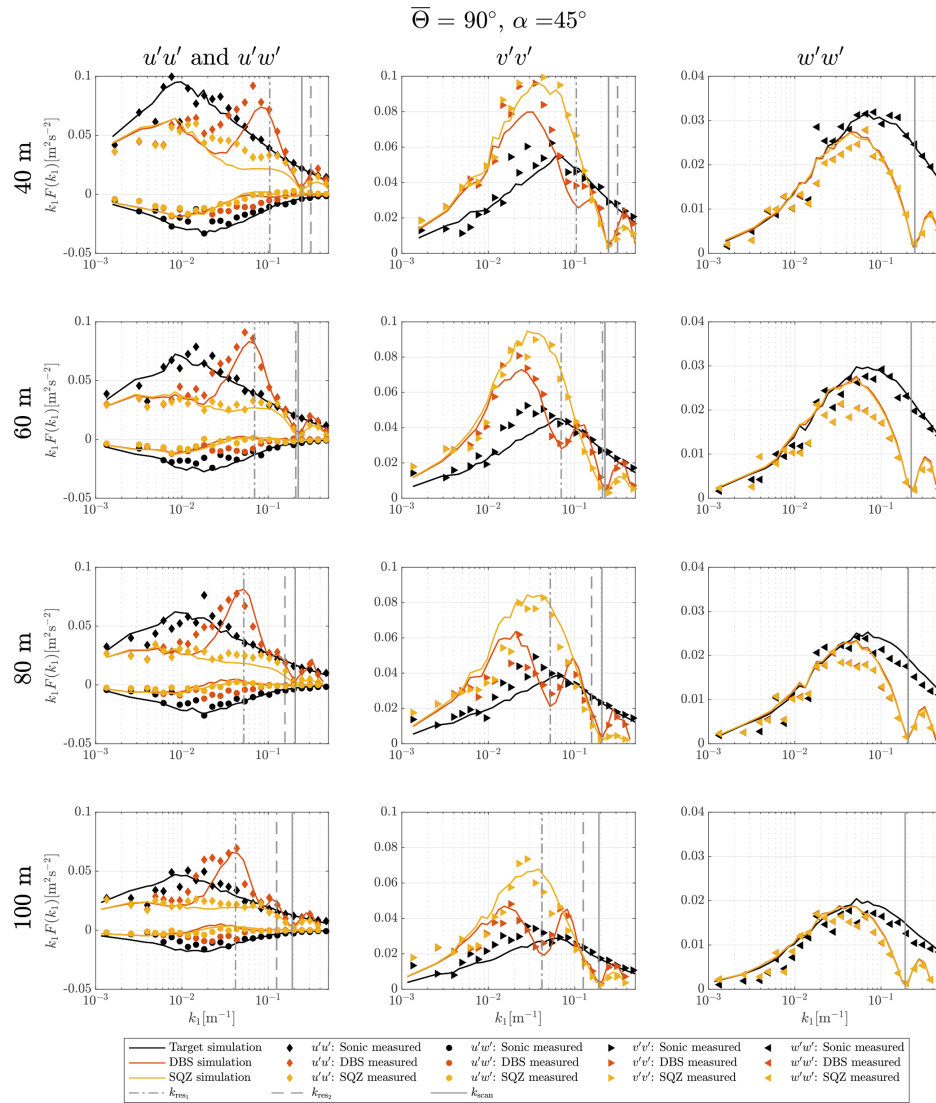


**Figure A3.** Turbulence velocity auto-spectra and  $uw$  cross-spectra derived from sampling in a turbulence box and measurements for the case of non-aligned inflow with  $\bar{\Theta}_3 = 90^\circ$  and  $\theta_0 = 45^\circ$ .

**Code and data availability.** All data and code used for this study can be downloaded from <https://doi.org/10.5281/zenodo.3514326> (Kelberlau and Mann, 2019b).

**Author contributions.** FK performed the data processing, analyzed the results and wrote the paper. JM supplied the measurement data and gave input and advice throughout the process.

**Competing interests.** The authors declare that they have no conflict of interest.

**Special issue statement.** This article is part of the special issue “Wind Energy Science Conference 2019”. It is a result of the Wind Energy Science Conference 2019, Cork, Ireland, 17–20 June 2019.

**Acknowledgements.** We thank Kam Sripada and Tania Bracchi for thoroughly proofreading the manuscript.

**Financial support.** This research has been supported by Energy and Sensor Systems (ENERSENSE) at the Norwegian University of Science and Technology (grant no. 68024013).

**Review statement.** This paper was edited by Julie Lundquist and reviewed by Stefan Emeis and two anonymous referees.

## References

- Bodini, N., Lundquist, J. K., and Kirincich, A.: U.S. East Coast Lidar Measurements Show Offshore Wind Turbines Will Encounter Very Low Atmospheric Turbulence, *Geophys. Res. Lett.*, 46, 5582–5591, <https://doi.org/10.1029/2019GL082636>, 2019.
- Browning, K. A. and Wexler, R.: The Determination of Kinematic Properties of a Wind Field Using Doppler Radar, *J. Appl. Meteorol. Clim.*, 7, 105–113, [https://doi.org/10.1175/1520-0450\(1968\)007<0105:TDOKPO>2.0.CO;2](https://doi.org/10.1175/1520-0450(1968)007<0105:TDOKPO>2.0.CO;2), 1968.
- Canadillas, B., Bégué, A., and Neumann, T.: Comparison of turbulence spectra derived from LiDAR and sonic measurements at the offshore platform FINO1, 10th German Wind Energy Conference (DEWEK 2010), 17–18 November 2010, Bremen, Germany, 2010.
- de Maré, M. and Mann, J.: On the Space-Time Structure of Sheared Turbulence, *Bound.-Lay. Meteorol.*, 160, 453–474, <https://doi.org/10.1007/s10546-016-0143-z>, 2016.
- Eberhard, W. L., Cupp, R. E., and Healy, K. R.: Doppler Lidar Measurement of Profiles of Turbulence and Momentum Flux, *J. Atmos. Ocean. Tech.*, 6, 809–819, [https://doi.org/10.1175/1520-0426\(1989\)006<0809:DLMOPQ>2.0.CO;2](https://doi.org/10.1175/1520-0426(1989)006<0809:DLMOPQ>2.0.CO;2), 1989.
- Eliassen, L. and Obhrai, C.: Coherence of turbulent wind under neutral wind conditions at FINO1, *Energy. Proced.*, 94, 388–398, <https://doi.org/10.1016/j.egypro.2016.09.199>, 2016.
- Emeis, S., Harris, M., and Banta, R. M.: Boundary-layer anemometry by optical remote sensing for wind energy applications, *Meteorol. Z.*, 16, 337–347, <https://doi.org/10.1127/0941-2948/2007/0225>, 2007.
- Frehlich, R., Hannon, S. M., and Henderson, S. W.: Coherent Doppler Lidar Measurements of Wind Field Statistics, *Bound.-Lay. Meteorol.*, 86, 233–256, <https://doi.org/10.1023/A:1000676021745>, 1998.
- Gasch, P., Wieser, A., Lundquist, J. K., and Kalthoff, N.: An LES-based airborne Doppler lidar simulator and its application to wind profiling in inhomogeneous flow conditions, *Atmos. Meas. Tech.*, 13, 1609–1631, <https://doi.org/10.5194/amt-13-1609-2020>, 2020.
- Gottschall, J., Courtney, M. S., Wagner, R., Jørgensen, H. E., and Antoniou, I.: Lidar profilers in the context of wind energy—a verification procedure for traceable measurements, *Wind Energy*, 15, 147–159, <https://doi.org/10.1002/we.518>, 2012.
- Held, D. P. and Mann, J.: Lidar estimation of rotor-effective wind speed – an experimental comparison, *Wind Eng. Sci.*, 4, 421–438, <https://doi.org/10.5194/wes-4-421-2019>, 2019.
- IEC: 61400-1 Wind energy generation systems – Part 1: Design requirements, 4.0 edn., International Electrotechnical Commission, Geneva, Switzerland, 2019.
- Kelberlau, F. and Mann, J.: Better turbulence spectra from velocity–azimuth display scanning wind lidar, *Atmos. Meas. Tech.*, 12, 1871–1888, <https://doi.org/10.5194/amt-12-1871-2019>, 2019a.
- Kelberlau, F. and Mann, J.: Cross-contamination effect on turbulence spectra from Doppler beam swinging wind lidar (data and code) [Data set], *Wind energy science*, Zenodo, <https://doi.org/10.5281/zenodo.3514326>, 2019b.
- Kim, D., Kim, T., Oh, G., Huh, J., and Ko, K.: A comparison of ground-based LiDAR and met mast wind measurements for wind resource assessment over various terrain conditions, *J. Wind Eng. Ind. Aerodyn.*, 158, 109–121, <https://doi.org/10.1016/j.jweia.2016.09.011>, 2016.
- Krishnamurthy, R., Calhoun, R., Billings, B., and Doyle, J.: Wind turbulence estimates in a valley by coherent Doppler lidar, *Meteorol. Appl.*, 18, 361–371, <https://doi.org/10.1002/met.263>, 2011.
- Kumer, V.-M., Reuder, J., Dorninger, M., Zauner, R., and Grubišić, V.: Turbulent kinetic energy estimates from profiling wind LiDAR measurements and their potential for wind energy applications, *Renew. Energ.*, 99, 898–910, <https://doi.org/10.1016/j.renene.2016.07.014>, 2016.
- Lindelöw, P.: Fiber Based Coherent Lidars for Remote Wind Sensing, PhD thesis, Danish Technical University, Kongens Lyngby, Denmark, 2008.
- Mann, J.: The spatial structure of neutral atmospheric surface-layer turbulence, *J. Fluid Mech.*, 273, 141–168, <https://doi.org/10.1017/S0022112094001886>, 1994.
- Mann, J.: Wind Field Simulation, *Probab. Eng. Mech.*, 13, 269–282, [https://doi.org/10.1016/S0266-8920\(97\)00036-2](https://doi.org/10.1016/S0266-8920(97)00036-2), 1998.
- Mann, J., Cariou, J.-P., Courtney, M. S., Parmentier, R., Mikkelsen, T., Wagner, R., Lindelöw, P., Sjöholm, M., and Enevoldsen, K.: Comparison of 3D turbulence measurements using three staring wind lidars and a sonic anemometer, *Meteorol. Z.*, 18, 135–140, 2009.
- Newman, J. F., Klein, P. M., Wharton, S., Sathe, A., Bonin, T. A., Chilson, P. B., and Muschinski, A.: Evaluation of three lidar scanning strategies for turbulence measurements, *Atmos. Meas.*

- Tech., 9, 1993–2013, <https://doi.org/10.5194/amt-9-1993-2016>, 2016.
- Peña, A., Floors, R., Sathe, A., Gryning, S.-E., Wagner, R., Courtney, M. S., Larsen, X. G., Hahmann, A. N., and Hasager, C. B.: Ten Years of Boundary-Layer and Wind-Power Meteorology at Høvsøre, Denmark, *Bound.-Lay. Meteorol.*, 158, 1–26, <https://doi.org/10.1007/s10546-015-0079-8>, 2016.
- Sathe, A. and Mann, J.: Measurement of turbulence spectra using scanning pulsed wind lidars, *J. Geophys. Res.-Atmos.*, 117, D01201, <https://doi.org/10.1029/2011JD016786>, 2012.
- Sathe, A. and Mann, J.: A review of turbulence measurements using ground-based wind lidars, *Atmos. Meas. Tech.*, 6, 3147–3167, <https://doi.org/10.5194/amt-6-3147-2013>, 2013.
- Sathe, A., Mann, J., Gottschall, J., and Courtney, M. S.: Can wind lidars measure turbulence?, *J. Atmos. Ocean. Tech.*, 28, 853–868, <https://doi.org/10.1175/JTECH-D-10-05004.1>, 2011.
- Smalikho, I.: Techniques of Wind Vector Estimation from Data Measured with a Scanning Coherent Doppler Lidar, *J. Atmos. Ocean. Tech.*, 20, 276–291, [https://doi.org/10.1175/1520-0426\(2003\)020<0276:TOWVEF>2.0.CO;2](https://doi.org/10.1175/1520-0426(2003)020<0276:TOWVEF>2.0.CO;2), 2003.
- Smith, D. A., Harris, M., Coffey, A. S., Mikkelsen, T., Jørgensen, H. E., Mann, J., and Danielian, R.: Wind lidar evaluation at the Danish wind test site Høvsøre, *Wind Energy*, 9, 87–93, <https://doi.org/10.1002/we.193>, 2006.
- Stawiarski, C., Träumner, K., Kottmeier, C., Knigge, C., and Raasch, S.: Assessment of Surface-Layer Coherent Structure Detection in Dual-Doppler Lidar Data Based on Virtual Measurements, *Bound.-Lay. Meteorol.*, 156, 371–393, <https://doi.org/10.1007/s10546-015-0039-3>, 2015.
- Stull, R. B.: An Introduction to Boundary Layer Meteorology, chap.: Some Mathematical & Conceptual Tools: Part 2. Time Series, 13, 295–345, Kluwer Academic Publishers, Dordrecht, the Netherlands, [https://doi.org/10.1007/978-94-009-3027-8\\_8](https://doi.org/10.1007/978-94-009-3027-8_8), 1988.
- Taylor, G. I.: The Spectrum of Turbulence, *P. Roy. Soc. A-Math. Phys.*, 164, 476–490, <https://doi.org/10.1098/rspa.1938.0032>, 1938.



## **Chapter 7**

### **Article 3:**

# **Taking the Motion out of Floating Lidar: Turbulence Intensity Estimates with a Continuous-Wave Wind Lidar**





Article

# Taking the Motion out of Floating Lidar: Turbulence Intensity Estimates with a Continuous-Wave Wind Lidar

Felix Kelberlau <sup>1,\*</sup>, Vegar Neshaug <sup>2</sup>, Lasse Lønseth <sup>2,\*</sup>, Tania Bracchi <sup>1</sup> and Jakob Mann <sup>3</sup>

<sup>1</sup> NTNU, Department of Energy and Process Engineering, Norwegian University of Science and Technology, 7491 Trondheim, Norway; tania.bracchi@ntnu.no

<sup>2</sup> Fugro Norway AS, Havnegata 9, 7462 Trondheim, Norway; v.neshaug@fugro.com

<sup>3</sup> DTU Wind Energy, Technical University of Denmark, 4000 Roskilde, Denmark; jmsq@dtu.dk

\* Correspondence: felix.kelberlau@ntnu.no (F.K.); l.lonseth@fugro.com (L.L.)

Received: 11 February 2020; Accepted: 6 March 2020; Published: 10 March 2020

**Abstract:** Due to their motion, floating wind lidars overestimate turbulence intensity (*TI*) compared to fixed lidars. We show how the motion of a floating continuous-wave velocity–azimuth display (VAD) scanning lidar in all six degrees of freedom influences the *TI* estimates, and present a method to compensate for it. The approach presented here uses line-of-sight measurements of the lidar and high-frequency motion data. The compensation algorithm takes into account the changing radial velocity, scanning geometry, and measurement height of the lidar beam as the lidar moves and rotates. It also incorporates a strategy to synchronize lidar and motion data. We test this method with measurement data from a ZX300 mounted on a Fugro SEAWATCH Wind LiDAR Buoy deployed offshore and compare its *TI* estimates with and without motion compensation to measurements taken by a fixed land-based reference wind lidar of the same type located nearby. Results show that the *TI* values of the floating lidar without motion compensation are around 50% higher than the reference values. The motion compensation algorithm detects the amount of motion-induced *TI* and removes it from the measurement data successfully. Motion compensation leads to good agreement between the *TI* estimates of floating and fixed lidar under all investigated wind conditions and sea states.

**Keywords:** floating lidar; turbulence intensity; line-of-sight; motion compensation; wind vector reconstruction

## 1. Introduction

Wind velocity measurements are important for the wind energy industry to validate assumptions about wind conditions at a wind farm site. Lidar measurements that sense the wind remotely from the ground can be used instead of in-situ anemometry on meteorological masts. The installation of such masts offshore is even more expensive than onshore. As wind projects move further offshore into deeper water areas, masts are no longer a feasible alternative. Floating lidars are more cost-effective than masts [1] and potentially the only viable option. Validation campaigns testing floating lidar systems against data from meteorological masts have shown that estimations of the mean wind velocity by floating lidar are robust and reliable [2,3]. Even without any form of motion compensation, the errors in mean wind speed are small [4–6]. For estimates of the wind direction, a simple yaw compensation at the ten-minute level is sufficient [2].

By contrast, estimates of turbulence intensity (*TI*) require advanced motion compensation because floating lidar systems show stronger wind velocity fluctuations than non-moving lidars [5]. The magnitude of this motion-induced error depends on the amplitude and period of the motion which

result from the floating platform type used and the prevailing sea state [7]. Trusting in such erroneously high  $TI$  values could, for example, result in extra costs caused by choosing oversized wind turbines. Different methods have therefore been proposed to mitigate or remove the motion-induced error in  $TI$  estimates from floating lidar systems.

As suggested in Tiana-Alsina et al. [8], the lidar device could be mounted on a cardanic frame that compensates for most of the rotational motion. Such a hardware solution increases the costs for a floating lidar system and cannot compensate for errors that are caused by significant translational motion of the platform; for example, those due to heave caused by waves. Gutiérrez et al. [9] proposed simple window averaging of the time series of horizontal wind speed estimates, which acts as a low-pass filter. The basic idea is that the motion-induced turbulence has the same frequency as the buoy motion and can therefore be filtered out. The main drawback of this method is that the sampling frequency of the lidar-measured time series must be higher than the frequency of the motion of the platform. For many setups with currently available hardware, this is not the case. Gutiérrez-Antuñano et al. [7] presented a simulation tool for more advanced motion compensation. Based on amplitude and period of the buoy rotation, and mean wind conditions, the simulator estimates the motion-induced error in the turbulence measurements. Corrected measurement data show overall better results compared to reference lidar measurements, but the success of the method varies depending on sea state. Yamaguchi and Ishihara [10] suggested a motion compensation algorithm based on numerical simulations that shows promising results. However, the method requires simultaneously measured line-of-sight velocities from different measurement heights, which are available only from pulsed wind lidars. Gottschall et al. [5] described a motion compensation algorithm to correct for the rotation of a floating pulsed wind lidar in roll, pitch, and yaw degrees of freedom and show promising results. In Gottschall et al. [11], they describe an algorithm that corrects the lidar derived line-of-sight velocities for the influence of motion in all six degrees of freedom but do not disclose any details of the algorithm and do not describe the motion-corrected results.

The aim of the work presented here was to develop and validate a method that corrects  $TI$  estimates from a floating continuous-wave wind lidar aboard a buoy being deployed offshore. For our approach, we measure the motion of the buoy in all six degrees of freedom and record the line-of-sight velocity spectra of the lidar. We then compensate for the motion of the lidar before we reconstruct the wind vectors under consideration of the rotation of the buoy. A method to synchronize the lidar and motion data is an integral feature of our approach. We applied this motion compensation algorithm to measurement data from a SEAWATCH Wind LiDAR Buoy by Fugro carrying a ZX300M by ZX Lidar (Ledbury, United Kingdom) and a MRU 6000 motion reference unit (MRU) by Norwegian Subsea (Oslo, Norway) and analyzed the results in comparison to data from a nearby land-based fixed reference lidar of the same type. The scope of this work is the question of whether a motion-compensated floating lidar system can measure  $TI$  as reliably as a fixed reference lidar of the same type.  $TI$  is the most widely-used parameter of turbulence. We will therefore limit our analysis to it after briefly presenting the horizontal mean wind speeds. This article does not discuss the effects that lead to deviations between lidar-derived turbulence estimates and in-situ anemometric values [12–14].

In Section 2, we describe the theory behind  $TI$ , the coordinate systems we use, and how the motion of a velocity–azimuth display (VAD) scanning wind lidar influences its measurements. Section 3 describes our method to compensate for the lidar motion. This includes an explanation of how to overcome the challenge of synchronizing the timing of lidar and motion data and how we emulated the internal data processing of the lidar, which is typically not accessible. We also describe the measurement setup and describe the wind and sea conditions during the experimental validation. The results of the measurements are shown and discussed in Section 4 and we conclude the findings of this study in Section 5. Readers who do not seek to understand how the motion compensation algorithm works but are interested in its validation can continue reading from Section 3.5.

## 2. Theory

### 2.1. Turbulence Intensity

Wind velocities at one point in space can be described by the vector

$$\vec{u} = \begin{bmatrix} u_1 \\ u_2 \\ u_3 \end{bmatrix} \quad (1)$$

where  $u_1$  is the longitudinal component of the horizontal wind velocity in mean wind direction clockwise from north  $\bar{\Theta}$ ,  $u_2$  is the transversal component of the horizontal wind velocity, and  $u_3$  is the vertical wind velocity component in a right-handed coordinate system. The mean wind conditions  $\bar{U}$  are determined by averaging the values of  $\vec{u}$  for a time interval. The ZX300 wind lidar stores the time series of reconstructed wind vectors in the form of, first, the horizontal wind speed  $u_{hor}$ ; second, the wind direction  $\Theta$ ; and third, the vertical wind speed  $u_{ver}$ . In our analysis we look at ten-minute intervals of wind data. The average wind speed  $U_{hor}$  is the arithmetic mean of all  $N$  estimates of  $u_{hor}$  within each interval according to

$$U_{hor} = \frac{1}{N} \sum_{i=1}^N u_{hor_i} \quad (2)$$

As a measure for the amount of variation of  $u_{hor}$  around  $U_{hor}$ , we introduce the standard deviation of the horizontal wind speed

$$\sigma_{u_{hor}} = \sqrt{\frac{1}{N-1} \sum_{i=1}^N (u_{hor_i} - U_{hor})^2} \quad (3)$$

which is an indicator of turbulence. Since turbulence is partly driven by frictional forces caused by the mean wind speed, we normalize the wind speed variations by the mean wind speed  $U_{hor}$ , which leads us to the definition of turbulence intensity:

$$TI = \frac{\sigma_{u_{hor}}}{U_{hor}} \quad (4)$$

$TI$  increases with surface roughness and decreases with height above ground [15]. Thermal buoyancy forces are the second driver of turbulence. Their influence leads to high  $TI$  values at low wind speeds. Unstable atmospheric stratification is also associated with high  $TI$  values, while stable conditions decrease it.

### 2.2. Coordinate System and Vector Rotations

The SEAWATCH Wind LiDAR Buoy is depicted in Figure 1. The buoy is anchored to the seabed with a catenary mooring line and floats on the water's surface. In its initial position without the influence of any wave, wind or current loads, its  $x$ ,  $y$ , and  $z$ -axes are respectively pointing north, east, and vertically down. In the presence of external forces, the buoy can move in all six degrees of freedom. Translational motion in  $x$ ,  $y$ , and  $z$ -directions is called surge, sway, and heave, respectively. The horizontal distances are limited by the mooring system, and the vertical heave position follows waves and the tide. Rotations around these three axes are called roll, pitch, and yaw, respectively. The rotation in roll and pitch can be combined and their Pythagorean sum is then called tilt. The motion in roll, pitch, and heave is mostly determined by the sea state, as the buoy follows the wave motion with its characteristic periodicity. Surge, sway, and yaw motions typically occur with much longer periods and are mostly caused by wind and current forces that balance out the restoring forces from the mooring.

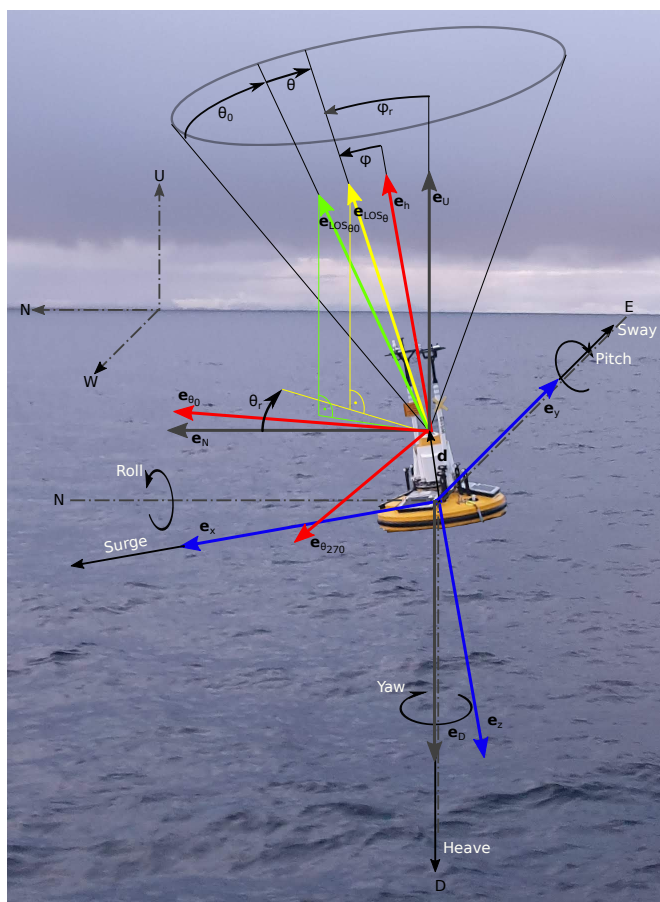


**Figure 1.** Visualization of the SEAWATCH Wind LiDAR Buoy in pitched orientation. Shown are the global right-handed North-West-Up (NWU) coordinate system and the north-east-down (NED) reference frame of the motion reference unit (MRU) (gray); unit vectors  $\vec{e}_x$ ,  $\vec{e}_y$ , and  $\vec{e}_z$  along the rotated body coordinate axes of the (MRU) (blue); unit vectors  $\vec{e}_{\theta_0}$ ,  $\vec{e}_{\theta_{270}}$ , and  $\vec{e}_h$  defining the lidar frame of reference (red); the line-of-sight (LOS) unit vector  $\vec{e}_{LOS_{\theta_0}}$  for the azimuth offset angle  $\theta_0$  (green); and the LOS unit vector  $\vec{e}_{LOS_{\theta}}$  for an arbitrary  $\theta$  (yellow). Additionally, the separation vector  $\vec{d}$  between the MRU and lidar prism is shown, as are the nominal and real azimuth ( $\theta$  and  $\theta_r$ ) and zenith angles ( $\phi$  and  $\phi_r$ ). (Sketch not to scale).

For our computations, we use a global right-handed Cartesian north-west-up (NWU) coordinate system. The MRU we use in this study is set up to calculate and record translational and rotational position and velocity data in all six degrees of freedom; namely, translations in surge, sway, and heave, and the Tait-Bryan angles roll, pitch, and yaw. The motion data is based on a right-handed north-east-down coordinate system. The MRU is located approximately 1300 mm below the rotating prism of the lidar. The lidar is positioned parallel to the  $x$ - $y$  plane of the MRU but its heading is rotated around the  $z$ -axis by  $\theta_0 = 30^\circ$  from the  $x$ -direction towards the  $y$ -direction. Information about the direction of each line-of-sight measurement relative to the lidar frame of reference is given in the form of the fixed zenith angle  $\phi$  and the azimuth angle  $\theta$  relative to the heading  $\theta_0$  of the lidar. A series of vector rotations is required to transform this information and the orientation data, i.e., roll, pitch,

and yaw angles,  $R$ ,  $P$ , and  $Y$ , measured by the MRU, into information about the real zenith angle  $\phi_r$  and real azimuth angle  $\theta_r$  of the lidar beam in the global coordinate system. The unit vector in the  $x$ -direction  $\vec{e}_x$  of the MRU in global NWU coordinates after rotation is in accordance with C.3.8 in Grewal et al. [16] given by

$$\vec{e}_x = \begin{bmatrix} \cos Y \cos P \\ -\sin Y \cos P \\ \sin P \end{bmatrix}. \tag{5}$$

The unit vector in the  $y$ -direction of the MRU in NWU coordinates after rotation is given by

$$\vec{e}_y = \begin{bmatrix} -\cos R \sin Y + \sin R \cos Y \sin P \\ -\cos R \cos Y - \sin R \sin Y \sin P \\ -\sin R \cos P \end{bmatrix}. \tag{6}$$

The unit vector in the  $z$ -direction of the MRU in NWU coordinates after rotation is given by

$$\vec{e}_z = \begin{bmatrix} \sin R \sin Y + \cos R \cos Y \sin P \\ \sin R \cos Y - \cos R \sin Y \sin P \\ -\cos R \cos P \end{bmatrix}. \tag{7}$$

$\vec{e}_z$  points downwards. We change its sign to create a unit vector  $\vec{e}_h$  that points upwards into the direction of the laser beam before it is deflected by the lidar prism.

$$\vec{e}_h = -\vec{e}_z. \tag{8}$$

$\vec{e}_{\theta_0}$ , the unit vector in the direction of the lidar heading is determined by rotating  $\vec{e}_x$  by the yaw-offset angle  $\theta_0 = 30^\circ$  around  $\vec{e}_h$ . This can be done by multiplying  $\vec{e}_x$  by the rotation matrix

$$R = \begin{bmatrix} e_1^2(1 - \cos \alpha) + \cos \alpha & e_1 e_2(1 - \cos \alpha) - e_3 \sin \alpha & e_1 e_3(1 - \cos \alpha) + e_2 \sin \alpha \\ e_2 e_1(1 - \cos \alpha) + e_3 \sin \alpha & e_2^2(1 - \cos \alpha) + \cos \alpha & e_2 e_3(1 - \cos \alpha) - e_1 \sin \alpha \\ e_3 e_1(1 - \cos \alpha) - e_2 \sin \alpha & e_3 e_2(1 - \cos \alpha) + e_1 \sin \alpha & e_3^2(1 - \cos \alpha) + \cos \alpha \end{bmatrix} \tag{9}$$

where  $\vec{e} = \vec{e}_h$  is the axis of rotation and  $\alpha = -\theta_0$  the angle of rotation. A derivation of Equation (9) can be found in Section 9.2 of Cole [17]. In order find the  $\vec{e}_{\theta_{270}}$  unit vector we simply use

$$\vec{e}_{\theta_{270}} = \vec{e}_h \times \vec{e}_{\theta_0}. \tag{10}$$

$\vec{e}_{LOS_{\theta_0}}$ , the unit vector that points into the line-of-sight direction for  $\theta = 0^\circ$  is defined by rotating  $\vec{e}_h$  by the half cone opening angle  $\alpha = \phi = 30.6^\circ$  around  $\vec{e} = \vec{e}_{\theta_{270}}$ . The unit vector for a line-of-sight measurement at a particular azimuth angle  $\vec{e}_{LOS_\theta}$  is found by rotating  $\vec{e}_{LOS_0}$  by the negative azimuth angle  $\alpha = -\theta$  around  $\vec{e} = \vec{e}_h$ .

The real zenith angle  $\phi_r$  is the angle between the vertical up direction and the line-of-sight measurement direction. It can deviate from  $\phi$  when the buoy is rotated and can be determined by

$$\phi_r = \arccos \vec{e}_{LOS_\theta} \cdot \vec{e}_U \tag{11}$$

where  $\vec{e}_U$  is the unit vector in the upwards direction. The real azimuth angle  $\theta_r$  is the angle between the horizontal north direction and the projection of the line-of-sight measurement direction onto the horizontal plane. It can be determined by

$$\theta_r = \arccos \frac{\begin{bmatrix} e_{LOS\theta,1} \\ e_{LOS\theta,2} \\ 0 \end{bmatrix}}{\left\| \begin{bmatrix} e_{LOS\theta,1} \\ e_{LOS\theta,2} \end{bmatrix} \right\|} \cdot \vec{e}_N \quad (12)$$

where  $\vec{e}_N$  is the unit vector in the north direction. The sign of  $\theta_r$  must be switched for  $e_{LOS\theta,2} > 0$ .

The next task is to determine the influence of the buoy motion on the line-of-sight velocities. We first calculate the velocity vector of the lidar at the position of its prism and define the distance vector

$$\vec{d} = -1.3\vec{e}_z \quad (13)$$

that separates the location of motion measurement from the location of the lidar prism. The velocity at the lidar prism is the sum of the translational velocities measured at the location of the MRU and the rigid body motion caused by the angular velocity measured at the MRU location according to

$$\vec{v}_{lidar} = \vec{e}_x v_x + \vec{e}_y v_y + \vec{e}_D v_D + (\vec{e}_x \omega_x) \times \vec{d} + (\vec{e}_y \omega_y) \times \vec{d} \quad (14)$$

The selection of the unit vectors  $\vec{e}_x$ ,  $\vec{e}_y$ , and  $\vec{e}_D$  where the subscript  $D$  stands for “down” corresponds to the orientation of the velocity data  $v_x$ ,  $v_y$ , and  $v_D$ , as defined in the setup of the MRU. The terms for the influence of roll and pitch angular velocity  $\omega_x$  and  $\omega_y$  on the translational velocity are sufficient when the distance vector  $\vec{d}$  is oriented along the  $z$ -axis of the MRU. If  $\vec{d}$  contains non-zero elements for the first or second coordinate, a third term  $\omega_z$  for azimuthal rotation is required.

As a last step, the velocity vector  $\vec{v}_{lidar}$  must be projected onto the line-of-sight unit vector  $\vec{e}_{LOS\theta}$  so that

$$v_{LOS} = \vec{e}_{LOS\theta} \cdot \vec{v}_{lidar} \quad (15)$$

is the projection of the translational velocity onto the line-of-sight unit vector.  $v_{LOS}$  is the motion-induced error in the line-of-sight velocity caused by motion.

### 2.3. The Motion-Induced Error in TI Measurements

Reconstructed wind vectors from a moving and a fixed lidar system differ. In the following subsection, we categorize the measurement errors caused by lidar motion into three different effects.

#### 2.3.1. Error in Radial Velocities due to Translational Motion

Translational motion of the lidar window in surge, sway, and heave according to Equation (14) changes the relative velocity between the emitted laser light and the scatterers. Thus, it shifts the detected Doppler frequency, which is proportional to the measured line-of-sight velocity. Stationary motion in the three translational degrees of freedom leads to a one-to-one change in measured wind velocity; e.g., a lidar being transported on a ship with velocity  $\vec{v}$  along the ocean’s surface would measure a wind velocity error of the same magnitude  $\Delta\vec{u} = \vec{v}$ . With the exception of a lidar being mounted on a ship [18,19], all three velocity components of a floating lidar typically average zero during a ten-minute interval, so that  $\vec{V} = \vec{v} = \vec{0}$ . This leads to zero error in mean wind speed  $\vec{U}$ , but the measurements of the instantaneous wind speed  $\vec{u}$  and the derived turbulence parameters like  $TI$  are affected. The effect of translational motion on the instantaneous wind measurement is frequency dependent.

Oscillatory motion with a low frequency  $f_v \ll 1$  Hz affects the wind component of the same orientation; i.e., the surge and sway components of motion  $v_1$  and  $v_2$  influence the horizontal wind speed components  $u_1$  and  $u_2$ ; heave velocity  $v_3$  influences the vertical wind speed  $u_3$ . Figure 2a shows this effect of translational motion. The figure shows line-of-sight velocities of a VAD scanning lidar on the  $y$ -axis plotted against the azimuth angle of the lidar beam  $\theta$  on the  $x$ -axis. In all plots, the wind direction is assumed to be aligned with the heading of the lidar so that  $\Theta = \theta_0$ . The wind velocity is  $U_{\text{hor}} = 5 \text{ ms}^{-1}$ . We also define that surge motion occurs with an arbitrary amplitude of  $\hat{v}_1 = 1 \text{ ms}^{-1}$  along the wind direction. Sway and heave have the same amplitude and are directed perpendicularly to the wind direction. The figure visualizes the lidar-measured LOS velocities in three ways: contribution of the wind, the lidar's motion, and combined. The green lines represent the contribution of the wind to the line-of-sight measurement as if it were to be measured by a lidar without any translational motion. It has a cosine shape with peaks in the upwind and downwind directions. The contribution of the translational motion on the line-of-sight velocities is visualized by the blue lines of varying darkness. The red lines show the sum of both contributions. We ignore that the lidar used in this study cannot detect the sign of the radial velocities. We therefore show the results of the wind vector reconstruction based on the absolute line-of-sight velocities according to Equations (20) and (21) as markers: cyan colored circle markers show the reconstructed horizontal wind speeds and brown cross markers show the reconstructed vertical wind speeds. Their location on the  $x$ -axis represents the reconstructed wind direction. It can be seen in Figure 2a that e.g., a slow back and forth motion in the wind direction (first row: surge) is detected in the same way as horizontal wind fluctuations; sideways motion (second row: sway) is perceived as transversal wind; and up and down motion (third row: heave) leads to a change of radial velocities in all line-of-sight directions. We see as expected that surge motion influences the horizontal wind speed  $u_{\text{hor}}$ ; sway motion influences the wind direction  $\Theta$ ; and heave motion leads exclusively to variation of the vertical wind speed component  $u_{\text{ver}}$ .

But these behaviors are valid only for translational motion that fluctuates very slowly; i.e., with a frequency much lower than one Hz,  $f_v \ll 1$  Hz, which is the frequency of the rotating prism in the lidar corresponding to the time it takes to measure one full rotation of  $\theta$ . Cross-contamination occurs for fluctuations that occur with a frequency close to this value. Cross-contamination in this context means that horizontal motion is interpreted as vertical wind speed fluctuations, and vertical buoy motion is interpreted as horizontal wind speed fluctuations. In other words, surge and sway motion of the buoy contribute to the estimates of vertical wind fluctuations, and heave motion is attributed to the fluctuations of horizontal wind; i.e.,  $TI$ . We can see this in Figure 2 column b. The plots show what happens when translation occurs with a frequency of  $f_v = 1$  Hz. We call this the "resonance case" because the azimuth angle  $\theta$  and the magnitude of the surge/sway/heave velocity oscillate with the same frequency. While the azimuth angle  $\theta$  of the laser beam rotates by  $180^\circ$ , the sign of the motion velocity also changes. That means, the influence of motion on the line-of-sight velocities visualized in blue reaches its peak in this situation not after one full prism rotation as in the case of very slow fluctuations (see column a), but after every half rotation. As a consequence, the influence of motion is attributed to the wind velocity in a different orientation. Horizontal surge and sway motion in resonance leads to variations in vertical wind speed, and heave motion in resonance leads to variations in horizontal wind speed and wind direction. A lidar device with a half cone opening angle  $\phi < 45^\circ$ , like the one used in this study, is more sensitive to vertical heave motion than to horizontal motion in surge and sway. Heave in resonance therefore has a stronger influence on the horizontal wind speed than surge and sway have on the vertical wind speed.

From this analysis, we learn that heave motion in the resonance case and low-frequency fluctuations in surge and sway influence the  $TI$  estimates of a floating lidar. Heave motion must not be ignored because the period of waves is close enough to 1 s to create cross-contamination. Motion of the lidar in the surge and sway directions is not only created directly by translation of the buoy but

also by tilting it when the center of rotation is not at the position of the lidar prism. Successful motion compensation therefore requires consideration of all degrees of freedom of motion.

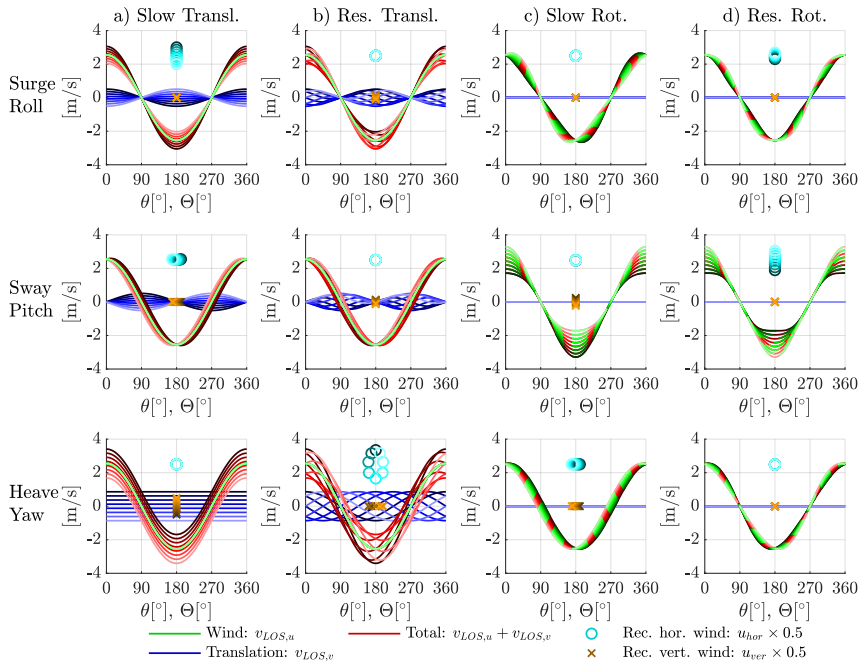


**Figure 2.** Overview of the influence of motion on line-of-sight estimates and reconstructed wind vectors of a velocity–azimuth display (VAD) scanning floating lidar system. Shown are examples of translational motion with  $\hat{v} = 1 \text{ ms}^{-1}$  amplitude oscillating with frequency (a)  $f_v \ll 1 \text{ Hz}$  and (b)  $f_v = 1 \text{ Hz}$ , and the rotational motion of  $10.5^\circ$  peak angle oscillating with (c)  $f_v \ll 1 \text{ Hz}$  and (d)  $f_v = 1 \text{ Hz}$ , where  $1 \text{ Hz}$  is the rotation frequency of the lidar prism. Green lines (dashed in c,d) are the radial velocity components of constant horizontal wind blowing in  $\theta = 0^\circ$  direction with a magnitude of  $U = 5 \text{ ms}^{-1}$  as a function of the lidar azimuth angle  $\theta$ . Blue lines are the influence of translational motion. Red lines are the total line-of-sight velocities. Color shades represent different phases of the oscillatory motion. Circle and cross markers represent the reconstructed wind vectors after conventional VAD processing, where the position on the  $y$ -axis is the magnitude and the position on the  $x$ -axis is the wind direction  $\Theta$ . More information in Section 2.3.1.

### 2.3.2. Change in Scanning Geometry due to Rotational Motion

A second effect of motion-induced measurement errors on a floating lidar is caused by tilting of the platform. Rotations in pitch and roll directions change the real zenith angle  $\phi_r$  of the lidar beam. For example, a beam with an increased real zenith angle  $\phi_r > \phi$  has a higher sensitivity for the horizontal wind components than what is assumed in the internal wind vector reconstruction process using the constant half cone opening angle  $\phi = 30.6^\circ$ . Low-frequency tilting of the platform ( $f_v \ll 1 \text{ Hz}$ ) can be imagined as tilting the complete measurement cone with its original half cone opening angle  $\phi$ . The cone then has an increased real zenith angle  $\phi_r$  on one side and a decreased real zenith angle on the other side. In such a situation, horizontal inflow causes the unsigned line-of-sight velocities to differ between the two sides of the cone. With the conventional VAD processing, horizontal wind is then misinterpreted as vertical wind. The third column c in Figure 2 visualizes this situation. Translational motion is no longer involved in these examples. Instead, we see that the steady inflow of horizontal wind leads to varying wind-induced line-of-sight velocities marked as dashed green

lines due to the changing zenith angles  $\phi_r$ . The magnitudes and shapes of these variations depend on the amplitude and orientation of the low-frequency tilt motion. Pitch motion (second row) leads to increased magnitude of the perceived wind velocity on one side of the measurement cone and a decreased value on the opposite side. Because no translational motion is involved, the total line-of-sight velocity marked in red is equal to the wind-induced line-of-sight velocity. The VAD processing leads to wind data that show nearly exclusively vertical turbulence. Roll rotation (first row) leads to a deviation from the sine shape of line-of-sight velocities but no systematic amplification on either side of the cone. The deviations result in an increased residual in the best-fit of the wind data reconstruction but do not lead to additional turbulence. Slow changes in the yaw angle (third row) lead to a phase shift in the line-of-sight velocities, and as a result, to varying wind directions but do not cause any error in  $TI$  because the estimates of  $u_{\text{hor}}$  stay the same. In summary, static misalignment and slow changes in the orientation do not have any influence on the estimates of  $TI$ .

However, when tilting occurs with a higher frequency close to  $f_v = 1$  Hz, the measurement cone appears to become wider or narrower because the tilt angle of motion changes its sign as quickly as the lidar azimuth angle moves by  $180^\circ$  to its opposite side. We can better understand this effect with the help of the plots in the last column **d** of Figure 2. Pitch motion in resonance with the lidar prism frequency (second row) can be understood as a stretched measurement cone with its maximum deviation from the original shape at the two ends that point into and against the mean wind direction. This geometry leads to either higher or lower sensitivity for the mean wind velocity on both sides of the cone at the same time. The result is increased horizontal turbulence in the reconstructed wind data. Rotations with resonance frequency in roll orientation (first row) also lead to increased turbulence in the wind data but to a lower extent than pitch rotations. The reason is that the apparently widened/narrowed cone has its maximum/minimum zenith angle at  $\theta = 90^\circ$  and  $\theta = 270^\circ$  where the beams point perpendicular to the wind inflow angle. Yawing with resonance frequency (third row) hardly occurs in reality, but it would have no effect on turbulence estimates. Instead, the cone averaging would swallow the resulting asymmetry in the line-of-sight velocities.

Static tilt leads to a decrease in mean wind speed, and dynamic tilting also has a small effect on mean wind speed that shall not be discussed here. We refer to Tiana-Alsina et al. [4] for more information. We have learned that dynamic tilting of the floating lidar that occurs with a frequency close to the lidar's prism rotation frequency causes an increase in  $TI$ . The extent of this increase depends on the mean wind speed and the angle between wind direction and tilt orientation. By contrast, static and very low-frequency tilt motion, and yaw rotations, have no significant influence on the  $TI$  estimates.

### 2.3.3. Changing Measurement Elevation due to Rotation under the Influence of Wind Shear and Veer

Tilting the lidar not only leads to a changed scanning geometry, as described before in Section 2.3.2, but also leads to changing measurement elevations. If the horizontal mean wind speed  $U_{\text{hor}}$  and its direction  $\Theta$  were to be identical at all heights above the ground, this would not have any consequences for the turbulence measurements. But the presence of wind shear and veer, i.e., usually higher wind velocities at higher elevations and changing wind directions with height, respectively, leads to a third effect that is not captured in our above explanations. First, we look at the influence of wind shear. We ignore the elevation variations caused by heave motion because they are small and assume that the change in measurement elevation is exclusively created by tilting the lidar. When a lidar beam tilts towards the horizon, so that its zenith angle is increased, its sensitivity for the horizontal mean wind speed is also increased. Yet it measures the wind at a lower elevation, where the wind typically has lower horizontal mean speed. Conversely, a beam rotated towards the zenith measures a lower fraction of the horizontal mean wind speed, which is typically increased at the higher measurement elevation. That means, the effect of wind shear is always directed against the effect of changed scanning geometry. We can determine the relative magnitude between the two effects.

$$dv_{r,2}(\alpha, z) = U(z)(\sin(\phi + \alpha) - \sin \phi) \quad (16)$$

is the change in line-of-sight velocity of a beam pointing into the direction of the mean wind  $U$  with a half cone opening angle of  $\phi$  that is tilted by tilt angle  $\alpha$  towards the horizon. This equation does not consider wind shear and represents only the changed scanning geometry, and therefore, the subscript 2 that refers to the second effect described in this section. With  $z$  being the initial measurement elevation, we can calculate the change in elevation according to

$$dz(\alpha, z) = z \left( \frac{\cos(\phi + \alpha)}{\cos \phi} - 1 \right). \quad (17)$$

The change in line-of-sight velocity that considers not only the changed geometry as in Equation (16) but also the wind shear is

$$dv_{r,2\&3}(\alpha, z) = U(z + dz(\alpha, z))(\sin(\phi + \alpha) - \sin \phi). \quad (18)$$

With these equations, we can define a wind shear reduction factor

$$k(\alpha, z) = 1 - \frac{dv_{r,2\&3}(\alpha, z) - dv_{r,2\&3}(-\alpha, z)}{dv_{r,2}(\alpha, z) - dv_{r,2}(-\alpha, z)} \quad (19)$$

where the numerator is the change in line-of-sight velocity for a rotation from  $-\alpha$  to  $\alpha$  when wind shear is considered. The denominator describes the same but without considering wind shear. As a result,  $k$  is the factor by which the effect of changed scanning geometry is reduced by the effect of wind shear. Measured mean wind velocities can be used to create wind profiles by linear inter and extrapolation. The resulting wind shear reduction factor is usually low. We found out that the dependency of  $k$  on the tilt angle  $\alpha$  is low, and it varies more with the measurement height  $z$ . Based on the measurement data used for this study, we calculated the average values for all height levels  $z$  and tilt angles  $\alpha$  to be  $k = 5.8\%$ . We therefore assume that the effect of wind shear compensates for this amount of the effect of changed scanning geometry. The effect of wind veer might increase the measured turbulence again to some unknown extent. The effect is difficult to quantify, because wind veer involves dynamic changes in the wind direction which lead to significant deviations from the figures-of-eight, as explained in Section 2.3.2. However, we consider wind veer in the motion compensation algorithm that we present in Section 3.2.

All three effects described in this section are fully independent of the line-of-sight averaging. That means motion-compensated wind statistics will miss the same amount of turbulence due to averaging along the lines-of-sight as their uncompensated counterparts. The time of approximately 20 ms—during which the backscatter is accumulated for each line-of-sight Doppler spectrum—is so short that we assume the motion as static during this time.

Wolken-Möhlmann et al. [20] reported that the influence of rotation on the total error is stronger than the influence of translational motion, and our study supports this finding. Our computations also show that the error of shear and veer in turbulent fluctuations is nearly negligible, but its influence on the mean wind speed might be significant.

### 3. Method

#### 3.1. Emulation of Conventional VAD Processing

The method we use in this study aims at eliminating the three previously described errors: firstly, by correcting the radial velocity measurements for the influence of the lidar translation; secondly, by employing a set of linear equations in the wind vector reconstruction process that consider the real azimuth and zenith angles; and lastly, by interpolating the mean wind speed and direction onto the actual measurement elevation. The method requires access to the radial velocity measurements for each line-of-sight. The ZX300M used for this study stores wind data on its internal hard drive by default for each reconstructed wind vector (“Wind\_XXX@Y20yy\_Mmm\_Ddd.ZPH,” 1 Hz files) and

their average over a period of ten minutes (“Wind10\_xxx@Y20yy\_Mmm\_Ddd.ZPH,” 10-min files). None of these standard output file types contains the required information about the line-of-sight wind velocities. We therefore used the software “Waltz<sup>TM</sup>” to stream the Doppler spectra of all line-of-sight measurements to the hard drive of a connected computer. Files saved in this way have user-defined filenames with the ending .RAW.ZPH and can be extracted to readable comma separated files via Waltz. These files do not contain the radial velocities as such, but they contain the Doppler spectra for each line-of-sight measurement. In order to estimate the radial velocities from the spectra, we first calculated the mean and the standard deviation of the twenty bins of highest Doppler frequency (“FFTBin236” to “FFTBin255”) for each line-of-sight measurement. We assume that these high speed bins are not influenced by the wind under normal conditions but contain only noise. We then removed this noise floor from all bins by setting all spectral values to zero that are smaller than six of the standard deviations after subtracting the mean values from all bins. Of the resulting spectra we calculated the centroid bin and multiplied it by  $0.1528 \text{ ms}^{-1}$  to get the radial velocities of each line-of-sight measurement [21,22]. We know from Pitter et al. [23] that the internal data processing algorithms are more advanced than what we describe here. It likely incorporates cloud detection and fog filters. Parameters for both are not known to us and can therefore not be imitated. Instead we use the unfiltered line-of-sight velocities.

Forty-nine line-of-sight measurements which were consecutively taken at one height level are the data basis for the reconstruction of each wind vector. From the radial velocities  $v_r$  and associated azimuth angles  $\theta$ , the three-dimensional wind data can be calculated by applying a least-squares fit to

$$v_r = |A \cos(\theta - B) + C| \quad (20)$$

where  $A$ ,  $B$ , and  $C$  are parameters that contain the wind data according to

$$\begin{aligned} u_{\text{hor}} &= A / \sin \phi \\ \Theta &= B \pm 180^\circ \\ u_{\text{ver}} &= C / \cos \phi. \end{aligned} \quad (21)$$

The sign ambiguity of the wind direction results from the use of unsigned line-of-sight velocities. It is resolved with the help of wind direction measurements of a local weather station, though flipping the sign of the wind vector neither influences the mean wind speed nor the turbulence intensity. As a next step, we compare the time series of wind data with the results of the internal data processing (i.e., the “Wind\_xxx@Y20yy\_Mmm\_Ddd.ZPH” files) and filter out all values that are marked with a “9998” or “9999” flag by the ZX300. Wind data processed in this way were intended to be identical to the internally processed wind data. But a comparison shows deviations that are stronger and more frequent at higher elevation levels.

Figure 3 shows a scatter plot of  $TI$  values estimated from the time series of wind data of the floating lidar system. The  $TI_{\text{unc}}$  values on the  $x$ -axis are based on horizontal wind velocities reconstructed by the internal data processing while the  $TI_{\text{emu,unc}}$  values on the  $y$ -axis are based on our own processing of the raw data, which emulates the internal processing. The figure shows an interval of  $\pm 0.01$  around the 1:1 line. 19%, 33%, and 50% of all  $TI$  values measured at 30 m, 100 m, and 250 m elevations respectively lie outside of this interval. This indicates that the simple centroid method we use for finding radial velocities deviates from the unknown method ZX lidar uses. An analysis of Doppler spectra which underlie the wind vectors showing the strongest deviations shows often double peaks that might indicate the presence of clouds. Therefore, we assume that the differences are mostly caused by filtering and cloud detection on a line-of-sight level and describe how we circumvent this problem in Section 3.4.

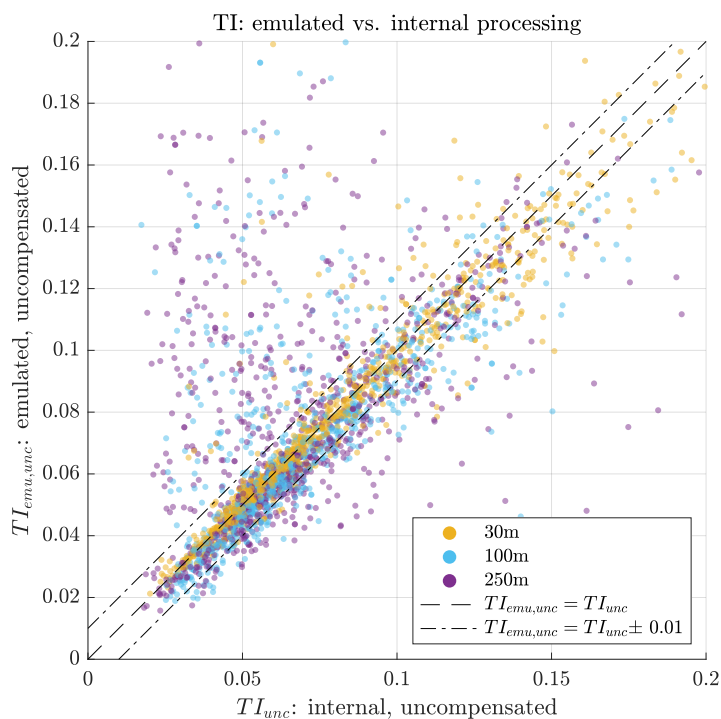


**Figure 3.** Comparison of turbulence intensity ( $TI$ ) estimates based on wind data time series from internal data processing vs. emulated data processing. Only three height levels shown for clarity. The dashed-dotted lines limit a  $\pm 0.01$  interval parallel to the dashed  $y = x$  line.

### 3.2. The Motion Compensation Algorithm

The first challenge that must be addressed for applying motion compensation on a line-of-sight level involves the signs of the radial velocities. Radial wind velocity estimates from the ZX300 are unsigned. That means that air moving along a single laser beam away from the lidar cannot be differentiated from air moving towards the lidar, and the radial velocity is positive in both cases. In order to still be able to subtract the motion-induced velocity component, we must assign a sign to each line-of-sight velocity. We do this by reading the wind direction of each reconstructed wind vector and assigning a negative sign to the half of the line-of-sight measurements that point into the wind direction  $\Theta \pm 90^\circ$ . This method requires that the mean wind  $\vec{U}$  determines the sign of the individual line-of-sight measurements and not turbulent fluctuations  $\vec{u}'$ . This is an assumption which might be violated at azimuth angles that are close to orthogonal to the wind direction  $\Theta$ . These sideways beams hardly detect the mean wind but mostly the turbulence of the transversal and vertical wind velocity components. Mann et al. [24] and Dellwik et al. [25] report that radial velocity estimates from these directions are biased away from zero, and thus erroneous in any case. Additionally, in periods with very low mean wind speed, the assumption that the sign of radial velocities is determined by the wind direction could be violated. Here it should be noted that measurements of very low wind speeds are often of minor interest due to low power production and low structural loads associated with low wind speeds. Additionally, under unstable atmospheric conditions with high variance of the vertical wind speed component, sign errors are more likely because the sensitivity for vertical fluctuations is larger than the sensitivity for horizontal fluctuations because of the half-cone opening angle  $\phi < 45^\circ$ . The signed line-of-sight velocities can then be corrected for the influence of the buoy's motion. First, the motion measured by the MRU in all six degrees of freedom must be projected onto unit vectors that

point into the lidar beam direction according to Section 2.2. The magnitude of this projection is equal to the contribution of the motion to the radial velocity measurement, which we therefore subtract from the line-of-sight estimate.

In order to compensate for the effect of the lidar being rotated around its default orientation in roll, pitch, and yaw directions, the velocity–azimuth display wind vector reconstruction function (Equation (20)) is replaced by solving the following linear system

$$\begin{bmatrix} v_{r1} - v_{LOS1} \\ v_{r2} - v_{LOS2} \\ \vdots \\ v_{rN} - v_{LOS N} \end{bmatrix} = \begin{bmatrix} u \\ v \\ w \end{bmatrix} \begin{bmatrix} \sin \theta_{r1} \sin \phi_{r1} & \cos \theta_{r1} \sin \phi_{r1} & \cos \phi_{r1} \\ \sin \theta_{r2} \sin \phi_{r2} & \cos \theta_{r2} \sin \phi_{r2} & \cos \phi_{r2} \\ \vdots & \vdots & \vdots \\ \sin \theta_{rN} \sin \phi_{rN} & \cos \theta_{rN} \sin \phi_{rN} & \cos \phi_{rN} \end{bmatrix} \quad (22)$$

for  $u$ ,  $v$ , and  $w$  where  $N$  is the number of line-of-sight measurements contributing to one measurement circle. Because  $N = 49$  in most cases, the linear system is overdetermined and must be solved using least squares.  $u$  and  $v$  are the two horizontal wind speed components oriented towards  $\theta = 0^\circ$  and  $\theta = 90^\circ$  respectively. Their Pythagorean sum is equal to  $u_{hor}$  and the angle they create is  $\Theta$ .  $w$  is equal to  $u_{ver}$ .

In order to compensate for the effect of wind shear and veer on the measurements, we determine the change in elevation due to rotation according to

$$\Delta z = h \left( \frac{e_{LOS\theta_3}}{\cos \phi} - 1 \right) \quad (23)$$

for each line-of-sight. We must then interpolate the measured mean wind vectors  $\vec{U}$  at all measurement heights  $h$  to get a velocity profile  $\vec{U}(z)$  that can be used to determine the resulting mean wind difference vector

$$\Delta \vec{U}(z) = \vec{U}(z) - \vec{U}(z + \Delta z) \quad (24)$$

which we multiply by the line-of-sight unit vector  $\vec{e}_{LOS_\theta}$  to get the value we eventually subtract from the measured line-of-sight velocity.

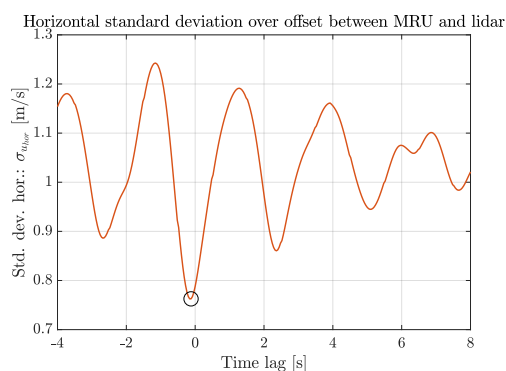
### 3.3. Time Synchronization

In order to correct the radial velocities for the influence of the motion, we must assign a timestamp to each line-of-sight measurement. This timestamp must, first, be related to the timestamp of the MRU, and second, be fine enough to resolve each line-of-sight measurement. In the default setup, two different types of temporal information are contained in the lidar raw data output: “timestamps” and “uptimems.” “Timestamps” contain information about date and time of each measurement, but they are updated only once per second, which is too coarse in the context of wave motion. “Uptimems” values, by contrast, assign a timestamp in milliseconds to each line-of-sight measurement, but these values use a different clock independent of the clock used for “timestamps.” “Uptimems” values are reset once the unit is switched off, and can therefore not be translated into date and time information directly. We decided to combine the information of both variables as follows. First, we select the first line-of-sight measurement of each day which has an updated “timestamps” but the same “reference” value as the one immediately preceding. All line-of-sight velocities that are used for one wind vector reconstruction have the same “reference” value. By using the same “reference” we avoid picking a line-of-sight measurement that is the first after the lidar refocuses to a new measurement height, which takes some unknown time. By doing so, we pick a line-of-sight measurement that was taken less than approximately 20 ms after a new second of “timestamps” started. We then subtract the “uptimems” value of this measurement from all “uptimems” values of the whole day. To create new timestamps in milliseconds, we simply add the “timestamps” value of the selected measurement and these new “uptimems” values. When we compare the “uptimems” data with the original “timestamps” data

over a longer period, we find that while 24 hours of “timestamps” time passes, on average  $\approx 1.2$  s less than 24 hours of “uptimes” time passes. That means that the newly created timestamps are finely resolved but contain the same  $\approx 1.2$  s drift per day relative to the lidar’s system time. We will solve this issue along with the synchronization of the MRU motion data and the lidar line-of-sight data.

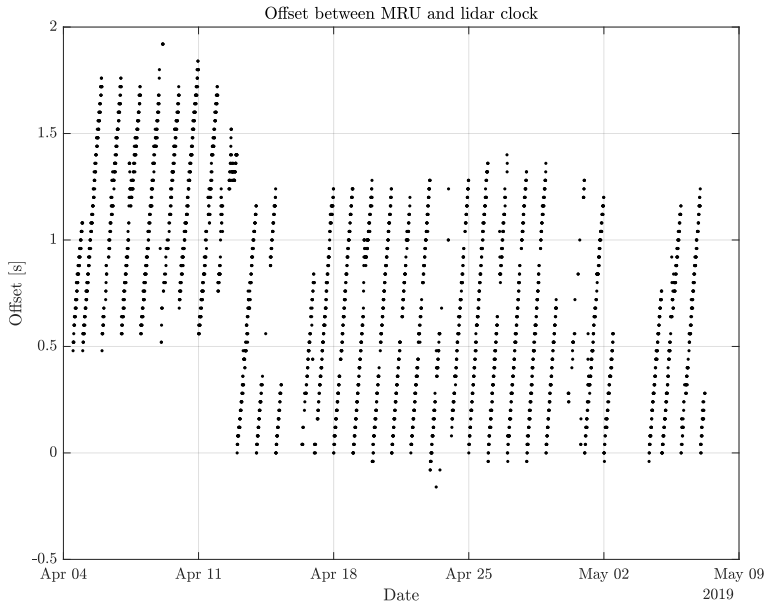
Synchronization is crucial for successful motion compensation. The Doppler spectra of the lidar are streamed to an embedded PC, and the motion data is saved by means of a data acquisition system with a sample rate of 50 Hz. Both units are independently synchronized with a common GPS time server, but they are not synchronized with each other. Therefore, we expect an offset between the timestamps of the MRU and the lidar. To tackle this issue, we implement a method to synchronize the two measurement devices. Its underlying basic assumption is that the motion of the buoy caused by waves, current, and local wind is independent of the simultaneous wind vectors at measurement height. From this assumption it follows that the motion-induced error described in Section 2.3 and the current wind velocity are also independent variables. The turbulence measured by a floating lidar in motion must therefore be larger than measurements with a fixed lidar of the same type. The ideal motion compensation algorithm can reduce the measured turbulence down to exactly the level of a fixed lidar if the timing between motion and lidar data is correct. A timing error must lead to worse functionality; i.e., less compensation and consequently higher remaining turbulence. Due to the periodicity of ocean waves, the compensation can even become negative if the timing offset equals half the period length of the waves. In such a situation the algorithm would assume that the buoy is for example moving upwards although the real motion is directed downwards. The motion compensation would in that situation add turbulence instead of subtracting it. With these thoughts in mind, it is now simple to find the correct timing between MRU and lidar data. We need to calculate the motion compensation for different time lag values between MRU and lidar and determine the offset at which the motion-compensated turbulence reaches its minimum.

Figure 4 shows the result of this procedure for an arbitrary ten-minute interval. The  $y$ -axis shows motion-corrected standard deviation values of the horizontal wind speed  $\sigma_{u_{\text{hor}}}$  averaged over all measurement heights. The corresponding time lag between lidar and MRU timestamp is shown on the  $x$ -axis. The absolute minimum is found at  $-0.16$  s. This is the average offset between lidar and MRU data for this ten-minute interval. The periodicity of the waves is visible, and leads to local minima each separated by approximately 2.5 s. These local minima must not be confused with the absolute minimum, which is the sweet spot we aim for.



**Figure 4.** Standard deviation of the motion compensated horizontal wind speed  $\sigma_{u_{\text{hor}}}$  as a function of timing offset between MRU and lidar data.  $\sigma_{u_{\text{hor}}}$  is the mean of all height levels for one arbitrary ten-minute interval. The absolute minimum at  $-0.16$  s indicates the sweet spot that corresponds to the real offset between the two datasets.

Figure 5 shows this sweet spot for all ten-minute intervals we processed for this study. We see the drift of approximately 1.2 s before the custom lidar timestamp is reset once per day, as described earlier in this section. The drift seems to occur linearly, and a sweet spot is found for all intervals.



**Figure 5.** Timing offset at which the sweet spot from Figure 4 is found for all available ten-minute intervals.

### 3.4. Data Handling

After applying the motion compensation algorithm, we have three different sets of horizontal wind speed time series from the floating lidar. Of all three time series, we estimate  $TI$  according to Equation (4). These are  $TI_{unc}$  from the internally-processed uncompensated values as they are stored in the 1 Hz files,  $TI_{emu,unc}$  the values based on the emulated processing described in Section 3.1, and  $TI_{emu,com}$  from the motion-compensated time series. As shown in Figure 3,  $TI_{unc}$  and  $TI_{emu,unc}$  are not identical. In order to get motion-compensated turbulence estimates from the floating unit that are comparable to the internally-processed values of a fixed reference unit, we define the motion-compensated turbulence intensities as

$$TI_{com} = TI_{unc} - (TI_{emu,unc} - TI_{emu,com}). \quad (25)$$

Effectively, the amount of motion-induced turbulence  $TI_{emu,unc} - TI_{emu,com}$  is deducted from the uncompensated internally processed values to get compensated values that are comparable to a reference lidar with the same internal data processing.

### 3.5. Instrumentation and Measurement Setup

In order to validate the performance of the motion compensation algorithm, we compare measurements of the floating lidar with data from a fixed reference lidar. The validation campaign took place between 04.04.2019 and 07.05.2019 close to Titran on the Norwegian island of Frøya.

The floating lidar system is a ZX300M (unit 593, filter version 1.061) by ZX Lidars (Ledbury, United Kingdom) which is a vertical profiling, continuous-wave wind lidar. It is mounted on a SEAWATCH Wind LiDAR Buoy by Fugro (Leidschendam, Netherlands). The buoy is equipped with an MRU 6000

motion reference unit by Norwegian Subsea (Oslo, Norway) that measures the motion of the buoy in all six degrees of freedom with an update frequency of 50 Hz. For land-based reference measurements, a fixed ZX300 (unit 495, filter version 1.061) operating nearby onshore was used. The location of both lidars is marked on the map in Figure 6.

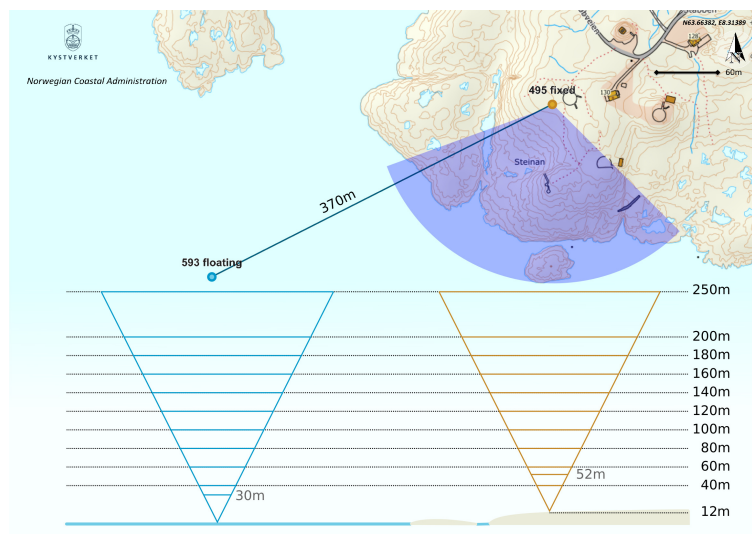


**Figure 6.** Map indicating the location of the floating lidar unit 593 and the land-based fixed reference lidar unit 495. The elevation difference above sea level and the geometry of the measurement cones is shown for all measurement heights. The selected offshore wind sector  $[135^\circ, 250^\circ]$  is indicated in dark blue. (Map data adapted from [www.kartverket.no](http://www.kartverket.no)).

Both lidar units are configured to measure the wind velocities at eleven heights, including the fixed reference height of 38 m above ground. The ground elevation at the location of the land-based reference lidar is 12 m above the mean sea level, and the window height is 2 m above the ground. The floating lidar is located at sea level and its window height is 2 m above sea level. The measurement heights are selected so that both lidars measure at ten identical elevations between 40 m and 250 m above sea level, as shown in Figure 6. Validation tests such as described in Mark et al. [26] support the assumption that lidar measurements with this setup are comparable for horizontal mean wind speed and wind direction. Due to the 12 m higher elevation of the fixed reference lidar compared to the floating lidar, its focus distances are slightly shorter for the same measurement height above sea level. This results in reduced line-of-sight averaging and also a reduced diameter of the measurement cone. The internal  $TI$  estimation of the ZX300 uses an empirical correction factor to make the lidar derived  $TI$  values more comparable to values from cup anemometers [27]. This correction factor is a function of measurement height and lidar measured  $TI$ . We do not apply this correction factor to our  $TI$  estimates but we can use it to get an approximate idea of the impact of the reduced line-of-sight averaging and reduced diameter of the measurement cone of the fixed reference lidar. We can take the average value of  $TI = 5.0\%$  that we measured with the fixed reference lidar during the measurement period. The mean correction factor for all measurement heights is then 0.0086 higher for measurements taken at 12 m higher elevations. From this we can conclude that we expect the floating lidar to measure approximately 0.04% less turbulence intensity at comparable heights due to its longer focus length. This is the only information we use the correction factor for in this study. All results shown in Section 4 of this paper are presented without application of the correction factor.

To make a meaningful comparison of turbulence measurements at the two locations, it is important to choose inflow wind directions in which the surface roughness is identical for both lidars. Thus, we decided to include data from the southern offshore sector with the limits  $135^\circ$  and  $250^\circ$ , as shown in Figure 6. In this sector, no land is present within a radius of 6.4 km. Because this stretch of undisturbed inflow is long compared to the distance between the two lidar units, we assume that both devices see approximately the same turbulence.

### 3.6. Data Filtering

The measurement campaign consists of 4860 ten-minute intervals. However, as seen in Figure 5, some data are missing due to irregularities in the required manual raw-data streaming, so only 4284 ten-minute intervals of raw data are available from the floating lidar. Before computations start, we exclude intervals where for at least one height level the output in the ten-minute files is flagged with either 9998 or 9999. These intervals are usually characterized by fog, very clear air with not enough backscatter, or very low wind speeds. We also exclude intervals during which at least at one height the measured mean wind velocity is below  $1.5 \text{ ms}^{-1}$ , since they are of low relevance for wind power and the wind vector reconstruction might be less accurate. Starting a new raw data file during one ten-minute interval causes the raw data to be split into two files. We do not merge them but filter out files for which less than 75% of the raw dataset is available. After this initial filtering, 3863 intervals remain for data processing.

During processing of the remaining files, we check the internally-processed 1 Hz wind data files for 9998 and 9999 flags and filter out each reconstructed wind vector which is flagged by the lidar software. We also filter out all intervals for which the fixed reference lidar outputs a 9998 or 9999 mean value for at least one height level. This keeps all intervals for which data are available from all height levels from both lidar units. We then filter for inflow from the offshore sector [ $135^\circ, 250^\circ$ ], leaving us with a total of 889 intervals for comparison. Table 1 gives an overview of the wind conditions and the motion states of the buoy during the observation periods that are included in the comparison after filtering.

**Table 1.** Overview of wind conditions and motion state of the buoy during the periods that are included in the results section. Wind conditions as measured by the fixed reference lidar.

Name	Symbol	Mean	Min	Max	Std. dev.	Unit
Mean wind speed	$U$	7.2	1.4	22.1	3.2	$[\text{ms}^{-1}]$
Turbulence intensity	$TI$	5.0	0.6	41.6	3.7	$[\%]$
Mean dynamic tilt angle	$\bar{\alpha}$	2.91	0.62	8.73	1.84	$[\circ]$
Mean tilt period	$\bar{T}_\alpha$	2.51	2.11	2.70	0.10	$[\text{s}]$
Mean heave velocity	$ \bar{v}_{\text{heave}} $	0.13	0.03	0.41	0.08	$[\text{ms}^{-1}]$
Mean heave displacement	$ \bar{\delta}_{\text{heave}} $	0.12	0.03	0.41	0.08	$[\text{m}]$

### 3.7. Measurement Uncertainty

We know of several sources of error that might lead to uncertainties in our results. During the process of synchronizing the MRU and lidar data, we choose a time step of 40 ms in order to find a good compromise between precision and computation time. For that reason, we expect that the sweet spots shown in Figure 5 are on average 20 ms away from the correct values. In Figure 4 we see that the resulting error has approximately a cosine shape with an average period of 2.5 s. We therefore expect only a small statistical error of  $1 - \cos(0.02 \times 2\pi/2.5) = 0.1\%$  of the motion-induced  $TI$  due to this timing error.

The manufacturer of the MRU has indicated an accuracy of the roll and pitch angle measurements of  $\pm 0.02^\circ$ . Considering that the mean tilt angle is approximately two orders of magnitude higher, we assume that the measurement error due to wrong tilt angles is below 1% of the rotation-induced  $TI$ . The yaw angle error of the MRU is  $\pm 0.5^\circ$ . A similar uncertainty should be expected from the alignment

between the lidar  $\theta_0$  beam direction and the  $x$ -direction of the MRU. Both can result in increased directional inaccuracy, which is not the object of investigation here. Uncertainties in surge and sway velocities are unfortunately not specified by the manufacturer, but results from a hexapod test with a JONSWAP motion spectrum with a peak period of 10 s and a significant amplitude of 0.5 m show a velocity error of  $\pm 0.03 \text{ ms}^{-1}$ . Velocities in the heave direction are expected to have a smaller error due to the well-defined zero baseline, which corresponds to an error of up to 0.4% of the  $TI$  induced by translation at a horizontal mean wind speed of  $7.2 \text{ ms}^{-1}$ . We can conclude that the accuracy of the MRU is well-suited to the task, and we expect less than 1.5% combined systematic error due to timing and precision of the motion measurement.

Strong statistical uncertainty arises from the test setup with two lidars measuring at two locations separated by 370 m. In most cases, the mean wind direction is not aligned with the separation distance. We assume that the wind vectors at both locations are independent. In addition, the lidars do not sample the wind continuously. Measurement at eleven height levels plus the time required to refocus the laser beam result in on average only  $N = 37$  samples for each height during one ten-minute interval. In the results (Section 4.5), we will quantify the statistical error of this slow sampling of independent wind vectors with lidar devices to approximately 40% of the measured  $TI$ . We must therefore assume that even if the motion compensation algorithm were to work perfectly, a high amount of scatter would be found between the values measured by the fixed land reference lidar and the motion-compensated floating lidar.

## 4. Results and Discussion

### 4.1. Mean Wind

Correct measurements of the mean wind velocity are an essential prerequisite for valid estimates of  $TI$ . We therefore refer to Figure 7 which shows the average horizontal mean wind speeds for all intervals included by measurement height. The mean wind speed of all measurements included in the data comparison is  $7.15 \text{ ms}^{-1}$ . The floating lidar measures on average 0.5% percent lower wind velocities. When motion compensation is applied, the error is reduced to 0.2%. Most of this deviation is found in measurements at elevations between 80 m and 120 m. It is difficult to say if the real wind speed is absolutely identical at all elevations at both measurement locations. It is possible that the small change in ground elevation between the two lidar units leads to a small speed up or the increased surface roughness results in slowing the wind down slightly. Overall we conclude that the two measurement locations are comparable in terms of horizontal mean wind velocity, as previously reported [26], and that the motion compensation algorithm has a small influence that appears to improve the mean wind velocities.

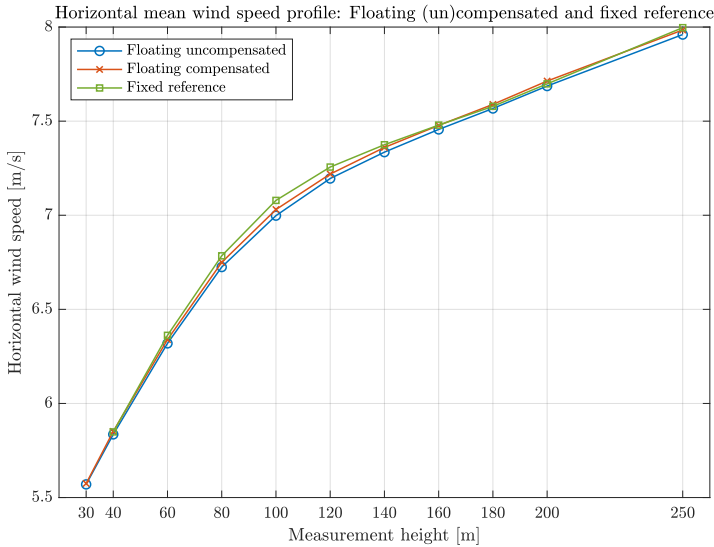


**Figure 7.** Average of measured horizontal mean wind velocities from the floating lidar with (red) and without (blue) motion compensation, as well as from the fixed reference lidar (green), sorted by measurement height.

#### 4.2. TI Profile

Figure 8 shows that the reference lidar measures an average value of  $TI_{ref} = 5.00\%$  across all test intervals. This  $TI$  value might seem low when compared with other offshore wind data. However, the ZX lidar  $TI$  correction factor of, in this case, 1.37 that we did not include in our results would lift the values to what we would expect from an offshore site [28]. Looking at  $TI_{ref}$  at different height levels, we observe a characteristic profile with higher turbulence close to the ground, which creates turbulence from uniform shear.  $TI$  decreases for increasing height and reaches its minimum at around 120 m. For the highest elevation at 250 m, measured  $TI$  increases again slightly. Such a behavior has been reported by Svensson et al. [29]. We think this could be due to lower Doppler signal quality at high elevations that lead to an increased standard error of the wind vectors and thus higher  $TI$  estimates.

The floating lidar without any compensation measures a mean  $TI_{unc} = 7.37\%$ . The shape of the profile is similar to the reference profile, but all values are on average approximately 50% higher due to motion-induced turbulence. The motion compensation reduces the  $TI$  estimates to a level of  $TI_{com} = 5.01\%$ , which is very close to the reference value and equals a motion reduction factor of 99.8%. Overall, the  $TI_{com}$  profile follows the  $TI_{ref}$  profile. The bar plots in Figure 8 visualize the amount of motion-induced  $TI$  in two ways: first, we present the difference between the uncompensated floating  $TI_{unc}$  and fixed  $TI_{ref}$  measurements (green); second, we show the amount of motion-induced  $TI$  detected by the algorithm (red), which is the difference between uncompensated floating  $TI_{unc}$  and compensated floating  $TI_{com}$ . Each pair of bars would have the same length if the motion compensation algorithm were perfect and the measurements from both locations were fully comparable.

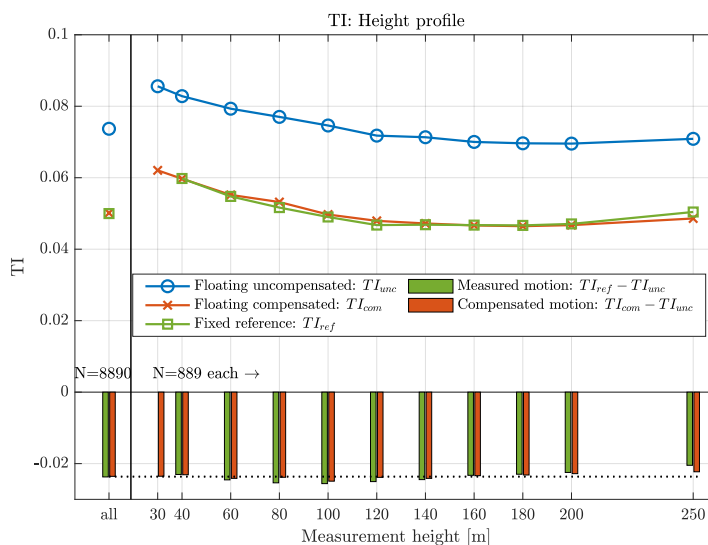


**Figure 8.** Average  $TI$  for all measurements and sorted by measurement heights. Blue circle markers indicate  $TI$  based on uncompensated measurements from the floating lidar. Red cross markers show corresponding values with motion compensation. Green square markers stand for values from the land-based fixed reference lidar for comparison. Bar plots show the motion-induced  $TI$  as the difference between measurements with the floating lidar and the fixed lidar (green) compared to the amount of motion-induced  $TI$  detected by the algorithm (red). The number of available measurement values at each height is given.

We will now analyze the motion-induced  $TI$  at all but the highest elevation, which we will analyze later. The lengths of all bars representing measured motion-induced  $TI$  at heights from 40 m to 200 m lie in a narrow band of  $[-5\%; +9\%]$  around the mean of all heights marked by the horizontal dotted line. The measured motion-induced  $TI$  values show above-average values from 60 m to 140 m. These height levels coincide with where we measured lower values of mean wind speed from the floating lidar (see Figure 7). We can show that the lower mean wind speed is responsible for approximately half of the deviations from the mean measured motion-induced  $TI$ . With this correction in mind, we can say that motion-induced  $TI$  is only weakly dependent on measurement height, with a slight tendency towards lower values at high elevations. This suggests that rotational motion, as described in Section 2.3.2, is dominant compared to the contribution of translational motion described in Section 2.3.1. Rotational motion contributes velocity variance proportional to the mean wind speed. Because  $TI$  values are normalized by the mean wind speed, the influence of rotation on the results has to be identical at all measurement heights. By contrast, translational motion introduces an identical amount of velocity variance at all heights, which results in lower motion-induced  $TI$  values at greater heights, where the mean wind speed is faster. The effect of wind shear and veer described in Section 2.3.3 can be different at each height, but we consider it to be of minor importance.

The motion-induced  $TI$  detected by our algorithm is very similar to the measured values, especially when the remaining differences in mean wind speed from 80 m to 120 m are taken into consideration.

As mentioned before, the fixed reference lidar measures slightly higher  $TI$  at its highest measurement level, 250 m, which could be caused by weak backscatter signal quality at this elevation. The floating lidar shows the same effect but to a smaller extent. It seems that although both lidars are of the same type, the error caused by low backscatter at the highest elevation affects the reference lidar more than the floating lidar. This would explain why the measured, motion-induced  $TI$  is erroneously low compared to the value our algorithm calculates. If this explanation is correct,

the overall  $TI$  measured by the reference lidar is a bit higher than what we measure with a perfectly motion-compensated floating lidar. Additionally, the shorter focus lengths and reduced measurement cone diameters lead to slightly increased  $TI$  values from the reference lidar, as shown with the help of the correction factor in Section 3.5. In this case, both effects combined seem to outweigh the imperfections of the motion compensation nearly exactly, which explains the 99.8% overall performance of the motion compensation algorithm.

4.3.  $TI$  vs. Velocity

In order to find out if the motion compensation algorithm works similarly well under the influence of varying mean wind conditions, we look at Figure 9. The  $TI_{ref}$  estimates measured by the land-based reference lidar gradually decrease with increasing wind velocity. At the lowest wind speeds, the turbulence is dominated by thermal effects that do not increase with wind speed proportionally [15].  $TI$  therefore decreases at increasing wind speeds. However, for the strongest wind speed bin,  $TI$  is slightly higher again, which can be explained by the increased surface roughness of the wavy sea [28]. The increasingly rough sea state at increasing wind speeds is represented in the figure by the gray and blue markers that indicate the measured mean tilt amplitude and mean velocity of the buoy, respectively.

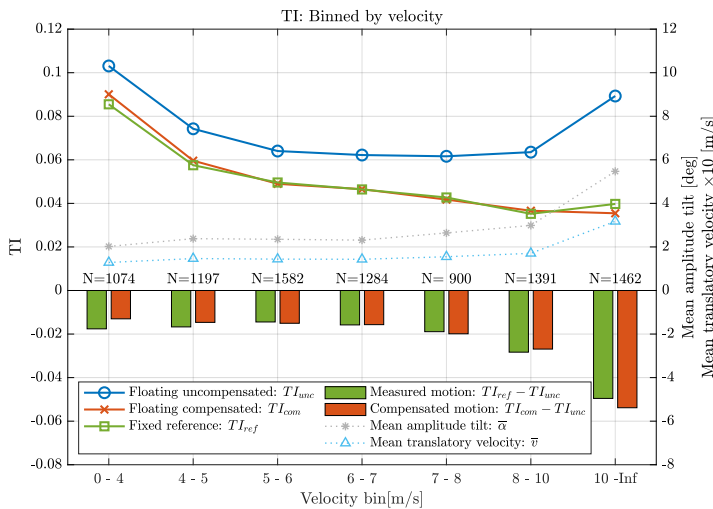


Figure 9.  $TI$  from all measurement heights binned by mean wind velocity. Legend as in Figure 8 plus gray markers for the mean tilt amplitude  $\bar{\alpha}$  and mean translational velocity  $\bar{v}$  that scale with the right hand side  $y$ -axis.

The floating lidar shows higher  $TI$  values. We see that at low wind speeds  $< 4 \text{ ms}^{-1}$  the measured motion-induced  $TI$  is slightly higher than at intermediate wind speeds between  $4 \text{ ms}^{-1}$  and  $7 \text{ ms}^{-1}$ , although the motion parameters tilt amplitude and translational velocity are the lowest. The reason is probably that the translational motion is more important for the total motion-induced  $TI$  at very low wind speeds. As an example, we can imagine two cases in which the amounts of translational and rotational motion are identical but the mean wind speed is different. The identical amount of translational motion leads to the same amount of measured velocity variance but higher motion-induced  $TI$  in the low wind speed case. The identical amount of rotational motion leads to an increase in velocity variance that is dependent on the wind velocity, and therefore leads to the same amount of motion-induced  $TI$ . Taken together, motion-induced  $TI$  is higher for the low wind speed case. In our lowest wind speed case, the amount of motion is lower than for higher wind speeds, but it

is not as low as it would need to be to compensate for the effect we just sketched out. At higher wind speeds above  $5 \text{ ms}^{-1}$  motion-induced,  $TI$  increases with wind speed due to the dominance of the effect of rotational motion.

When the  $TI$  of the land reference lidar is now compared to the motion-compensated  $TI$  of the floating lidar, we see overall good agreement, which means that the motion compensation algorithm is able to correct for motion under all tested wind conditions. The strongest deviation is found for the lowest wind velocities, where the actual  $TI$  reduction is underestimated by the motion compensation algorithm. The reason could lie in how we assign a sign to the radial velocities. As described in Section 3.2, the risk of assigning the wrong sign is higher for low wind speeds. With the wrong sign assigned to some radial velocities, the motion compensation does not work correctly. This could explain why we under-compensate the motion during low wind phases. Further investigation, e.g., with in-situ anemometry, is required to test this explanation.

At high wind speeds above  $10 \text{ ms}^{-1}$  the algorithm slightly overestimates the amount of motion-induced  $TI$ . Such high mean wind speeds appear jointly with high tilt amplitudes. In the next subsection we provide a detailed analysis of this error.

#### 4.4. $TI$ vs. Tilt Angle

Figure 10 shows the  $TI$  values binned by mean tilt angles.  $TI$  measured by the land-based reference lidar lies between 3.5% and 6.3%. Low tilt angles are correlated with high  $TI$  values via low wind speeds. High tilt angles are also correlated with high  $TI$  values via rough sea states. It is therefore not surprising that we do not see a systematic trend in the fixed reference lidar measurements.

The floating lidar overestimates  $TI$ . The extent of this overestimation is strongly dependent on the tilt amplitude. Strong motion leads to measurements of high motion-induced  $TI$ . When the mean tilt amplitude is below  $\bar{\alpha} < 1^\circ$ , the measured motion-induced  $TI$  is only 0.04%, which seems unrealistically low in comparison to the value of 0.63% measured for  $1^\circ < \bar{\alpha} < 1.5^\circ$ . The reason could be that the reference lidar always measures slightly higher amounts of  $TI$  compared to the floating lidar due to its elevated location and lower measurement height above the ground.

Moreover, the motion compensation algorithm shows steadily increasing motion-induced turbulence intensities for increasing tilt angles. However, while it slightly underestimates the real conditions in most cases, an overestimation of the motion-induced turbulence is found at high tilt angles  $\bar{\alpha} > 5^\circ$ . We suspect that deviations between the lidar's internal data processing and the results of our emulated processing correlate with the overestimation of motion-induced  $TI$ . We therefore included the relative deviation of the mean wind speeds from internal processing  $U_{\text{unc}}$  and emulated processing  $U_{\text{emu,unc}}$  into Figure 10 and see that the highest emulation error coincides with the overestimation of motion-induced  $TI$  at high tilt amplitudes. A high emulation error is probably due to the presence of clouds or fog that are handled differently by internal and emulated data processing. Nearly all of the 100 intervals in the high tilt bin are shown in the strong motion example given in Figure 11, which we will analyze next.

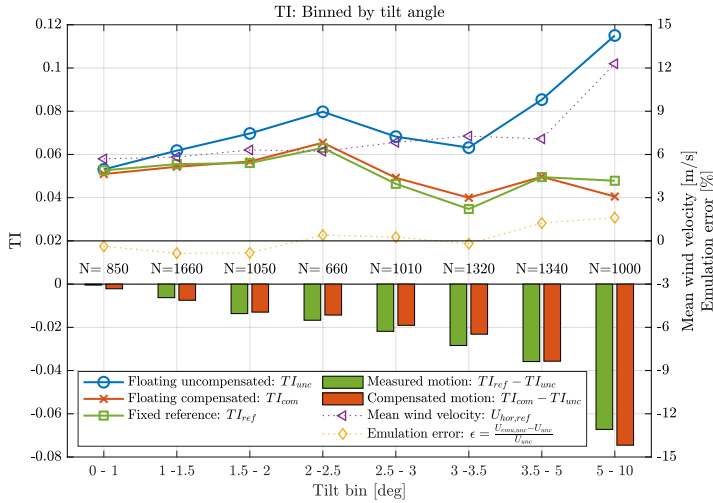


**Figure 10.** TI from all measurement heights binned by  $\bar{\alpha}$ , the mean tilt angle of the buoy. Legend as in Figure 8 plus markers for the horizontal mean wind velocity  $U$  and the relative emulation error  $\epsilon$  that refer to the right hand side  $y$ -axis.

4.5. Individual Error Analysis

All 889 intervals that contain measurements of 10 comparable height levels are shown in Figure 11a. The figure depicts the difference between the TI values of the floating lidar and the fixed reference lidar. These differences are the measurement error of the floating lidar with regard to the fixed reference lidar. In accordance with the color scheme used for the profiles in Figures 8–10, the errors of the uncompensated lidar are marked in blue, and the values of the compensated lidar are marked in red. The degree of transparency of each marker represents the measurement height at which the corresponding values are taken. Increasing transparency means increasing height. In addition to the individual values, the moving means over 30-minutes of data are also plotted. Positive values mean higher TI measured by the floating lidar. In gray, the mean tilt amplitude  $\bar{\alpha}$  is also plotted, which is a good indicator of the error of the uncompensated floating lidar.

We see clearly that the biggest errors are found where the tilt angle is highest. Subfigure b to the left under the main plot zooms into this strong motion case with a mean tilt amplitude of  $\bar{\alpha} > 5^\circ$ . TI measured by the uncompensated floating lidar is much higher than the reference measurements for nearly all intervals. However, around intervals 375, 422, and 437, they drop significantly, and at interval 452, the turbulence measured by the floating lidar without any compensation is even lower than the measurements from the fixed reference. This is even more surprising when considering that the mean tilt amplitude during these intervals is always  $> 5^\circ$ . We must therefore assume severe measurement issues in one or both of the lidars. This assumption is supported by finding high emulation errors at the same time intervals. This emulation error marked in yellow is, as explained before, an indirect measure of the amount of filtering or cloud detection in the internal data processing of the floating lidar. The values of motion-compensated TI in the proximity of these four intervals (375, 422, 437, and 452) are on average below the reference line. We remember from Figure 10 that the strong wind case which we look at here is characterized by overcompensated motion. But now it appears that the error does not lie in the motion compensation but might already be contained in the turbulence measurements of one or both of the lidar units. To strengthen this hypothesis, we now look at the test cases with low motion where  $\bar{\alpha} < 1^\circ$ , shown in detail in the next subfigure.

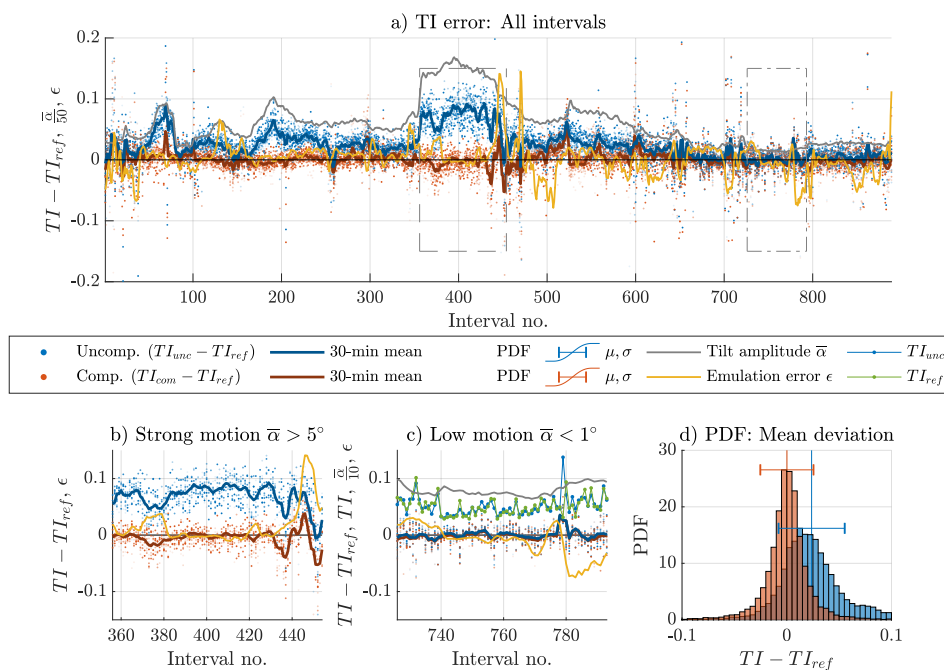


**Figure 11.** Top: (a) Overview of the individual error between  $TI$  measured by reference lidar and uncompensated floating lidar (blue) and compensated floating lidar (red). Bottom: Close up view of two examples of the plot above where the motion-induced turbulence is particularly high (b) and low (c). (d) Probability density functions (PDF) of the error

The intervals in Figure 11c are in general characterized by a low error between floating and fixed lidar measurements visible by the floating mean lines fluctuating around zero. The effect of applied motion compensation is so low that both lines often overlap, which is reasonable, since the mean tilt amplitude is always very low with an average value of  $\bar{\alpha} \approx 0.8^\circ$ . Around interval 779 the  $TI$  error suddenly jumps to 3% for both the uncompensated and the compensated cases, which have nearly identical values. The cause of this significant error becomes clear when the 10-min mean values of  $TI_{ref}$  of the fixed reference lidar (green lines) are compared with the  $TI_{unc}$  of the uncompensated floating lidar (blue lines with markers). During interval 779, the floating lidar measures much stronger  $TI$  values than the reference lidar. We think that the discrepancy between these two measurements cannot be caused by the very low motion of the floating lidar. Instead, we assume that it is caused by poor signal quality of the floating lidar in this particular situation. We cannot test this hypothesis, but it is supported by the high level of activity of the filter in the floating unit just before and after the suspicious interval.

The low motion case can be used for a second purpose, which is the approximate estimation of the scatter resulting from measurements with two lidars at two different locations that take a low number of samples per ten-minute interval ( $N \approx 37$ ). The average  $TI$  measured by the reference lidar during the low motion case is  $TI_{ref,low} = 5.1\%$ . The turbulence conditions are thus representative of the complete studied dataset ( $TI_{ref} = 5.0\%$ ). The motion-induced  $TI$  for the low motion case according to the motion compensation algorithm is just 0.2%. This value is so low that we now assume that the uncompensated measurements from the floating lidar during the low motion case are comparable to measurements from a fixed lidar. The error we find between the floating lidar and the fixed reference must therefore be caused by the measurement setup. We calculate the standard error of the uncompensated samples in the low motion case to be  $\sigma_{err,unc,low} = 2.0\%$ . This means the statistical error involved in sampling

independent wind vectors with two lidar devices and only 37 measurements per ten minutes is  $\frac{2.0\%}{5.1\%} \approx 40\%$  of the measured  $TI$ . Expressed differently, this means that  $\frac{2.0\%}{2.5\%} \approx 80\%$  of the total standard error we find in the compensated data for the entire campaign ( $\sigma_{\text{err,com}} = 2.5\%$ ) is caused by the measurement setup.

The histogram plotted in Figure 11d shows the probability density function of all individual samples of the error between floating and reference lidar for uncompensated (blue) and compensated (red) measurement data. While the uncompensated values show a bias of  $\mu_{\text{err,unc}} = 2.37\%$  and a standard deviation of  $\sigma_{\text{err,unc}} = 3.16\%$ , the compensated values show a bias of only  $\mu_{\text{err,com}} = 0.01\%$  and a standard deviation of  $\sigma_{\text{err,com}} = 2.54\%$ . Uncompensated values have a positive skewness of  $s_{\text{err,unc}} = 0.42$ . The motion compensation reduces this positive skewness and results in  $s_{\text{err,com}} = 0.22$ . The remaining skewness can be explained by the possibility for  $TI$  values to theoretically be infinitely high but not negative. This limitation explains the skewness, which means that high positive error values are more likely than high negative error values.

The analysis of the  $TI$  error leads to the conclusion that the biggest errors found between the motion-compensated  $TI$  values from the floating lidar, and the  $TI$  values from the reference lidar are likely not caused by an insufficiency of the motion compensation but rather by measuring  $TI$  with two different units at two different locations. A longer dataset would probably mitigate the resulting effect on statistical  $TI$  profiles like Figures 9 and 10.

#### 4.6. Scatter Analysis

Figure 12 shows a scatter plot of the results. For each single  $TI$  measurement from each measurement height, we plot the value of the floating lidar on the  $y$ -axis and the value of the fixed reference lidar on the  $x$ -axis. The uncompensated data pairs are, as before, marked in blue, while the results after compensation are shown in red. Additionally, here, the degree of transparency of each marker represents the measurement height. Because all three datasets were acquired using the same lidar measurement technology, we can assume that the reference values from the fixed land-based lidar have significant uncertainty as high as the uncertainty of the floating lidar with perfect motion compensation. We therefore decided to add Deming regression lines with  $\lambda = 1$  according to Adcock [30] that are characterized by having minimized squared perpendicular distances from the data points. This orthogonal regression avoids the positive offset and slope  $< 1$  found when conventional linear regression is applied to data with similar uncertainty for  $x$  and  $y$  values [31]. Data pairs from a perfectly motion-compensated and a fixed lidar would be scattered around the  $y = x$  diagonal line (black dashed line). It is apparent also from the scatter plots that the uncompensated  $TI$  estimates of the floating lidar are too high, as most blue markers lie above the  $y = x$  line. This overestimation of  $TI$  or positive turbulence intensity error appears to be nearly constant across the entire range of turbulence intensities contained in the dataset. The blue regression line shows an offset of 2.2% for very low turbulence cases. With its slope of 1.04, it reaches an error of 2.6% for  $TI_{\text{ref}} = 10\%$  where the data density is too low for statistically relevant conclusions. The standard error of the regression line is  $\sigma = 0.16$ .

The red markers representing the compensated floating lidar results versus the reference lidar also show high scatter of  $\sigma = 0.13$ , which is nearly centered around the  $y = x$  line. The determined offset at the origin is only  $-0.03\%$  and the slope of 1.01 leads to an error of motion-induced turbulence of 0.07% for cases with  $TI_{\text{ref}} = 10\%$ . Due to the minimization of the quadratic distances, the influence of data points with high scatter is overrepresented in the calculation of the regression lines. But a repeated analysis that excluded all  $TI$  values  $> 10\%$  showed a regression line with a slope of 0.98, an offset of 0.1%, and  $\sigma = 0.08$ . These values predicted by the linear regression model are very good.

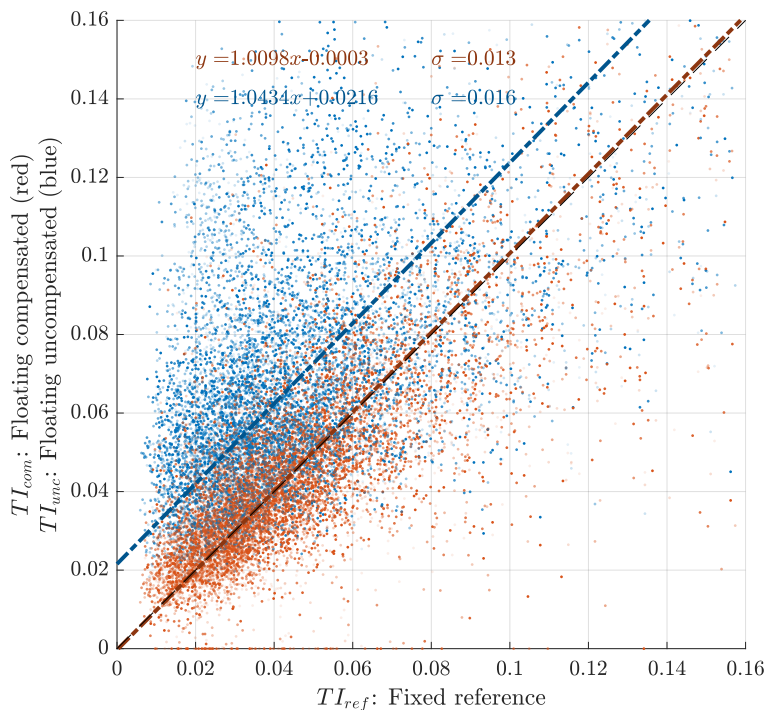


**Figure 12.** Scatter plot of turbulence intensities from the floating lidar uncompensated (blue) and compensated (red) vs. from the land-based reference lidar. Deming regression lines are given in corresponding colors. The equations of the regression lines and their standard deviations are listed. The black dashed line is the  $y = x$  line. Some datapoints lie outside the plotted area.

## 5. Conclusions

We show that estimates of  $TI$  measured by a floating VAD scanning continuous-wave wind lidar are comparable to those of a fixed land-based reference lidar of the same type when implementing an algorithm to compensate for the motion of the floating lidar at the line-of-sight level in all six degrees of freedom. A comparison of mean values of  $TI$  shows good agreement between motion-compensated measurements from a floating lidar and a fixed reference lidar for a wide range of mean wind speeds and buoy tilt angles. Strong scatter caused by the low sampling rate of the reconstructed wind vectors at each measurement height is present in the results due to the high number of scanned elevation levels (eleven), which results in a low number of samples per ten-minute interval. Additionally, the relatively wide spatial separation between the floating lidar and the land-based reference lidar (370 m) increases the expected amount of scatter. All reported  $TI$  values are lidar-measured. We expect them to deviate from the real  $TI$  values and in this study do not try to assess or improve the capability of profiling wind lidars to measure turbulence.

Successful motion compensation requires reliable time synchronization between motion data and lidar data. We achieved this by computing the motion compensation within a range of time lags and selecting the offset that results in the strongest reduction in measured wind velocity variance. A more native solution, e.g., by increasing the resolution of the timestamp information of the lidar, would be desirable. The method presented in this study requires access to the line-of-sight wind velocity estimates of the ZX300 wind lidar. We therefore saved Doppler spectra measured by the unit on a connected PC. This prevents the presented method from being applied on existing ZX300 data without stored line-of-sight data. To determine the line-of-sight velocities from the Doppler spectra, we employ

a simple centroid method which deviates from the internal data processing that we do not have access to. To still get reliable motion-compensated turbulence information, we subtract the motion-induced  $TI$  calculated by our own processing from the values estimated by the lidar's internal data processing. It would be advantageous if the internally processed line-of-sight velocities were available for motion compensation by default, as is the case for example for the Windcube by Leosphere (Saclay, France). Moreover, the availability of signed line-of-sight velocities would help to improve the accuracy of motion compensation. Suggestions on how to determine the direction of the radial velocities measured by continuous-wave wind lidars can be found in [32,33].

Further research should analyze measurements of a floating and a closely collocated fixed lidar that simultaneously measure at only one height level. Such a setup would result in much smaller statistical error and would perhaps make a time series comparison useful. Applying the method presented here to a Doppler beam swinging wind lidar, such as the Windcube, could be a different option for further work. This lidar type outputs its internally processed line-of-sight velocities by default, but the accumulation time spent in each beam direction must be considered when processing motion data.

**Author Contributions:** conceptualization, F.K.; data curation, F.K.; formal analysis, F.K.; funding acquisition, V.N. and L.L.; investigation, V.N. and L.L.; methodology, F.K.; project administration, V.N. and L.L.; software, F.K.; supervision, T.B. and J.M.; visualization, F.K.; writing—original draft, F.K.; writing—review and editing, F.K., T.B., and J.M. All authors have read and agreed to the published version of the manuscript.

**Funding:** The Norwegian Public Roads Administration (Statens vegvesen) as part of the project “Metocean Data for Large Fjord Crossings on the E39” funded the SEAWATCH Wind LiDAR Buoy, including its measurement instrumentation. The presented work is part of a PhD project funded by Energy and Sensor Systems (ENERSENSE) at the Norwegian University of Science and Technology. The APC was funded by NTNU's Publishing Fund.

**Acknowledgments:** We acknowledge the work of Kam Sripada, who proofread the manuscript.

**Conflicts of Interest:** The authors declare no conflict of interest. The funders had no role in the design of the study; in the collection, analyses, or interpretation of data; in the writing of the manuscript, or in the decision to publish the results.

## Abbreviations

The following abbreviations are used in this article:

LOS	Line-of-sight
MRU	Motion reference unit
NWU	North-west-up
Res.	Resonance
Rot.	Rotational
Std. dev.	Standard deviation
$TI$	Turbulence intensity
Transl.	Translational
VAD	Velocity–azimuth display

## References

1. Petersen, S.; Sarmiento, A.; Cândido, J.; Godreau, C. Preliminary study on an offshore wind energy resource monitoring system. In *Renewable Energies Offshore*; Soarez, C.G., Ed.; Taylor & Francis: Abingdon, UK, 2015; pp. 213–218.
2. Gottschall, J.; Gribben, B.; Stein, D.; Würth, I. Floating lidar as an advanced offshore wind speed measurement technique: Current technology status and gap analysis in regard to full maturity. *WIREs Energy Environ.* **2017**, *6*. [[CrossRef](#)]
3. The Carbon Trust. Carbon Trust Offshore Wind Accelerator Roadmap for the Commercial Acceptance of Floating LiDAR Technology. Version 2.0, October 2018.

4. Tiana-Alsina, J.; Rocadenbosch, F.; Gutiérrez-Antuñano, M.A. Vertical azimuth display simulator for wind-Doppler lidar error assessment. In Proceedings of the 2017 IEEE International Geoscience and Remote Sensing Symposium (IGARSS), Fort Worth, TX, USA, 23–28 July 2017; pp. 1614–1617. [[CrossRef](#)]
5. Gottschall, J.; Wolken-Möhlmann, G.; Viergutz, T.; Lange, B. Results and conclusions of a floating-lidar offshore test. *Energy Procedia* **2014**, *53*, 156–161. [[CrossRef](#)]
6. Mathisen, J.P. Measurement of wind profile with a buoy mounted lidar. In Proceedings of the 10th Deep Sea Offshore Wind R&D Conference, DeepWind'2013, Trondheim, Norway, 24–25 January 2013.
7. Gutiérrez-Antuñano, M.A.; Tiana-Alsina, J.; Salcedo, A.; Rocadenbosch, F. Estimation of the Motion-Induced-Horizontal-Wind-Speed Standard Deviation in an Offshore Doppler Lidar. *Remote Sens.* **2018**, *10*, 2037. [[CrossRef](#)]
8. Tiana-Alsina, A.J.; Gutiérrez, M.A.; Würth, I.; Puigdefábregas, J.; Rocadenbosch, F. Motion compensation study for a floating Doppler wind LiDAR. In Proceedings of the 2015 IEEE International Geoscience and Remote Sensing Symposium (IGARSS), Milan, Italy, 26–31 July 2015. [[CrossRef](#)]
9. Gutiérrez, M.A.; Tiana-Alsina, J.; Bischoff, O.; Cateura, J.; Rocadenbosch, F. Performance evaluation of a floating Doppler wind lidar buoy in mediterranean near-shore conditions. In Proceedings of the 2015 IEEE International Geoscience and Remote Sensing Symposium (IGARSS), Milan, Italy, 26–31 July 2015. [[CrossRef](#)]
10. Yamaguchi, A.; Ishihara, T. A new motion compensation algorithm of floating lidar system for the assessment of turbulence intensity. *J. Phys. Conf. Ser.* **2016**, *753*. [[CrossRef](#)]
11. Gottschall, J.; Wolken-Möhlmann, G.; Lange, B. About offshore resource assessment with floating lidars with special respect to turbulence and extreme events. *J. Phys. Conf. Ser.* **2014**, *555*. [[CrossRef](#)]
12. Sathe, A.; Mann, J.; Gottschall, J.; Courtney, M.S. Can wind lidars measure turbulence? *J. Atmos. Ocean. Tech.* **2011**, *28*, 853–868. [[CrossRef](#)]
13. Kelberlau, F.; Mann, J. Better turbulence spectra from velocity-azimuth display scanning wind lidar. *Atmos. Meas. Tech.* **2019**, *12*, 1871–1888. [[CrossRef](#)]
14. Kelberlau, F.; Mann, J. Cross-contamination effect on turbulence spectra from Doppler beam swinging wind lidar. *Wind Energy Sci. Discuss.* **2019**. [[CrossRef](#)]
15. Emeis, S. *Wind Energy Meteorology*, 2nd ed.; Springer International Publishing AG: Berlin/Heidelberg, Germany, 2018. [[CrossRef](#)]
16. Grewal, M.S.; Weill, P.L.R.; Andrews, A.P. *Global Positioning Systems, Inertial Navigation, and Integration*; chapter Appendix C: Coordinate Transformations; John Wiley & Sons Inc.: Hoboken, NJ, USA, 2006; pp. 456–501. [[CrossRef](#)]
17. Cole, I.R. Modelling CPV. Ph.D. Thesis, Loughborough University, Loughborough, UK, 2015.
18. Gottschall, J.; Catalano, E.; Dörenkämper, M.; Witha, B. The NEWA Ferry Lidar Experiment: Measuring Mesoscale Winds in the Southern Baltic Sea. *Remote Sens.* **2018**, *10*, 1620. [[CrossRef](#)]
19. Zhai, X.; Wu, S.; Liu, B.; Song, X.; Yin, J. Shipborne Wind Measurement and Motion-induced Error Correction of a Coherent Doppler Lidar over the Yellow Sea in 2014. *Atmos. Meas. Tech.* **2018**, *11*, 1313–1331. [[CrossRef](#)]
20. Wolken-Möhlmann, G.; Lilov, H.; Lange, B. *Simulation of Motion Induced Measurement Errors for Wind Measurements Using LIDAR on Floating Platforms*; Fraunhofer IWES: Bremerhaven, Germany, 2010.
21. Branlard, E.; Pedersen, A.T.; Mann, J.; Angelou, N.; Fischer, A.; Mikkelsen, T.; Harris, M.; Slinger, C.; Montes, B. Retrieving wind statistics from average spectrum of continuous-wave lidar. *Atmos. Meas. Tech.* **2013**, *6*, 1673–1683. [[CrossRef](#)]
22. Angelou, N.; Foroughi Abari, F.; Mann, J.; Mikkelsen, T.; Sjöholm, M. Challenges in noise removal from Doppler spectra acquired by a continuous-wave lidar. In Proceedings of the 26th International Laser Radar Conference, Porto Heli, Greece, 25–29 June 2012.
23. Pitter, M.; Slinger, C.; Harris, M. Introduction to continuous-wave Doppler lidar. In *Remote Sensing for Wind Energy*; DTU Wind Energy-E-Report-E-0084; DNV GL-Energy: Kaiser-Wilhelm-Koog, Germany, 2015.
24. Mann, J.; Peña, A.; Bingöl, F.; Wagner, R.; Courtney, M.S. Lidar scanning of momentum flux in and above the surface layer. *J. Atmos. Ocean. Technol.* **2010**, *27*, 959–976. [[CrossRef](#)]
25. Dellwik, E.; Mann, J.; Bingöl, F. Flow tilt angles near forest edges – Part 2: Lidar anemometry. *Biogeosciences* **2010**, *7*, 1759–1768. [[CrossRef](#)]

26. Mark, A.; Köhne, V.; Stein, D. *Assessment of the Fugro OCEANOR Seawatch Wind LiDAR Buoy WS 170 Pre-Deployment Validation at Frøya, Norway*; Technical Report GLGH-4270 17 14462-R-0002, Rev. C; DNV GL-Energy: Kaiser-Wilhelm-Koog, Germany, 2017.
27. Wylie, S. Turbulence Intensity measurements from a ground-based vertically-profiling lidar. In Proceedings of the WindEurope Resource Assessment Workshop Session 4: Using Lidar to Reduce Uncertainty, Brussels, Belgium, 27–28 June 2019.
28. Türk, M.; Emeis, S. The dependence of offshore turbulence intensity on wind speed. *J. Wind Eng. Ind. Aerodyn.* **2010**, *98*, 466–471. [[CrossRef](#)]
29. Svensson, N.; Arnqvist, J.; Bergström, H.; Rutgersson, A.; Sahlée, E. Measurements and Modelling of Offshore Wind Profiles in a Semi-Enclosed Sea. *Atmosphere* **2019**, *10*, 194. [[CrossRef](#)]
30. Adcock, R.J. A Problem in Least Squares. *Analyst* **1878**, *5*, 53–54. [[CrossRef](#)]
31. Cornbleet, P.J.; Gochman, N. Incorrect least-squares regression coefficients in method-comparison analysis. *Clin. Chem.* **1979**, *25*, 432–438. [[CrossRef](#)] [[PubMed](#)]
32. Abari, C.F.; Pedersen, A.T.; Mann, J. An all-fiber image-reject homodyne coherent Doppler wind lidar. *Opt. Express* **2014**, *22*, 25880–25894. [[CrossRef](#)] [[PubMed](#)]
33. Gao, S.; Hui, R. Frequency-modulated continuous-wave lidar using I\Q modulator for simplified heterodyne detection. *Opt. Lett.* **2012**, *37*, 2022–2024. [[CrossRef](#)] [[PubMed](#)]



© 2020 by the authors. Licensee MDPI, Basel, Switzerland. This article is an open access article distributed under the terms and conditions of the Creative Commons Attribution (CC BY) license (<http://creativecommons.org/licenses/by/4.0/>).